

Modeling Surface-Atmosphere Exchange of Trace Gases and Energy within and above the Amazon Rain Forest

D I S S E R T A T I O N

Zur Erlangung des Grades
Doktor der Naturwissenschaften
Am Fachbereich Biologie
Der Johannes Gutenberg-Universität Mainz

Eric Simon

geboren am 23.2.1972
in Bernkastel-Kues

Mainz, 13. September 2004

Jahr der mündlichen Prüfung: 2004
D77 - Mainzer Dissertation

*“... die Tränen von gestern wird die Sonne trocknen,
und die Spuren der Verzweiflung wird der Wind verweh'n ...”*

(TON-STEINE-SCHERBEN)

Preface

The present dissertation is a result of more than three years of work which I carried out at the Max Planck Institute for Chemistry in Mainz. The dissertation focuses on the biogeochemistry of the vegetation layer (canopy) and the interactions between physiological and environmental processes which affect the climate and chemistry of the lower atmosphere. A main task is the quantification of vertical exchange of trace gases and energy with theoretical concepts considering the links and feedbacks between the partitioning of energy at the leaf surface, the uptake of CO₂, the emission of biogenic volatile organic compounds (VOC), the dry deposition of ozone, the vertical transport within the canopy and the ecosystem net exchange (vertical fluxes). This is achieved by implementing a sophisticated multi-layer canopy scheme of energy and trace gas exchange which is combined with a Lagrangian description of vertical transport within the canopy. Thereby, extensive data sets of field measurements in Amazonia are considered. Additionally, an alternative approach is applied to infer the link between physiological parameters of CO₂ and H₂O exchange and the emission of isoprene and monoterpenes, representing the most important non-methane VOC's. The tropical Amazon rain forest is still the largest forest ecosystem on earth and plays a particular role in the global climate. Therefore, a very detailed description and discussion of the canopy biochemistry and vertical exchange characteristics is given. Although the applied techniques and concepts are also applicable to other ecosystem types, the present work is restricted to the tropical rain forest canopy and does not consider the effects of deforestation and land-use change.

The work is organized in six chapters: *Chapter 1* contains a general introduction describing briefly the particular role of the terrestrial vegetation in the global climate system and current trends of climate change. After a description of methods and models of surface exchange, it leads to a comparison of different canopy model types and the motivation for the present work. The canopy model which has been developed for the present study, is described in the second part of Chapter 1. In *Chapter 2* the parameterizations for soil surface exchange,

canopy structure, the profile of horizontal wind speed, and the biochemistry of the rain forest canopy are inferred using available data sets from different intensive campaigns in Amazonia. Additionally, the calculations related to radiation attenuation and leaf surface exchange are evaluated and the uncertainty of key parameters is assessed. The vertical transport within the multi-layer scheme is simulated with a Lagrangian approach which is parameterized and evaluated in detail in *Chapter 3* using in-canopy turbulence measurements and observations of ^{222}Rn as a tracer of vertical dispersion, respectively. The radioactive ^{222}Rn is an inert gas emitted from natural soils. Special emphasis is given on nighttime conditions where common micrometeorological methods fail to produce reliable results (Eddy Covariance technique, \rightarrow EC). In *Chapter 4*, the canopy scheme is applied to late wet and late dry season conditions at a remote rain forest site in Rondônia, southwest Amazonia. Model predicted in-canopy profiles of CO_2 , H_2O , ozone, and isoprene concentration for day- and nighttime conditions are compared to observations. Predicted fluxes of sensible and latent heat, CO_2 and ozone are compared to EC measurements considering the effect of canopy storage. The sensitivity of model predictions to key parameters' uncertainties and the observed seasonality of net assimilation and transpiration are assessed. An alternative approach to predict the emission of VOC's is presented in *Chapter 5*. Isoprene and monoterpene emissions of different tree species from different seasons growing in different light environments are related to environmental and leaf physiological parameters using a neuronal approach. The performance of different parameter combinations serving as predictors of VOC emissions are compared to the results of the quasi-standard emission algorithm for isoprene given by Guenther et al. (1993). *Chapter 6* offers a summary and the main conclusions of the dissertation. Detailed descriptions of the canopy model calculations, the radon soil flux measurements, the neuronal approach and the applied or derived parameterizations are given in the *Appendices*, containing additionally a list of abbreviations and symbols.

Contents

1	Introduction	1
1.1	Background and motivation	1
1.2	Model description	5
1.2.1	General concept	5
1.2.2	Radiation absorption and surface exchange	8
2	Parameterization of Amazon rain forest surface characteristics	13
2.1	Introduction	14
2.2	Material and method	14
2.2.1	Inferred parameterizations	14
2.2.2	Site description and field data	17
2.3	Results and discussion	21
2.3.1	Inferring a mean canopy structure for Amazon rain forest	21
2.3.2	Inferring a normalized profile of horizontal wind speed	23
2.3.3	Evaluation of calculations related to radiation	24
2.3.4	Inferring parameters related to soil surface exchange	28
2.3.5	Inferring the light acclimation of photosynthetic capacity	29
2.3.6	Evaluation of calculations related to leaf surface exchange	31
2.4	Conclusions	36
3	On Lagrangian dispersion of ^{222}Rn, H_2O, and CO_2	39
3.1	Introduction	40
3.2	Material and method	42
3.2.1	Field data and measurement overview	42
3.2.2	Measurements of canopy structure at the Cuieiras site	44
3.2.3	Radon measurements	45
3.2.4	Implementation of the Localized Near-field theory (LNF)	46
3.3	Results and discussion	48
3.3.1	Parameterization of in-canopy turbulence profiles	48

3.3.2	Meteorological conditions at the Cuieiras site	51
3.3.3	Observed radon soil fluxes at the Cuieiras site	52
3.3.4	Forward modeling of ^{222}Rn activity concentrations	54
3.3.5	Effective transfer velocities and timescales	56
3.3.6	Inverse predictions of ^{222}Rn fluxes	56
3.3.7	Net fluxes for CO_2 , latent and sensible heat	57
3.3.8	Diurnal source/sink distributions for CO_2 and H_2O	60
3.3.9	Daily integrated net carbon exchange	62
3.4	Conclusions	63
4	Modeling seasonal exchange of energy, CO_2, isoprene, and ozone	65
4.1	Introduction	66
4.2	Material and method	67
4.2.1	Site location, period and field data	67
4.2.2	Meteorological overview	68
4.2.3	Model setup	70
4.2.4	Calculation of storage terms	71
4.2.5	Calculation of isoprene emission and ozone deposition	72
4.3	Results and discussion	73
4.3.1	Stable solutions for steady-state environmental conditions	73
4.3.2	Model sensitivity to key parameter uncertainty	76
4.3.3	Evaluating seasonal predictions of CO_2 and energy exchange	79
4.3.4	Evaluating seasonal predictions of isoprene exchange	86
4.3.5	Seasonal comparison and evaluation of predicted ozone exchange	90
4.4	Further model application examples	94
4.4.1	Global isoprene emissions from tropical rain forest	94
4.4.2	Seasonal comparison of predicted climate change due to elevated atmospheric CO_2 levels	95
4.5	Conclusions	96
5	Neuronal modeling of biogenic VOC emission	99
5.1	Introduction	100
5.2	Field measurements and site description	102
5.3	Neuronal approach	103
5.3.1	Simulations performed	104
5.3.2	Selection of input parameters	105
5.3.3	Parameter combinations	106
5.3.4	Aggregation of data sets	107
5.3.5	Derivation of network parameters	108
5.4	Results and Discussion	110
5.4.1	Approximating the algorithm of Guenther et al. (1993)	110
5.4.2	Single data sets with different parameter combinations	111

5.4.3	Aggregated data sets with different parameter combinations	114
5.5	Conclusions	120
6	Summary and main findings	123
	Bibliography	126
A	Calculations related to the canopy exchange scheme	147
A.1	The biochemical model of leaf photosynthesis	147
A.2	Radiative transfer parameters	149
A.3	Long-wave radiation	149
A.4	Solar parameters	150
A.5	The numerical solution of the leaf energy balance	151
A.6	Parameterization of soil surface exchange	152
A.7	Special functions	153
A.8	The normalized height function for the standard deviation of vertical wind speed (σ_w)	154
A.9	The isoprene emission algorithm of Guenther et al. (1993)	154
B	Calculations related to ^{220}Rn and ^{222}Rn flux measurements	157
C	The neuronal network with back propagation (BPN)	159
D	List of symbols and abbreviations	161
D.1	Abbreviations	161
D.2	Greek symbols	162
D.3	Latin symbols	162
	List of figures	165
	List of tables	169
	Zusammenfassung	171
	Selbständigkeitserklärung	174

1.1 Background and motivation

Atmospheric climate and the terrestrial vegetation The terrestrial vegetation contributes more than 60% to the global net primary production, which exceeds the annual CO₂ fossil fuel emissions by a factor of 10 (Jones, 1992). The vegetation also emits a large amount of (non-methane) volatile organic compounds (VOC) like isoprene and monoterpenes, (Guenther et al., 1995; Kesselmeier and Staudt, 1999), which co-regulate with NO_x (NO+NO₂) the formation of tropospheric ozone and OH radicals. Furthermore, it plays an important role in the life-time and abundance of air pollutants like ozone, SO₂, SO₄⁻² and NO_x, which are removed at the surfaces by dry deposition (Ganzeveld and Lelieveld, 1995; Wesely and Hicks, 2000). A substantial part of dry deposition is represented by active uptake into the leaf tissue and occurs mainly through the leaf stomatal pores. The stomatal opening regulates also transpiration and thus the partitioning of available energy into sensible and latent (water vapor) heat, which again determines the temperature of the surface and the climate of the atmospheric boundary-layer (represented by the lowest 100-1500 m of the atmosphere). As the largest forest ecosystem on earth the Amazon basin plays a particular role in the global climate. Additionally to the points mentioned above, the tropical rain forest contributes to the global budget of OH radicals and determines the oxidative power of the troposphere.

Global climate change Within the last decades, our understanding of atmospheric chemistry and climate has substantially improved. Until the beginning of the eighties, the general picture of the global climate system was relatively static. Climatic changes used to be regarded as geological processes taking place on large timescales of millions or at least thousands of years. The delicate balance between the biosphere and atmosphere has been recognized latest with the discovering of the “ozone hole” (Farman et al., 1985) and the key chemical mech-

anisms leading to stratospheric ozone depletion by chlorofluorocarbons (Molina and Molina, 1987). As a success of the International Montreal Protocol (1987) that regulates the emissions of ozone depleting substances, it is now expected that stratospheric ozone depletion due to halogens will recover during the next 50 to 100 years (Hofmann and Pyle, 1999). Concomitantly with stratospheric ozone the increasing atmospheric levels of other greenhouse gases came into discussion, e.g. the global mean concentrations of CO_2 , CH_4 and N_2O , which have been increased by 90 ppm (31%), 1050 ppb (151%), and 46 ppb (17%), respectively, in year 2000 compared to pre-industrialized periods (from year 1000 to 1750, see IPCC, 2001). As a direct effect of this climate forcing, the mean global temperature is expected to rise. Another serious problem is caused by air pollutants like NO_x , ozone, and aerosols, which represent immediate risk factors for biological organisms. In contrast to stratospheric ozone, tropospheric ozone is increasing ($35 \pm 15\%$ since the year 1750) due to the changing constitution and chemistry of the lower atmosphere (Crutzen et al., 1999; Lelieveld and Dentener, 2000). The projected longterm climate changes are still very uncertain. For example, current future scenarios predict a mean global surface temperature increase range of 1.4-5.8°C within the next hundred years (compared to 0.6°C in the 20th century) with a stabilizing atmospheric CO_2 concentration at 450-1200 ppm (IPCC, 2001). One reason for the high uncertainties of future climate scenarios are poorly understood potential feedbacks between the terrestrial vegetation and the changing climate conditions. In recent global modeling studies, the exchange processes at the surface are mostly treated as lower boundary conditions, which are parameterized by simple relationships. These relationships are purely empirical and can not be extrapolated to changing environmental conditions. The vegetation for example, will acclimate to increasing atmospheric CO_2 , surface temperatures and respond differently compared to the present day climate.

Different schemes of canopy exchange In fact, the surface schemes applied in current global circulation models are actually changing towards a new generation of deterministic and “interactive” canopy models. This is illustrated in Fig. 1.1 showing chronologically three different types of canopy models with increasing complexity. The most simplest approach assumes that the soil surface and the foliage are at the same temperature (Noilhan and Planton 1989, Fig. 1.1a). The surface conductance to water vapor flux determining the partitioning of available energy and surface temperature is described by a single bulk stomatal resistance r_s regulating the flux pathway between the surface layer and the air above. In a more realistic approach, soil and foliage temperature are allowed to differ and the fluxes at the soil and vegetation layer are calculated separately (Deardorff 1978, Fig. 1.1b). By including detailed descriptions of the soil moisture (Dickinson et al., 1993), radiation reflectance and canopy photosynthesis (Sellers et al., 1986, 1992, 1996) and dry deposition (Ganzeveld and Lelieveld, 1995), this model

type has become very complex. However, the canopy is still treated as one big leaf, which is parameterized “top-down” applying purely empirical relationships. In contrast, the design of the third model type (Fig. 1.1c) can be classified as a “bottom-up” scheme (Jarvis, 1993) that includes multiple canopy layers connected through a transport matrix (Raupach, 1989b; Baldocchi and Meyers, 1998). The leaf energy balance is solved numerically by the iterative calculation of the leaf surface exchange to obtain r_s, r_b and T_s , and the vertical exchange to obtain T_a . The latter approach is also applied in the present study.

Quantification of surface exchange The parameterization and calibration of any canopy model requires field observations, which are usually provided by enclosure (\rightarrow chamber) measurements at the leaf scale and micrometeorological measurements at the canopy scale. The enclosure techniques are well suited to obtain trace gas exchange rates from soil samples and single leaves or plants, which can be related to environmental factors. This is very helpful to establish relationships for trace gas emission or deposition e.g. for VOC’s (Guenther et al., 1995; Kesselmeier and Bode, 1997; Kesselmeier and Staudt, 1999), which can be used for regional or global estimates. However, the up-scaling of leaf scale measurements is highly uncertain because of large species dependent variabilities and the long- and short-term adaptations of ecophysiological processes to environmental conditions. Therefore, canopy fluxes are mostly derived by micrometeorological techniques, averaging over a larger horizontal area¹. The intensive application of the “Eddy Covariance” technique (EC) as the most prominent micrometeorological method, led to the implementation and operation of continental flux monitoring networks in North America and Europe (Kaiser and Schmidt, 1998; Gu and Baldocchi, 2002; Falge et al., 2002). The LBA initiative² operates a similar network of towers in the Amazon basin and coordinates the international climate research in Amazonia. All these efforts led to a tremendous increase of flux data, which are helping to quantify the surface exchange of energy and CO₂. However, the EC approach is limited to fetch conditions (horizontally homogenous surface) and still raises up unresolved problems i.e. the imbalance of the energy budget closure (Wilson et al., 2002) and the high uncertainty of nighttime fluxes (Goulden et al., 1996; Mahrt, 1999). Furthermore, it is also restricted to trace gases where fast-response sensors are available (H₂O, CO₂, O₃). The application of relaxed methods (e.g. “Relaxed Eddy Accumulation”), which were developed for other trace gases like VOC’s is much more difficult and probably inappropriate and too costly for longterm measurements. Furthermore, the ecosystem net fluxes are the result of complex process interactions (physiology, transport, air chemistry) and contributions from different ecological units (soil, vegetation), which can not be

¹which is the so-called “fetch”, representing the source area of the micrometeorological sensor, which depends on the topography, and wind and stability conditions

²Large-Scale Biosphere-Atmosphere Experiment in Amazonia

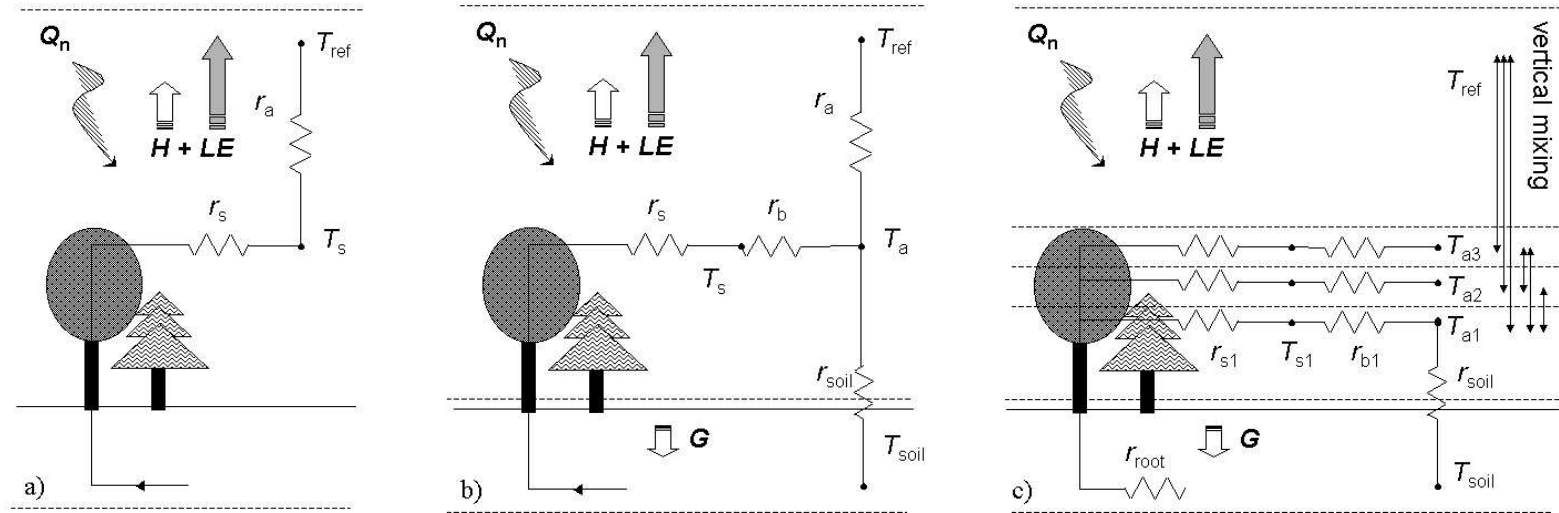


Figure 1.1: Calculation of the surface energy balance in three canopy parameterization schemes with increasing complexity: a) Single-layer scheme assuming $T_{soil} = T_s$ with $Q_n = H + LE$ b) Two-layer (soil + vegetation layer) big leaf approach with $Q_n - G = H + LE$ c) Multi-layer scheme (soil + 3 vegetation layers + 1 layer above the canopy) with $Q_n = \sum_i S_{H,i} + S_{LE,i}$ Symbols: soil (T_{soil}), canopy air (T_a), foliage (T_s), reference (T_{ref}) temperature; available net radiation (Q_n), sensible (H) and latent (LE) heat, soil heat flux (G); stomatal (r_s), leaf boundary-layer (r_b), aerodynamic (r_a), bulk soil surface (r_{soil}) and root (r_{root}) resistance.

assessed easily with such “top down” methods (Meixner and Eugster, 1999).

The increased knowledge and the availability of many field observations has facilitated the application of alternative concepts. The gap between leaf and canopy scale observational methods can be closed with a detailed modeling approach describing the vertical exchange within the canopy layer in a deterministic manner. Ideally designed for multiple purposes, it could serve as a substitution of measurements and help to design or substitute costly field experiments. Furthermore, it would be possible to assess the effects of feedback mechanisms between the vegetation and the climate system. Theoretically, the increase of atmospheric CO₂ is partly balanced by an increased net primary production and thus carbon fixation of the terrestrial vegetation. In practice, the result of this fertilization effect is more complex because it leads to a higher water-use efficiency, a down regulation of leaf transpiration and an increase of surface temperature, which may amplify or damp the direct effect of CO₂. Another example of possible interactions are biogenic VOC emissions, which will increase due to global warming according to the predictions of current emission algorithms. In contrast, Rosenstiel et al. (2003) recently demonstrated with experiments in growth chambers, that the emission of isoprene may be uncoupled and decrease with higher CO₂ levels. This effect is not considered within the current type of emission algorithms, which relate the emission of biogenic VOC’s solely to environmental parameters. Therefore, the potential benefit of an alternative approach that applies physiological predictors instead of leaf temperature and light is assessed in a separate study (Chapter 5). These complex interactions show, that a detailed and mechanistic description of biogeochemical processes at the surface is necessary for reliable global climate predictions.

1.2 Model description

1.2.1 General concept

A major problem on linking biochemical leaf models describing the physiological regulation of leaf gas exchange in an integrated canopy exchange scheme (“bottom-up”) is the scaling of physiological parameters (Jarvis, 1993). The relationships between canopy photosynthesis and nitrogen availability, allocation and optimization has been studied intensively (Field, 1983; Field and Mooney, 1986; Walters and Field, 1987; Evans, 1989) and led to the development of simple scaling principles for leaf physiological properties which can be applied in a multi-layer scheme of canopy exchange (Leuning et al., 1995). Additionally, stomatal response can be described by a simple but robust relationship which couples the exchange of water with CO₂ uptake (Ball et al., 1987). In the present study, the bottom-up approach of Leuning et al. (1995) is combined with a Lagrangian dispersion model of vertical transfer within plant canopies (Raupach, 1989b). Since

photosynthetic light response is strictly non-linear, CO₂ exchange of shaded and sunlit leaves is calculated separately according to Splitters (1986) and Goudriaan and van Laar (1994). In contrast to most existing schemes (Leuning et al., 1995, 1998; Wang and Leuning, 1998; Tuzet et al., 2003), where vertical concentration gradients within the canopy are neglected (\rightarrow big leaf assumption), the present scheme calculates the full energy balance by coupling the leaf surface exchange to the canopy microclimate. The vertical exchange is simulated in a single column model assuming horizontal homogeneity and steady-state environmental conditions. In addition, the exchange of other important trace gases like ozone and isoprene is calculated assuming no feedback response, an assumption which should be satisfied on short timescales (s.a).

Table 1.1: Micrometeorological input parameters

Parameter	Symbol	Unit
local time	t_d, t_h	[days,h]
temperature	T_{ref}	[K]
relative humidity	RH_{ref}	[%]
air pressure	P_0	[hPa]
incoming global radiation	$gRad$	[W m ⁻²]
mean horizontal wind speed	u_{ref}	[m s ⁻¹]
stdev. of vertical wind speed	σ_{wref}	[m s ⁻¹]
soil temperature	T_{soil}	[K]
soil water content	η_w	[%]
bulk soil surface conduct.	g_{soilH}	[mol m ⁻² s ⁻¹]

The major driving model variables (Table 1.1) are micrometeorological parameters above the canopy (global radiation, air temperature, pressure, relative humidity, horizontal wind speed, and standard deviation of vertical wind speed) and the upper soil (temperature, soil water content, and the bulk soil surface conductance for heat), generated during field campaigns (weather station data) or inferred from meteorological databases. For the calculations of dry deposition and/or emission of individual tracers like isoprene and ozone, background concentrations have to be included as well.

The components and interactions of the canopy exchange scheme are illustrated in Fig. 1.2. A very similar approach was already presented by Baldocchi and Harley (1995). The one dimensional canopy column is spatially limited by the soil surface ($z = 0$) and the mean canopy height h_c . It is divided into subsequent canopy layers $i = 1, \dots, m$ of thickness Δz_i and mean height z_i and a surface layer above the canopy with the upper limit $z_{ref} > h_c$. Given the conditions of horizontally homogeneity and steady-state environmental conditions, the scalar conservation equation can be applied. For an arbitrary tracer, the net flux at the

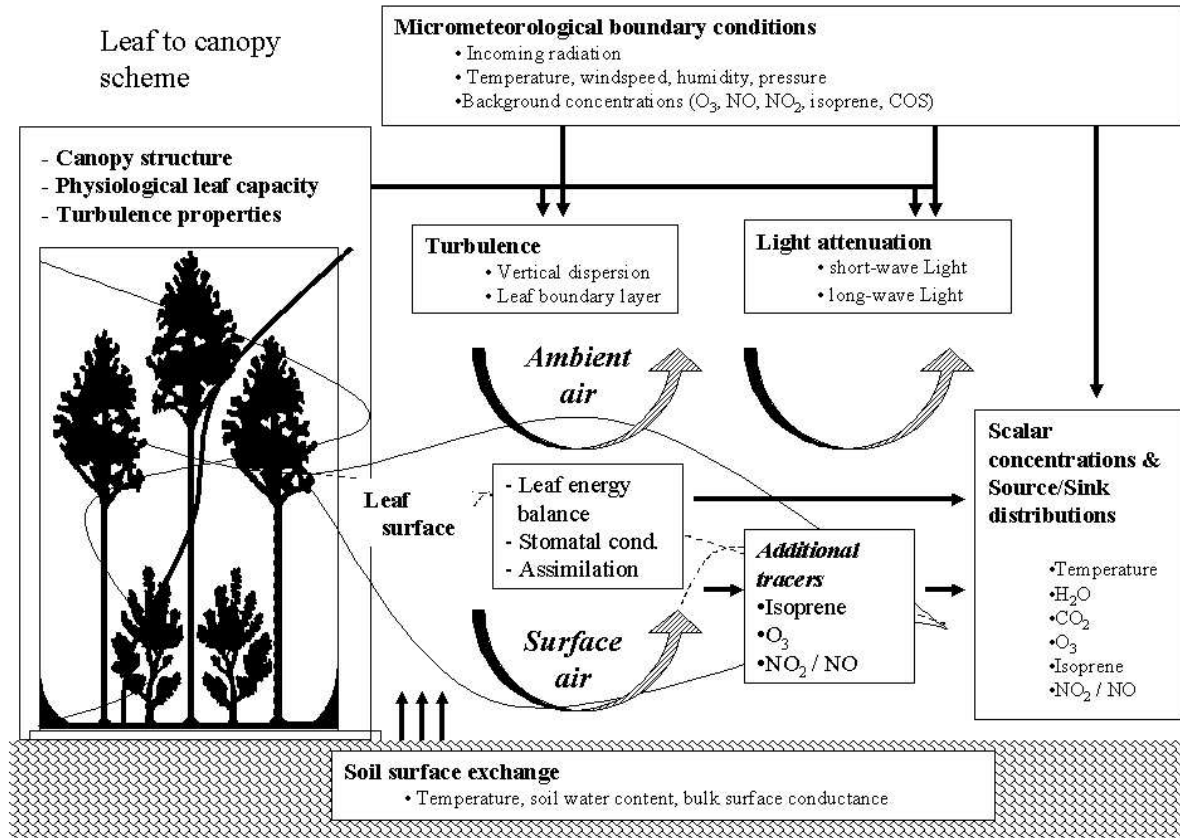


Figure 1.2: Components of the coupled canopy model. Left panel: site parameterization by appropriate profiles for biomass distribution (indicated as a bi-model distribution) and physiological leaf capacity (indicated by the thick line); upper and lower panel: forcing by micrometeorological parameters (Table 1.1); leaf surface and ambient air: iterative calculations at the leaf (energy balance), and canopy level (light attenuation, vertical dispersion); right panel: analytical calculation of the exchange of additional tracers and resulting vertical concentrations and source/sink distributions.

canopy top (F) is then given by the sum of integrated sources and sinks of the different ($S_i\Delta z_i$) according to

$$F = \sum_i^m S_i\Delta z_i. \quad (1.1)$$

Each layer has a leaf area $\Delta\Lambda_i$ which is applied to scale up the surface exchange based on leaf area (F_{leaf}) to S_i which is based on ground area according to

$$S_i\Delta z_i = \Delta\Lambda_i F_{leaf}(z_i) \quad (1.2)$$

The exchange of sunlit and shaded leaves is treated separately. Therefore, Λ_i is divided into a sunlit and shaded part determined by the fraction of sunlit leaves in each layer (Note: Temperature and scalar concentrations of the ambient air at z_{ref} , in layer j , and at the surface of layer i are hereafter denoted as C_{ref} , $C_a(z_j)$ and $C_s(z_i)$, respectively). For a given set of input parameters (Table 1.1), $C_a(z_j)$ is initialized with C_{ref} , and $C_s(z_j)$ again with $C_a(z_j)$. Then the absorbed short-wave radiation is calculated and the energy balance solved for F_{leaf} and C_s , separately for sunlit and shaded leaves. After applying Eq. 1.2, C_a is changed by

$$\Delta C_a(z_j) = \sum_i^m d(i, j) S_i \Delta z_i \quad (1.3)$$

where $d(i, j)$ represents the coefficients of the dispersion matrix connecting the temperature and concentration change $\Delta C_a(z_j)$ with S_i . Eq. 1.2-1.3 are repeated until the latter converges. The numerical solution of the leaf energy balance requires a set of coupled equations for stomatal conductance, photosynthesis and the partitioning of available energy which will be described in Sections 1.2.2. The calculation of the dispersion matrix is described in detail in Chapter 3.

1.2.2 Radiation absorption and surface exchange

Radiation attenuation of sunlit and shaded leaves Splitters (1986) has shown, that the non-linear light response of photosynthesis leads to an overestimation of canopy net assimilation, when absorption of shaded and sunlit leaves is not calculated separately. The partitioning, attenuation, and reflectance of radiation within the canopy is very complex and the most sophisticated modeling approaches require a detailed knowledge of canopy architecture (leaf angle distribution, clumping factor, etc.). Following Leuning et al. (1995), the relatively simple approach of Splitters (1986) assuming a spherical leaf angle distribution is adopted for the current scheme. The approach describes the absorption of sunlit and shaded leaves (two-leaf) at a given vertical canopy position and accounts for the different attenuation of visible and near-infrared incoming radiation (Q_{V0} and Q_{N0} , respectively). Absorbed radiation of shaded leaves (Q_{SH}) is given by

the sum of diffusive and scattered beam radiation while the absorption of sunlit leaves (Q_{SL}) includes additionally the direct beam component leading to

$$Q_{SH}(\Lambda_z) = Q_d(\Lambda_z) + Q_{sb}(\Lambda_z) \quad (1.4)$$

$$Q_{SL}(\Lambda_z) = Q_b(\Lambda_z) + Q_{SH}(\Lambda_z) \quad (1.5)$$

where Λ_z is the cumulative leaf area above z . Diffusive, scattered beam and direct beam components are denoted by subscripts d , sb and b , respectively and calculated according to

$$Q_d(\Lambda_z) = Q_{d0}k_d(1 - \rho_{cd}) \exp(-k_d\Lambda_z) \quad (1.6)$$

$$Q_{sb}(\Lambda_z) = Q_{b0}k_b(1 - \rho_{cb}) \exp(-k_b\Lambda_z) - Q_b(\Lambda_z) \quad (1.7)$$

$$Q_b(\Lambda_z) = Q_{b0}k_b^B(1 - \sigma_l) \exp(-k_b^B\Lambda_z) \quad (1.8)$$

where σ_l , ρ_c , and k are the scattering (reflection plus transmission), canopy reflection, and extinction coefficients, respectively. k^B is the extinction coefficient for black leaves (with no reflection or transmission). The scattered direct beam radiation is obtained by subtracting Q_b from the total absorbed beam radiation (direct + scattered). Fractions of sunlit and shaded leaves (f_{SL} and f_{SH} , respectively) are calculated as

$$f_{SL}(\Lambda_z) = \exp(-k_b\Lambda_z) \quad (1.9)$$

and $f_{SH}(\Lambda_z) = 1 - f_{SL}$.

The net long-wave radiation of a body is generally given by

$$Q_{LW} = Q_{LW} \downarrow - Q_{LW} \uparrow = \epsilon_a \sigma_B T_a^4 - \epsilon_s \sigma_B T_s^4 \quad (1.10)$$

where ϵ_s , ϵ_a and T_s , T_a represent the emissivity and temperature of the body and ambient air and \downarrow and \uparrow denote the incoming and outgoing parts of Q_{LW} , respectively. σ_B is the Stefan-Boltzmann constant. The parameters necessary to calculate Eqns 1.6-1.8 are given in Appendix A.2. The approach to solve Eq. 1.10 is described in detail in Appendix A.3.

A coupled solution of the surface energy balance The soil surface exchange is parameterized as described in Appendix A.6 whereas the leaf energy balance is solved numerically applying coupled equations for stomatal conductance (g_s), the assimilation of CO_2 (A_n) and leaf net radiation (Q_n). In general, Q_n can be either expressed in terms of a radiation budget or a budget of mass fluxes. In terms of radiation fluxes, Q_n is given by

$$Q_n = Q_{SW} \downarrow - Q_{SW} \uparrow + Q_{LW} \downarrow - Q_{LW} \uparrow \quad (1.11)$$

where Q_{SW} and Q_{LW} are the short- and long-wave radiation (Section 1.2.2). In terms of mass fluxes, the available energy at the surface is converted into latent heat (LE), sensible heat (H) and transformed into chemical energy by photosynthesis (A_n) according to

$$Q_n = \lambda^m E + H - \lambda^C A_n \quad (1.12)$$

where λ^m and λ^C are the molar latent heat of vaporization and the molar energy of CO₂ fixation. The energy storage into leaf tissue is usually $< 5\%$ on a timescale of one hour (Jones, 1992) and neglected. All terms on the right side of Eq. 1.12 can be expressed in a flux-gradient relationship

$$E = g_{tw}(D_a + s\Delta T) \quad (1.13)$$

$$H = g_{tH}c_p^m\Delta T \quad (1.14)$$

$$A_n = g_{tc}\Delta c \quad (1.15)$$

where g_t is total molar conductance for water vapor, heat, and CO₂ denoted by subscripts w , H , and c , respectively. $(D_a + s\Delta T)$, ΔT , and Δc , are the scalar gradients of water vapor pressure, temperature, and CO₂, respectively, across the surface pathway from inside the leaf to the ambient air. s and c_p^m are the slope relating water vapor pressure to temperature (de/dT , hPa K⁻¹) and the molar specific heat of dry air, respectively. For stomatal controlled transfer (CO₂,H₂O), g_t can be decomposed by the resistance analogous relationship into $1/g_t = 1/g_s + 1/g_b$ (Ball, 1987) where g_s and g_b are the leaf stomatal and boundary-layer conductance, respectively. In steady state, the partitioning of available energy can be described by combining Eqns (1.12-1.14) to the Penman-Monteith equation (Monteith, 1965)

$$\lambda^m E = \frac{Q_n + c_p^m D_a g_{tH}}{1 + \frac{\gamma_{air}}{s} [1 + (g_t H / g_{tw})]} \quad (1.16)$$

where γ_{air} is the psychrometric constant (hPa K⁻¹). Several versions of Eq. 1.16 exist (Jones, 1992). For the solution of the leaf energy balance, the 'isothermal' form will be applied as described in Appendix A.5. The simple semi-empirical relationship of Ball et al. (1987) (hereafter referred to as B87) links stomatal conductance (g_s) for CO₂ to net assimilation (A_n) according to

$$g_{sc} = g_{s0} + a_A A_n RH_s / c_s \quad (1.17)$$

where g_{s0} is the minimum stomatal conductance, RH_s the relative humidity at the leaf surface, and a_A an empirical coefficient. Different workers modified the B87 model by replacing the dependence on RH_s by a function of water pressure deficit $f(D)$ and by including a CO₂ compensation point (Γ) to avoid $c_s \rightarrow 0$ (Leuning, 1990; Lloyd, 1991). Additionally, the role of limited available water in

the root zone has been included by a dimensionless empirical function $f(\psi_{soil})$ (Wang and Leuning, 1998; Tuzet et al., 2003). Using the Lohammer function $f(D) = 1 + D_s/D_{s0}$ for humidity response (Lohammer et al., 1980) where D_s is the water vapor pressure deficit at the leaf surface and D_{s0} an empirical coefficient, the B87 model is rewritten into the form of Wang and Leuning (1998) to

$$g_{sc} = g_{s0} + \frac{a_A A_n}{(c_s - \Gamma)(1 + \frac{D_s}{D_{s0}})} f_{\psi_{soil}} \quad (1.18)$$

g_s for water and other scalars can be obtained by multiplying g_{sc} with the ratio of molecular diffusivities (Ball, 1987). A_n is constrained by three different processes: (1) the biochemical demand for CO_2 inside the chloroplast, (2) the supply of CO_2 by diffusion through the stomata and the leaf boundary layer ($c_i = c_a + A_n/g_t$, Eq. 1.15) and (3) the stomatal response to A_n (Eq. 1.18) which constrains again the demand function. A general description of the demand for CO_2 (1) is given by

$$A_n = \min\{A_v, A_J\} - R_d \quad (1.19)$$

where A_v is the gross rate of photosynthesis limited by the biochemical fixation of CO_2 and A_J the rate of photosynthesis limited by the regeneration of CO_2 acceptors. In the case of C_3 plants, A_v is limited by the CO_2 dependent activity of Ribulose biphosphate carboxylase-oxygenase (Rubisco) v_{cmax} and A_J is limited by the regeneration of Ribulose biphosphate (RuP_2), which depends on the light driven rate of electron transport across the chloroplast membrane (J). The widely applied biochemical approach of Farquhar et al. (1980) and Caemmerer and Farquhar (1981) is used to model the photosynthesis of C_3 plants and described in Appendix A.1. The C_4 pathway which can be described by a similar approach (Collatz et al., 1992) is not considered in the present work since it is restricted to non-woody plants and mostly annual grasses (Jones, 1992).

According to Monteith (1973), the conductance at the laminar leaf boundary-layer (g_b) can be decomposed into a forced (g_{bu}) and free convective (g_{bf}) part

$$g_b = g_{bu} + g_{bf}. \quad (1.20)$$

The single-sided forced and free convective leaf boundary layer conductance for heat (g_{buH} and g_{bHf} , respectively) are given by

$$g_{bHu} = 0.003\sqrt{u/w_l} \quad (1.21)$$

$$g_{bHf} = 0.5D_H Gr^{1/4}/w_l \quad (1.22)$$

where u , w_l , D_H and Gr are the mean horizontal wind speed, mean leaf width, the molecular diffusivity for heat and the Grashof number, respectively. Gr is calculated from ΔT according to $Gr = 1.6 \times 10^8 |\Delta T| w_l^3$.

Chapter 2

Parameterization of Amazon rain forest surface characteristics

Abstract

Useful parameterizations of Amazon rain forest surface characteristics are inferred and evaluated by using available data sets from various field experiments conducted in southwest and central Amazonia. Mean in-canopy light gradients observed at different field sites show a similar radiation field, which agrees with the predictions of a two-leaf model of radiation attenuation. A comparison of predicted and observed canopy albedo shows a high sensitivity of model predictions to the leaf optical parameters for near-infrared short-wave radiation (NIR). The observations agree much better when reflectance and transmission for NIR is reduced by 25-40%. Available vertical distributions of photosynthetic capacity and leaf nitrogen concentration suggest a low but significant light acclimation of the rain forest canopy that scales nearly linearly with accumulated leaf area. The biochemical model for leaf photosynthesis and two models of stomatal conductance are evaluated with dry and wet season gas exchange measurements from several tree species growing in different light environments. The results show a high sensitivity of model predictions to the kinetic parameters determining the temperature dependence and light response of photosynthesis. The two stomatal models apply semi-empirical relationships between stomatal conductance (g_s), assimilation and either leaf surface water vapor pressure deficit or relative humidity. Both models show a very similar performance and highly scattered predictions of g_s compared to observations. For wet and dry season conditions, optimal model parameters differ suggesting increased stomatal conductance and decreased assimilation in relation to recommended parameter values, respectively.

2.1 Introduction

A detailed modeling approach as described in Chapter 1 requires a detailed description of surface characteristics. The increased knowledge and availability of extensive data sets in several ecotypes and global regions enables the derivation and evaluation of the required site specific properties. As one of the largest ecosystems, the tropical rain forest plays a global role in the present and future climate system. Despite its large bio-diversity, the non-flooded areas are relatively homogenous covered by lowland deciduous tropical rain forest. Since the region is located in the inner tropics, the day length, mean temperature and daily integrated solar radiation are very constant.

In the present study, a general parameterization scheme of surface characteristics is proposed (Section 2.2.1), which can be adapted for other vegetation types. Available field data sets from several experiments in Amazonia (Section 2.2.2) are used to infer site specific vertical profiles of canopy structure, photosynthetic capacity, and horizontal wind speed. Additionally, the calculations and parameters related to the canopy radiation field and soil and leaf surface exchange are critically assessed (Section 2.3) considering wet and dry season conditions.

2.2 Material and method

2.2.1 Inferred parameterizations

Canopy structure Canopy structure is a key parameter of the present approach: 1. It determines the attenuation of short- and long wave radiation within the canopy (Section 1.2.2). 2. Mean light gradients determine the scaling of leaf biochemistry. 3. The integrated leaf exchange is linear related to the leaf surface of each layer (Eq. 1.2). 4. In-canopy turbulence and horizontal wind speed profiles are closely connected to canopy structure, although most parameterizations are height dependent (Kaimal and Finnigan, 1994a, see Chapter 3). Commonly, the canopy structure is prescribed as the vertical distribution of leaf area ($\text{m}^2 \text{ leaf m}^{-2} \text{ ground m}^{-1} \text{ height}$) given in the height integrated form as the accumulated leaf area Λ_z with $\Lambda_{hc} = 0$ and $\Lambda_0 = \text{total leaf area index (LAI)}$. In this form, skeletal organs and further physiologically inactive biomass is neglected, which may be a questionable assumption for some ecosystems with a low or variable fraction of active leaf area. However, Λ_z is usually derived with indirect optical methods that cannot distinguish between the active and non-active fractions of above-ground biomass. Furthermore, general well-defined scaling principles for active leaf area are currently not available. Instead of directly using single field observations, a general parameterization is proposed giving a smooth density profile, which can be applied to different canopy types and modified for sensitivity studies.

The vertical leaf area distributions of natural canopies are mostly non-uniform showing distinct canopy layers. This is modeled by defining Λ_z as the weighted sum of statistical distribution functions as

$$\Lambda_z = \Lambda_0 \sum_{i=1, N^{mode}} I_{x(z,i)}(a_{i1}, a_{i2}) w_i \quad (2.1)$$

where N^{mode} is the number of modes (maxima) of $d\Lambda_z/dz$ and $I_{x(z,i)}$ is the i -th distribution implemented as a beta distribution function (Press, 1997; Meyers and Paw, 1986; McNaughton, 1994) that has the limiting values $I_0 = 0$ and $I_1 = 1$ (see Appendix A.7). $x(z)$ is linearly transformed according to $x \rightarrow z : x = 1 - z/z_i^*$ with an upper boundary height z_i^* . Each mode function has two shape parameters a_{i1} and a_{i2} and is weighted by the fractions of each distribution on total LAI (w_i). An example for a bi-modal distribution for Λ_z is given in Fig. 2.1a.

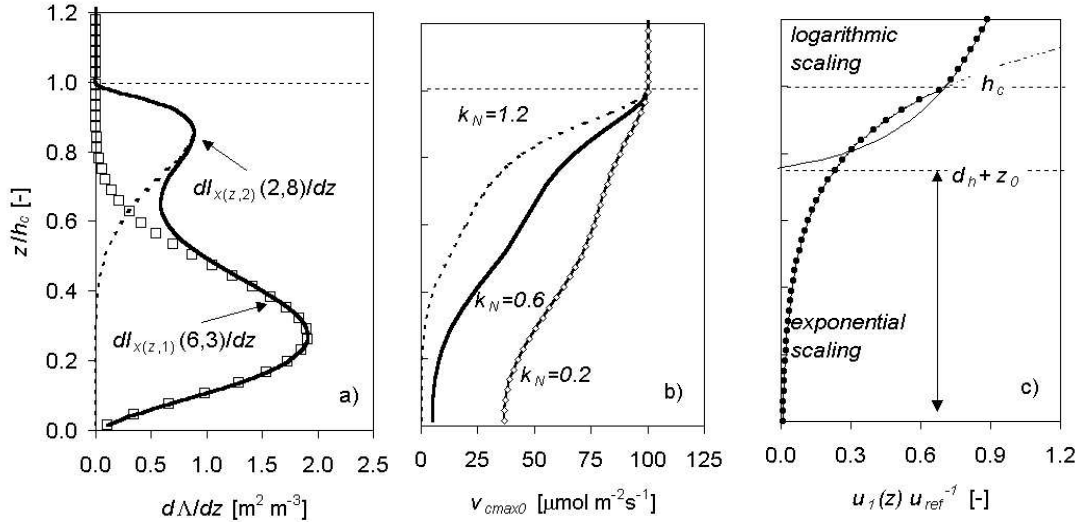


Figure 2.1: Illustration of site specific parameter profiles. Examples for a theoretical canopy. a) Leaf area distribution ($d\Lambda/dz$) simulated with an upper (dashed line, $\{2, 8\}$) and lower (open quarters, $\{6, 3\}$) density maximum. Total LAI and upper boundary heights are 1, the lower maximum has a weight of 75% on total LAI. b) Corresponding light acclimation of leaf biochemistry (maximum carboxylation rate v_{cmax0}) with respect to Λ_z (see a) using different values of extinction (k_N). c) Logarithmic (above canopy, solid line), exponential (below h_c , dashed line) and combined (closed circles) scaling of horizontal wind speed ($u_1(z)$). h_c , z_0 and d_h are the canopy height, roughness length and zero length displacement height, respectively. At $z_0 + d_h$, the logarithmic profiles crosses zero.

Light acclimation of photosynthetic capacity (v_{cmax0}) According to the light acclimation hypothesis, photosynthetic capacity expressed as v_{cmax0} of single

leaves, is co-distributed optimally with leaf nitrogen concentration (c_N) following the mean light gradients inside the canopy to maximize their carbon gain (Field, 1983; Hirose et al., 1988; Leuning, 1995; Hirose and Bazzaz, 1998). This relationship is used to derive $v_{cmax0}(z)$ from top canopy values ($v_{cmax0hc}$). By coupling the leaf carbon uptake with stomatal conductance (see Eq. 1.18) it is guaranteed that stomatal conductance scales with photosynthesis and thus with v_{cmax0} in different canopy layers. $v_{cmax0hc}$ can be estimated from ecological databases of nitrogen availability. For tropical rain forest, a low nitrogen availability is assumed (Schulze et al., 1994) giving a value of $50 \mu\text{mol m}^{-2} \text{s}^{-1}$. In contrast to $v_{cmax0hc}$, only few observations exist for the degree of leaf acclimation to light e.g. in Meir et al. (2002). Leuning et al. (1995) proposes a relationship based on Λ_z predicting

$$v_{cmax0}(\Lambda_z) = v_{cmax0hc} \exp(-k_N \Lambda_z) \quad (2.2)$$

where k_N is an extinction coefficient specifying the degree of acclimation. For illustration, Eq. 2.2 is applied using different values for k_N as shown in Fig. 2.1b. A high value of k_N is associated with a complete acclimation and strong decrease of v_{cmax0} . For the present parameterization of Amazon rain forest, k_N is inferred from published data of $v_{cmax0}(z)$ and leaf nitrogen distribution. The remaining parameters of the leaf photosynthesis and stomatal models are set to recommended parameter values (Table A.1), which are critically assessed in Section 2.3.6 using available data sets of gas exchange measurements from several sun and shade adapted Amazonian tree species.

Profile of horizontal wind speed Since the forced fraction of leaf boundary-layer conductance (g_b , see 1.2.2) is calculated from horizontal wind speed (u), a profile parameterization $f_u(z) = u(z)$ is necessary. For the present study, the combined approach of a logarithmic decrease above and an exponential decrease below the canopy height (h_c) is applied (Kaimal and Finnigan, 1994a) giving

$$u_1(z) = \begin{cases} u_{ref} a_{u2} \ln\left(\frac{z-d_h}{z_0}\right) & \text{if } z \geq h_c \\ u_1(h_c) \exp[-k_u \Lambda_0 (1 - z/h_c)] & \text{if } z < h_c \end{cases} \quad (2.3)$$

where a_{u1} is an empirical coefficient, z_0 and d_h are the roughness length and displacement height below the canopy top (h_c) and the extinction coefficient $0 < k_u < 1$. Eq. 2.3 is illustrated in Fig. 2.1c. First, the aerodynamic parameters z_0 and d_h are estimated from profile measurements $u(z \geq d_h)$, and a_{u1} is fitted to the logarithmic function in Eq. 2.3. After calculating $u(h_c)$, k_u is then derived by fitting the exponential function in Eq. 2.3 to further measurements $u(z \leq h_c)$. For dense vegetation, Eq. 2.3 predicts a zero value of $u(z)$ close to the ground, which is prevented by assuming an offset $u_0(z)$ independent of u_{ref} according to

$$u(z) = u_0(z) + a_{u1}(z)u_{ref} \quad (2.4)$$

Fractions of incoming and long-wave radiation Atmospheric emissivity (ϵ_{a0}) required to calculate the incoming long-wave radiation above the canopy ($Q_{LW\downarrow}$), is estimated by applying the empirical relationship of Brutsaert (1975), which predicts

$$\epsilon_{a0} = 1.24 \left(\frac{e_{ref}}{T_{ref}} \right)^{1/7} \quad (2.5)$$

where e_{ref} and T_{ref} are the water vapor pressure (hPa) and temperature (K) above the canopy. Although the fractions of incoming visible (Q_{V0}) and near-infrared radiation (Q_{N0}) show a slight dependence on the fraction of diffuse light, a constant factor in the visible range between 400-700 nm is commonly applied (Jones, 1992) and the photosynthetic active radiation (Q_{PAR} in units of $\mu\text{mol m}^{-2} \text{s}^{-1}$) is calculated according to

$$Q_{V0} = 0.45gRad \quad (2.6)$$

$$Q_{PAR} = 4.5\mu\text{mol J}^{-1}Q_V \quad (2.7)$$

where $gRad$ represents the incoming global radiation and $Q_{N0} = gRad - Q_{V0}$. Eqns 2.5-2.7 and the mean predicted light gradients within the canopy are evaluated in Section 2.3.3.

Soil surface exchange The soil heat flux is calculated by solving Eq. (1.14) for the pathway from the soil surface to the ambient air layer above. Therefore, the bulk soil surface conductance has to be specified a priori (see Section 1.2.2). For the present study, Eq. 1.14 is rearranged to $g_{soilH} = H/c_p^m(\Delta T)$ and g_{soilH} fitted to field data. Appropriate values for ψ_{soil}^* , η_w^* , and a_{psi} are given in Appendix A.6. The parameterization for soil respiration is calibrated with field data obtained from continuous soil chamber measurements.

2.2.2 Site description and field data

Since the middle of the nineties, many international climate research studies within the Amazon basin have been coordinated within the LBA initiative¹ and its European contribution LBA-EUSTACH². A precursor of LBA were the ABRA-COS campaigns³ on several forest and pasture sites in Amazonia from 1990 to 1994. Nearly all field data sets used in the present study were sampled at or around four micrometeorological towers installed at the two main primary forest research sites of ABRA-COS and LBA (see Table 2.1 and Fig. 2.2). The topography and vegetation cover of the Amazon basin is a relatively uniform. The

¹Large-Scale Biosphere-Atmosphere Experiment in Amazonia

²European Studies on Trace Gases and Atmospheric Chemistry as a Contribution to LBA

³Anglo-Brazilian Amazonian Climate Observation Study

network of rivers and permanently or seasonally inundated floodplains covers $\approx 10\%$ of the total area (≈ 4 mill. km², Fig. 2.2).

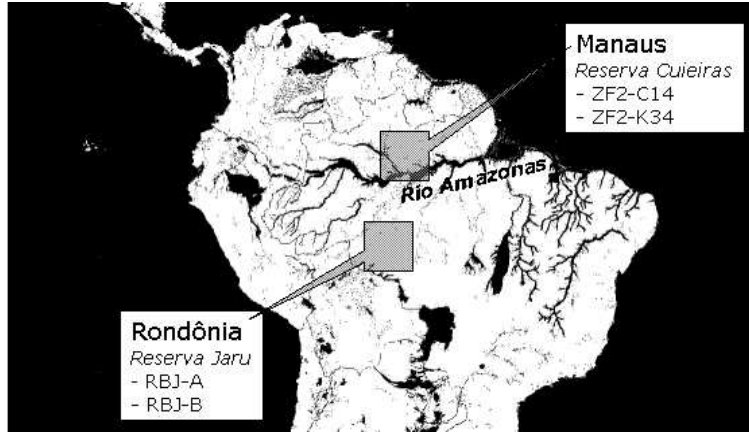


Figure 2.2: Tower location and wetlands of the Amazon basin (Edited map of “Lakes and Wetlands”, Atlas of the Biosphere, Center for Sustainability and the Global Environment, University of Wisconsin - Madison, USA).

Table 2.1: Site and tower locations (see Andreae et al., 2002).

Tower	Site	Location	Elevation	Height
RBJ-A	Jaru, Rondônia	10°04.92'S 61°55.80'W	147 m	53 m
RBJ-B	Jaru, Rondônia	10°04.70'S 61°56.02'W	145 m	60 m
ZF2-C14	Cuieiras, Manaus	02°35.35'S 60°06.89'W	90 m	40 m
ZF2-K34	Cuieiras, Manaus	02°35.55'S 60°12'46'W	93 m	53 m

Table 2.2 gives an overview of the employed data sets for model parameterization and evaluation. The Rondônia site in southwest Amazonia is part of the Reserva Biológica Jarú (RBJ) and belongs to the Instituto Brasileiro de Meio Ambiente e Recursos Renováveis (IBAMA). Most of the data from this site has been collected from April to May and from September to November 1999 during LBA-EUSTACH I+II coinciding with the 1999 wet-to-dry (I) and dry-to-wet (II) season transition periods, respectively. The Manaus site is part of the Reserva Biológica do Cuieiras and located ≈ 60 km NNW of Manaus in central Amazonia. It belongs to the Instituto Nacional de Pesquisas da Amazônia (INPA) and is accessible by a small road (ZF2). The first (older) tower is located close to km 14 of this road (ZF2-C14) while the second tower is close to km 34 (ZF2-K34). The Jarú site experiences a more marked dry season with a mean annual rainfall of 1600 mm compared to 2100 mm at the Cuieiras site (Gash et al., 1996). Furthermore, the forest at the Jarú site is classified as a *Floresta Ombrofila Aberta*

(palm-rich open tropical rain forest) in contrast to the Cuieiras site (*Floresta Ombrófila Densa*, dense tropical rain forest, see Grace et al., 1995; Carswell et al., 2000; Kruijt et al., 2000). However, the vegetation at both sites can be characterized as a lowland tropical rain forest (*terra firma*) growing on deeply weathered clayey soils. A mean canopy height of 40 m is assumed, which represents the upper limit of the wide range of estimates given by several authors (Grace et al., 1995; Kruijt et al., 2000; Rummel, 2004).

Table 2.2: Field data used for derivation and evaluation of model parameters.

Sec.	Parameter	Site	Period	Reference
2.3.1	Λ_z	Manaus		Roberts et al. (1993) ^{*,1}
		Manaus	10-11/'90	McWilliam et al. (1993) ^{*,2}
		RBJ-A	10-11/'99	Rummel (2004) ^{†,3}
		ZF2-C14	07/'01	unpublished ^{‡,3}
		ZF2-K34	07/'01	see Chapter 3 ^{‡,3}
2.3.2	$u(z)$	RBJ-A	10-11/'99	Rummel (2004) [†]
2.3.3	albedo	RBJ-A	'91-'93	Culf et al. (1995, 1996) [*]
		Manaus		
2.3.3	$Q_{PAR0}, Q_{LW0\downarrow}$ Q_{PAR0}	RBJ-B	10/'99	Andreae et al. (2002) [†]
		RBJ-A	10-11/'99	Rummel (2004) [†]
		ZF2-K34	7/'99	Araujo et al. (2002) [†]
2.3.3	$Q_{PAR}(\Lambda_z)$	RBJ-A	8-9/'92; 4-6/'93	McWilliam et al. (1996) ^{*,4}
		RBJ-A	10-11/'99	Rummel (2004) ^{†,5}
		ZF2-C14	11/'96	Carswell et al. (2000) ⁴
2.3.4	F_{csoil}, g_{soilH}	RBJ-A	10-11/'99	Gut et al. (2002a) [†]
2.3.5	$v_{cma0hc}(\Lambda_z)$	ZF2-C14	11/'96	Carswell et al. (2000) ⁶
		RBJ-A	'92/'93	Lloyd et al. (1995a) ^{*,6}
2.3.6	A_n A_n, g_s	RBJ-A	4;6/'93	McWilliam et al. (1996) ^{*,6,7}
		RBJ-C	4-5;9-11/'99	Kuhn et al. (2002a, 2004) ^{†,6,8}

* Pre-LBA studies; [†] LBA-EUSTACH, 1999; [‡] LBA-Claire2001; ¹ derived from literature data after Klinge (1973); Klinge et al. (1975) for Reserve Ducke in the north of Manaus; ² derived by destructive sampling from adjacent clearings for a site 60 Km north of Manaus; ³ optical method using LAI-2000 Plant Canopy Analyzer (Li-Cor, Lincoln, NE, USA); ⁴ regular profiles with simultaneous measurements on different heights; ⁵ irregular profiles with subsequent measurements on different heights; ⁶ combined with leaf area (Λ_z) measurements as described in Section 2.3.1; ⁷ porometry measurements on leaves from 7 tree species in different canopy layers; ⁸ 2-3 days cuvette measurements on branches from 3 tree species

Accumulated leaf area (Λ_z) measurements at ZF2 were made in July 2001 as part of another intensive campaign of LBA (CLAIRE-2001) using a LAI-2000 Plant Canopy Analyzer (LAI-2000 PCA; Li-Cor). The instrumentation setup and sampling method are described in more detail in Chapter 3. A comparison of different methods for Λ_z determination has shown that this approach gives satisfactory results compared to alternative methods (Eschenbach and Kappen, 1996), which are difficult to apply in natural forest canopies. At the ZF2-C14

tower, Λ_z was measured on 17th of July 2001 at 4, 8, 12, 16, 20, 24, 28, 32, and 40 m. References for the other data sets are given in Table 2.2. Profiles of horizontal wind speed $u(z)$ were measured at the RBJ-A tower at 1, 11, 20.7, 31.3, 42.2 and 51.7 m height (Rummel, 2004). Radiation measured at three towers (RBJ-A+B, ZF2-K34) is used to evaluate the parameterization for incoming PAR (Q_{PAR0} , Eq. 2.7), while incoming long-wave radiation (Q_{LW0} , Eq. 2.5) measurements are only available for the RBJ-B tower. The predicted fraction of reflected short-wave radiation (canopy albedo) is evaluated with the monthly mean values reported by Culf et al. (1995) and Culf et al. (1996) for the old Jaru tower (RBJ-A) and a second site near Manaus. Light gradients ($Q_{PAR}(z)$) are available from the ABRACOS experiment (RBJ-A), measured from August to September in 1992 and from April to June 1993 simultaneously at six different levels (35, 21.3, 15.7, 11.6, 6.1, 2.3 m) above the ground using multiple sensors. At the same tower, measurements were made from October to November 1999 using a single sensor mounted for several days alternately at 51.7, 31.3, 20.5, and 1 m height (Rummel, 2004). Carswell et al. (2000) reported mean light gradients for the ZF2-C14 tower at the Cuieiras site and additionally vertical distribution of photosynthetic capacity ($z = 32, 28, 24, 16, 12, 8, 4,$ and 0 m). The latter data are used in combination with a profile of leaf nitrogen concentration measured at RBJ-A (Lloyd et al., 1995a) to infer the light acclimation of Amazonian rain forest. The available height profiles of $Q_{PAR}(z)$, $v_{cmax0}(z)$, and $c_N(z)$ are combined with Λ_z measured at the the same towers (see Table 2.2). The parameterizations of soil respiration and heat flux (F_{csoil} , H_{soil}) are evaluated using continuous chamber, soil, and ambient air temperature measurements described in Gut et al. (2002a). The parameters for the leaf models are inferred and evaluated by comparing model predictions with gas exchange measurements sampled during the late wet, early dry, and late dry season on branches and leaves from 8 tree species found around the tower RBJ-A. The gas exchange data for species 1-3 obtained from two to three days of continuous cuvette measurements on tree branches are described and discussed in detail in Kuhn et al. (2002a, 2004) and represent hourly averages of the raw data recorded with a time resolution of 5 min. The gas exchange data for species 4-8 from McWilliam et al. (1996) were measured with a portable leaf chamber and represent mean values from three to five single leaves. All data subsets for different species, season, and canopy position have a minimum size of 10 and the total number of data points is $N = 498$ (183 for species 1-3). A general description of the two sites and an overview of the EU-STACH experiments is given in Andreae et al. (2002). A detailed description of the instrumentation and tower footprints at the Cuieiras site is given in Araujo et al. (2002).

2.3 Results and discussion

In Section 2.3.1, 2.3.2, and 2.3.5 the implementations of the site specific parameterizations described in Section 2.2.1 are presented. These include an average canopy structure of Amazon rain forest derived from available profile measurements, the implementation of a height function for horizontal wind speed, and the derivation of the light acclimation parameter k_N , which is necessary to scale v_{cmax0} with the profile of accumulated leaf area (Λ_z). In Section 2.3.3, calculations related to the radiation model component (Section 1.2.2) are evaluated. In Section 2.3.4 and 2.3.6, parameters related to the surface exchange calculations (Section 1.2.2) are derived and critically assessed.

2.3.1 Inferring a mean canopy structure for Amazon rain forest

It is assumed, that the measurements, which have been sampled on different sites, represent individual samples from the most prominent Amazonian vegetation type *terra firme* (see Section 2.2.2). From a comparison of the literature data and ecological principles, it is concluded that the vertical leaf area distribution has roughly a lower and upper maximum around 0-5 and 15-30 m height reflecting the ground vegetation and small growing trees in the lower canopy and tall trees, lianes, and epiphyta in the upper canopy, respectively. This simplifying approach is consistent with the descriptive analysis of Klinge et al. (1975) and supported by estimates of Λ_z reported by McWilliam et al. (1993) and Roberts et al. (1993) for the Manaus area and by recent measurements performed in Rondônia (Andreae et al., 2002; Rummel et al., 2002) and at the Cuieiras site near Manaus (see Chapter 3). Observed Λ_z values (see Table 2.2) are averaged for 3 m height intervals. Eq. 2.1 is then fitted to these mean values by prescribing the number of modes to two with I_B as the lower and I_T as the upper maximum of the leaf area distribution ($d\Lambda_z/dz$), the total LAI is set to $\Lambda_0 = 6$ as the mean value of all measurements, and the weights (w_i) and upper heights (z_i^*) to $w_B = 0.25$, $w_T = 0.75$ and $z_B^* = 13$ m, $z_T^* = h_c$ (40 m), respectively. Local optimization of a_{i1} and a_{i2} leads to the parameter values listed in Table 2.3. Additional estimates are given for a 'dense forest type' with a higher leaf area density in the upper canopy and $\Lambda_0 \approx 6.5$ and an 'open forest type' with a more pronounced lower maximum and $\Lambda_0 \approx 5.5$ (see Section 2.2.2).

The mean observed and predicted profiles Λ_z are shown in Fig. 2.3. As indicated by the scatter plot in Fig. 2.3a, the single measurements are approximated by the parameterization ($r^2 = 0.95$). Predicted and observed mean values for each height interval agree well. (Fig. 2.3b). The standard deviations of mean values lead to the assumed modifications for a dense (+) and open (-) forest type. The mean observed and predicted differential profiles ($d\Lambda_z$ for 3 m height intervals) are shown in Fig. 2.3c-d. Although the observations are very scattered, they ex-

hibit a bi-modal distribution as suggested above. The proposed parameterization can be helpful for current and future modeling studies for Amazonia requiring a specification of canopy structure. Different vegetation types can be prescribed by modifying the parameters listed in Table 2.3. Additional measurements will help to improve and generalize the derived parameterization.

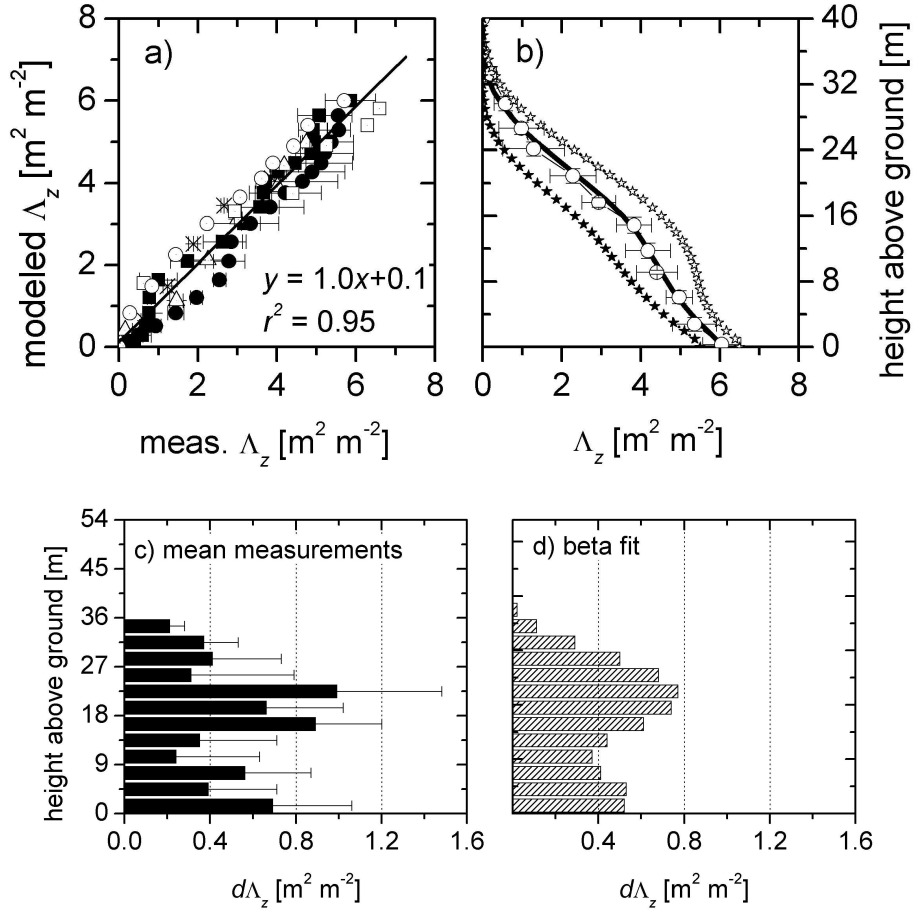


Figure 2.3: Parameterization of canopy structure and accumulated leaf area Λ_z . a) Comparison of the derived parameterization with available field data from the Manaus area of Roberts et al. (1993) (open quarters) and McWilliam et al. (1993) (open circles), and recent measurements made at the Cuieiras site (ZF2-K34 - open triangles, ZF2-C14 - stars, see 2.2.2) and the Jaru site (RBJ-A - closed quarters, RBJ-B, closed circles). b) Height distribution Λ_z derived from mean observed values in 3 m height intervals (open circles with standard deviations), and predicted with the parameterization for a mean (solid line), dense (open stars) and open (closed stars) forest type. c) Mean observed and d) predicted differential leaf area for 3 m height intervals.

2.3.2 Inferring a normalized profile of horizontal wind speed

The profile measurements of horizontal wind speed (u , Section 2.2.2) are fitted to Eq. 2.4 to derive the intercept (u_0) and slope parameters ($a_{u1} = u_1(z)/u_{ref}$). The observed and predicted values for $u_0(z)$ and $a_{u1}(z)$ are shown in Fig. 2.4a. Values for $a_{u1}(z)$ show a logarithmic decline at the upper levels leading $z_0 = 1.3$ m, $d_h = 29$ m and an optimal value of $a_{u2} = 1/3$. The exponential fit to a_{u1} for $z < h_c$ gives the optimal value $k_u = 0.8$. For the lower canopy levels, a significant positive intercept u_0 is obtained. A small constant value below and a linear decrease above d_h leads to $u_0(z) = 0.1 \text{ m s}^{-1}$, $z \leq d_h$ and $u_0(z) = 0.1[1 - (z - d_h)/(z_{ref} - d_h)]$, $z > d_h$, respectively. The exponential function matches $a_{u1}(z)$ at $z \leq h_c$ m quite well. The derived parameterization agrees well with the observations as indicated by the scatter plot in Fig. 2.4b ($r^2 = 0.94$). The applied and derived length scales are summarized in Table 2.4. The mean width of leaves (w_l), which is necessary to solve Eqns 1.21 and 1.22 is estimated from averaged values reported for the tree species analyzed in Section 2.3.6 (Ribeiro et al., 1999).

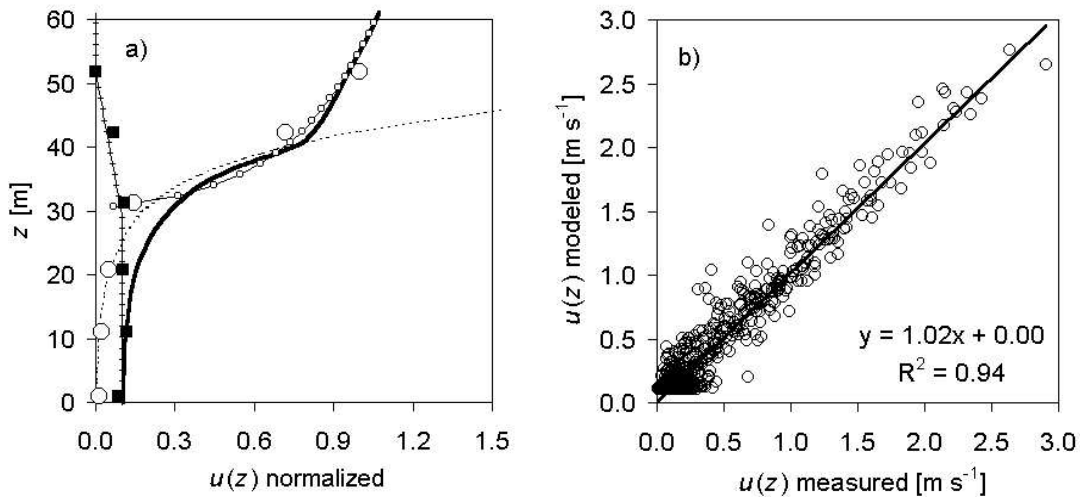


Figure 2.4: Horizontal wind speed as a function of height ($u(z)$). Derivation and evaluation with profile measurements from the RBJ-A tower made in October 1999 (see Table 2.2). a) Derived slope ($a_{u1}(z_i)$, open circles) and intercept ($u_0(z_i)$, closed quarters) parameters according to Eq. 2.4 obtained from measurements made at six height levels and the height functions: $a_{u1}(z)$ (Eq. 2.3, solid line) applies a logarithmic relationship above (line with small open circles) and an exponential relationship below (dashed line) canopy height ($h_c = 40$ m). $u_0(z)$ (line with crosses) has a constant value below d_h and decreases linearly above (see text). b) Comparison of measured and predicted $u(z)$ as described for a).

2.3.3 Evaluation of calculations related to radiation

The empirical relationship between atmospheric emissivity (ϵ_{a0}) and water vapor pressure and temperature (T_{ref} , Eq. 2.5) is evaluated by a comparison of the simulated and observed ϵ_{a0} and incoming long-wave radiation ($Q_{LW\downarrow}$) measured at the RBJ-B tower (Fig. 2.5).

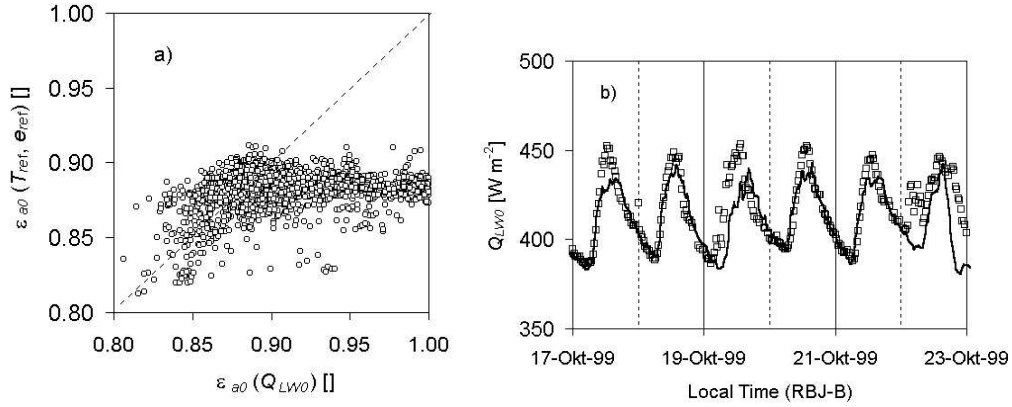


Figure 2.5: Observed and predicted Atmospheric emissivity (ϵ_{a0}) and incoming long-wave radiation ($Q_{LW\downarrow}$) at the tower RBJ-B for a one week period. a) Predictions of Eq. 2.5 (open circles) plotted against the derived observations $\epsilon_{a0} = Q_{LW\downarrow}/(\sigma_B T_{ref}^4)$. b) Measured (open quarters) and predicted time series (solid line) for $Q_{LW\downarrow}$.

For high emissivity values ($\epsilon_{a0} > 0.9$), the parameterization shows a saturation at $\epsilon_{a0} > 0.9$ giving a systematic error of 1-10%. Although this can not be clearly related to day- or night time conditions, the time series for predicted $Q_{LW\downarrow}$ (Fig. 2.5b) exhibits a systematic underestimation of 10-20 W m⁻² at noon time. However, the relative uncertainty is only less than 5% because $Q_{LW\downarrow}$ is mainly determined by T_{ref} .

Since the canopy model represents a discrete approximation of the vertical source/sink distributions, the calculated net fluxes have an error that depends on the number of layers used for the numerical integration. This is illustrated for the total absorbed radiation (Q_{abs}) in Fig. 2.6a showing the relative error of predicted and theoretical Q_{abs} for a canopy with black leaves (no reflectance and transmittance) in relation to the number of equidistant model layers (n). The relative error decreases linearly in relation to the layer thickness (Δz) from $\approx 9\%$ for $n = 3$ ($\Delta z = 13.3$ m) to 1% for $n = 13$ ($\Delta z = 3$ m). For application, the exponentially increasing computation time and the numerical stability must be considered when Δz is decreased. As a good compromise between prediction error and computation costs, a number of 8 canopy layers is inferred (Fig. 2.6a). The numerical stability is addressed in Chapter 4. The fractions of radiation

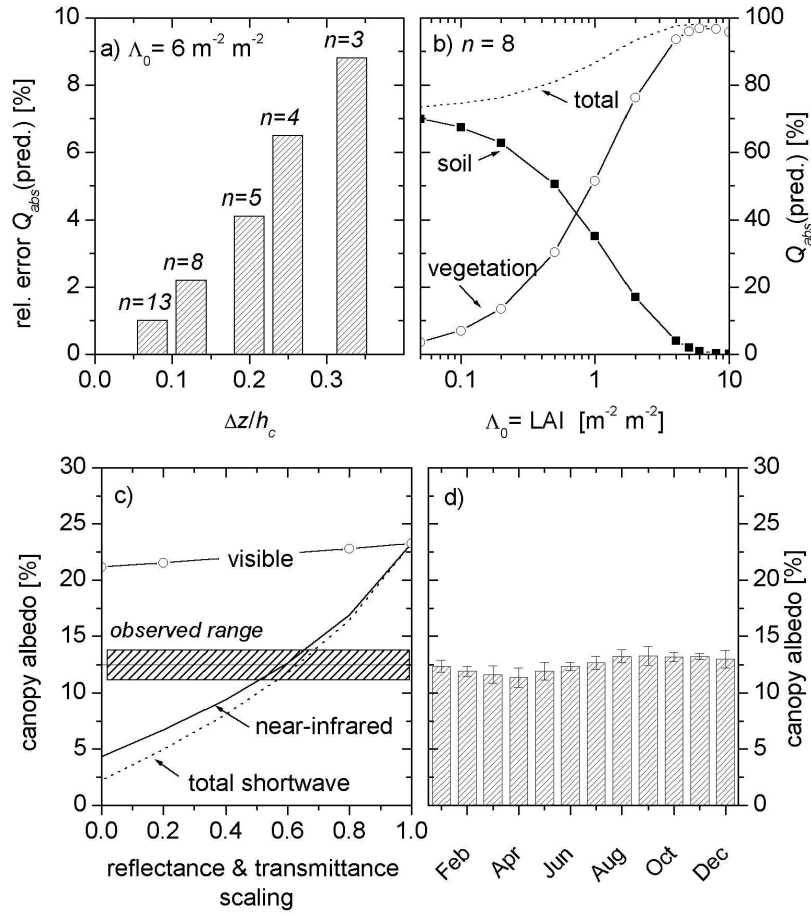


Figure 2.6: Absorbed radiation (Q_{abs}) and albedo in relation to the number of canopy layers, leaf area index, and leaf optical parameters. a) Relative error of predicted total absorbed radiation for a canopy with black leaves (no reflectance and transmittance) in relation to the number (n) and thickness ($\Delta z/h_c$) of canopy layers (total leaf area index $\Lambda_0 = 6$, midday and clear sky conditions with a diffusive fraction $f_{d0} = 0.2$). b) Total (dotted line), soil (line with filled quarters), and vegetation (line with open circles) fractions of absorbed radiation in relation to the total leaf area (Λ_0) using 8 canopy layers ($\Delta z = 4 \text{ m} = 0.125 z/h_c$, $f_{d0} = 0.2$, canopy with black leaves, s. a). c) Observed (striped box, s. a) and predicted midday canopy albedo for clear sky conditions ($f_{d0} = 0.2$) as a function of relative canopy reflectance and transmittance (1.0 = recommended parameter values, 0.0 = black leaves) for visible (line with open circles), near-infrared (solid line) and total short-wave radiation (dotted line). d) Annual cycle of canopy albedo as observed at the Jaru site and a second site near Manaus (Reserva Ducke) in 1991-1993 (Culf et al., 1995, 1996). Mean and standard deviations of monthly values for both sites are shown ($r^2 = 0.87$).

absorbed by the soil and the vegetation is largely determined by the total leaf area index LAI (Λ_0 , Fig. 2.6b). The same type of simulations as described for Fig. 2.6a is repeated by varying LAI between zero and 10 ($\Delta z = 5$ m for $h_c = 40$ m). For dense canopies ($\text{LAI} \geq 4$), the soil contributes only a small fraction to the energy balance, because the amount of absorbed short-wave radiation is quite small. Furthermore, it can be expected from Fig. 2.6b, that the model predicted energy fluxes are not very sensitive to the assumed total leaf area index (Section 2.3.1). In a real canopy, a small fraction of incoming radiation is reflected (canopy albedo) depending on canopy and leaf optical properties. In the applied radiation model, these properties are represented by the leaf scattering coefficient (σ_l) and the canopy reflection coefficient (ρ_c , see Section 1.2.2 and Appendix A.2). In Fig. 2.6c-d, the predicted canopy albedo for clear sky conditions at midday is compared to the longterm observations of Culf et al. (1995) and Culf et al. (1996) at the Jaru site and at a second site near Manaus. Using the recommended parameter values for σ_l and ρ_c , the predicted canopy albedo is nearly double as high as the observations. Since the radiation absorption by leaves is maximal in the visible range, the predicted albedo has a much higher sensitivity to the parameter values for near-infrared radiation, which is shown in Fig. 2.6a. Reducing the scattering and reflection coefficients for visible radiation from 100 to 0% (from 0.2 and 0.057 to 0 for σ_{lV} and ρ_{cdV} , respectively) reduces the canopy albedo only by $\approx 2.1\%$ whereas the same scaling for near-infrared radiation parameters (from 0.8 and 0.389 to 0 for σ_{lN} and ρ_{cdN} , respectively) gives a reduction from 23.2 to 4.3%. Since the recommended parameter values lead to a large disagreement between the observed and canopy albedo, the radiation parameters are scaled as listed in Table 2.5 to derive optimal values for mean, wet, and dry season conditions.

It can not be clearly ascertained, whether this is a real effect of the leaf optical parameters since the radiation absorption model makes the simplifying assumption of a spherical leaf angle distribution, which may be violated in many natural ecosystems, e.g. the orientation of leaves may change during the day (Jones, 1992) and optimize the ratio of absorbed to reflected canopy radiation. The significance for these modifications for model predictions are discussed in Chapter 4.

Eq. 2.6 and 2.7 imply the relationship $Q_{PAR} = 2.025 \mu\text{mol J}^{-1} g\text{Rad}$, which is evaluated by a comparison of measured and predicted values for a one month period at the two Jaru towers and ZF2-K34. As shown in Fig. 2.7a, this gives an excellent fit to the data ($r^2 = 0.99$).

The calculations of radiation attenuation (Section 1.2.2) is evaluated by comparing the mean observed and predicted light gradients $Q_{PAR}(\Lambda_z)/Q_{PAR0}$ at different positions Λ_z inside the canopy (Fig. 2.7b). The predictions of the two-leaf absorption model are obtained from a simulation for the RBJ-A tower using data from October 1999. Mean light gradients are derived from the weighted sums of radiation absorbed by sunlit and shaded leaves at several positions inside the canopy. In addition to the measured and predicted mean relative profiles of

Table 2.3: Parameter values for the height function of cumulative leaf area (Λ_z , see Eq. 2.1). A total leaf area index of $\Lambda_0 = 6$ is assumed. Further parameters are the dimensionless weights w_i , the beta function parameters a_{i1}, a_{i2} and the scaling heights z_i^* in meter. Numbers in brackets give estimated values for dense (+, $\Lambda_0 = 6.5$) and open palm rich (-, $\Lambda_0 = 5.5$) site specific forest characteristics (see text).

canopy layer	w_i (+, -)	z_i^* (+, -)	a_{i1}	a_{i2}
top	0.75 (0.85,0.65)	40 (42,34)	4.2	4.6
bottom	0.25 (0.15,0.35)	13 (8,13)	2.3	1.1

Table 2.4: Applied length scales for the normalized profile of horizontal wind speed and the leaf boundary layer conductance.

Parameter	Value	Unit
h_c	40	[m]
d_h	29	[m]
z_0	1.3	[m]
w_l	0.15 ± 0.05	[m]

Table 2.5: Leaf optical parameters of the radiation absorption model as recommended by Leuning et al. (1995) and derived by fitting canopy albedo to observations (see Fig. 2.6c-d).

Parameter	recommended	mean	wet season	dry season
scaling	1.00	0.66	0.60	0.75
σ_{IV}	0.2	0.132	0.120	0.150
σ_{IN}	0.8	0.528	0.480	0.600
ρ_{cdV}	0.057	0.038	0.034	0.043
ρ_{cdN}	0.389	0.257	0.233	0.293
albedo	0.232	0.130	0.1180	0.151

$Q_{PAR}(\Lambda_z)$, an exponential fit to all measurements is shown. In general, all measurements show a similar log-linear extinction of the ratio $Q_{PAR}(\Lambda_z)/Q_{PAR0}$. The model predicts a lower ratio near the canopy top and a higher ratio at $\Lambda_z \geq 4$. Nevertheless, the agreement with the observations is acceptable taking the high uncertainties for Λ_z deep in the canopy into consideration. Possibly, the leaf area measurements underestimate Λ_z in the lower canopy region. This may level out the systematic overestimation of active or real leaf area due to the inclusion of skeletal organs (branches, stems), but leads to an underestimation of total plant area (see also 2.3.1). The fit for a simple exponential model gives an optimal extinction coefficient of 0.82, which is close to the extinction coefficient for diffuse radiation and black leaves ($k_d^B = 0.8$, Appendix A.2). In summary, these results

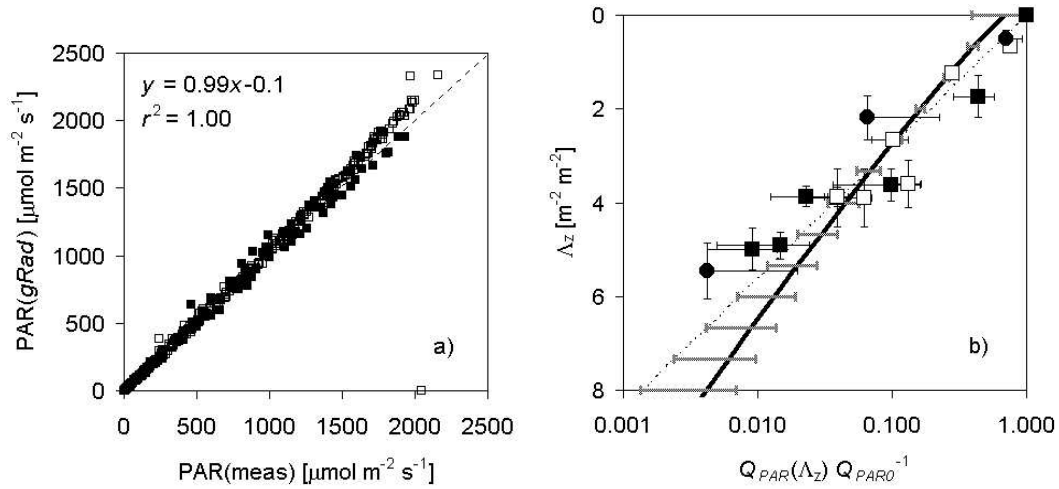


Figure 2.7: a) Incoming PAR (Q_{PAR0}) derived from Eq. 2.6-2.7 and observed at towers RBJ-A (closed quarter), RBJ-B (closed circle), and ZF2-K34 (open quarters). b) Profiles of mean relative PAR $Q_{PAR}(\Lambda_z)/Q_{PAR0}$. Observed values at towers ZF2-C14 (open quarters), RBJ-A in '92/'93 (closed quarters) and RBJ-A in 1999 (closed circles, only positive error bars) and predictions of the two-leaf radiation absorption model constrained with the meteorology measured at RBJ-A in October 1999 (solid line with standard deviations). The dotted line represents the exponential fit $y = \exp^{-ax}$, $a = 0.82$.

support the assumption, that the investigated sites have a comparable canopy structure and radiation field. Further significance to use a two-leaf radiation absorption model instead of a simple extinction approach has to be proofed by the analysis of sunlit and shaded leaf exchange and their contribution to canopy net fluxes (Chapter 4).

2.3.4 Inferring parameters related to soil surface exchange

The soil heat flux (G) and soil temperature (T_{soil}) measured at -0.05 m soil depth and air temperature measured at 1 m height are used to derive the bulk soil surface conductance for heat (g_{soilH} , RBJ-A tower, see Table 2.2 and Section 1.2.2). As shown in Fig. 2.8a-b, the assumption of a constant value $1/g_{soilH} = 500 \text{ s m}^{-1}$ gives an excellent fit between measured and predicted values of G ($r^2 = 0.92$). Typically for dense forests, G is relatively small ($< 15 \text{ W m}^{-2}$). Fig. 2.8b shows a comparison of measurements and predictions for a short time period in the late dry season. Obviously, the parameterization can explain most of the observed variations of G . Nevertheless, the relationship is purely empirical and valid only for moderately wet soils. The parameterization of soil evaporation could not be evaluated independently (Appendix A.6). For a sandy loam, which

is the dominant soil type at the Jaru site (Gut et al., 2002b), Garrat (1992) gives $\psi_{soil}^* = -0.218$, $a_\psi = 4.9$, and $\eta_w^* \approx 0.5$. The latter estimate is in agreement with the value given by Gut et al. (2002b) for the Jaru site. However, an evaluation of the actual parameterization is not possible, since appropriate data sets are missing. Jones (1992) estimates that E_{soil} is usually less than 5% of the total evapotranspiration for canopies with a total LAI of 4 and more, even when the soil surface is wet.

Parameters for the temperature relationship of soil respiration F_{csoil} (Eq. A.42) are derived from continuous measurements from 3 soil chambers made by Gut et al. (2002a) in October and November 1999 at the Jaru site. Fig. 2.8c shows the mean values and standard deviations for F_{csoil} determined for 0.5 °C intervals. For a reference temperature of $T_{soil0} = 298.15$ K, a respiration of $F_{csoil0} = 3.3 \mu\text{mol m}^{-2} \text{s}^{-1}$ is derived, which is close to the mean value of $3.13 \pm 1.3 \mu\text{mol m}^{-2} \text{s}^{-1}$ (mean soil temperature is 24.5°C). The frequency distribution of F_{csoil} has only a single mode (Fig. 2.8d). Although the observed temperature range is very narrow (4 degrees), a plot of mean values against temperature intervals (Fig. 2.8c) shows a strong exponential increase. Fitting Eq. A.42 to these mean values gives an optimal activation energy of $H_{asoil} = 200 \text{ kJ mol}^{-1}$, which is equivalent to an unrealistic high Q_{10} value of 10 (Q_{10} describes the relative increase rate of a biological process for a temperature increase of 10°C). For another rain forest site in Amazonia, Meir et al. (1996) found a much lower of 2.3 in combination with a higher mean value for F_{csoil} ($5.5 \pm 1.6 \mu\text{mol m}^{-2} \text{s}^{-1}$). The large Q_{10} value derived for the RBJ-A tower site are mainly caused by the low and high values at the beginning and end of the temperature range (23 and 26.5°C, respectively), where less data points ($N < 10$) are available compared to the temperature intervals in between ($N > 20^\circ\text{C}$, see also Fig. 2.8c). In general, these uncertainties reflect the large variability of soil respiration.

2.3.5 Inferring the light acclimation of photosynthetic capacity

There is still controversy whether leaf nitrogen concentration (c_N) and maximum carboxylation rate (v_{cmax}) are better expressed on a leaf area or mass basis. At the global scale, a linear relationship on a mass basis was found for canopy maximum assimilation, maximum surface conductance, and c_N by a comparison of different ecosystems (Schulze et al., 1994; Meir et al., 2002). At the canopy and leaf scale several authors propose a leaf area based relationship (Hirose and Werger, 1987; Leuning et al., 1995), which is supported by several field studies for undisturbed Amazon *terra firme* (Reich and Walters, 1994; Lloyd et al., 1995a; Carswell et al., 2000). Consequently, a linear $v_{cmax} - c_N$ relationship expressed on leaf area basis and an exponential decrease with accumulated leaf area Λ_z is applied (Eq. 2.2) to characterize the biochemical properties of rain forest canopy.

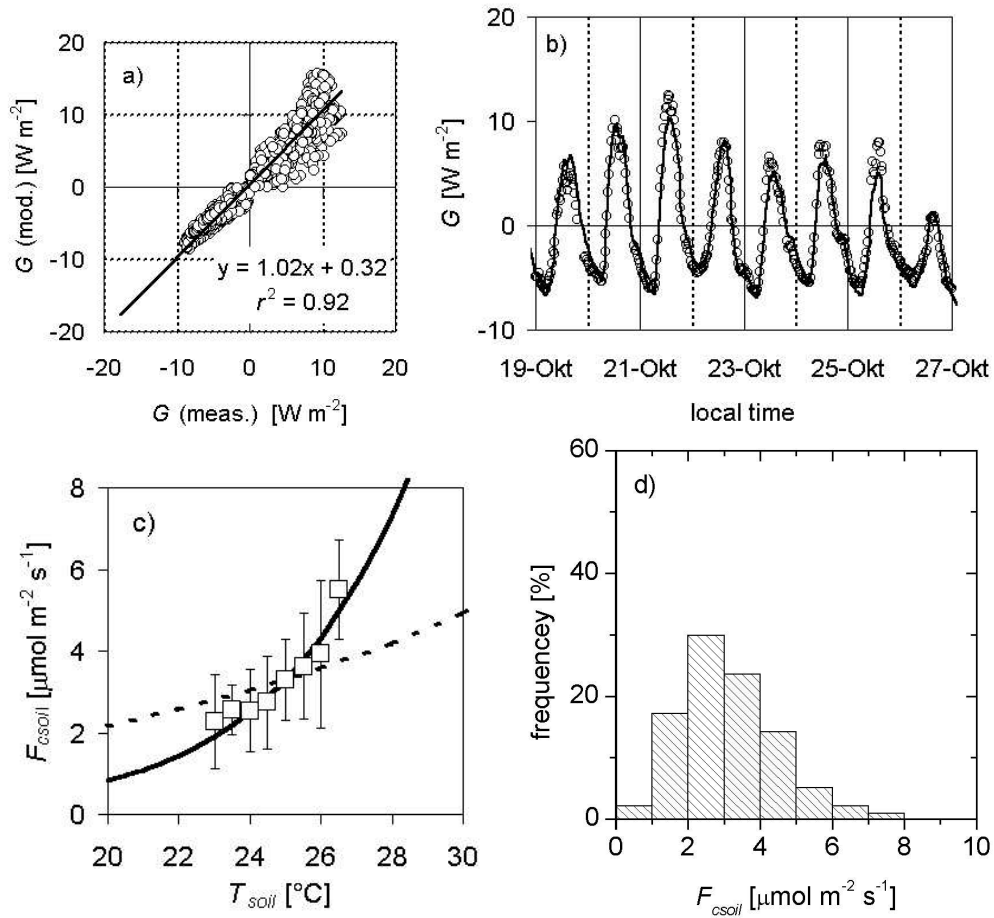


Figure 2.8: a-b) Simulated (open circles) and measured (solid line in b) soil heat flux (G) at the tower RBJ-A in 1999 using a constant bulk (0-1 m) soil surface conductance for heat ($1/g_{soilH} = 500 \text{ s m}^{-1}$). c-d) Parameterization of soil respiration (F_{csoil}) using one hourly averaged measurements from three continuous soil chambers and soil temperature (T_{soil}) measured at -0.05 m in 1999 (dry season data from the Jaru site, RBJ-A tower, see Table 2.2). c) Mean observations and standard deviations for $0.5 \text{ }^\circ\text{C}$ intervals (open quarters) and predictions of Eq. A.42 using an optimal $Q_{10} \approx 10$ (solid line) and $Q_{10} \approx 2.3$ (dashed line) as derived for another site in Amazonia by Meir et al. (1996). d) Frequency distribution of chamber measurements (total $N = 269$).

In Fig. 2.9a, the v_{camax0} data of Carswell et al. (2000) is plotted against Λ_z measured at the same tower. The degree of acclimation is low as indicated by the low value of $k_N = 0.2$ but agrees with the shape of leaf nitrogen distribution that has been measured by Lloyd et al. (1995a) at the RBJ-B tower (Fig. 2.9b). The correlation between v_{camax0} and Λ_z is nearly linear ($r^2 = 0.9$). Extrapolation of

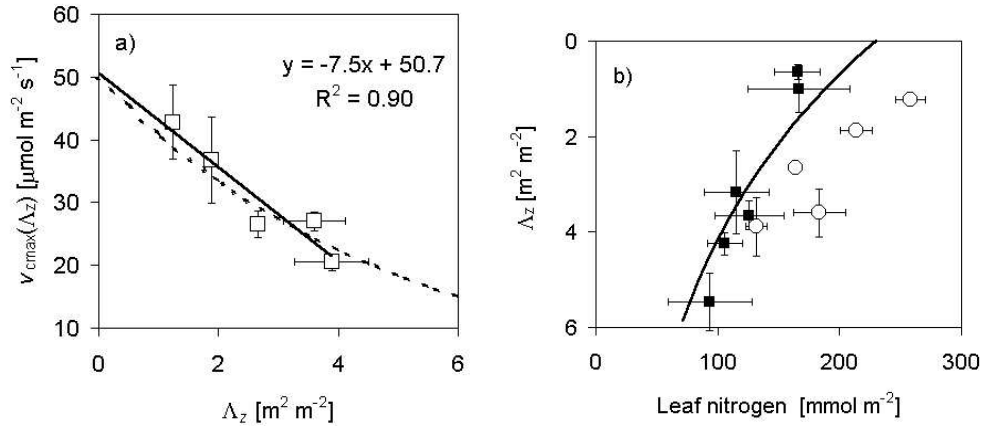


Figure 2.9: a) Relation between measured accumulated leaf area Λ_z (see 2.3.1) and v_{cmax0} as published by Carswell et al. (2000) for the Cuieiras site. The dotted and solid lines represent an exponential ($k_N = 0.2$) and linear relationship, respectively. b) Vertical distribution of leaf nitrogen concentration measured by Carswell et al. (2000) and Lloyd et al. (1995a) at the Cuieiras (open circles) and Jaru site (closed quarters), respectively, plotted against Λ_z measured at the same towers (Section 2.3.1). The data of Lloyd et al. (1995a) is averaged for different height classes (0-2, 9-12, 13-15, 16-21, 22-26, and 27-3 m). The solid line represents an exponential relationship using a value of 230 mmol m^{-2} at the canopy top and an extinction coefficient of 0.2.

the fitted line to the canopy top predicts $v_{cmax0hc} \approx 50.7 \mu\text{mol m}^{-2} \text{s}^{-1}$, which is very close to the mean estimate for tropical rain forest reported by Wullschleger (1993, $51 \mu\text{mol m}^{-2} \text{s}^{-1}$) and the value for low nitrogen plants estimated by Leuning et al. (1995, $50 \mu\text{mol m}^{-2} \text{s}^{-1}$).

2.3.6 Evaluation of calculations related to leaf surface exchange

Data sets Leaf level gas exchange measurements from 8 Amazonian tree species are used to evaluate the photosynthesis and stomatal conductance models described in Section 1.2.2 and critically assess single parameter values for three seasonal periods (late wet, early dry, and late dry season). The photosynthesis model is constrained with measurements of leaf surface temperature, incident PAR outside the leaf chamber (Q_{PAR}), and intercellular carbon dioxide concentration calculated according to Ball (1987). The absorbed radiation (Q_{abs}) is calculated as a fixed fraction of Q_{PAR} assuming $Q_{abs} = 0.9Q_{PAR}$ (Appendix A.1).

Vertical canopy position (Λ_z) is estimated from the mean observed light gradients (species 1-3) and the branch height above ground (species 4-8) combined

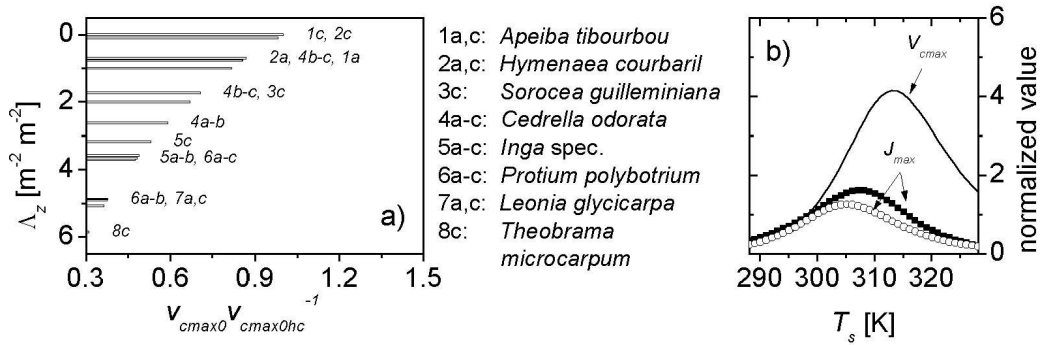


Figure 2.10: Scaling of leaf physiology for the evaluation of leaf photosynthesis and stomatal model parameters with gas exchange measurements from 8 tree species sampled at the Jaru site. a) Derived canopy position (Λ_z) and scaling of maximum carboxylation rate (v_{cmax0}) for the single data sets that have been collected during the late wet (1 – 8a), early dry (1 – 8b) and late dry (1 – 8c) season. The data sets 1a – 3c and 4a – 8c are described in detail in Kuhn et al. (2002a, 2004) and McWilliam et al. (1996), respectively. b) The temperature dependence of v_{cmax} and J_{max} using the parameter values of Harley et al. (1992) normalized with their value at $T_{s0} = 298.15$ K. The second J_{max} (open circles) is obtained using modified parameter values (see text).

with Λ_z measured at RBJ-A (Section 2.3.1 and 2.3.3). The models are calibrated with recommended parameter values as listed in Table A.1. Maximum carboxylation rates (v_{cmax0}) and related parameters are scaled according to Eq. 2.2 using $k_N = 0.2$ (Section 2.3.5) as shown in Fig. 2.10a. The reference leaf temperature for kinetic parameters is adopted from the common value $T_{s0} = 293.15$ (Harley et al., 1992; Leuning, 1995) to 298.15 K (Carswell et al., 2000; Lloyd et al., 1995a). Predicted optimum leaf temperature for v_{cmax} and J_{max} are 40.2 and 34.4°C, respectively. As will be shown later, the predictions of the photosynthesis model are very sensitive to the values of activation energy (H_{vJ}) and entropy (S_J) for J_{max} . Therefore, results using the same values as for v_{cmax} and slightly modified parameters predicting an optimal leaf temperature of 32°C for J_{max} will be also discussed (Fig. 2.10b).

Leaf photosynthesis model The observed and predicted light response for late wet, early dry and late dry season conditions are shown in Fig. 2.11a-f. In general, the observations show a lower quantum yield of whole chain electron transport (α) compared to the model calibrated with common parameter values. This is indicated by the lower initial slope of light response. Furthermore, net assimilation rates at saturating irradiance above 800 $\mu\text{mol m}^{-2} \text{s}^{-1}$ are over-estimated by 30-70%. The measurements exhibit even a decline of A_n at very

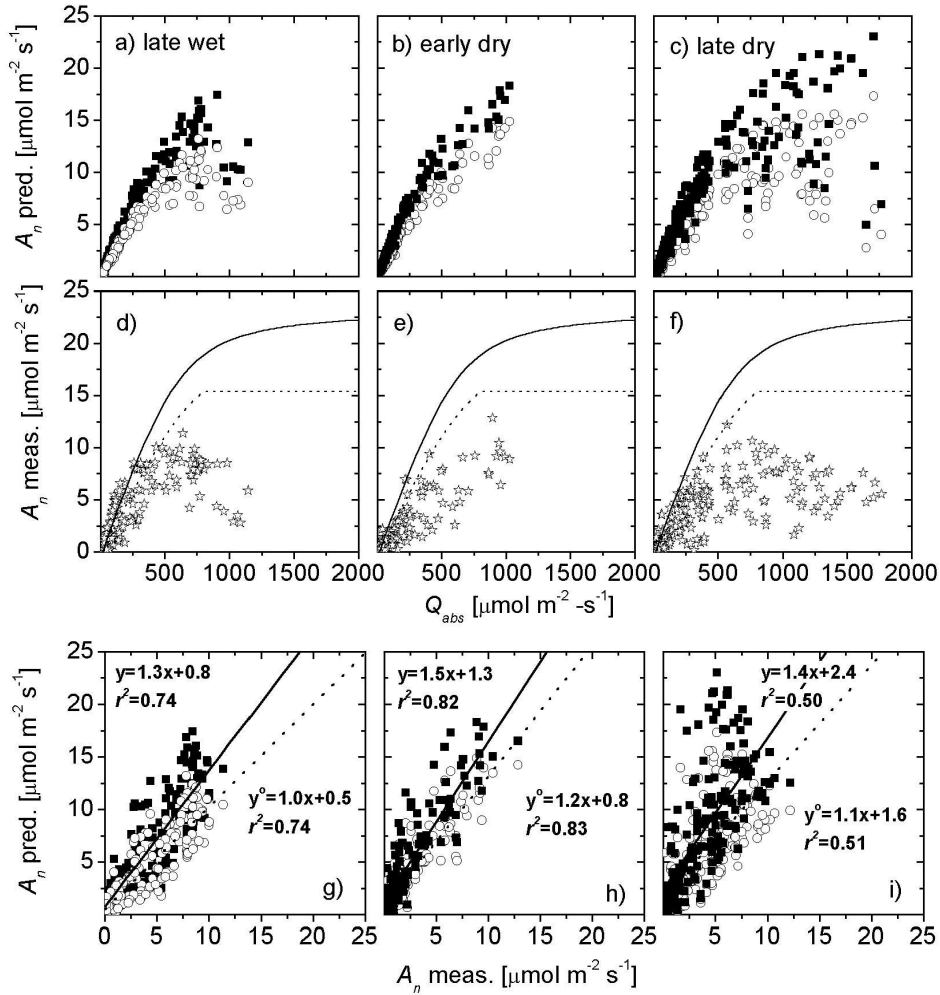


Figure 2.11: Light response and comparison of observed and predicted net assimilation (A_n) under different seasonal conditions (late wet: a, d, g; early dry: b, e, h; late dry season: c, f, i) for gas exchange measurements described in Section 2.2.2 and species listed in Fig. 2.10a. a-c) Light response predicted by the photosynthesis model constrained with observed values of T_s , Q_{PAR} , c_i and parameterized with recommended (closed quarters) and optimized (open circles) values for the activation energy and entropy of J_{max} (see Fig. 2.10b), and the quantum yield of whole chain electron transport (α). d-f) Observed light response (open stars) and model results for $v_{cmax0} = v_{cmax0hc}$, $c_i = 320 \mu\text{mol mol}^{-1}$ and $T_s = 302 \text{ K}$ (solid and dashed lines are related to the common (closed quarters) and optimized (open circles) parameterization in a-c). g-i) Scatter plot for predicted and observed net assimilation. Regression lines y and y^o are given for common and optimized parameter values, respectively.

high irradiance as observed especially for late dry season conditions. By applying slightly modified parameter values with $\alpha = 0.15$ instead of 0.2 and the lower optimum temperature for J_{max} (32°C , s.a.), the model performance can be increased substantially indicated by the lower slope parameter of the linear regression line (Fig. 2.11g-i). Although the positive intercept can also be reduced by applying the optimized parameter values, the remaining offset indicates a systematic overestimation. The highest deviations between predictions and observations is found for the late dry season data from species 1 and 4. For these data sets, A_n is overestimated on average by $\approx 7 \mu\text{mol m}^{-2} \text{s}^{-1}$ (not shown separately). Obviously, the net assimilation rates of single species is significantly reduced compared to the wet season and a seasonal change of leaf physiological parameters can not be excluded. Taking the uncertainties of measurements and the large seasonal and species dependent variability into consideration, the model results agree reasonably well with the observations. However, the results demonstrate the high sensitivity of model predictions to the choice of individual parameter values.

Stomatal conductance model The stomatal models of Ball et al. (1987) and Leuning et al. (1995), hereafter referred to as B87 and L95, respectively, are constrained with measured assimilation (A_n), relative humidity (h_s), water pressure deficit (D_s) and concentration of CO_2 (c_s) at the leaf surface assuming a fixed CO_2 compensation point ($\gamma^* = 38.5 \mu\text{mol mol}^{-1}$), and common values for D_{s0} (15 hPa, empirical parameter expressing the sensitivity of stomatas to D_s), g_{s0} ($0.01 \text{ mol m}^{-2} \text{ s}^{-1}$, minimum stomatal conductance, Leuning, 1995) and a_A (10, empirical coefficient relating g_s to A_n , Ball et al., 1987; Harley et al., 1992). Since not all constraining parameters for the stomatal models are available for species 4-8, the analysis of g_s is restricted to the data sets from the first three species listed in Fig. 2.10a ($N = 183$).

A comparison of model predictions and observations is shown Fig. 2.12. For the applied value of D_{s0} , the L95 and B87 models agree well and differ only at $D_s > 30$ hPa (Fig. 2.12a). Such values are only observed during the late dry season whereby the observed g_s response to D_s (Fig. 2.12b) lies between the two model approaches. Larger values of D_s can also partly explain the lower conductance rates and g_s - A_n relationship observed during the dry season (Fig. 2.12c). A direct comparison of model predictions and measurements of g_s is shown in Fig. 2.12d-e. Both models can not account for large variations of the observed g_s . However, the systematic deviations are small, taking into consideration that the model parameters (g_{s0} , a_A and D_{s0}) have not been optimized locally. The relatively poor fit for both stomatal models is to some extent in agreement with results of Lloyd et al. (1995a) who additionally evaluated the empirical model of Jarvis (1976). Although this approach can principally lead to better results, its application requires additional site specific parameters that increase the degrees of freedom and thus the model uncertainty without appropriate calibration. In

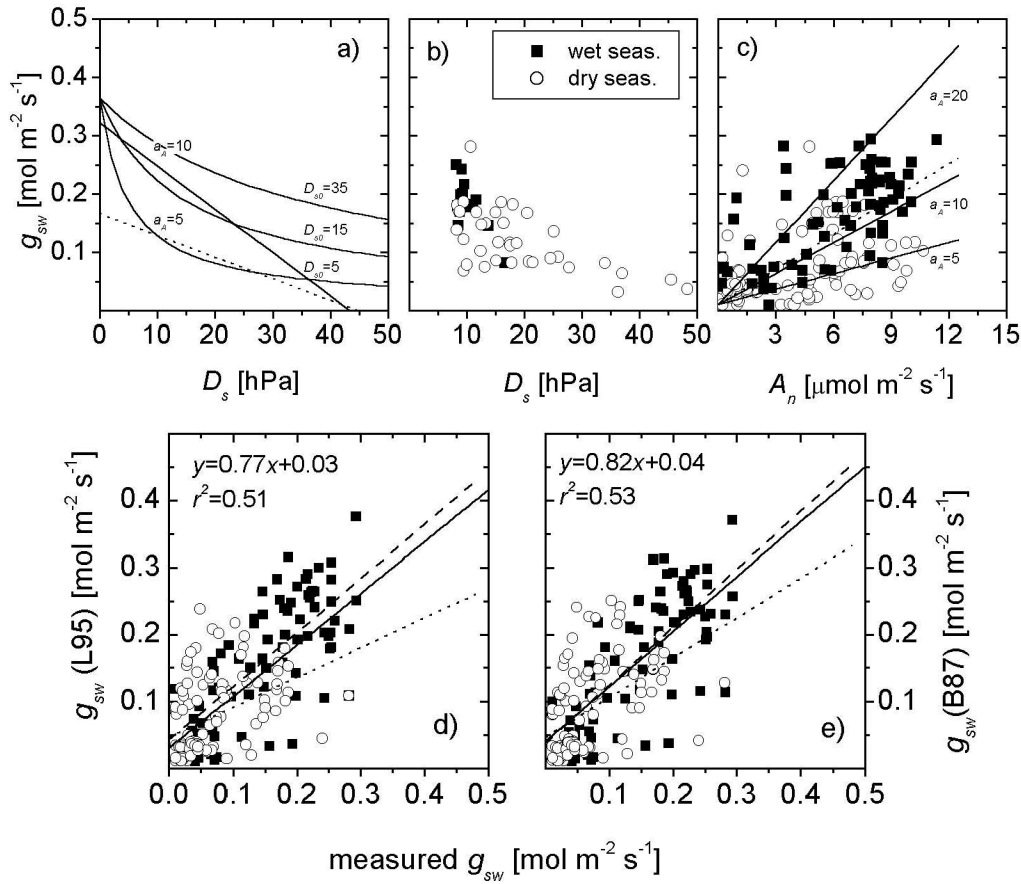


Figure 2.12: Observed and predicted stomatal conductance for water (g_{sw}) during the late wet (closed quarters) and late dry season (closed circles) for species 1-3 listed in Fig. 2.10. a) Response to water vapor pressure deficit at the leaf surface (D_s). Predicted slopes for the B87 model (Ball et al., 1987) using $a_A = 10$ and $a_A = 5$ (dotted line) and predicted curves for the L95 model (Leuning, 1995) using different values for D_{s0} ($a_A = 10$). The constraining parameters are set to $A_n = 10 \mu\text{mol m}^{-2} \text{s}^{-1}$ and $c_s = 320 \mu\text{mol mol}^{-1}$. b) Observed response to D_s for $D_s > 10$ hPa and $A_n > 2 \mu\text{mol m}^{-2} \text{s}^{-1}$. c) Observed response to A_n and predicted relationship for $D_s = 15$ and $c_s = 320 \mu\text{mol mol}^{-1}$ (B87 model as dotted line with $a_A = 10$, L95 model as solid lines for different values of a_A). d-e) Comparison of observed and predicted g_{sw} for the models of L95 (d) and B87 (e). Linear regression lines are given separately for late wet (dashed line) and late dry season conditions (dotted line).

contrast, the simple B87 and L95 models apply a robust relationship between g_s and A_n resulting in a reasonable description of stomatal behavior over a wide range of environmental and ecophysiological conditions.

2.4 Conclusions

From the preliminary evaluation of model parameters derived for Amazonian tropical rain forest, the following conclusions can be drawn:

- Although an accurate height parameterization for $u(z)$ can be derived, the leaf boundary layer conductance, which is mainly derived from $u(z)$ remains speculative, because direct measurements as given in Roberts et al. (1990) are difficult. For a complete evaluation the whole leaf energy balance would be required to include also the free convective part.
- Fractions of incoming radiation can be derived with high accuracy from global radiation. Caused by an underestimation of atmospheric emissivity under high emissivity conditions, the simulated incoming long wave radiation is systematically underestimated (1-5%), which is equivalent to a maximum of 25 W m^{-2} at noon time.
- The derived distribution function for a mean canopy structure with a lower and upper density maximum agrees well with available observations from different sites and methods in Amazonia. Site specific modifications can be achieved by changing the scaling and shape parameters of the distribution function.
- The predicted canopy albedo is relatively insensitive to total leaf area (if $\text{LAI} > 4$) but strongly dependent on leaf optical parameters. Best agreement is obtained when reflectance and transmittance parameters are reduced by 25-40% compared to recommended values. For model application, a number of 8 canopy layers ($\Delta z = 5 \text{ m}$) is derived
- Mean incident PAR observed at different sites showed a similar decrease at different canopy levels when attenuation is related to accumulated leaf area above the height level. Exponential extinction coefficients of 0.6-1 are found. A good correspondence is obtained between PAR measurements and predicted mean PAR absorbed by sunlit and shaded leaves using a two-leaf radiation absorption model.
- Although the scaling of canopy biochemistry remains uncertain, the available field data supports an incomplete light acclimation of undisturbed Amazonian rain forest ($k_N = 0.2$). While irradiance decreases exponentially with accumulated leaf area, photosynthetic capacity was found to decrease nearly linearly. Derived top canopy value for the maximum rate of carboxylation agree well with typical values for tropical plants ($50 \mu\text{mol m}^{-2} \text{ s}^{-1}$).

- Although the two stomatal models examined could not explain considerable variations of stomatal conductance (g_s) observed, the applied relationships seem to be robust predictors of stomatal behavior. The systematic deviations found for several tree species are small taken into consideration, that model parameters have not been optimized locally. For the photosynthesis model instead, a better correlation between predictions and measurements is found. Nevertheless, the predicted assimilation rates are very sensitive to specified temperature optimum of the maximum rate of electron transport. Small decrease of temperature optimum (32 instead of 34 °C) and of the quantum yield of whole electron transport (0.15 instead of 0.2) reduced the assimilation rates by 20-40% and the systematic overestimation by model predictions by more than 70 %.
- The comparison of leaf model predictions and gas exchange measurements suggest a seasonal variability of the leaf physiological parameters, at least for single tree species. For the wet season, a better agreement with the observed stomatal conductance rates is obtained when the stomatal parameter a_1 is increased. For the dry season, a better agreement with the observed assimilation rates is obtained when the quantum yield parameter of photosynthesis (α) is reduced.

Chapter 3

Parameterization and evaluation of forward and inverse Lagrangian dispersion of ^{222}Rn , H_2O , and CO_2

Abstract

The present study focuses on the description of vertical dispersion of trace gases within the Amazon rain forest. A Lagrangian approach is parameterized using in-canopy turbulence measurements made at a site in Rondônia (Reserva Jaru). In contrast to the common scaling scheme that applies friction parameters measured above the canopy, a combined scaling is proposed for nighttime conditions accounting for free convective mixing in the lower canopy of dense vegetations. ^{222}Rn concentration profiles and soil flux measurements made at another site near Manaus (Reserva Cuieiras) are used to evaluate the derived parameterization and the uncertainties of the forward (prediction of concentration profiles) and inverse (prediction of vertical source/sink distributions) solution of the transfer equations. Averaged day- and nighttime predictions of the forward solution agree with the observations within their uncertainty range. During nighttime, a weak but effective free convective mixing process in the lower canopy ensures a relatively high flushing rate of < 1 hour at half canopy height in contradiction to earlier estimates for Amazon rain forest. The inverse solution for ^{222}Rn shows a high sensitivity to small measurement errors in the upper canopy, especially for daytime conditions, when turbulent mixing in the upper canopy is high and profile gradients are small. The inverse approach is also applied to CO_2 and H_2O profiles. The predicted net fluxes show a reasonable agreement with Eddy Covariance measurements made above the forest canopy, although the scatter is high and the solutions for CO_2 are very sensitive to measurement errors.

3.1 Introduction

The vertical dispersion of trace gases within the canopy is the essential link between the source and sink processes occurring at the levels of leaf and soil surfaces, trace gas concentration and chemical reactions in the free air, and the net flux above the canopy. For an horizontally homogenous vegetation layer and steady-state environmental conditions, the dispersion process can be described universally by the multi-linear equation system

$$C_a(z_j) - C_{ref} = \sum_i^m d(i, j) S_i \Delta z_i \quad (3.1)$$

where C_{ref} and $d(i, j)$ represent the concentration at a reference height above the canopy and the dispersion matrix element connecting the source S in layer $i = 1..m$ with the concentration at height $z_j, j = 1..n$, respectively. The canopy net flux equals the sum of vertical sources and sinks ($F = \sum_{i=1}^m S_i \Delta z_i$, see Chapter 2). Eq. 3.1 refers to the forward problem of canopy dispersion and represents the transfer scheme of a multi-layer canopy exchange model where $m = n$ (Chapter 2). The spatial and temporal integration of leaf and soil surface exchange within the forest canopy (i.e. the measurement of S_i) is usually not easily possible (Ehleringer and Field, 1993) whereas the concentration profile $C(z_j)$ can be measured in many cases routinely. When the number of profile levels is higher than the number of source layers ($n > m$), Eq. 3.1 can be inverted and S_i inferred by applying a least-square optimization method which is referred to as the inverse approach. Until the end of the eighties, applicable transport models treated in-canopy turbulence analogously to molecular diffusion and applied a flux-gradient relationship, known as ‘‘K-Theory’’ to parameterize the vertical exchange coefficients. It is now widely accepted, that K-theory fails within the vegetation as a consequence of the inhomogeneous, intermittent nature of in-canopy turbulence (Finnigan and Raupach, 1987; Raupach, 1988; Kaimal and Finnigan, 1994b). Based on a Lagrangian analysis of canopy transfer processes, Raupach (1989b) presented the Localized Near-field Theory (LNF), which led to the development of several new approaches, e.g. one dimensional Lagrangian models (Raupach, 1989b; Warland and Thurtell, 2000), higher-order closure models (Katul and Albertson, 1999), hybrid Eulerian-Lagrangian models (Siqueira et al., 2000), and two dimensional stochastic Lagrangian models (Reynolds, 1998; Hsieh et al., 2003).

Most applications of LNF theory are related to the inverse problem (Raupach et al., 1992; Kruijt et al., 1996; Katul et al., 1997; Nemitz et al., 2000; Denmead et al., 2000; Leuning, 2000). Due to numerical reasons, the inverse solution exhibits much more sensitivity to the input data, i.e. the concentration profile measurements and their inevitable errors. Furthermore, the evaluation of model predictions with measurements is very difficult because the source/sink distribution is unknown in most cases. A pioneer work in this respect was done by Coppin et al. (1986), who measured heat dispersion from an artificial source in

a wind tunnel experiment. As far as we know, this is the only data set used for dispersion analysis with a known source strength. Indeed, this data was used to develop and evaluate the initial version of the LNF technique (Raupach, 1989a), as well as the analytical solution of Warland and Thurtell (2000) and the hybrid Eulerian-Lagrangian approach of Siqueira et al. (2000). For real vegetation canopies, a partial verification of the inverse solution can be achieved by comparing the derived net vertical flux with common micrometeorological measurements (see Chapter 1) applied above the canopy, or as shown in a few studies, in-canopy or soil flux measurements (Denmead and Raupach, 1993; Kruijt et al., 1996; Katul et al., 1997).

Currently, there is a discussion about the importance of stability effects for the in-canopy transport schemes described above (Leuning, 2000; Leuning et al., 2000; Siqueira et al., 2000; Siqueira and Katul, 2002; Hsieh et al., 2003). The proposed modifications by Leuning et al. (2000) for the Lagrangian scheme, and by Siqueira and Katul (2002) for the second-order Eulerian scheme apply surface stability parameters to distinguish stable, neutral, and unstable stratification classes. However, for the Amazonian rain forest, it has been shown, that the lower canopy can be strongly decoupled from the surface-layer and the boundary-layer above, showing a complementary thermal stratification to boundary and surface layer stability conditions (Kruijt et al., 2000; Rummel, 2004). During daytime, the upper canopy is strongly heated by global radiation resulting in a positive temperature gradient and a stable stratification of the lower canopy. This effect is favored by the shape of vertical biomass distribution showing a leaf area density maximum in the upper canopy (Kruijt et al., 2000). During nighttime, the temperature gradient of the lower canopy can become negative due to radiative cooling of the upper canopy generating a weakly unstable free convective layer, which is a general observation for dense vegetation (Jacobs et al., 1994; Bosveld et al., 1999b,a; Simon, 1999). It is hypothesized, that the convective mixing can have a significant impact on nocturnal exchange processes, especially during calm nights, when radiative cooling is strongest, and forced mixing is weak.

The noble gas radon is produced by rock material in all natural soils in the α -decay chains of uranium (^{222}Rn with a half-life of 3.85 days) and thoronium (^{220}Rn with a half-life of 56 seconds). In several studies, the short-lived ^{220}Rn has been applied as an inert tracer of near-surface turbulent transport (Lehmann et al., 1999; Gut et al., 2002a) whereas the longer-lived species ^{222}Rn is applied in studies of soil diffusivity (Lehmann and Lehmann, 2000; Gut et al., 2002b) and of whole canopy exchange (Ussler et al., 1994; Butterweck et al., 1994; Lehmann and Lehmann, 2000; Gut et al., 2002b; Martens et al., 2002). Based on in-canopy profiles of ^{222}Rn and CO_2 measured at a rain forest site near Manaus, Trumbore et al. (1990) calculated a mean canopy residence time of ≤ 1 and 3.4 – 5.5 hours for day- and nighttime conditions, respectively. In further studies, this estimate was applied to interpret observed profiles of ozone and nitrogen oxides within the Amazon (Fan et al., 1990; Bakwin et al., 1990). Furthermore, it is a boundary-

condition for a model of the canopy reduction effect on NO_x flux from Amazon forest (Jacob and Wofsy, 1990; Jacob and Bakwin, 1991), which in part is used for the global model of soil-biogenic NO_x emission of Yienger and Levy (1995). Despite this impact, only few studies focusing on characteristic timescales and mixing rates within the Amazon rain forest exist (e.g. in Kruijt et al., 2000; Rummel, 2004).

In the present study, the original LNF approach (Raupach, 1989b,a,c) is applied. A first-order parameterization of the vertical transport is derived from direct turbulence measurements within a rain forest in Rondônia (Reserva Jaru) and the LNF technique is applied to ^{222}Rn flux and concentration measurements within a second rain forest near Manaus (Reserva Cuieiras). The significance of nighttime free convective mixing inside the canopy is assessed by applying a combined scaling of vertical turbulence properties that are commonly parameterized solely with friction parameters measured above the canopy. The soil fluxes and the concentration profiles of ^{222}Rn were measured simultaneously, which allows to evaluate the forward and inverse LNF solution separately and to discriminate uncertainties related to the turbulence parameterization and the inversion of the transfer equations. The observed and predicted effective transfer velocities and timescales of ^{222}Rn transport are compared to the estimates of Trumbore et al. (1990). The evaluated scheme is then also applied to scalar profiles of H_2O and CO_2 measured at the Cuieiras site to infer their vertical source/sink distributions. H_2O and CO_2 vertical net fluxes obtained with the Eddy Covariance method are compared with the summed source/sink distributions. Finally, day- and nighttime averaged carbon fluxes are integrated and discussed.

3.2 Material and method

3.2.1 Field data and measurement overview

Measurements from two different sites are used for the present study. The sites and tower locations are described in more detail in Chapter 2. Turbulence measurements made at the Jaru site in Rondônia (RBJ-A tower) are used for the parameterization of the LNF model. The parameterized model is then applied to radon, CO_2 , and H_2O measurements made at the Cuieiras site near Manaus (ZF2-K34 tower). The mean canopy height for both sites is estimated as $h_c = 40$ m (Chapter 2). ^{222}Rn activity concentration was measured with a profile sampling system at six different height levels. Soil fluxes of both radon species (^{220}Rn and ^{222}Rn) were measured with a static chamber system. Inverse LNF calculations are also applied to CO_2 and H_2O concentration measured at six canopy levels. The forward and inverse applications schemes and level heights of the LNF model are outlined in Fig. 3.1. For ^{222}Rn dispersion, the canopy is divided into two layers consisting of a bottom layer from 0-0.1 m representing the soil surface, and an

overlying canopy layer from 0.1 to canopy height (Figure 3.1a). For the inverse application to H_2O and CO_2 , a three-source-layer scheme is chosen consisting of a bottom (soil and ground vegetation), middle (palms and emerging trees), and upper layer (crown region) from 0-5, 5-20, and 20-40 m height, respectively (Fig. 3.1b). Eddy Covariance measurements of CO_2 and H_2O flux made above the canopy are used for a comparison with LNF model predictions. The radon measurements were part of LBA-Claire in 2001 (Chapter 2) and are described in more detail later. The H_2O and CO_2 data are part of longterm measurements of energy and CO_2 fluxes, which also include the turbulence forcing variable of the LNF model (the standard deviation of vertical wind speed above the forest, see Section 3.2.4). For a detailed description see Araujo et al. (2002).

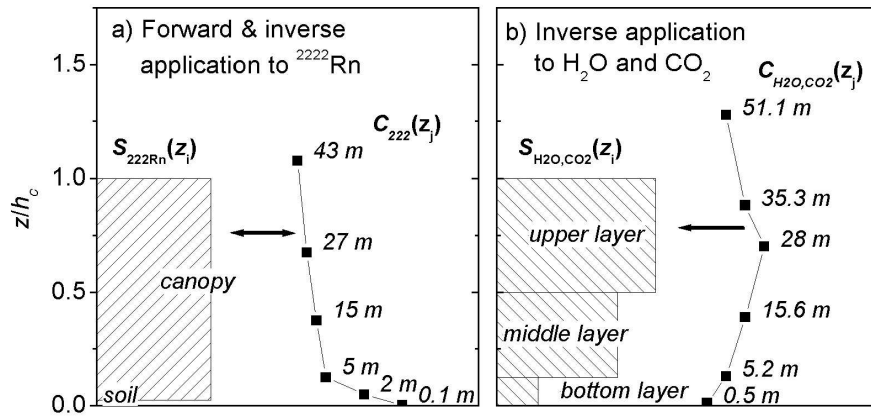


Figure 3.1: Sample heights $j = 1..n$ of concentration profiles (z_j) and source layers $i = 1..m$ of the LNF scheme (Eq. 3.1) for the application to ^{222}Rn (a) and H_2O and CO_2 (b). The forward problem incorporates the simulation of the concentration profile $C(z_j)$ for a given source/sink distribution $S(z_i)$, whereas the inverse approach infers $S(z_i)$ from $C(z_j)$.

The fast in-canopy turbulence measurements used for the parameterization of the LNF transfer scheme were measured in 1999 during EUSTACH I+II at the Jaru site in Rondônia (RBJ-A tower, see Chapter 2). High resolution horizontal and vertical wind components were measured with three-dimensional sonic anemometers (Gill Instruments). Most of the time, three instruments were operated simultaneously at 53, 11, and 1 m height above the ground from October to November 1999. During short periods, the 11 and 1 m device were mounted at 42.2, 31.3, and 20.5 m. Half hourly mean values for each height level are divided into four classes discriminating between day- (8:30-16:30 h) and nighttime (22:00-4:30 h), and conditions with low ($u < 2 \text{ m s}^{-1}$) and high wind speed ($u > 2 \text{ m s}^{-1}$). For nighttime conditions, separation for wind speed is only performed for levels 1, 5, and 6 as too few data points are available for high wind speed conditions.

Periods with rain are not considered. A detailed description and characterization of the turbulence data is given in Rummel et al. (2002) and Rummel (2004).

3.2.2 Measurements of canopy structure at the Cuieiras site

Since the data for model parameterization and application have been sampled on different sites, a comparison of canopy structure observed at the Jaru and Cuieiras towers is given in the following Section (see Chapter 2 for a general discussion of canopy structure). Leaf area index (LAI, Λ_z) was measured at both sites with two optical sensors of a commercial device (LAI-2000, Li-Cor). At the Cuieiras site (ZF2-K34 tower), LAI was measured at 8 differential levels ($z_{ref} = 40.0$ m; $z_i = 33.0, 29.5, 25.5, 21.5, 17.5, 13.5, 9.5, 5.5$ m). At each height level, 12 equally distributed single measurements were performed in a concentric circle just around the tower. On 5th and 16th of July, a total number of three adjacent and decent profiles could be measured under prevailing cloudy conditions. The Jaru data (RBJ-A tower) was provided by Rummel (2004) and is averaged to the sampling height levels of the Cuieiras tower (ZF2-K34). The mean LAI profiles are shown in Fig. 3.2 that includes additionally the height levels of the turbulence measurements made at the Jaru tower (Section 3.2.1). The measurements represent the conditions close to the tower. It should be remarked, that some parts of the understory vegetation at the Cuieiras tower have been removed due to of ongoing installation work. Therefore, the total leaf area index (LAI) may be underestimated by the observed value of ≈ 5 since the lowest five meter are missing. In Chapter 2, a mean value of ≈ 6 is estimated based on the comparison of observations at different sites in Amazonia. The differential profile has a maximum leaf area density at 20-30 m and $\approx 0.5h_c$ for Cuieiras and Jaru, respectively, which coincides with the highest uncertainties for Jaru. For Cuieiras, a second and third maximum are observed above 10 m and below 5 m with a relatively open stem space in between these height levels. The observed distribution would probably vanish to the bi-modal distribution proposed in Chapter 2, when multiple point measurements are applied.

As already discussed in Chapter 2, the vegetation type on the two sites under investigation are classified differently by some authors. Whereas the Cuieiras forest near Manaus is characterized as a dense tropical forest type, the Jaru forest in Rondônia is described as a palm-rich open tropical forest type (McWilliam et al., 1993; Kruijt et al., 2000; Andreae et al., 2002). However, such differences can also be found locally at the ecosystem scale. The Manaus area exhibits a small-scale relief of plateaus and lowlands that has favored a pattern of dense vegetation with higher trees at the plateaus and a palm-rich open forest vegetation type in the lowlands (Ribeiro et al., 1999). As demonstrated by Araujo et al. (2002), the footprint of the Cuieiras tower (\rightarrow ZF2-K34) shows a relatively low

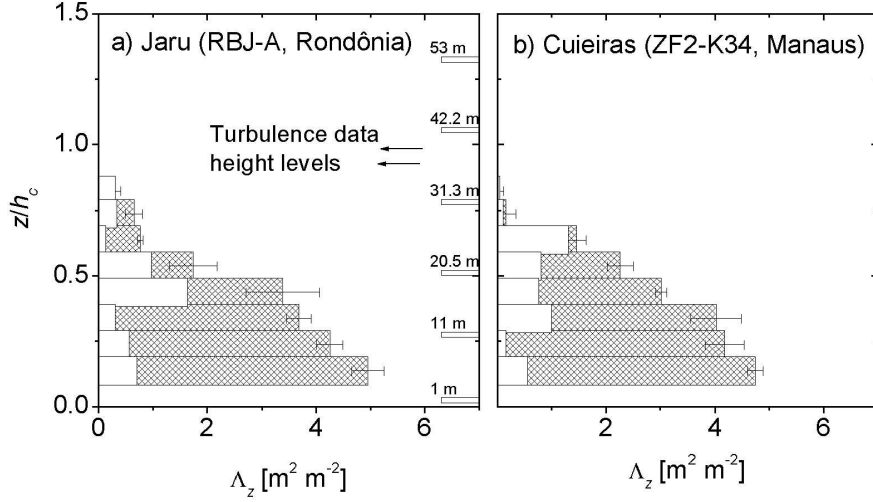


Figure 3.2: Comparison of accumulated leaf area (Λ_z) observed at the Jaru (a) and Cuieiras sites (b). For Cuieiras, no measurements with $z < 5$ m are available and therefore missing on both panels. Also shown are the differential profiles for each height level (white boxes) and the height levels of the turbulence measurements at Jaru.

fraction of plateaus ($\approx 50\%$, 40% on 1 km radius) compared to the 11 km nearby tower (\rightarrow ZF2-C14, $\approx 60\%$, 53% on 1 km radius). It is thus concluded, that both sites have a comparable canopy structure and vegetation type which can be classified as primary lowland tropical rain forest.

3.2.3 Radon measurements

Radon measurements at the Cuieiras site were performed with four alpha-decay detector units (AG-A,...,AG-D; ALPHAGUARD 2000 PRO, Genitron Instruments, Frankfurt) that are calibrated for ^{222}Rn by the manufacturer. The precision and detection limit are $\pm 10\%$ and 3 Bq m^{-3} for a 10 min sampling interval. Air was pumped through Teflon tubes (1/4") from the sample heights shown in Fig. 3.1a. The flow rate was $300 \text{ cm}^3 \text{ min}^{-1}$ and controlled by pressure sensors (AG-C, AG-D) or regulated by mass flow controllers (AG-A, AG-B). Data acquisition operated in the smallest possible time interval of 1 min. Units AG-C and AG-D were installed at 24 and 42 m, respectively. Unit AG-D measured continuously at the 43 m level above the canopy whereas for unit AG-C, a valve system was operated to switch every 30 minutes between the 27 and 15 m height level. ^{222}Rn activity at the three remaining height levels (0.1, 2, 5 m) was quantified by Unit AG-B with a time interval of 40 min. On the way to the detectors of the profile system the air passed a delay device (2000 cm^3 plastic canister), where the short-lived ^{220}Rn practically totally decayed.

Each first 10 min of sampling time for the lower 5 levels switching between different heights are generally discarded (flushing time). The integration period for the upper (AG-D and AG-C) and lower units (AG-B) are 30 and 40 min, respectively (inclusive flushing time). The observed activity of ^{222}Rn above the canopy at 43 m was usually very small and close to the detection limit of the radon devices. Thus the temporal evolution of the radon profile is strongly masked by the random-like variability leading to high levels of relative measurement uncertainty. The accuracy of individual profile measurements is also limited due to the fact, that a complete profile sampling cycle took about 2 hours for all six measurement levels. Therefore, the 30 and 40 min interval measurements are smoothed by applying a symmetric triangular weighted moving average covering an interval of 2 hours before and after mean sampling time. The smoothed profile data are divided into day- and nighttime and high and low wind speed condition classes in the same way as described for the turbulence measurements at the Jaru site (see Section 3.2.1). The air stream for the lower three levels was sporadically switched to a closed circuit to derive the radon soil fluxes from a static chamber system containing the units AG-B and AG-A. Before reaching the delay device of AG-B, the air passed the fourth unit AG-A, where the summed activity of ^{220}Rn and ^{222}Rn was measured. The static chamber system and the flux calculations are described in detail in Lehmann et al. (2004). A summary of the applied mathematical calculations is given in Appendix B. The activity of radon (in units of decays per second \rightarrow Bq) is directly proportional to the particle concentrations, depending only on the decay constants (that are $\lambda_{220} = 0.0125$ and $\lambda_{222} = 2.110^{-6}$ s^{-1} for ^{220}Rn and ^{222}Rn , respectively). To avoid the ambiguous term “activity profile”, the expression “activity concentration profile” ($C_{222}(z)$) is used hereafter (Butterweck et al., 1994).

3.2.4 Implementation of the Localized Near-field theory (LNF)

The LNF technique and its theoretical background is described in detail in Raupach (1989a,b,c). In the following section, a summary of the original implementation and a discussion of the turbulence parameterization is given. A first step to parameterize the dispersion matrix $d(i, j)$ given in Eq. 3.1 is done by decomposing the dispersion into a part that results from a diffusive-like far-field (d^{far}) and a second part that results from a persistent near-field (d^{near}):

$$d_{i,j} = d_{i,j}^{far} + d_{i,j}^{near}. \quad (3.2)$$

These two fields are calculated from the integrated reciprocal far-field diffusivity k^{far} and the approximated near-field kernel k^{near} according to

$$k^{far}(z) = \sigma_w^2(z)T_L(z) \quad (3.3)$$

$$k^{near}(\chi) \approx -0.39894 \ln [1 - \exp(-\chi)] - 0.15623 \exp(-|\chi|) \quad (3.4)$$

with χ being the dimensionless height $\chi = (z - z_i)/(\sigma_w(z_i)T_L(z_i))$ and $\sigma_w(z)$ and $T_L(z)$ the standard deviation of vertical wind speed and the Lagrangian timescale, respectively.

Table 3.1: Different parameterizations of the standard deviation of vertical wind speed (σ_w) given in the literature. Parameterizations based on u_* are derived for near neutral conditions

Reference	LAI	h_c [m]	$\sigma_w(h_c)$	$\sigma_w(0 \text{ m})$	shape
Raupach (1989a) ¹	> 3		$1.25u_*$	$0.25u_*$	linear
Raupach (1989a) ²	0.23	0.06	$1.25u_*$	$0.5u_*$	linear
Raupach et al. (1992)	3.5	0.75	$1.3u_*$	$0.2u_*$	power
Kruijt et al. (1996)	≈ 5.5	≈ 32	$\sigma_w(z_{ref})$	$0.15\sigma_w(z_{ref})$	power
Katul et al. (1997)	≈ 5	13	$\sigma_w(z_{ref})$	$0.9\sigma_w(9\text{m})$	linear
Nemitz et al. (2000)	5.3	1.4	$\approx 1.25u_*$	$\approx 0.1u_*$	power
Leuning et al. (2000)	3.1	0.73	$1.25u_*$	$0.2u_*$	exp
Denmead et al. (2000) ³	5	2.75	$\sigma_w(z_{ref})$	$0.15\sigma_w(z_{ref})$	linear

¹ “family portrait”, ² elevated heat source, ³ based on LAI

For an individual canopy, appropriate profiles for $\sigma_w(z)$ and $T_L(z)$ have to be specified a priori. According to Raupach (1989a), shear dominates the turbulent flow within the canopy when atmospheric stability is close to neutral conditions and thus $\sigma_w(z)$ and T_L scale well with height and σ_{wref} or friction velocity u_* above the canopy. This description is supported by the “family portrait” of turbulence observations within different canopy types given by Raupach (1988). For a wide range of canopy heights (0.06-16.2 m) and LAI values (0.23-4), $\sigma_w(z)/u_*$ decreased from a typical value of 1.25 above canopy height (h_c) to a small value of 0-0.5 close to the ground as expressed by the general parameterization function

$$\frac{\sigma_w(z/h_c)}{\sigma_{wref}} \approx \frac{\sigma_w(z/h_c)}{1.25u_*} = a_{\sigma_f}(z/h_c) \quad (3.5)$$

where $a_{\sigma_f}(z/h_c)$ is a monotonic increasing function of height with $a_{\sigma_f}(0) \ll 0.5$ and $a_{\sigma_f}(z/h_c \geq 1) = 1$. Several implementations of Eq. 3.5 exist for individual canopy types as listed in Table 3.1. Since all these functions are normalized with friction velocity (u_*) or σ_{wref} measured above the canopy, they can be summarized as friction based scaling functions. When u_* is used, a stability correction for the ratio σ_{wref}/u_* should be applied (Leuning et al., 2000). In the present study, nighttime free convection is included as an additional source of vertical mixing in the lower canopy, and a combination of friction and convective based scaling is proposed for nighttime conditions (see Section 3.1). In a first step, $\sigma_w(z)$ is decomposed into a friction part that scales with σ_{wref} (Eq. 3.5) and a free convective part a_{σ_c} that is independent of σ_{wref} leading to

$$\sigma_w(z) = a_{\sigma_c} + a_{\sigma_f}\sigma_{wref}. \quad (3.6)$$

Appropriate implementations for a_{σ_c} and a_{σ_f} are obtained from direct turbulence measurements. In a first step, Eq. 3.6 is fitted separately to the measurements for each height level that have been divided into daytime and wind speed classes (Section 3.2.1). For a purely friction based relationship, a zero intercept would be expected. In contrast, a significant positive intercept would indicate an additional source of vertical mixing that is independent of σ_{wref} (i.e. free convective mixing). In a second step, the derived intercept ($a_{\sigma_c}(z_i)$) and slope ($a_{\sigma_f}(z_i)$) parameters are fitted to two independent height functions described in Appendix A.8.

The parameterization for $T_L(z)$ is even more speculative since it is a purely Lagrangian quantity. Two empirical relationships to Eulerian quantities are established:

$$T_L(z) \approx \frac{L_w(z)}{\sigma_w(z)} \approx \frac{0.71L_s}{\sigma_{wref}}. \quad (3.7)$$

L_w is the Eulerian length scale of the vertical wind and can be estimated from the Eulerian timescale (T_E) and horizontal wind speed (u) as $L_w(z) = u(z)T_E(z)$ using Taylor's frozen turbulence hypothesis (Raupach, 1989a). The simpler approach using the canopy length scale $L_s \approx 0.5h_c$ (Raupach et al., 1996) gives an estimate of $T_L\sigma_{wref}/h_c \approx 0.4$, respectively $T_Lu_*/h_c \approx 0.3$. In the present study, the simple relationship is compared to the height parameterization $T_L(z)\sigma_{wref} = u(z)T_E(z)/\sigma_w(z)$.

3.3 Results and discussion

3.3.1 Parameterization of in-canopy turbulence profiles

The turbulence measurements made at the six different levels at the Jaru site are used to infer the profile functions of the standard deviation of vertical wind speed $\sigma_w(z)$ and the Lagrangian timescale $T_L(z)$. Day- and nighttime as well as high and low wind speed conditions are considered (Section 3.2.4). A graphical representation of the class averaged measurements for $\sigma_w(z)$ is given in Fig. 3.3a. The daytime profiles show a linear increase from close to zero at 1 m height up 0.25-0.5 m s⁻¹ at the third level. At canopy height (h_c), the profile for high wind speed conditions exhibits a global maximum. Averaged nighttime values are in general smaller in absolute numbers and amplitude for different height levels and wind conditions. A small local maximum value can be observed at 11 m height (≈ 0.065 m s⁻¹ at $0.28h_c$), which gives a first indication for nocturnal free convection occurring in the lower canopy (Section 3.1 and 3.2.4).

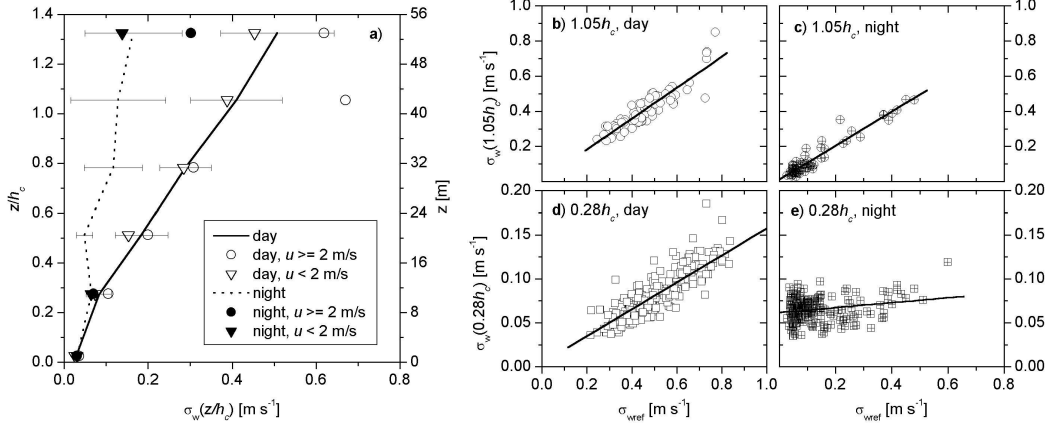


Figure 3.3: a) Mean and standard deviation of $\sigma_w(z)$ measurements for day- and nighttime and different horizontal wind speed (u) conditions. For nighttime conditions, no separation for wind speed is performed at levels 2-4 because of lacking data. b-e) scatter plots for $\sigma_w(z)$ and the standard deviation of vertical wind speed above the canopy (σ_{wref}).

To derive the profile functions, Eq. 3.6 is fitted separately to the measurements for each level and daytime class (Section 3.2.4). Exemplified, this is shown for the day- and nighttime measurements at the 42.2 ($1.05h_c$) and 11 m ($0.28h_c$) level (Fig. 3.3b-e). A zero intercept indicating purely friction based scaling is observed for all levels and daytime and also for the uppermost levels and nighttime (Fig. 3.3b-d). In contrast, a significant positive intercept (0.065 m s^{-1}) is observed for the nighttime measurements at the lower canopy level ($0.28h_c$) which is typical for all 4 lower levels and gives a strong indication for an additional source of vertical mixing (i.e. free convection).

For the further analysis, the height functions for friction and free convective based scaling (Appendix A.8) are fitted to the derived slope and intercept parameters for day- (forced zero intercept) and nighttime conditions separately. For the friction based function, a minimum value $a_{f0} = 0.054$ and zero are obtained for day- and nighttime conditions, respectively. The optimal scaling heights varies between 32.4 (nighttime at high u), 36.5 (daytime, high u), and 46.1 m (daytime low u) resulting in $z_{\sigma f} = h_c \pm 20\%$. All derived parameter values for the two height functions are listed in Table 3.2. Uncertainties are estimated from the variability of optimal parameters for different wind speed conditions. A comparison of the optimized profile functions with the derived slope and intercept parameters for single height levels is shown in Fig. 3.4a-c. The combined scatter plot of all measurements and the values predicted by the parameterization functions are shown in Fig. 3.4d. The excellent agreement between the profile measurements and function predictions ($r^2 = 0.98$, standard error $\approx 0.02 \text{ m s}^{-1}$) shows that $\sigma_w(z)$

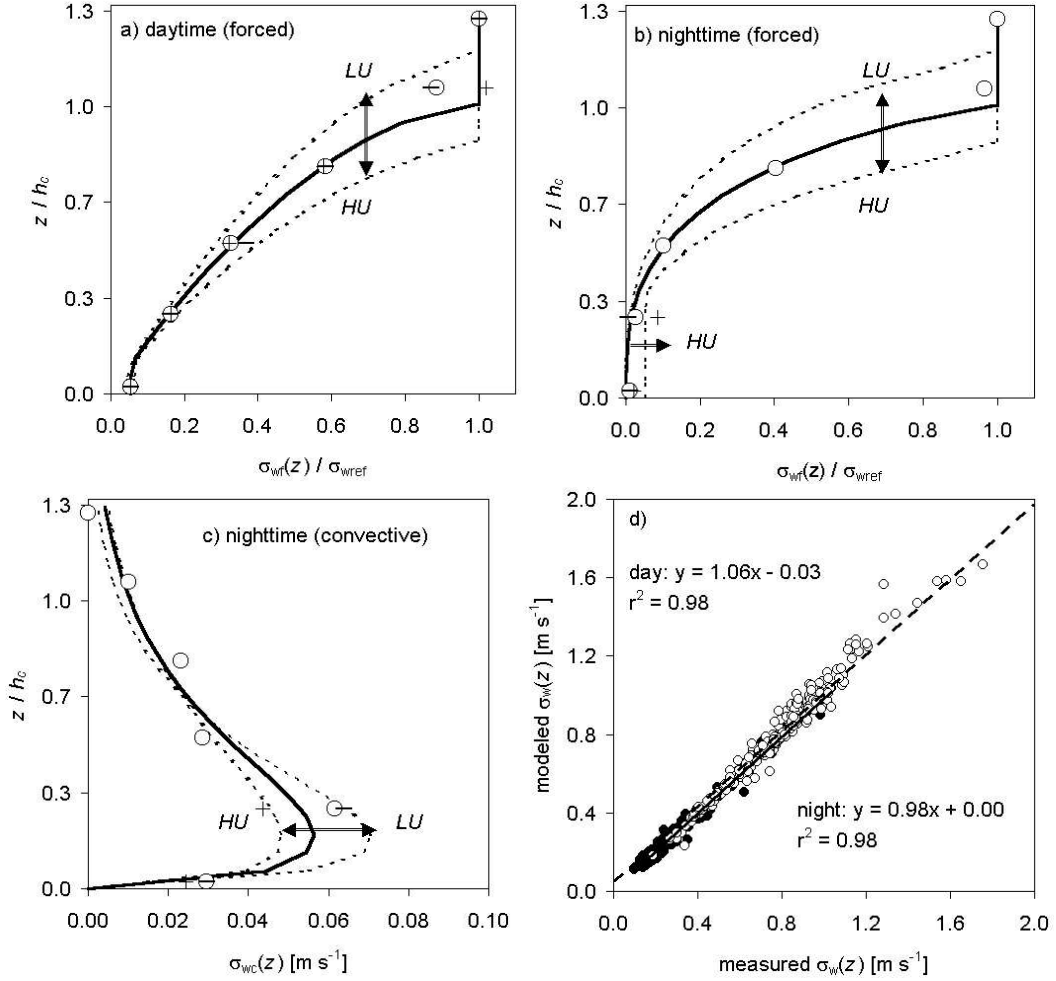


Figure 3.4: Comparison of derived profile functions and representative measurements (after regression analysis) for the standard deviation of vertical wind speed $\sigma_w(z)$, decomposed into a forced fraction (σ_{wf}) that scales with top-level values (σ_{wref} a,b) and a nighttime free convective fraction (σ_{wc} , c). Symbols in a-c) represent observed values derived after linear regression (slope and intercept). Open circles, plus, and minus symbols represent all conditions, and conditions with high and low wind speed, respectively. The solid lines represent the fitted functions, whereas the dotted lines represent derived uncertainties for high (HU) and low (LU) wind speed conditions as listed in Table 3.2. d) Scatter plot for all measured and modeled $\sigma_w(z)$. Open and closed circles represent day- and nighttime values, respectively.

can be parameterized with high accuracy by the derived height functions.

Unfortunately, the Lagrangian timescale parameter T_L has a much higher uncertainty. Fig. 3.5 shows a comparison of the two empirical relationships de-

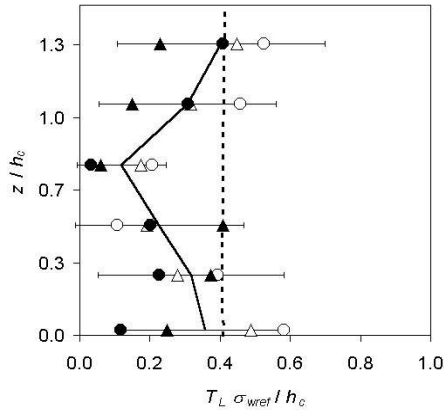


Figure 3.5: Derivation of the Lagrangian timescale T_L . The relationships $T_L = L_w/\sigma_w$ (dashed line) and $L_w = uT_E$ (symbols) are applied (see Section 3.2.4). Open and closed symbols represent day- and nighttime conditions, circles and triangles represent low ($< 2 \text{ m s}^{-1}$) and high wind speed conditions, respectively. The solid line represents mean values for all conditions, with standard deviations as error bars, the dashed line represents the common parameterization using a constant value of 0.4 (Raupach et al., 1996).

scribed in Section 3.2.4. Error bars are calculated by propagation of variances for the different conditions and reflect the uncertainties of the parameterization. Between the upper and lower height levels where only few data points are available, the height dependent parameterization shows a bow-shape inflection of $T_L(z)$ that resembles the observed profiles of Legg et al. (1986) who derived T_L by inverting the far-field diffusivity relationship $K_f = \sigma_w^2 T_L$. Thus, a height dependent relationship might be discussed and should be investigated experimentally in more detail. Nevertheless, with enough data points available (level 1, 5, and 6), the calculations match the simple approach $T_L \sigma_{wref}/h_c = 0.4$ (see Section 3.2.4) reasonably well.

Table 3.2: Parameters for the normalized profiles of the standard deviation of vertical wind speed $\sigma_w(z/h_c)$ described in Appendix A.8 (see text).

Conditions	a_0 [m s^{-1}]	a_1	a_2	z^*
day	0.054 ± 0.01	1.05 ± 0.05	0.58 ± 0.02	$h_c \pm 15\%$
night(f)	$0.0(+0.054)$	3.0 ± 0.2	0.8 ± 0.1	$h_c \pm 15\%$
night(c)	-	1.6 ± 0.1	8.0 ± 2.0	$26.7m$

3.3.2 Meteorological conditions at the Cuieiras site

Fig. 3.6 gives an overview of the meteorological conditions observed during the intensive investigation period at the Cuieiras site. At the beginning of the two weeks period, cloudy conditions and frequent rain events could be observed. At the end of the first week, global radiation, horizontal wind speed, and diurnal amplitudes of ambient temperature and relative humidity increased. The general

'clear-sky' weather conditions until the end of July were interrupted by the second period with clouds and rain between 22 and 24 of July. Longer periods with heavy rainfall were not be observed. Consequently, the radon soil fluxes could be regarded as not be extremely suppressed by soil water logging.

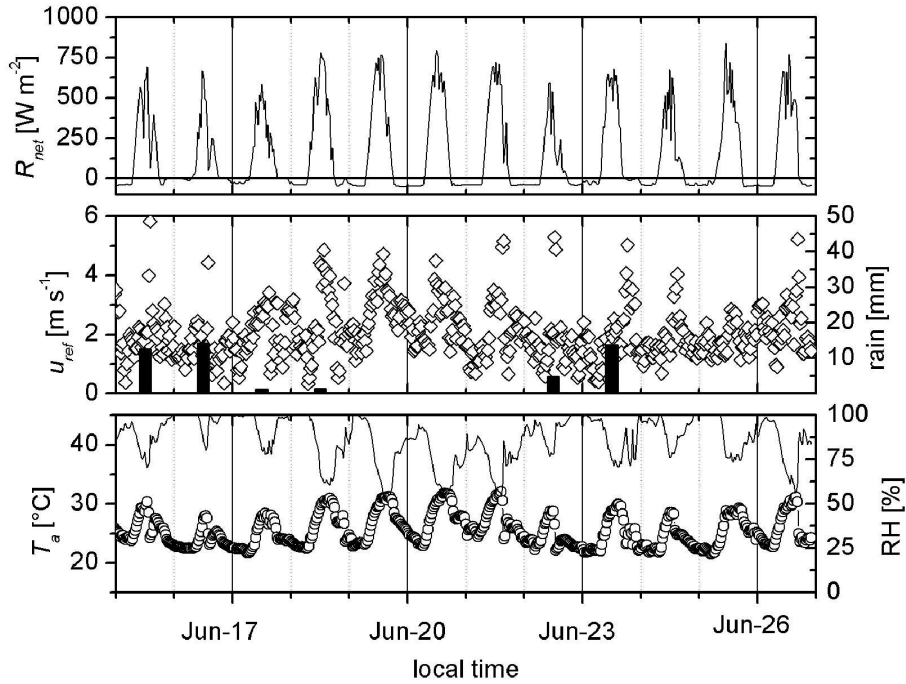


Figure 3.6: Overview of the meteorological conditions observed at the Cuieiras site (tower ZF2-K34) between 15th and 27th of July 2001 (net radiation R_{net} , mean horizontal wind speed u_{ref} , daily rainfall as column bars, ambient temperature T_{ref} as open circles, and relative humidity RH as solid line). All data except rain fall (daily sum) represent half hourly mean values.

3.3.3 Observed radon soil fluxes at the Cuieiras site

A total number of 15 simultaneous soil flux measurements for ^{220}Rn (J_{220}) and ^{222}Rn (J_{222}) could be derived as described in Section 3.2.3 and Appendix B. Observed values for the short-lived ^{220}Rn ranged from 10-25 $\text{Bq m}^{-2} \text{s}^{-1}$ with a mean value of $17.7 \pm 4.2 \text{ Bq m}^{-2} \text{s}^{-1}$ whereas the fluxes of the longer lived ^{222}Rn are one order of magnitude lower (0.019-0.052 $\text{Bq m}^{-2} \text{s}^{-1}$) with a mean value of $0.0366 \pm 0.0101 \text{ Bq m}^{-2} \text{s}^{-1}$). The frequency distributions for J_{220} and J_{222} are shown in Fig. 3.7a-b. Table 3.3 compiles the actual data and those found in the literature for the Amazon basin. Compared to the wet season measurements made by Trumbore et al. (1990), the observations of the present study are higher by a

factor of 4.5 and two times higher than the global average estimate of Wilkening et al. (1972). For the Jaru site, the estimate of Gut et al. (2002b, using the same detectors) agrees well with our measurements. In general, the observed values for the dry season are relatively high especially for ^{220}Rn , but not unusual (see Nazaroff, 1992).

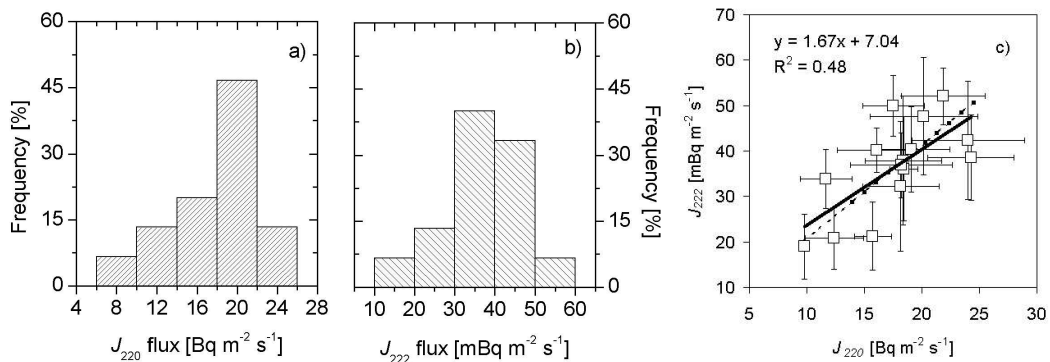


Figure 3.7: Frequency distribution of derived ^{220}Rn (a) and ^{222}Rn (b) flux (J_{220} and J_{222} , respectively) and flux correlation (c). The dotted line represents predictions of the soil diffusion model outlined in Appendix B using the ratio of mean values for J_{220} and J_{222} and a varying water filled soil space of 0.2-0.5 as input (see text). The solid line is obtained after linear regression.

The observed flux variability and the flux correlation between the two radon species were tested for plausibility by applying a simple soil diffusion model (Nazaroff, 1992; Lehmann and Lehmann, 2000) described in Appendix B. With common parameter values this model verifies whether the species dependent lifetime and assumed variability of soil diffusivity can explain the observed variations and correlation between J_{220} and J_{222} . Inserting the mean observed fluxes ($J_{220} = 17.7$ and $J_{222} = 0.036.6 \text{ Bq m}^{-2} \text{ s}^{-1}$) into Eq. B.3 gives a ratio of 0.160 for the equilibrium activities and predicts $J_{222} \approx 0.002J_{220}$ that agrees with our observations (Fig. 3.7c). If the soil water content is modified moderately in a typical range from 0.2 to 0.5, the predicted variation of both species agrees with the observed range of fluxes within their uncertainty. For the radon dispersion experiment, the mean observed value $J_{222} = 0.0366 \text{ Bq m}^{-2} \text{ s}^{-1}$ is regarded to be representative for the site and investigation period. Since only single-point measurements could be derived, a high uncertainty of 50% is assumed. Sources or sinks within the canopy are neglected. As discussed by Trumbore et al. (1990), they contribute less than 5% to the total exchange.

Table 3.3: Comparison of mean observed radon soil flux (J_{222}) with other measurements in the Amazon basin (values in units of $\text{mBq m}^{-2} \text{s}^{-1}$).

Reference	Range (Mean)	Season	Soil
Trumbore et al. (1990)	5.3-13.7 (8.0)	wet (Apr.- May 1987)	<i>yellow oxisol</i>
Gut et al. (2002b)	15.0-40.0 (28.3)	late dry (Oct. 1999)	<i>orthic acrisol</i>
<i>this work</i>	19.0-52.1 (36.6)	early dry (Jul. 2001)	clayey oxisol [†]

[†] see Araujo et al. (2002)

3.3.4 Forward modeling of ^{222}Rn activity concentrations

The inferred turbulence parameterization (Section 3.3.1) using the derived profile functions for the standard deviation of vertical wind speed $\sigma_w(z)$ and the Lagrangian timescale are evaluated by comparing the forward predicted and mean observed profiles of ^{222}Rn activity concentration. The mean observed surface flux $J_{222} = 0.0366 \text{ Bq m}^{-2} \text{ s}^{-1}$ (Section 3.3.3) is used as a constant input source of the soil layer whereas the canopy layer source is set to zero (Fig. 3.1a). Prediction uncertainties are assessed by varying J_{222} about 50% and by applying the modified turbulence parameterizations for high and low wind speed conditions (see Section 3.3.1).

A comparison of predicted and measured activity concentration profiles is shown in Fig. 3.8. In general, the model simulations match the observations within their uncertainty range. Day- and nighttime profiles have a slightly different shape. Daytime concentrations in the upper and middle canopy increase more rapidly with height although the vertical gradients are in general very small. The largest gradients are observed and predicted in the lowest five meters. For nighttime conditions, the range of predicted activities is very narrow for the two wind speed classes compared to daytime conditions because the effect of depressed forced mixing for low wind speed conditions (σ_{wref} , Fig. 3.3a) is compensated by higher free convective mixing (Fig. 3.4c). Considering the high uncertainty of the measured soil fluxes and intermittent inhomogeneous nature of vertical mixing within the canopy, the predicted profiles agree reasonably well with the observations.

For a reasonable prediction of the nighttime profiles, the combined scaling of $\sigma_w(z)$ (Section 3.2.4) is quite essential. As demonstrated in Fig. 3.9, neglecting nighttime free convection leads to 'false' profiles with activities two orders of magnitude higher than the observation in the lower canopy. The higher values of $\sigma_w(z)$ obtained from friction based scaling for high wind speed (Figure 3.4b) have only marginal effects on the predicted profile whereas the free convective scaling with $a_{\sigma_c} \approx 0.05 \text{ m s}^{-1}$ (Fig. 3.4c) has a large impact on the whole activity concentration profile. Obviously, nighttime free convection couples the lower and upper canopy very efficiently. This application shows, that this process is highly significant for the nighttime vertical distribution of trace gases within the canopy.

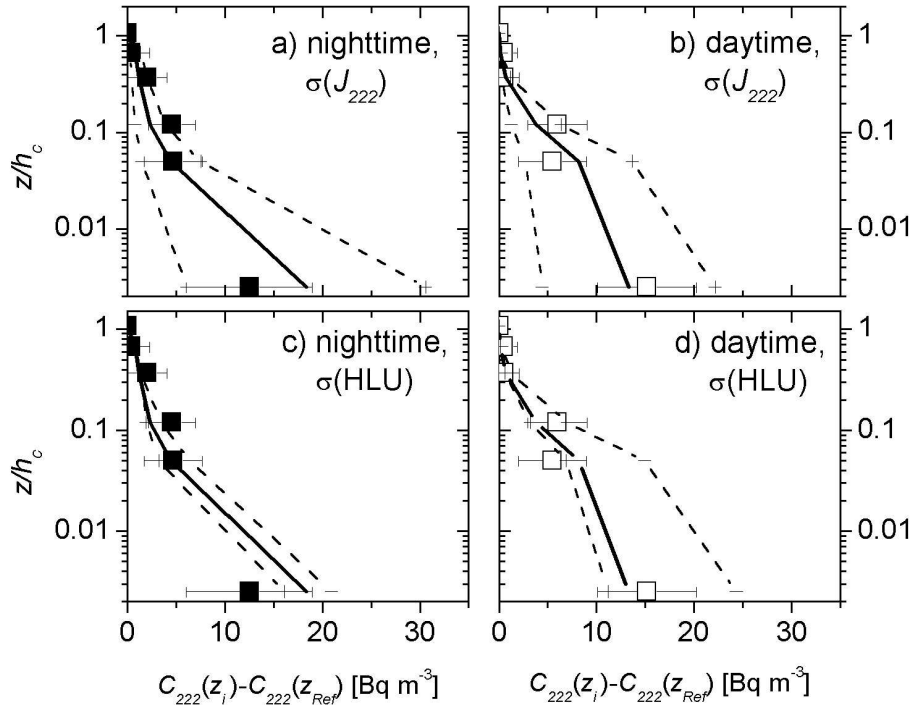


Figure 3.8: Comparison of mean observed (squares) and forward predicted (lines) activity concentration profiles for nighttime (a,c) and daytime (b,d) conditions (where $C_{222}(z_j) - C_{222ref}$ is the activity concentration difference between height z_j and z_{ref} at 43 m) using an averaged soil flux of $J_{222} = 0.036 \text{ Bq m}^{-2} \text{ s}^{-1}$ (Section 3.3.3). Error bars represent standard deviations of the measurements. The dotted lines represent uncertainties predicted for a 50% variation of J_{222} ($\sigma(J_{222})$, a-b) and the modified turbulence parameterization for high ($u \geq 2 \text{ m s}^{-1}$) and low ($u < 2 \text{ m s}^{-1}$) wind speed conditions ($\sigma(\text{HLU})$, c-d, see Section 3.3.1).

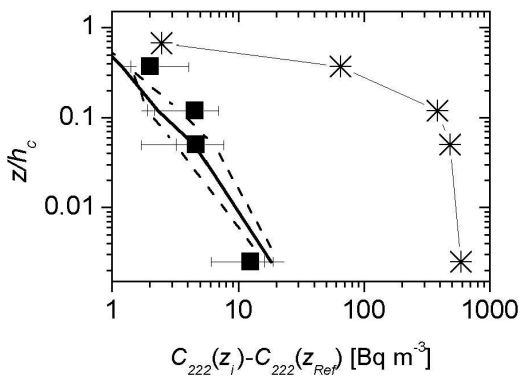


Figure 3.9: Comparison of observed (filled quarters) and predicted (lines) nighttime activity concentrations (see Fig. 3.8c) on a logarithmic scale applying additionally a turbulence parameterization for high wind speed where nighttime free convection is neglected (line with star symbols).

3.3.5 Effective transfer velocities and timescales

Effective timescales and transfer velocities within the canopy are of special interest for surface-atmospheric exchange of reactive trace gases like nitric oxide and ozone (Section 3.1). Since radon sources and sinks within the canopy can be neglected, the effective transfer velocities and timescales can be calculated according to

$$\nu_{ref}(z_i) = \frac{J_{222} + dC_{222}/dt}{C_{222}(z_i) - C_{222ref}} \quad (3.8)$$

$$\tau_{ref}(z_i) = \frac{1}{\nu_{ref}(z_i)} (z_{ref} - z_i). \quad (3.9)$$

$\tau_{ref}(z_i)$ represents the period needed by an air parcel with a mean transfer velocity $\nu_{ref}(z_i)$ to emanate from height z_i within the canopy to z_{ref} , which is 43 m in this case. Although the storage term dC_{222}/dt in Eq. 3.8 can become significant on short timescales of an half hour, it is small in the current case where day- and nighttime profiles are averaged and can be neglected.

The resulting profiles $\tau_{ref}(z_i)$ and $\nu_{ref}(z_i)$ for the mean measured and predicted activity concentrations (Fig. 3.8) are shown in Fig. 3.10. At $0.5h_c$, τ_{ref} is ≈ 40 and ≈ 11 min for night- and daytime conditions, respectively, suggesting a much higher canopy ventilation rate than earlier estimates for another site near Manaus. Based on ^{222}Rn measurements, Trumbore et al. (1990) derived a flushing time of $\tau_{ref} = 3.4$ hours for the ventilation of the entire canopy air during nighttime and a mean transfer coefficient $\nu_{ref} = 0.33 \pm 0.15 \text{ cm s}^{-1}$, which agrees with the results of the present study only for the lowest 5 m above the ground. The higher ventilation rates estimated here correspond to the results of Rummel (2004) for the Jaru site.

3.3.6 Inverse predictions of ^{222}Rn fluxes

In the previous two sections it has been shown that the turbulence parameterization implemented in the LNF model offers a good description of vertical dispersion for the rain forest site under investigation. Solving the inverse problem to infer vertical source/sink distributions from concentration profiles introduces another uncertainty to the model, which will be addressed in the following section using the same discretization of source layers and profile heights for the inverse approach (Fig. 3.1a). Uncertainties are inferred by calculating the sensitivity (standard error) of the source predictions to systematic changes of the input concentration profile (Simon et al., 2002). It is assumed that ^{222}Rn activity concentration measurements have an accuracy of 3 Bq m^{-3} (Section 3.2.3). Ideally, the inferred soil source strength should agree with the mean observed soil flux ($0.0366 \text{ Bq m}^{-2} \text{ s}^{-1}$), whereas the predicted canopy source/sink should be zero.

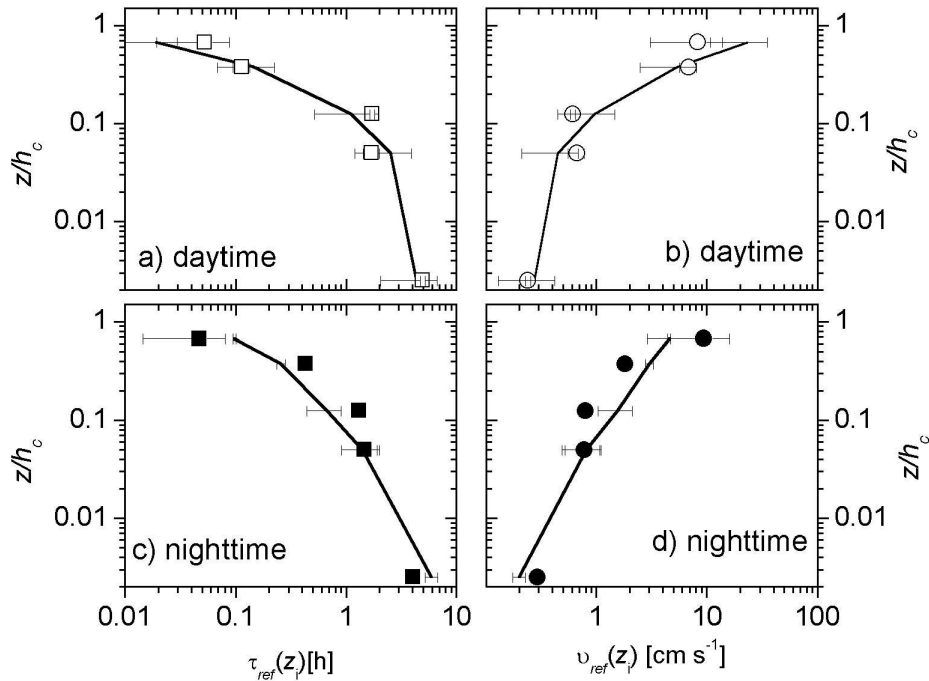


Figure 3.10: Comparison of effective timescales (τ_{ref} , a,c) and transfer velocities (ν_{ref} , b,d) derived from observed ^{222}Rn profiles (symbols, Fig. 3.8) and predicted by the LNF model (solid lines). Error bars are calculated from variances obtained for different wind conditions and turbulence parameterizations

The simulated daytime soil flux agrees with the mean observation whereas the nighttime predictions are reduced to nearly 50% of the measured values (Fig. 3.11a). The modeled canopy layer source term has in general a very high sensitivity to the input concentration profile (Fig. 3.11b-c). A change of 1 Bq m^{-3} at one profile height level causes a predicted source change of 20-40% in relation to the observed soil flux. For daytime condition the highest sensitivities are found for the lowest (0.02 m) and fourth (5 m) height level. Although the sensitivities for nighttime conditions are lower, the resulting canopy source uncertainty for an assumed precision of 3 Bq m^{-3} is of the same order of magnitude than the predicted nighttime source (Fig. 3.11a, error bars). On average, the derived and assumed source/sink distributions for ^{222}Rn are within their uncertainty range.

3.3.7 Net fluxes for CO_2 , latent and sensible heat

The inverse LNF approach evaluated with radon measurements is also applied to profiles of carbon dioxide and water vapor at the Cuieiras site (Fig. 3.1b). The predicted vertical net flux is compared to Eddy Covariance (EC) measurements

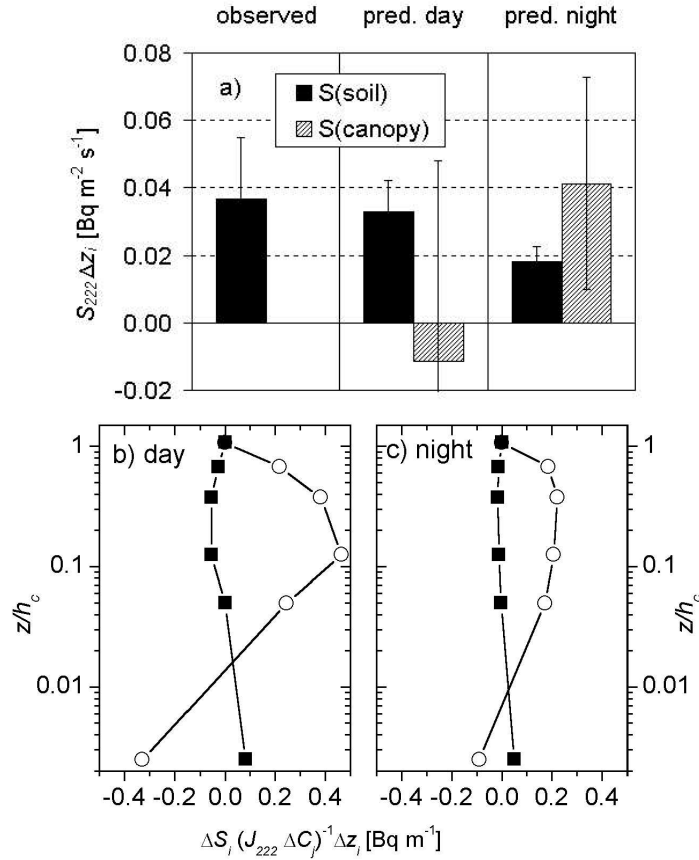


Figure 3.11: a) Mean observed and inversely predicted source/sink distribution of ^{222}Rn . The inverse approach is applied to the observed concentration profiles described in Section 3.2.3 using a soil (0-0.01 m) and a canopy source layer (0.01-40 m). Measured soil source $S_{222}(\text{soil})$ is equivalent to the mean soil flux J_{222} whereas canopy source strength is assumed to be zero. Positive and negative error bars for predictions represent estimated standard errors calculated from the sensitivity profiles shown in b) and c). These profiles represent the relative sensitivity of the inverse solution to the input concentration profile (soil and canopy layer as closed quarters and open circles, respectively). Changing the input concentration at height z_j by $\Delta C = 1 \text{ Bq m}^{-3}$ causes a relative change $\Delta S_i / J_{222} \Delta z_i$ in the predicted source strength of layer i .

above the canopy (Section 3.2.1). A four days period is selected for a detailed comparison of model predictions with EC measurements (which are not available for the whole period). Time series and scatter plots of the measured and predicted net fluxes are shown in Fig. 3.12a-d. The error bars for model results represent the standard errors resulting from assumed measurement accuracies of $0.5 \mu\text{mol mol}^{-1}$ and $0.05 \text{ mmol mol}^{-1}$ for CO_2 and H_2O concentrations, respectively, and

calculated as earlier described for radon (Section 3.3.6). In general, the model predictions show a good agreement with the EC measurements.

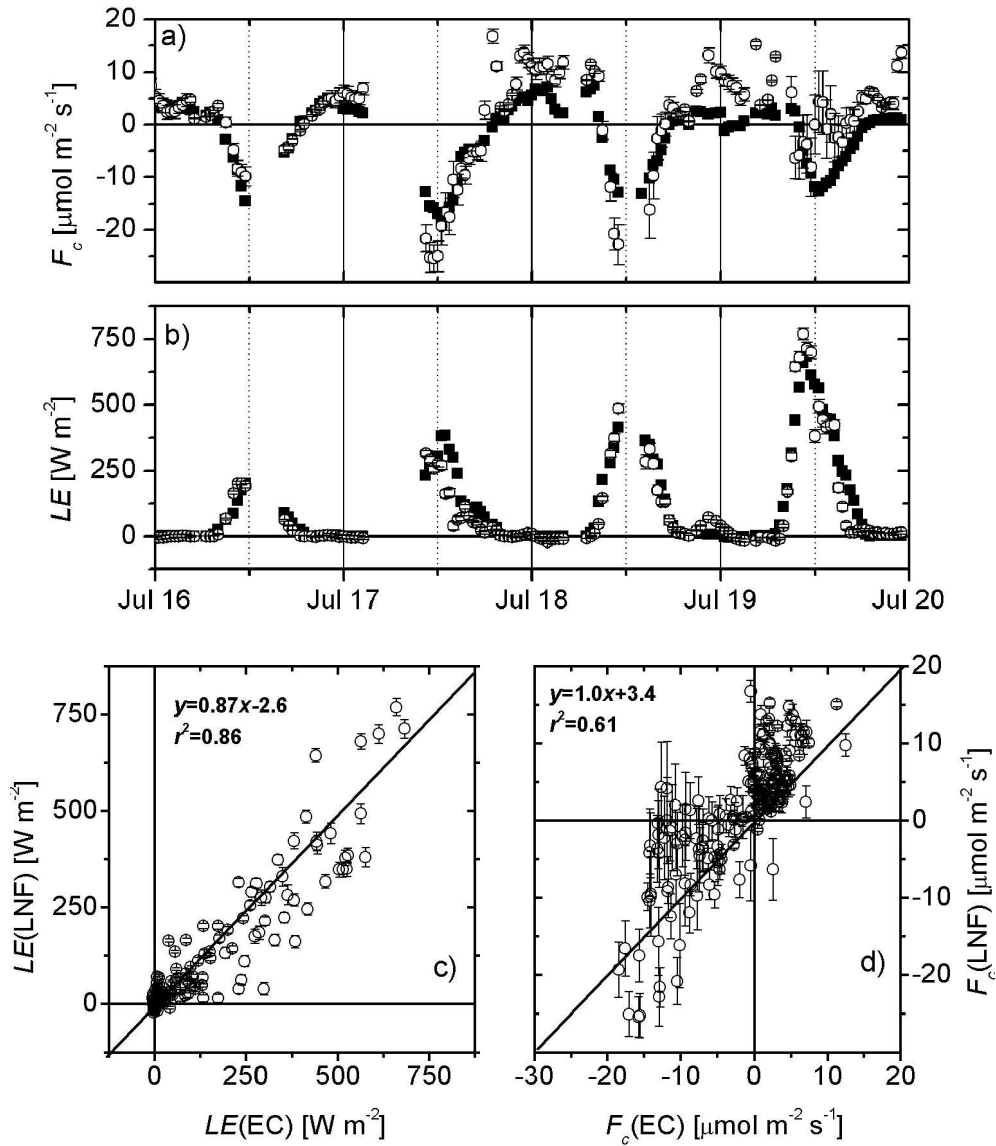


Figure 3.12: Comparison of observed (Eddy Covariance technique EC, a-b: closed quarters, c-d: abscissa) and inverse predicted (LNF, a-b: open circles, c-d: ordinates) net fluxes of CO_2 (F_c , a,d) and latent heat (LE , b,c) for two hourly averaged input parameters. Error bars for model predictions represent standard errors obtained with an uncertainty of $0.5 \mu\text{mol mol}^{-1}$ and $0.05 \text{mmol mol}^{-1}$ for CO_2 and H_2O concentration, respectively.

The relative uncertainties of simulated daytime CO_2 fluxes (F_c) are one order

of magnitude higher compared to the latent heat flux (LE) and may explain the disagreement of simulations and observations during noon time and especially on 19th July (Fig. 3.12a). Given typical values $\sigma_{wref} = 0.3 \text{ m s}^{-1}$, $F_c = 15 \text{ } \mu\text{mol m}^{-2} \text{ s}^{-1}$ and $LE = 300 \text{ W m}^{-2}$ the relative uncertainty for CO_2 is $\Delta F_c/F_c \approx 16\%$ compared to only 4% for H_2O . These values increase to 42% and 9%, respectively, for high turbulence intensities usually observed at noon time with $\sigma_{wref} \approx 0.8 \text{ m s}^{-1}$. Although it is predicted that LE has a much higher relative uncertainty for nighttime conditions (50-100%), this reflects only the very small flux values ($\leq 10 \text{ W m}^{-2}$). The nighttime fluxes for CO_2 predicted by the LNF model are significantly higher than the values observed by EC method leading to a positive intercept of the regression line (Fig. 3.12d). In general, the scatter is very high reflecting the large uncertainties of the inverse approach. Especially during daytime, effective mixing in the upper canopy leads to small gradients of the scalar profiles, which are for CO_2 on a similar order of magnitude as the measurement accuracy. Therefore, cases with very high averaged turbulence intensities with $\sigma_{wref} > 0.6$ were discarded for the following analysis of averaged diurnal source/sink distributions and daily integrated carbon fluxes.

3.3.8 Diurnal source/sink distributions for CO_2 and H_2O

The source/sink distributions, which are related to the predicted net fluxes of CO_2 and H_2O (previous section), are averaged diurnally. Results for the lower (0-5 m), middle (5-20 m) and upper (20-40 m) canopy are shown in Fig. 3.13. The given time represents the starting time for each interval (e.g. 9:00 from 9-10 h). The shown diurnal courses should be interpreted with some caution taking into consideration the sensitivity of predicted upper canopy source/sink strength in general (as shown for ^{222}Rn in Fig. 3.11b) and the uncertainty for CO_2 in special (as discussed above).

Before noon time, the total budgets of CO_2 and H_2O are dominated by carbon uptake and transpiration loss of the upper canopy. In the afternoon, the exchange of the middle canopy becomes more important, especially for carbon exchange. Surprisingly, the LNF technique predicts the upper canopy to act as a carbon source in the late afternoon around 15-16 h while the transpiration term is still significantly positive. The bottom canopy layer, which mainly represents the soil activity, shows a less pronounced diurnal course. It has a positive sign for CO_2 all over the day suggesting only a weak photosynthetic activity of the ground vegetation. Predicted values are 3 to $10 \text{ } \mu\text{mol m}^{-2} \text{ s}^{-1}$, which agree with soil respiration measurements of Meir et al. (1996) made at the Jaru site ($5.5 \pm 0.7 \text{ } \mu\text{mol m}^{-2} \text{ s}^{-1}$) and the observed range for the measurements described in Chapter 2. Latent heat flux of the lower canopy layer is less than 15% of the total evapotranspiration, which is a typical value for dense vegetation (Jones, 1992).

It is not possible to evaluate these results quantitatively with independent measurements because appropriate methods are not available. Alternatively, this

can be done with a model approach that simulates physiological exchange of the analyzed tracers (Chapter 4). Nevertheless, the observed features of diurnal exchange for water and carbon as described above are not too contradictory to our knowledge of the physical and physiological processes inside the canopy. From stomatal regulation research it is well known, that stomatal exchange and consequently CO_2 uptake of sunlit leaves is often suppressed when water vapor pressure deficit becomes high in the early afternoon (see also McWilliam et al., 1996). Shaded leaves in the middle and lower canopy instead are light limited and the vapor pressure deficit is lower. This is a plausible explanation for the observed vertical shift of physiological activity from upper to lower canopy regions, in the course of the day.

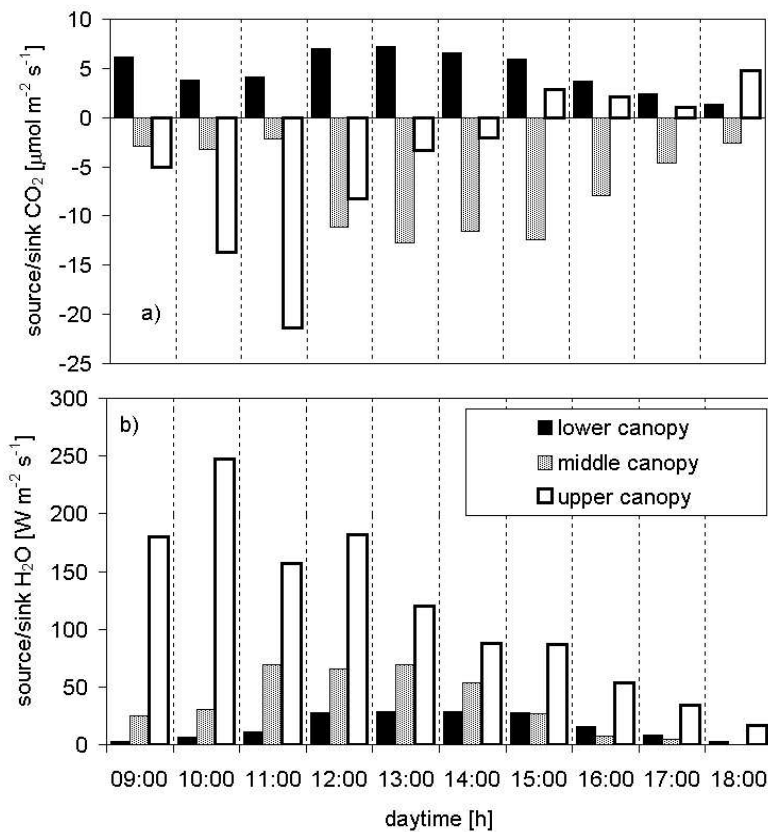


Figure 3.13: Mean predicted diurnal source/sink distribution for CO_2 (a) and latent heat (b). Lower, middle, and upper canopy layers are from 0-10, 10-20, 20-40 m height, respectively (Fig. 3.1b).

3.3.9 Daily integrated net carbon exchange

As already outlined in Chapter 1 and Section 3.1, the integrated carbon dioxide flux of the Amazonian rain forest is of special interest for regional as well as global carbon and greenhouse gas budget studies. Therefore, the averaged diurnal courses of CO_2 source/sink distributions are integrated to a daily net ecosystem exchange (NEE). Fig. 3.14 shows the accumulated day- and nighttime values and the total budget, which predicts a carbon sink of $0.03 \text{ mol C m}^{-2} \text{ d}^{-1}$. On a simple yearly projection this results in an annual sink of $2.8 \text{ t C ha}^{-1} \text{ yr}^{-1}$, which is on the lower range of the $1 \text{ to } 8 \text{ t C ha}^{-1} \text{ yr}^{-1}$ estimated by Araujo et al. (2002) for a one year record of EC data for the same tower. Compared to this and other earlier estimates (Malhi et al., 1998; Carswell et al., 2002) the daytime values derived for the short observational period agree well with EC measurements, although the uncertainty range is high. Predicted nighttime fluxes are significantly higher, especially for calm wind conditions. This observation goes along with results from recent studies stating that total ecosystem carbon sink is probably overestimated by EC method due to an underestimated nighttime flux (Culf et al., 1999). Thus, a potential benefit of the presented LNF application is its independent estimate of nighttime CO_2 exchange. Therefore, the corresponding results are analyzed in more detail. Fig. 3.14b-c show the frequency distribution of the derived net fluxes for nighttime conditions. Most predictions give values from $3\text{-}10 \mu\text{mol m}^{-2} \text{ s}^{-1}$ with an arithmetic mean value of $\approx 7.5 \mu\text{mol m}^{-2} \text{ s}^{-1}$. This is $1.5 \mu\text{mol m}^{-2} \text{ s}^{-1}$ higher than the respective median value of the distribution skewed with a single mode. The EC method shows similar values for conditions with high nighttime friction velocities $u_* > 0.2$ resulting in the lower range estimate of total NEE ($1 \text{ t C ha}^{-1} \text{ yr}^{-1}$, Araujo et al., 2002).

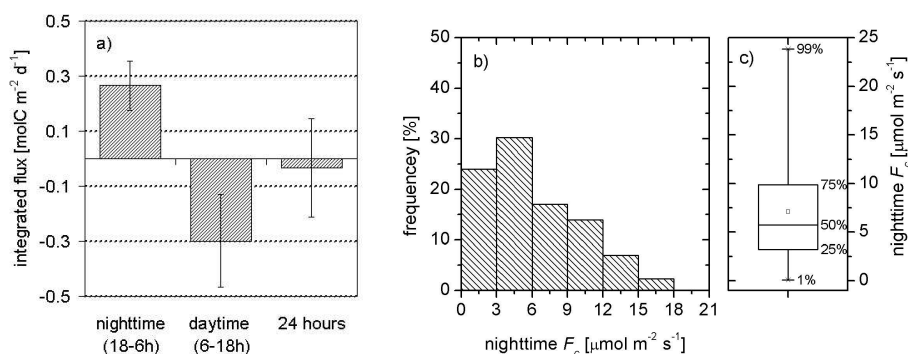


Figure 3.14: a) Daily integrated carbon exchange (daytime averages from 6-18h, nighttime averages from 18-6 h local time, respectively). b-c) frequency distribution and box chart of CO_2 nighttime fluxes

3.4 Conclusions

- The normalized profile of the standard deviation of vertical wind speed derived for the Rondônia site showed a high accuracy compared to direct measurements. The application of statistical distribution functions allows suitable modifications for different meteorological conditions and canopy types. This simplifies their application in future studies. There is a need for more reliable parameterizations of the Lagrangian timescale as shown by the evaluation of the actually available empirical relationships.
- It is demonstrated, that ^{222}Rn is a useful tracer to study the vertical exchange of scalars within the canopy. As one of the few studies, where the source/sink distribution and concentration profile are known simultaneously, the forward and inverse solution of the applied transfer scheme could be evaluated separately. This allows to distinguish uncertainties related to the parameterization of vertical transport and the inversion of the transfer equations.
- Although the flux and concentration measurements of ^{222}Rn have high uncertainties, appropriate time averaged values can reasonably well prove the forward solution of the Localized Near Field theory (LNF) and the presented implementation for the Amazon rain forest.
- The inverse solutions to infer the source/sink distributions from scalar profiles show a very high sensitivity to the profile measurements, especially for the upper canopy and under high turbulence intensities. In future applications, the uncertainties of the inverse solutions should be quantified as described in the present study.
- For reliable predictions of nighttime exchange it is essential to include free convective mixing in the lower canopy in the turbulence parameterization scheme. In the present study, this is achieved with a linear model (convective + friction based scaling) of $\sigma_w(z)$. Although the convective fraction of $\sigma_w(z)$ is low in absolute numbers ($\approx 0.065 \text{ m s}^{-1}$), it is of the same order of magnitude than friction induced values above the canopy, especially during calm nights and sustains an effective coupling between the lower and upper canopy.
- The earlier estimate of canopy residence time (Trumbore et al., 1990) could not be supported. For the investigated site, a much lower value ≤ 1 hour is suggested for nighttime conditions. This may affect the predicted canopy reduction effect on net fluxes of trace gases that are emitted from the soil, since chemical and biological removal processes in the vegetation layer would be less effective.

- The application of LNF theory to the CO_2 exchange of the rain forest shows a reasonable agreement with Eddy Covariance (EC) measurements. Modeled nighttime fluxes are 10-40% higher compared to EC method predicting a smaller net carbon sink.

Chapter 4

Modeling seasonal exchange of energy, CO₂, isoprene, and ozone in the Amazon rain forest

Abstract

A multi-layer scheme of canopy trace gas exchange which combines the coupled equations of leaf surface exchange for sensible heat, water vapor and CO₂ with a Lagrangian dispersion model of vertical transfer within plant canopies is applied to a rain forest canopy in southwest Amazonia (Jaru site). Predicted net fluxes and concentration profiles for the late wet and late dry season are compared to observations during two intensive field campaigns in 1999. For steady-state environmental conditions during day- and nighttime, stable numerical solutions for the temperature at the leaf surfaces and within the canopy air space are found. The predicted day- and nighttime thermal stratification of the canopy layer is consistent with observations in dense canopies. The model predictions have a high sensitivity to stomatal conductance and leaf photosynthesis.

The comparison between observed and simulated net fluxes above and concentration profiles within the canopy shows a good agreement. The observed seasonal variability of diurnal canopy fluxes can be explained by changing environmental conditions (radiation, temperature, water pressure deficit) and a slight modification of leaf physiological parameters assuming increased stomatal conductances and decreased assimilation rates for wet and dry season conditions, respectively. The resulting integrated net carbon sink and midday Bowen ratio range between 1 and 2.5 and 0.5 and 0.8 t C ha⁻¹ yr⁻¹, respectively. Exchange of isoprene and ozone are also calculated. The predicted canopy net emissions of isoprene increased from the late wet to the late dry season by 30% without and by 40% including seasonal changes in leaf physiology. Assuming a constant emission capacity in all canopy layers, a disagreement between observed and predicted profiles of isoprene concentrations in the lower canopy is found suggesting a reduction of emission capacity for shade adapted leaves and additional deposition

processes to soil or leaf surfaces. Assuming a strong light acclimation of isoprene emission capacity, the predicted net fluxes are reduced by 30%. The predicted ozone deposition and concentrations show a good agreement with the observed dry season deposition velocities and the day- and nighttime vertical concentrations profiles of ozone within the canopy. However, for wet season conditions, the observed daytime deposition velocities increase by 150-250% which can not be explained solely by physiological changes, nor by changes in canopy structure. Instead, the observed fluxes can be reproduced assuming an enhanced cuticular uptake, equivalent to a decrease of the cuticular resistance to ozone deposition from 5000 to 1000 s m⁻¹ suggesting an additional uptake mechanism during the wet season.

4.1 Introduction

In Chapter 2, a multi-layer canopy model coupling the equations of leaf surface exchange with a Lagrangian dispersion transfer scheme has been presented. A parameterization of Amazon rain forest surface characteristics has been inferred and evaluated using available field measurements from several sites in central and southwest Amazonia. In Chapter 3, a parameterization of turbulence properties for day- and nighttime conditions has been derived and the Lagrangian dispersion model has been evaluated intensively using radon as an inert tracer of in-canopy turbulence. In this Chapter, the model is applied using the derived parameterization for the mean meteorological conditions observed during the late wet and late dry season 1999 at the Jaru site in Rondônia coinciding with the LBA/EUSTACH-I (Apr-May) + II (Oct-Nov) campaigns (hereafter referred to as EUST-I and EUST-II, see also Chapter 2). The following questions are addressed:

1. Are the applied environmental boundary-conditions in steady-state or does the coupling of surface exchange and vertical dispersion result in numerical instabilities of the predicted canopy temperature and H₂O and CO₂ concentrations?
2. Is the model predicted thermal stratification of the canopy consistent with observations?
3. What are the key parameters and uncertainties of the model?
4. How well does the model perform compared to observations?
5. To what extent does the model explain the observed flux and concentration variabilities?
6. How does the model contribute to our understanding of the exchange of other important atmospheric trace gases?

(1) The first point is related to the conceptual framework of the presented approach. It has to be shown, that the interactive coupling of surface exchange and vertical mixing does not result in unstable or unrealistic numerical solutions. This might occur if for example the air temperature or CO₂ concentrations of a single canopy layer increases with every iteration step of surface exchange because the calculated vertical mixing rate is too slow. (2) The thermal stratification in the lower part of dense canopies shows a typical diurnal pattern, which is the reverse compared to the atmospheric boundary-layer (see Chapter 3). The derived solutions for canopy air and surface temperature will be discussed within this context. (3) The sensitivity of model predictions is assessed considering the uncertainties of the parameters related to canopy structure, leaf surface exchange and radiation absorption derived and discussed in Chapter 2. (4) As a result of the intensive field campaigns at the Jaru site in Rondônia, 1999 during LBA/EUSTACH-I+II (Chapter 2), an extensive database can be used for model evaluation. In contrast to similar modeling studies, it was possible to use independent data sets for parameterization (Chapter 2) and evaluation, respectively. Especially the combination of fluxes and concentration profiles represents a very meaningful evaluation as the right fluxes could also be predicted with the wrong concentrations. (5) Concerning the variability of energy and trace gas exchange of the Amazon rain forest, short- and longterm frequencies have to be distinguished, which are both regulated by the diurnal and yearly solar cycles, respectively. The diurnal variability is assessed by comparing mean diurnal courses of net fluxes and day- and nighttime profiles of CO₂ and H₂O concentration within the canopy with the observations. The longterm variability is characterized mainly by periods of high and low rainfall, which may trigger ecophysiological (stomatal conductance, photosynthesis) or structural (LAI) acclimations of the rain forest canopy (Malhi et al., 1998; Williams et al., 1998; Andreae et al., 2002). This question can partly be assessed by combining the model parameter sensitivity (see above) with the observed flux variability. (6) Finally, the application of the model allows to study the exchange of other important atmospheric trace gases beside CO₂. This is demonstrated by the comparison of predicted and observed concentration profiles of isoprene and ozone and ozone net fluxes.

4.2 Material and method

4.2.1 Site location, period and field data

A detailed description of the Jaru site has been given in Chapter 2. The late wet (Apr-May) and late dry (Sep-Oct) season periods in 1999 have been chosen for application because extensive data sets have been delivered (Andreae et al., 2002). To assess the seasonal variability of net fluxes and concentrations, the input and evaluation data sets, which are available with a time resolution of 30

min, are averaged to hourly diurnal cycles. The time is indicated by the starting time (e.g. 8 h represents the time interval from 8-9 h) for late wet (EUST-I) and late dry (EUST-II) season conditions. A comparison of the arithmetic mean and median values showed a good agreement for all data, i.e. the micrometeorological input parameters, the model output, and the evaluation data. An exception is the standard deviation of vertical wind speed (turbulence parameter σ_{wref}) at nighttime conditions, where the median is up to 40% smaller compared to the arithmetic mean as a consequence of few 'untypical' nighttime cases with high turbulence (see also Chapter 3). This has consequences for the predicted nighttime concentration profiles, especially for CO₂, which will be discussed in more detail in Section 4.3.3.

The predicted net fluxes and profiles for sensible heat, water vapor (latent heat) and CO₂ are evaluated with Eddy Covariance fluxes above and concentration profile measurements inside the canopy. Simultaneous measurements from two closely located towers at the Jaru site (see Chapter 2) are available for the investigation period: First from the old ABRACOS tower RBJ-A (flux: $z_{ref} = 53$ m, profile $z_i = 51.7, 42.2, 31.3, 20.5, 11.3, 4, 1,$ and 0.3 m, see Rummel, 2004, for a detailed description) and secondly from the newer tower RBJ-B (flux: $z_{ref} = 62$ m, profile $z_i = 62.7, 45, 35, 25, 2.7,$ and 0.05 m, see Andreae et al., 2002, for a detailed description). Additionally, a few measurements of isoprene concentrations made simultaneously at 1, 25, 45 and 52 m height at RBJ-A during the end of the dry season in 1999 are used for evaluation of isoprene exchange. The sampling procedure, chemical analysis and observed concentrations of isoprene and other volatile organic compounds are described and discussed in detail in Kesselmeier et al. (2002b). A detailed description of the ozone flux and profile measurements is given in Rummel (2004). The time resolution, profile heights and averaging procedure of ozone measurements for wet and dry season conditions are identical to those for CO₂ and H₂O.

4.2.2 Meteorological overview

The mean diurnal cycles of micrometeorological input parameters observed at the tower RBJ-A during the late wet (EUST-I) and late dry (EUST-II) season are shown in Fig. 4.1. A seasonal comparison of additional climatic variables is listed in Table 4.1. Global radiation reaches maximum values of 400-900 W m⁻² around noon time with distinct larger values during the late dry season. The CO₂ concentration shows strong diurnal variations with maximum and minimum values of 460 and 365 ppm during night- (4-6 h) and daytime (15-16 h), respectively. The wet season daytime minimum values are slightly smaller (361 ppm) compared to the dry season (367 ppm). Furthermore, the wet season mean relative humidity is larger and incoming radiation and temperature are lower compared to the dry season. Mean daytime maximum temperature and diurnal amplitude is 3°C higher in the dry season coinciding with a decrease of minimum relative

humidity from 72% to 60%, whereas the mean specific humidity above the canopy is twice as high. The soil temperature is only slightly higher during the dry season whereas the mean soil water content has decreased approximately from 25 to 15%. The wet-to-dry seasonal changes of humidity, temperature, and radiation are accompanied by the occurrence of large-scale biomass burning leading to a strong increase of aerosol particle and ozone concentrations, (see Table 4.1). In contrast, the mean diurnal cycles of horizontal wind speed (Fig. 4.1c,d) and other quantities related to turbulent mixing, are very similar.

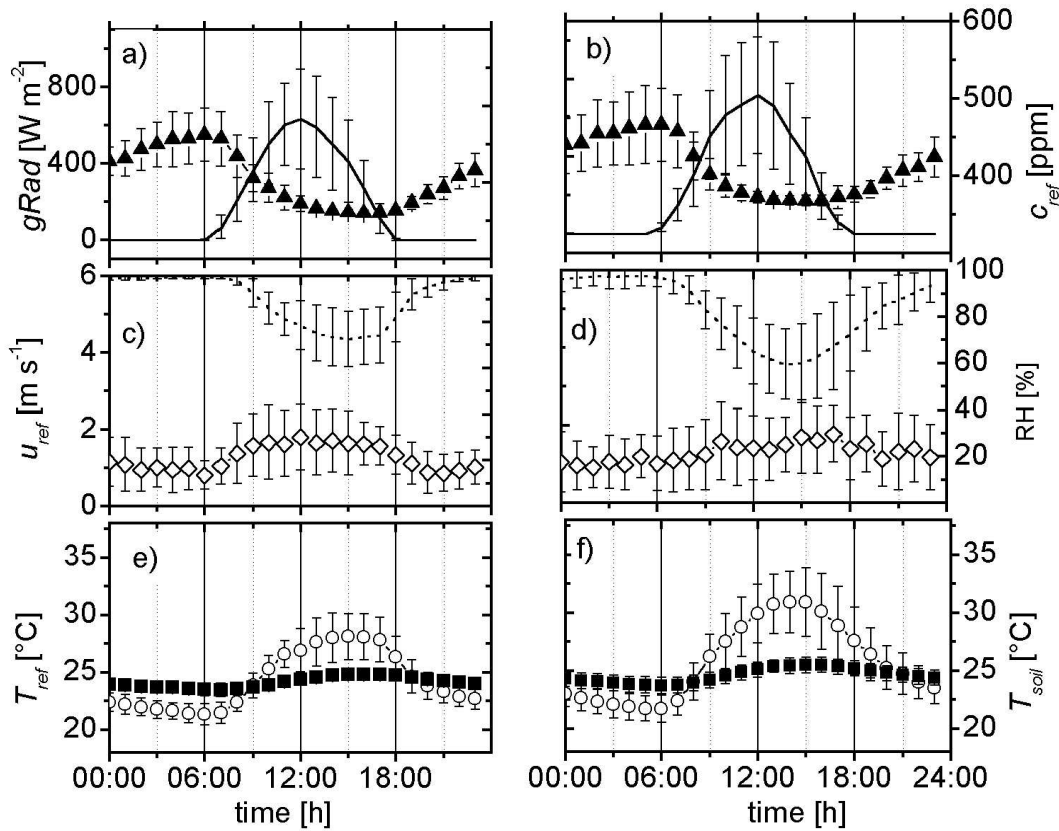


Figure 4.1: Mean values and standard deviations of micrometeorological quantities during the late wet (Apr-May, EUST-I) and late dry (Sep-Oct, EUST-II) season at the Jaru site in Rondônia in 1999. a,b) Incoming global radiation ($gRad$, solid line) and CO_2 concentration (c_{ref} , filled triangles). c,d) Mean horizontal wind speed (u_{ref} , open diamonds) and relative humidity (RH , dotted line). e,f) Air (T_{ref} , open circles) and soil temperature (T_{soil} , closed quarters). All quantities except T_{soil} (-0.05 cm) were measured at the reference height (53 m) above the canopy.

Table 4.1: Seasonal comparison of climatic variables observed at the Jaru site in Rondônia.

Parameter		EUST-I	EUST-II
Precipitation ^{*,a,c}	[mm]	950	550
Radiation ^c	[MJ m ⁻² d ⁻¹]	16.7	19.9
Mean temperature ^c	[°C]	24.3	25.7
Mean humidity ^c	[g kg ⁻¹]	2.5	5.2
Mean soil water content ^d	[-]	0.25	0.15
Ozone concentration ^{†,a-c}	[ppb]	10	40
Isoprene concentration ^{†,b}	[ppb]	4	12
Aerosols particle concentration ^a	[cm ⁻³]	450 ± 320	6200 ± 4800

^a Andreae et al. (2002), ^b Kesselmeier et al. (2002b), ^c Rummel (2004), ^d Gut et al. (2002b)

* total sum from Dec'98 to May'99 and Jun-Nov'99

† typical midday values above the canopy

4.2.3 Model setup

A detailed description and discussion of the model parameterization is given in Chapter 2. The transport model applies the derived profile parameterization for the standard deviation of vertical wind speed and the Lagrangian timescale as described in Chapter 3. A mean canopy structure with an upper and lower leaf area density maximum, a total leaf area index of LAI=6 and a mean canopy height $h_c = 40$ m is applied. A number of 9 layers is chosen with 8 equidistant layers of 5 m depth within the canopy, and a top layer of 13 m depth above (hereafter referred to as the surface layer, $z_{ref} = 53$ m). The leaf optical parameters are adjusted to the optimal values derived for Amazon rain forest. Soil respiration is calculated applying the observed reference value of $3.3 \mu\text{mol m}^{-2} \text{s}^{-1}$ at 25° and an activation energy of 60 kJ mol^{-1} . The light acclimation parameter for leaf photosynthesis is set to $k_N = 0.2$ with a maximum carboxylation rate of $50.0 \mu\text{mol m}^{-2} \text{s}^{-1}$ at the canopy top. The temperature dependence of leaf photosynthesis is calculated using the modified values for the activation of the electron transport rate and entropy ($H_{vJ} = 108$ and $S_J = 0.66 \text{ kJ mol}^{-1}$, respectively).

To assess the model prediction uncertainty, key parameters are modified within a reasonable range, which is inferred from the results of Chapter 2 (Table 4.2). These parameters include the leaf transmittance (σ_l) and reflectance (ρ_c) for visible and near-infrared radiation and the vertical leaf area distribution and total LAI. Additionally, a seasonal modification of leaf physiology is considered by applying a model parameterization with higher stomatal conductances for EUST-I meteorology (wet season conditions) and a lower assimilation rate for EUST-II meteorology (dry season conditions): (1) For wet season conditions, the parameter correlating stomatal conductance with assimilation (a_A) is increased from 10 to 15 (see also Lloyd et al., 1995a). (2) For dry season conditions, the quantum

Table 4.2: Values of key parameters (described in Chapter 2) applied in the sensitivity study (Section 4.3.2). For the model evaluation and application (Section 4.3.3-4.4.2, only bold font values are applied.

No.	Model (Parameter)	Ref.	Max	Min
1	Stomatal conductance (a_A)*	10	15	5
2	Photosynthesis (α) [†]	0.15	0.20	0.13
3	Photosynthesis (θ) [‡]	0.9	0.95	0.85
4	Canopy structure (LAI) [§]	6.0	6.5	5.5
5	Albedo (parameter scaling) [¶]	0.66	0.60	0.75
6	Photosynthetic capacity ($v_{cmax0hc}$ in $\mu\text{mol m}^{-2} \text{s}^{-1}$)	50	70	40
7	Photosynthetic light acclimation (k_N)	0.2	0.0	1.0

* empirical coefficient relating stomatal conductance (g_s) to net assimilation (A_n)

† quantum yield of whole chain electron transport

‡ shape parameter of the hyperbolic light response function

§ Total leaf area index (LAI) and modifications for open and dense canopy types

¶ Scaling of leaf transmittance and reflectance for short-wave radiation (see Table 2.5)

yield of whole chain electron transport (α , the initial slope of light response) is reduced from 0.15 to 0.13 and the shape parameter of the hyperbolic light response function (θ) is reduced from the recommended value of 0.9 to 0.85. It is tested whether these modifications can explain observed seasonal variations of the canopy net fluxes shown and discussed in Andreae et al. (2002). Hereafter, the parameterization without seasonal modifications (Column Ref. in Table 4.2) is referred to as the reference parameterization.

4.2.4 Calculation of storage terms

The observed Eddy covariances (EC) of temperature, H₂O, CO₂, and ozone described in Section 4.2.1 represent the vertical net fluxes above the canopy whereas the model predictions represent the sum of “instantaneous” fluxes from the canopy layers. The difference between both terms is given by the so-called storage flux inside the canopy volume, which can be inferred from the temporal evolution of the scalar profiles or empirically, from the change of concentration with time above the canopy. Since the storage flux may become important in forest canopies, EC measurements are corrected to obtain the instantaneous fluxes. The canopy storage fluxes for CO₂ and ozone are calculated from the temporal evolution of the diurnally averaged vertical profiles as described for CO₂ by Grace et al. (1995). The heat storage terms for sensible (biomass + air space) and latent energy are calculated according to Moore and Fisch (1986) from the mean diurnal course of temperature and humidity measured above the canopy. The validity of the latter relationship for the RBJ-A tower has been shown by a comparison with the storage flux obtained from temperature profile measurements by Rummel (2004).

4.2.5 Calculation of isoprene emission and ozone deposition

Leaf isoprene emission is calculated according to Guenther et al. (1993). A detailed discussion and description of the algorithm is given in Appendix A.9 and Chapter 5. A canopy standard emission factor of 24 $\mu\text{g C g}^{-1} \text{h}^{-1}$ and a specific leaf dry weight of 125 g m^{-2} is applied as estimated for tropical rainforest by Guenther et al. (1995). This bulk approach is essentially the same, as a bottom-up approach using a fraction of 30% isoprene emitting species with standard emission factor of 80 $\mu\text{g C g}^{-1} \text{h}^{-1}$ (see also Harley et al. 2004). The leaf uptake of ozone is calculated by applying the concept of dry deposition velocity

$$v_{d,x} = \frac{F_x}{c_x(z_{ref})} \quad (4.1)$$

whereby the deposition velocity ($v_{d,x}$) represents the kinematic flux (F_x) of a tracer x normalized by the tracer concentration at height z_{ref} above the canopy. Eq. 4.1 is applicable for all trace gases which are deposited to the surface (e.g. SO₂, NO₂, and O₃, see Baldocchi et al. 1987; Ganzeveld and Lelieveld 1995). The total deposition velocity is given by the parallel uptake in all canopy layers according to

$$v_{d,x} = v_{d,soil} + \sum_{i=0}^m v_{d,i} \quad (4.2)$$

where the deposition to the leaf surface in layer i ($v_{d,i}$) and the soil ($v_{d,soil}$) are given by

$$v_{d,i} = \frac{1}{r_a(z_i) + r_{leaf,O_3}} \quad (4.3)$$

$$v_{d,soil} = \frac{1}{r_a(soil) + r_{soil,O_3}}. \quad (4.4)$$

The aerodynamic resistance to turbulent transport from z_{ref} to z_i is equivalent to the integrated dispersion coefficient between these heights (see Chapter 3). According to Baldocchi et al. (1987), the total leaf resistance to ozone uptake (r_{leaf,O_3}) for hypo-stomatous leaves can be divided into a stomatal and cuticular pathway according to

$$\frac{1}{r_{leaf,O_3}} = \frac{1}{r_{b,O_3} + r_{s,O_3} + r_{m,O_3}} + \frac{2}{r_{b,O_3} + r_{cut,O_3}}. \quad (4.5)$$

The leaf boundary-layer (r_b) and stomatal (r_s) resistance are derived from the conductances for water vapor using the ratio's of molecular diffusivities (Massman, 1998). The mesophyll resistance and consequently the inter cellular ozone concentration is assumed to be zero (Chameides, 1989; Weseley, 1989; Neubert

et al., 1993; Gut et al., 2002a). Although the cuticular resistance (r_{cut,O_3}) is relatively large (Gut et al., 2002a), the significance of this pathway to total deposition has been shown by Rummel (2004) estimating a value of 4000-5000 s m⁻¹. The resistance to soil deposition was determined by Gut et al. (2002a) for the RBJ-A site giving a mean value of 188 s m⁻¹. Adding the turbulent resistance (turbulent transport from the mean height of the lowest canopy layer at 2.5 m to the soil surface) and the soil surface boundary layer resistance (which have been determined as a bulk soil surface resistance in Chapter 2) results in a total soil resistance of $r_{soil,O_3} \approx 700$ s m⁻¹.

4.3 Results and discussion

4.3.1 Stable solutions for steady-state environmental conditions

The assumption of steady-state environmental conditions (Chapter 1) implies that the exchange processes at the leaf surface and the vertical exchange with the lower atmosphere are in balance. This assumption is fulfilled under normal day- and nighttime conditions, where meteorological quantities change slowly. However, for short periods these conditions can change rapidly due to rainfall or large scale turbulence structures. By defining appropriate rejection criteria (no rain) and applying time-averaged micrometeorological quantities as input parameters, it is ensured, that the applied boundary-conditions represent 'typical' situations (Section 4.2).

The morning and evening hours around sunrise and sunset represent situations, where environmental conditions are not in steady-state. This is illustrated in Fig. 4.2a showing the diurnal course of the simulated gradients between the mean foliage temperature, the ambient air within and the surface layer above the canopy for EUST-I. The mean foliage and ambient air temperatures are calculated as the surface (leaf) area and layer volume weighted average of the vertical profiles of leaf (T_s) and air (T_a) temperature, respectively. T_s is calculated as the sunlit and shaded leaf fraction weighted surface temperature. During daytime, the surfaces are heated by the absorbed short wave radiation whereas the ambient air receives turbulent heat fluxes which are vertically dispersed in the canopy air volume. The model predicts 1-2° and 0-1°C gradients between the surface and ambient air, and ambient air and the surface layer above the canopy, respectively. During nighttime, the radiation budget of the canopy is negative resulting in opposite signs of both gradients. As shown in Fig. 4.2b, there are 2-10 iterations required before the solutions for $T_a(z_i)$, $T_{s,sun}(z_i)$, and $T_{s,shade}(z_i)$ converge. For nighttime conditions, the number of iterations is nearly constant (4), whereas for daytime conditions, the required number is negatively correlated with the temperature gradients. During sunrise and sunset, the temperature gradients change

their sign due to the heating and cooling of the leaf surfaces and canopy air space. This causes numerical instabilities, when the boundary conditions (soil and reference air temperature) are kept constant. This relationship between the numerical stability of the model predictions and the stationary of environmental conditions highlights interesting interactions between the vegetation layer, soil surface and the lower atmosphere.

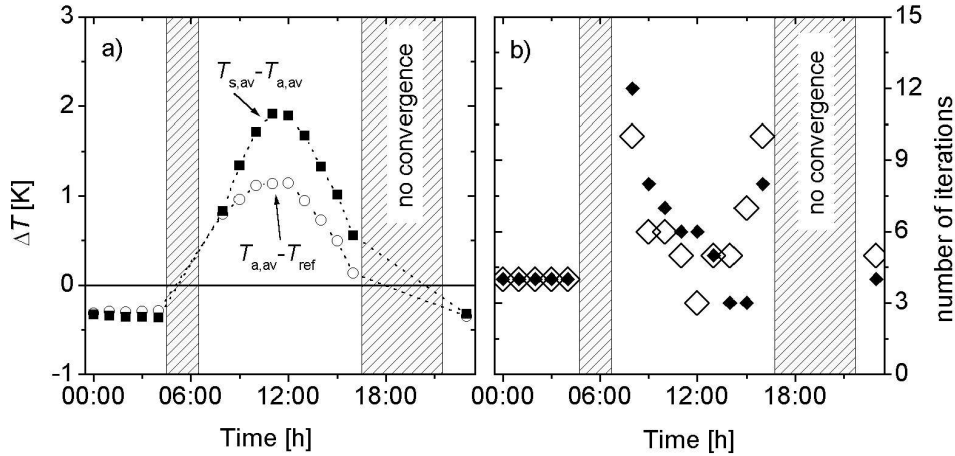


Figure 4.2: a) Diurnal course of the predicted gradients for EUST-I (Fig. 4.1 a,c,f) and the reference parameterization (Column Ref. in Table 4.2) between the mean foliage and ambient air temperature ($T_{s,av} - T_{a,av}$, solid quarters) and between the ambient and surface layer air temperature ($T_{a,av} - T_{ref}$, circles). b) Number of iterations required to achieve convergence of the temperature profile (T_a) for EUST-I (closed diamonds) and EUST-II (open diamonds) using the reference parameterization. Simulations for unsteady environmental conditions during sunrise (5-7 h) and sunset (17-22 h) failed to converged as indicated by the striped areas (see text).

Stable solutions for $T_s(z_i)$ (sunlit, shaded and mean surface) and $T_a(z_i)$ for day- (10, 12, and 15 h) and nighttime (2 h) conditions have been found (Fig. 4.3). For daytime conditions, the model predicts large temperature gradients across the leaf boundary layer ($T_s - T_a$) and sunlit and shaded leaf surfaces, respectively. This has an important impact on the calculation of the physiological exchange processes, which imply usually a non-linear temperature response (Chapter 2). Assuming a typical Q_{10} -value of 2 for a temperature difference of 5°C causes the physiological response to change by 50%.

As observed in nature, the surface temperatures reach their maxima in the upper canopy, where the highest irradiance is absorbed. The mean surface temperature is generally reflected by the profile of sunlit leaf temperature down to $\approx 75\%$ of the canopy height where it starts reflecting more the shaded leaf tem-

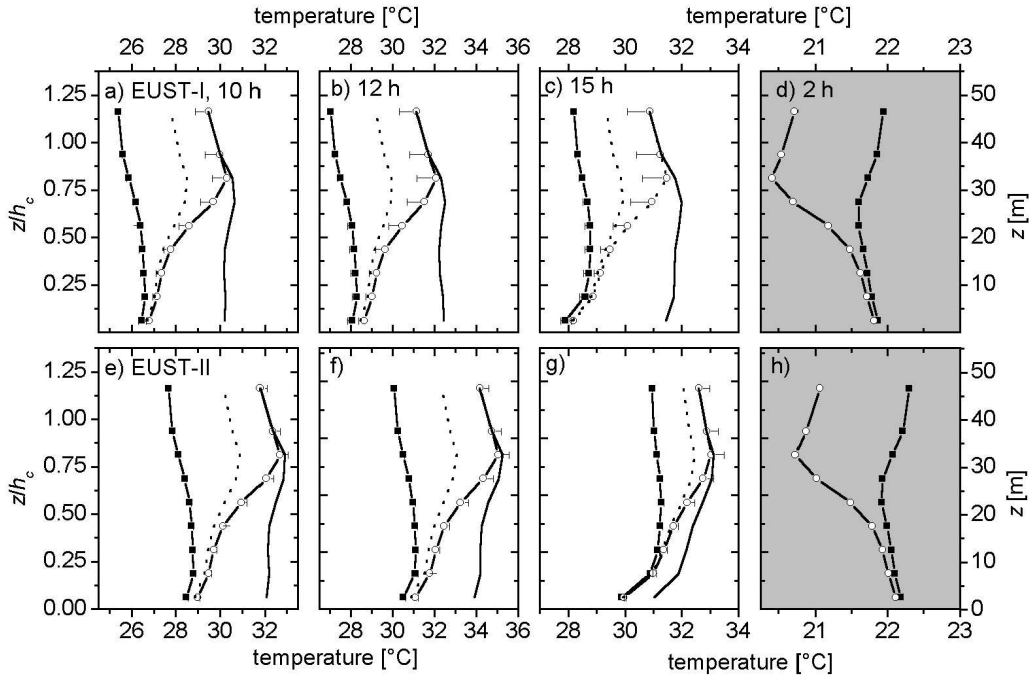


Figure 4.3: Predicted vertical profiles of air temperature (line with closed symbols), mean (line with open symbols), sunlit (solid line), and shaded (dotted line) leaf surface temperature for EUST-I (a-d) and EUST-II (e-h) at 10 (a,e), 12 (b,f), 15 (c,g), and 2 h (d-h). Error bars represent predictions using higher stomatal (EUST-I) and lower photosynthesis (EUST-II, see Section 4.2.3) parameters, respectively.

perature, which is typically 2-4°C lower. Simultaneously, the gradients across the leaf boundary layer ($T_s - T_a$) become smaller close to the ground. A higher stomatal conductance and a lower photosynthesis parameter (Table 4.2) causes a decrease of 0.3-1.2°C for EUST-I and an increase of 0.1-0.5°C for EUST-II, respectively. The sensitivity of model predictions to the leaf physiological parameters is discussed in more detail in Section 4.3.2.

The vertical gradients of ambient air temperature reflect the thermal stratification of the canopy air space, which influences the stability and turbulence regime. The predicted diurnal pattern is very similar to what can be expected for dense vegetations (see Chapter 2). In the early morning, the soil is warmer than the canopy, which is starting to heat up due to radiation absorption resulting in an upward temperature gradient (dT/dz) and instable stratification of the whole canopy. Since the maximum radiation absorption occurs in the upper canopy, the temperature gradients of the lower canopy change the sign and become stable up to 10 m height ($0.25 h_c$) at 15 h. During the night, the stratification of the atmospheric boundary-layer is usually very stable because the surface layer is cooler

than the air above (Stull, 1988). However within dense canopies, the stratification can be reversed, i.e. unstable because the maximum cooling effect occurs in the upper canopy with the highest biomass density. In combination with the heat stored within the soil body during the day, a weak but efficient convective energy flux is generated in the lower canopy (see Chapter 3). Consistently, the model predicts a weakly unstable stratification with a higher soil temperature (Fig. 4.1e,f), a minimum temperature at 20-30 m, and a warmer stable nocturnal boundary-layer above the canopy.

4.3.2 Model sensitivity to key parameter uncertainty

In the following Section, the sensitivity of model predictions to key parameter values is analyzed (Section 4.2.3). For this purpose, model predictions for EUST-I and EUST-II obtained with modified parameterizations (Table 4.2) are compared.

As described in Chapter 2, the recommended values for leaf reflectance (σ_l) and transmittance (ρ_c) predict a much higher canopy albedo as observed. Measurements are best matched, when σ_l and ρ_c are scaled down to 60-75% of the recommended values. As shown in Fig. 4.4a-b, the model predictions are not very sensitive to the uncertainty of these parameters. Although the mean canopy albedo varies between 14 and 18% for the applied range for σ_l and ρ_c (Fig. 4.4a), the resulting difference for the predicted available energy as the sum of the sensible and latent heat fluxes ($H + LE$) is less than 5% (Fig. 4.4b). Similarly, a low sensitivity of the available energy to canopy structure is inferred. For the applied dense and open canopy types, $H + LE$ differ to less than 2% (Fig. 4.5c). For net assimilation, a 5% reduction and a 2% increase for the open and dense canopy type, respectively, are predicted (Fig. 4.5d). This is also consistent with the relationship between total LAI and absorbed short wave radiation (Q_{abs}) described in Chapter 2, which predicts a saturation of Q_{abs} for $LAI \geq 5$. Surprisingly, the sensitivity of canopy net assimilation to the photosynthetic capacity at the canopy top is also relatively low (Fig. 4.5e,f). Increasing $v_{cmax0hc}$ by 40% increases the net assimilation (A_n) only by 5%. For LE , these differences are even smaller. The second important parameter related to canopy biochemistry is k_N representing the extinction coefficient of photosynthetic capacity. In Chapter 2, a value of 0.2 was inferred for Amazon rain forest (a zero value means no acclimation with $v_{cmax0}(z = 0 \text{ m}) = v_{cmax0hc}$). Fig. 4.4g,h show, that net assimilation and transpiration are not reduced for such a low degree of acclimation whereas a significant stronger acclimation leads to a reduction of A_n (40%) and LE (20%). Since the parameterization of leaf respiration (R_d) is coupled to v_{cmax0} , lower canopy R_d increases as the gross assimilation rate increases if no acclimation is assumed ($k_N = 0$). In sum, the resulting net assimilation is nearly identical, when the higher v_{cmax0} values are assumed for the lower canopy indicating an optimal vertical distribution of photosynthetic capacity.

Compared to the parameters described above, the predicted energy fluxes are

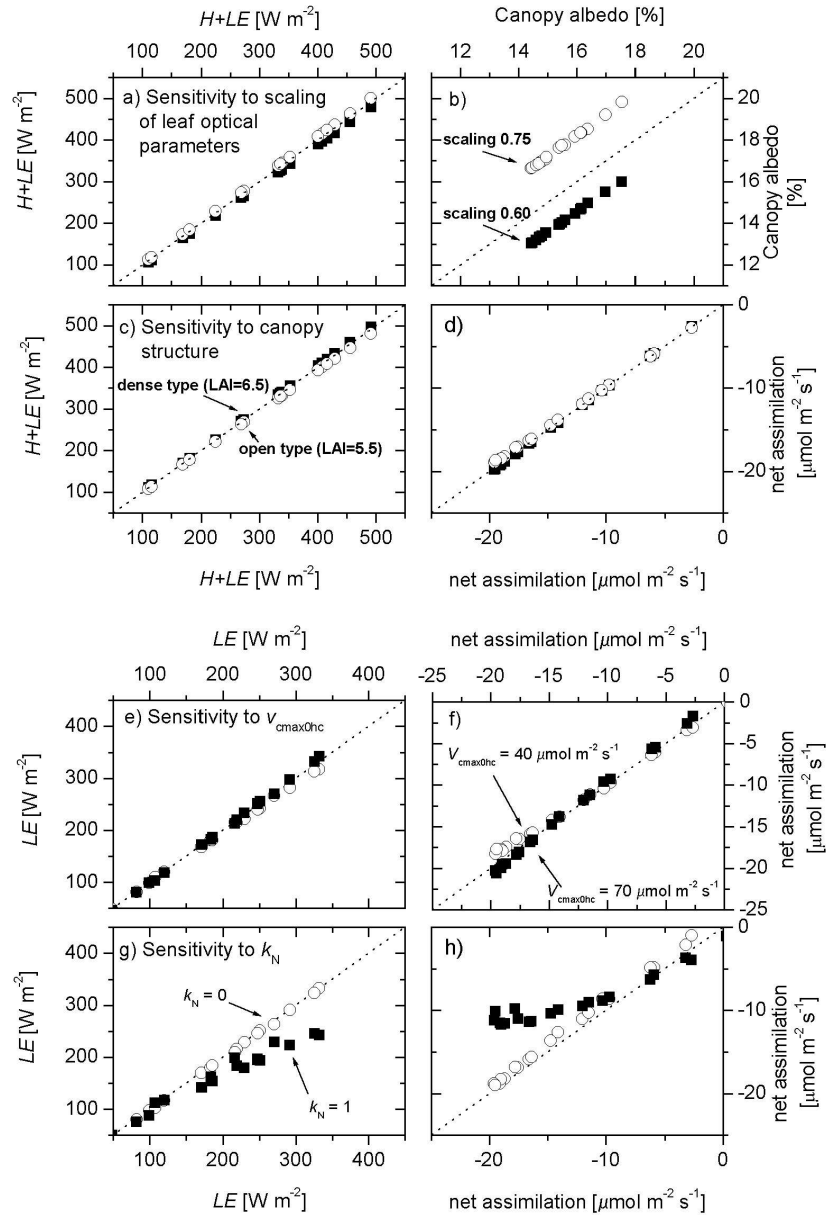


Figure 4.4: Sensitivity of predicted available energy ($H + LE$, a,c), canopy albedo (b), latent heat (LE ; e,g) and net assimilation (d,f,h) to the scaling of leaf optical parameters (a,b), the canopy structure type (c,d), the maximum rate of photosynthetic carboxylation above the canopy ($v_{cmax0hc}$; e,f) and the light acclimation parameter (k_N ; g,h) as listed in Table 4.2. Predicted results for maximum and minimum modifications are related to predictions for the reference parameterization.

much more sensitive to the parameters of leaf photosynthesis and stomatal conductance (see also the comparison of leaf scale measurements in Chapter 2). In general, the observed relationships between predicted net fluxes and the photosynthesis and stomatal parameter values are not solely linear. The energy fluxes (H and LE) and Bowen ratio (H/LE) are more sensitive to the stomatal parameter (a_A) whereas net assimilation (A_n) is more sensitive to the photosynthesis parameters (α, θ). Reducing a_A from 10 to 5 results in a 35% reduction of LE and a 33% increase of H whereas A_n is reduced at least by 15%. Increasing a_A from 10 to 15 results in a 21% increase of LE , a 18% decrease of H and only a 5% increase of A_n . Compared to H and LE , the sensitivity to the photosynthesis parameters is highest for the predicted net assimilation ranging between -15% +24% for parameter reduction ($\alpha = 0.3, \theta = 0.85$) and increase ($\alpha = 0.2, \theta = 0.95$), respectively. The variability of H and LE is < 15%. The results reflect the high sensitivity of model predictions to the choice of physiological parameters and accentuate the need for leaf level evaluation as shown in Chapter 2.

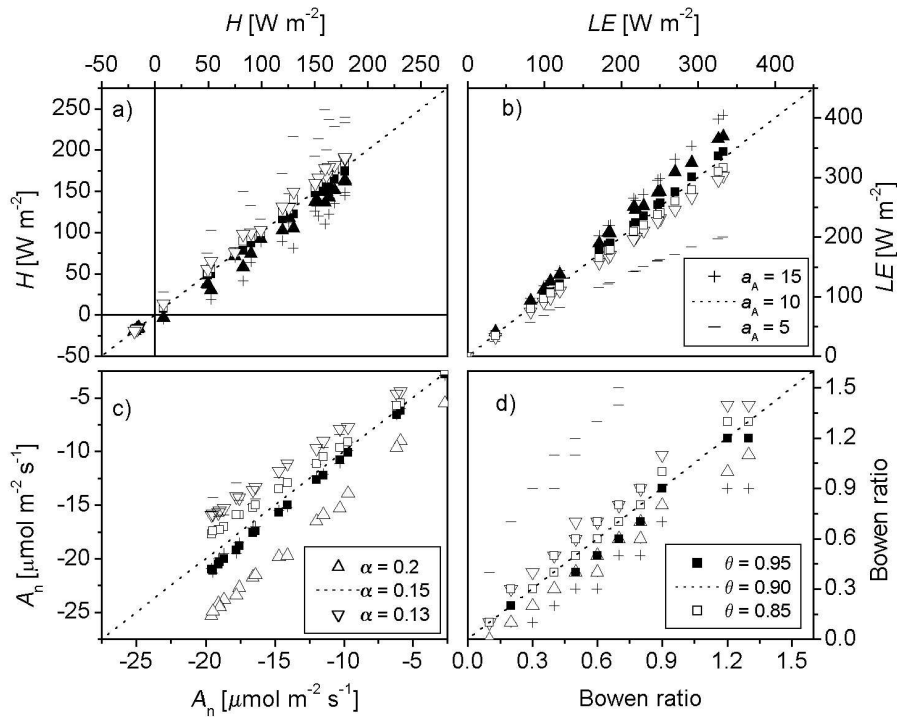


Figure 4.5: Model sensitivity to stomatal and photosynthesis parameters. Predicted net sensible heat flux (H , a), latent heat flux (LE , b), net assimilation (A_n , c), and Bowen ratio (H/LE , d) for EUST-I and EUST-II (Fig. 4.1) using modified values for the stomatal and photosynthesis parameter a_A , α and θ (Table 4.2) in relation to the predictions obtained with the reference parameterization.

4.3.3 Evaluating seasonal predictions of CO₂ and energy exchange

In the following section, predicted net fluxes and concentration profiles obtained for EUST-I (late wet) and EUST-II (late dry season) meteorology are compared to measurements at the two Jaru towers RBJ-A and RBJ-B. A comparison between the mean observed and predicted diurnal cycles of net assimilation (A_n), and latent (LE) and sensible (H) heat is shown in Fig. 4.6 and 4.7. The predicted midday vertical source/sink distributions, flux profiles and the relative contribution of sunlit leaves to the exchange of single canopy layers is shown in Fig. 4.8. The measured fluxes above the canopy (Eddy covariance measurements, EC) have been corrected for the canopy storage (Section 4.2.4).

In the early morning and late afternoon, the canopy storage (ΔS) can become very important, especially for CO₂, even exceeding the measured net flux above the canopy. For H and LE , ΔS contributes up to 60 and 40 W m⁻² to canopy flux, respectively. There is generally a good agreement between the RBJ-A and RBJ-B tower EC measurements and storage fluxes. The sensible heat and CO₂ fluxes measured at RBJ-A in the afternoon and morning hours, respectively, are slightly higher compared to RBJ-B, whereas the LE fluxes in the morning are somewhat lower (< 4%). These variability can result from the different source areas of both towers and may reflect the uncertainty of the measurements (for a discussion of the source area and fetch conditions at RBJ-A see Rummel, 2004). A similar good agreement is obtained between model predictions and observations, when a physiological variability for wet and dry season conditions is considered. The meteorological differences between EUST-I and EUST-II described above (Fig. 4.1) are accompanied by higher energy fluxes and bowen ratios (i.e. a larger fraction of sensible heat) and lower assimilation rates (in relation to the incoming radiation). Using the reference parameterization (see Section 4.2.3), the model predicts $\approx 20\%$ higher sensible heat fluxes for EUST-I compared to the observations obtained from EC method. This leads also to a higher Bowen ratio (Fig. 4.6i-j). When an increased stomatal conductance ($a_A = 15$) is assumed for EUST-I, observations and model predictions agree quite well. For midday conditions, this goes along with a shift of nearly 50 W m⁻², which is emitted as latent instead of sensible heat (Fig. 4.8). For the prediction of net assimilation (A_n) this modification is less important as A_n is much less sensitive to a_A than H and LE (see Section 4.5). In contrast, for late dry season conditions (EUST-II), the predicted latent heat flux and canopy net assimilation are 10-20% higher applying the reference parameterization. When the photosynthesis parameters (α, θ) are reduced, the agreement between model predictions and observations improves significantly. Peak net photosynthesis at noon time is reduced from 19.5 to 15.8 $\mu\text{mol m}^{-2} \text{s}^{-1}$ (Fig. 4.8f). The large contribution (> 60%) of sunlit leaves to net assimilation of the lower canopy highlights the non-linearity of photosynthetic light response and the significance of a two-leaf radiation absorption approach

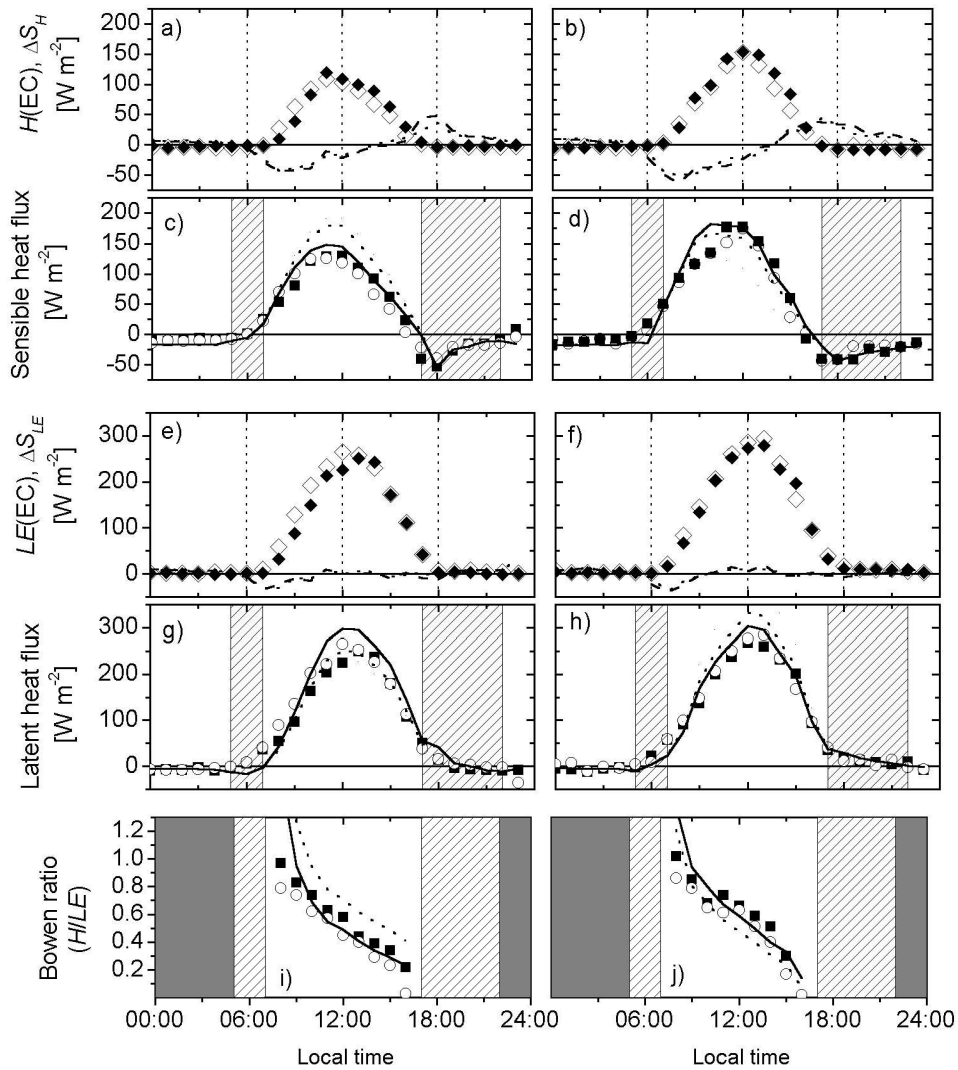


Figure 4.6: Comparison of observed and predicted fluxes of sensible heat (H), latent heat (LE) and Bowen Ratios (H/LE) for EUST-I (left panels) and EUST-II (right panels). The observed above canopy Eddy covariance flux measurements (EC in a-b, e-f) for RBJ-A (closed symbols) and RBJ-B (open symbols) are corrected for canopy storage (ΔS as dashed lines for RBJ-A and as dotted lines for RBJ-B) to obtain the “instantaneous” fluxes in c-d, g-h, and i-j (see Section 4.2.4), showing also the model predictions obtained for the reference parameterization (dotted line) and changed physiology (solid lines) with increased stomatal conductances (EUST-I) or decreased photosynthesis (EUST-II, see bold font values in Table 4.2). For unsteady sunrise and sunset periods (striped area), the numerical calculation of canopy air temperature is stopped after one iteration (see Fig. 4.2).

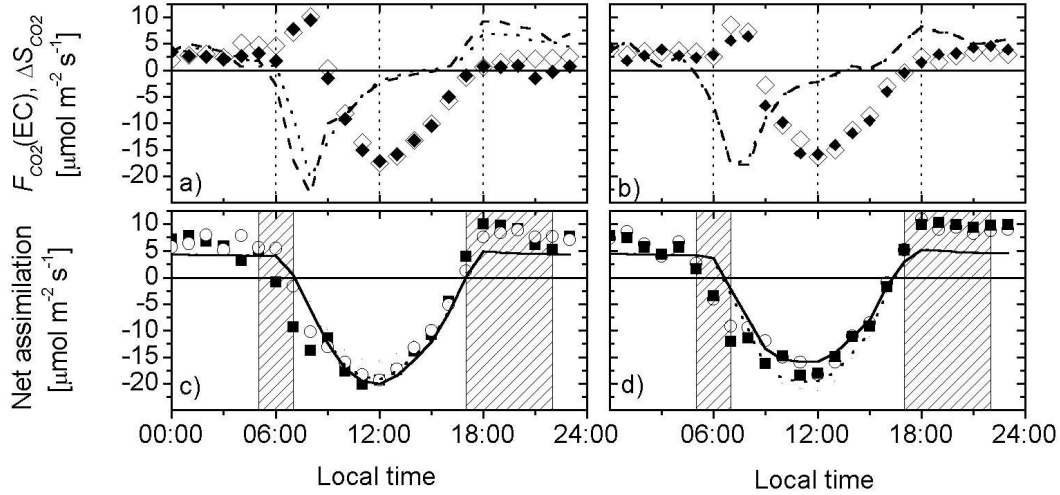


Figure 4.7: Comparison of observed and predicted CO_2 fluxes for EUST-I (left panels) and EUST-II (right panels). The observed above canopy Eddy covariance flux measurements (EC in a-b) for RBJ-A (closed symbols) and RBJ-B (open symbols) are corrected for canopy storage (ΔS as dashed lines for RBJ-A and as dotted lines for RBJ-B) to obtain the “instantaneous” fluxes in c-d (see Section 4.2.4), showing also the model predictions obtained for the reference parameterization (dotted line) and changed physiology (solid lines) with increased stomatal conductances (EUST-I) or decreased photosynthesis (EUST-II, see bold font values in Table 4.2). For unsteady sunrise and sunset periods (striped area), the numerical calculation of canopy air temperature is stopped after one iteration (see Fig. 4.2).

accounting for the different attenuation of diffusive and direct beam radiation (Chapter 2). For sensible and latent heat this effect is less pronounced, although the contribution to the heat flux of the lower canopy layers is also much higher ($> 30\%$) compared to the area fraction of sunlit leaves ($< 5\%$). The maximum source/sink strength for sensible heat, latent heat and net assimilation is located in the upper canopy at 25-30 m with contributions of 34-35, 31-33, and 40-43% to the canopy net flux, respectively. The location of the maxima coincides with the maximum leaf area density several meters below the maxima of leaf surface temperature (Fig. 4.3, see also Chapter 2).

The nighttime energy fluxes are in general very small, especially for latent heat. In this case, the modifications of physiological parameters have no effect because stomatal conductance and leaf CO_2 exchange depend only on the applied value of minimum stomatal conductance ($g_{s0} = 0.01 \text{ mol m}^{-2} \text{ s}^{-1}$) and the dark respiration rate (see Chapter 2). The predicted nighttime sensible heat flux agrees well with the observed values of $10\text{-}30 \text{ W m}^{-2}$. In contrast, the nighttime CO_2

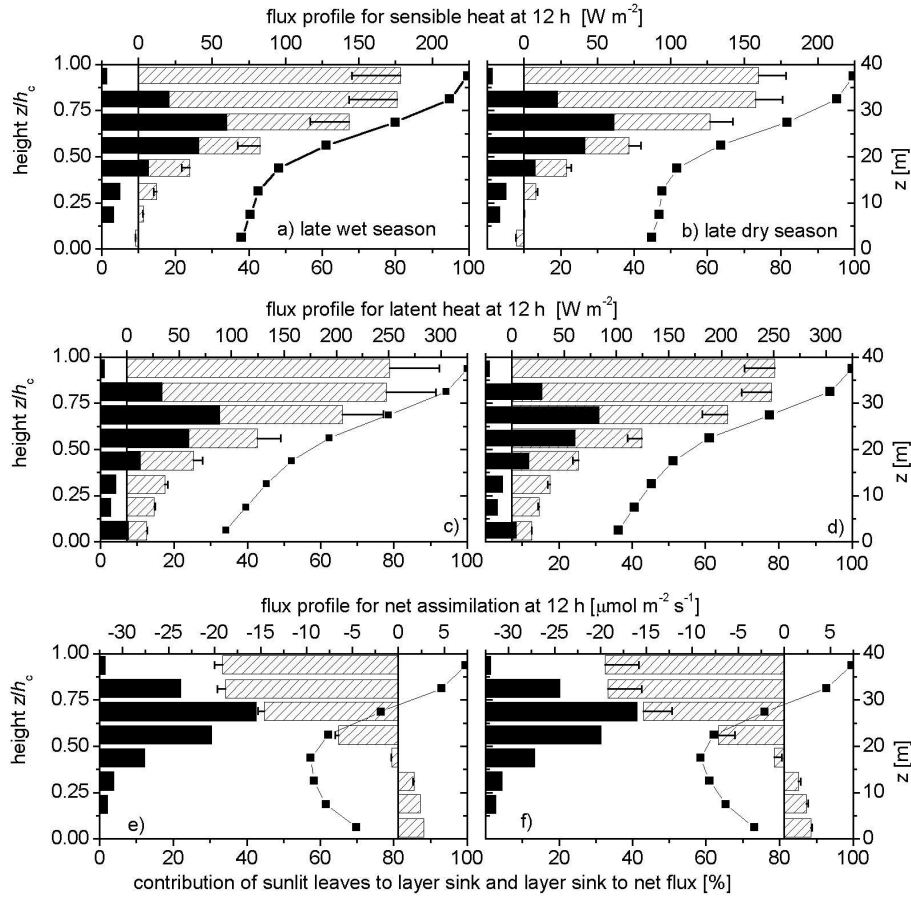


Figure 4.8: Midday (12 h) flux profiles for EUST-I (a,c,e) and EUST-II (b,d,f) meteorology (striped bars), relative source distribution (black bars) and contribution of sunlit leaves to layers source (solid line with closed quarters) for sensible heat (a,b), latent heat (c,d) and net assimilation (e,f) for the reference parameterization and a modified physiology (error bars) with increased stomatal conductances (EUST-I) or decreased photosynthesis (EUST-II, see bold font values in Table 4.2).

flux is underestimated. The predicted value of $\approx 4.5 \mu\text{mol m}^{-2} \text{s}^{-1}$ is significantly lower compared to the observations ($A_n \approx 6.5$, $F_{CO_2}(EC) \approx 3.2$, $\Delta S_{CO_2} \approx 3.3 \mu\text{mol m}^{-2} \text{s}^{-1}$). However, the large uncertainty of nighttime EC measurements have to be considered (a detailed discussion is given in Chapter 3). In addition, the parameterization for leaf respiration is derived for day light conditions, where the mitochondrial respiration is suppressed (Brooks and Farquhar, 1985; Lloyd et al., 1995b) and might be questionable for nighttime conditions.

For the comparison of observed and predicted in-canopy concentrations of CO₂ and H₂O, single profiles for day- (14-15 h) and nighttime (2-3 h) conditions

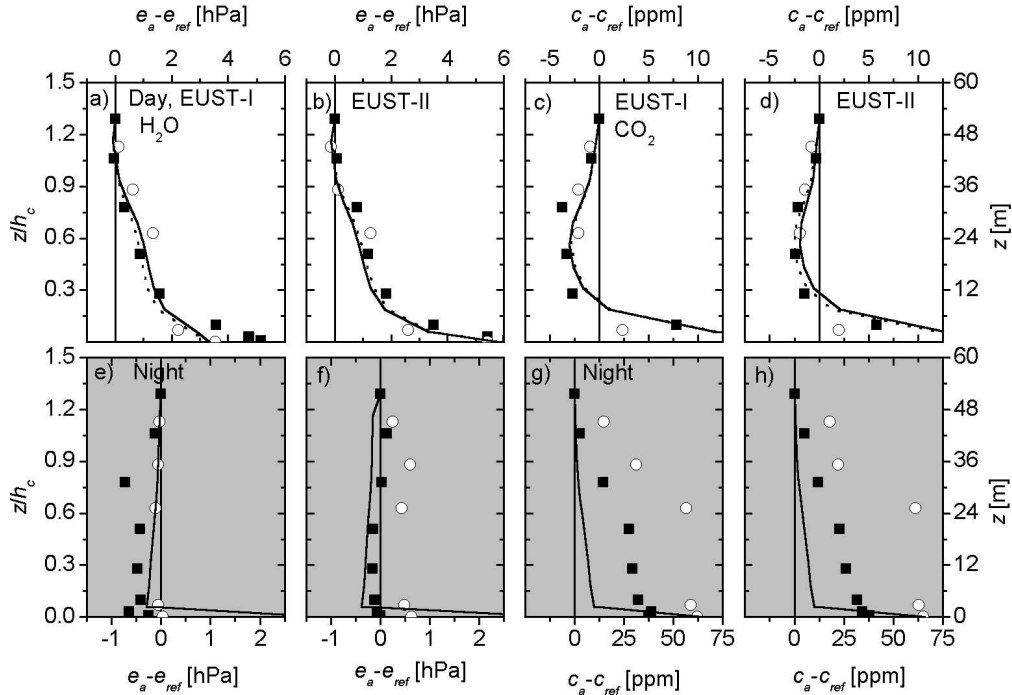


Figure 4.9: Comparison of mean observed (RBJ-A: closed quarters, RBJ-B open circles) and predicted (reference parameterization: dotted line, parameterization for wet and dry season: solid lines, see Section 4.2.3) day- (14 h, a-d) and night-time (2 h, e-h) H₂O (a,b,e,f) and CO₂ (c,d,g,h) concentration profiles for EUST-I (a,c,e,g) and EUST-II (b,d,f,h).

have been selected (Fig. 4.9a-h), where the storage flux is relatively small (see also Fig. 4.6e,f and Fig. 4.7a,b). In general, the variability of observed and predicted profiles is not very large during day and night and the selected profiles represent a typical pattern. The largest emission and uptake rates for H₂O and CO₂, respectively, usually coincide with the highest turbulence intensities around noon time (see also Chapter 3). Consequently, the development of vertical concentration gradients is counterbalanced by increased vertical mixing rates. Since the whole vegetation layer represents a strong H₂O source during the day, H₂O concentration increases with decreasing height and reaches maximum concentrations close to the soil surface where turbulent mixing is weak. As shown in Fig. 4.9a,b, the predicted profiles for EUST-I and EUST-II meteorology agree with the observations and can also explain the steeper H₂O gradients near the soil surface observed during EUST-II. A good agreement between observations and model predictions is also obtained for the daytime profiles of CO₂ concentration. The vegetational uptake and the soil emissions change the sign of the vertical gradient at ≈ 10 m above ground. This is predicted exactly by the model. Although the

soil CO₂ emissions are much lower than the uptake by the vegetation, the negative gradients (with respect to z_{ref}) above 10 m are small due to higher ventilation rates. For both, H₂O and CO₂, the predicted vertical profile is rather insensitive to modifications of the physiological parameters for stomatal conductance and photosynthesis, in contrast to the net fluxes (see Fig. 4.5).

For nighttime conditions, the model fails to predict the observed gradients of CO₂ in size and shape (Fig. 4.9g-h). The observed concentrations at RBJ-A and RBJ-B are 10-30 and 20-60 ppm higher, respectively, than model predictions. However, the differences between the observations at both towers are on the same order of magnitude as those between predictions and the observations at RBJ-A. Apparently, the nighttime profiles of CO₂ are influenced by additional processes, which are inferred with four different simulations: (1) Increased leaf respiration (200%): As mentioned above, the nighttime CO₂ flux is probably underestimated since leaf respiration in the dark is increased. (2) Increased soil respiration (150%): Additionally, the predicted soil respiration has a high uncertainty of at least 50 % (Chapter 2), which may significantly contribute to near-surface CO₂ concentrations. (3) Canopy storage ($3.3 \mu\text{mol m}^{-2} \text{s}^{-1} \text{h}^{-1}$): As shown in Fig. 4.7a-b, a significant fraction ($\approx 50\%$) of the emitted CO₂ does not immediately leave the canopy air volume and is stored till the early morning hours with the onset of turbulence (storage flux). (4) Depressed vertical mixing (60%): As mentioned in Section 4.2.1, the applied arithmetic mean value of the friction parameter of vertical turbulent transport (σ_{wref}) is up to 40% higher than the typical values for most nighttime cases (median).

The results of the different simulation tests are shown in Fig. 4.10a. Neither the increased leaf, nor soil respiration can explain the differences between observations and predictions. Whereas the effect of dark respiration is in general too small, the increased soil respiration has only a significant impact on the CO₂ concentration close to the ground. The storage flux and mixing effects in contrast may explain the disagreement between predictions and observations. Combining both effects, i.e. considering the mean observed storage integrated for the period from 21-2 h and a 20% reduction of the mixing parameter, the corrected predictions agree quite well with the observed profiles (Fig. 4.10b-c). To illustrate the steady accumulation of CO₂ during nighttime, the temporal change of the CO₂ concentration above the canopy $c_{ref}(t)$ is shown in Fig. 4.10d. Due to the decoupling from the lower atmosphere, $c_{ref}(t)$ increases from 393 ppm with a mean rate of 8.4 ppm h^{-1} from 23-4 h predicting a bulk storage flux of $\approx 5 \mu\text{mol m}^{-2} \text{s}^{-1}$. When the temporal evolution at all profile levels is considered, the applied value of $3.3 \mu\text{mol m}^{-2} \text{s}^{-1} \text{h}^{-1}$ is derived (see above). In summary, the simulated nighttime profiles of CO₂ are not in contradiction to the observations. Further experimental work is necessary to explain the observed differences between the profiles measured at both towers. Additional factors like instrumental calibration and/or horizontal flux divergence (“drainage flow”) have to be taken into consideration but are beyond the scope of the present study.

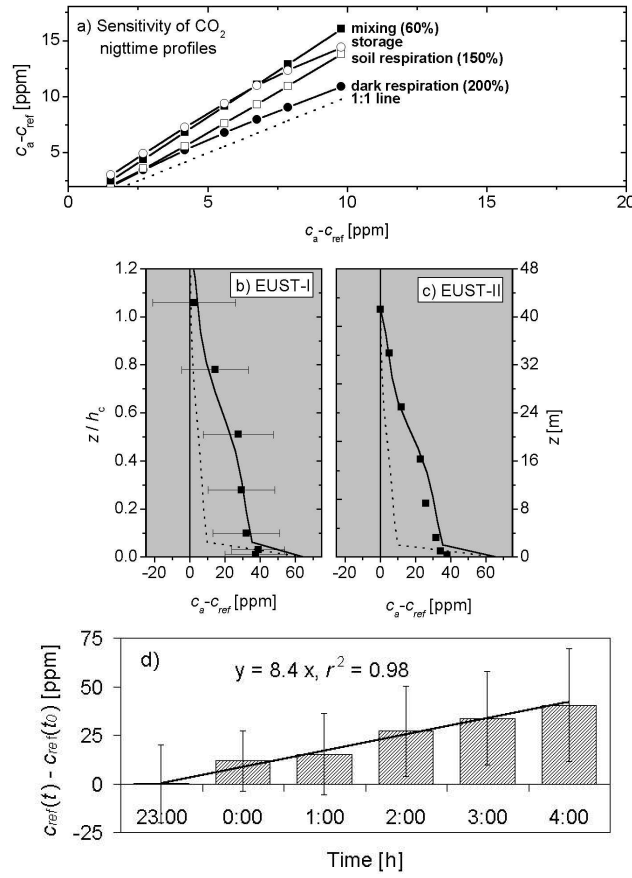


Figure 4.10: a) Sensitivity of predicted CO₂ nighttime profiles to parameter uncertainty. Model predictions for 100% increased dark respiration (closed circles), 50% increased soil respiration (open quarters), a storage flux of $5 \mu\text{mol m}^{-2} \text{s}^{-1}$ for a period of one hour (open circles, see also d) and a 60% reduction of friction induced turbulence (observed ratio of median to arithmetic average of σ_{wref} at 2 h, closed quarters) in relation to the original predictions for EUST-I (Fig. 4.9g). b-c) Comparison of observed (closed quarters, error bars shown in b) represent standard deviations) and predicted CO₂ nighttime profiles (2 h) for EUST-I (b) and EUST-II (c). The dotted lines represent predictions with no corrections (1:1 line in a), the solid lines represent the predicted profiles corrected for an integrated nighttime storage flux of $20 \mu\text{mol m}^{-2} \text{s}^{-1}$ for the period from 21-2h (Fig. 4.7a-b, $3.3 \mu\text{mol m}^{-2} \text{s}^{-1} \text{h}^{-1}$) and reduced turbulence of 80% (see a). d) Nighttime increase of CO₂ concentration above the canopy (z_{ref}) during EUST-I starting at $t_0 = 23$ h. Error bars represent standard deviations. The value of $8.4 \mu\text{mol mol}^{-1} \text{h}^{-1}$ is equivalent to a storage flux of $5 \mu\text{mol m}^{-2} \text{s}^{-1}$ ($dc/dt \times z_{ref} \times \rho_{air}^m \times 3600^{-1} \text{h s}^{-1}$). The value of $3.3 \mu\text{mol m}^{-2} \text{s}^{-1}$ applied in b+c is derived from the temporal evolution dC/dt at all profile heights (see Section 4.2.4).

4.3.4 Evaluating seasonal predictions of isoprene exchange

Isoprene emission was calculated for EUST-I and EUST-II meteorology applying the algorithm of Guenther et al. (1993) to the predicted sunlit and shaded leaf irradiances and temperatures. The emission model is parameterized with recommended values for tropical forests using a canopy standard emission factor of $24 \mu\text{g C g}^{-1} \text{h}^{-1}$ and a specific leaf dry weight of 125 g m^{-2} (see Section 4.2.5). A seasonal comparison of the predicted isoprene midday flux profile, source distribution and the diurnal course of net fluxes for EUST-I and EUST-II is shown in Fig. 4.11. Compared to the net assimilation and energy exchange (Fig. 4.7 and Fig. 4.6), the different meteorology observed during the two periods leads to a larger seasonal variability in the predicted isoprene fluxes. Using the same model parameterization for both periods results in a 40% increase in the midday canopy emissions for EUST-II. Physiological changes in the H₂O and CO₂ exchange (error bars in Fig. 4.11) result in a 60% increase of the flux variability. Obviously, a reduction of net assimilation for EUST-II (Fig. 4.7d) results in increasing isoprene fluxes as a consequence of reduced stomatal conductances, higher bowen ratios (Fig. 4.6j) and higher leaf temperatures. The shape of the vertical distribution of isoprene emission (Fig. 4.11a-b) shows very small seasonal variations. In general, $\approx 80\%$ of the total midday flux is emitted by the upper canopy ($z > 20 \text{ m}$), and $\approx 60\%$ is emitted in the layer between 20 and 30 m with the highest leaf area density. Similar to net assimilation, the non-linearity of the emission algorithm (Appendix A.9) predicts a large contribution ($> 60\%$) of the sunlit leaves to the layer source strength also near the ground where the sunlit leaf fraction is small ($< 4\%$). This is even more pronounced for the late dry season meteorological conditions (EUST-II), where the relative contribution of sunlit leaves to the layers source even increases close to the surface due to the high differences in irradiance i.e. ≈ 300 compared to $\approx 10 \mu\text{mol m}^{-2} \text{s}^{-1}$ for sunlit and shaded leaves, respectively.

Concentration measurements made simultaneously at different canopy levels within the forest during EUST-II have been used to evaluate the predicted isoprene exchange. Fig. 4.12 shows a comparison of observed and predicted profiles for morning (10 h), midday (12 h) and late afternoon (16 h) periods on 28. and 29. October 1999 at RBJ-A. Using the recommended parameter values for the emission algorithm (see above) and no additional sources or sinks within the canopy, the model predicts a clearly different profile shape compared to the observations. Whereas the observations show the maximum concentrations in the upper canopy close to the sources, the model predicts an accumulation of isoprene close to the ground as a consequence of low mixing rates and missing sinks. Similar to the results for CO₂ and H₂O, the predicted profiles are compared to the net fluxes not very sensitive to the parameterization of leaf physiology (see Fig. 4.9). Possible explanations for the disagreement between the observed and predicted concentration profiles have been assessed by several additional simulations:

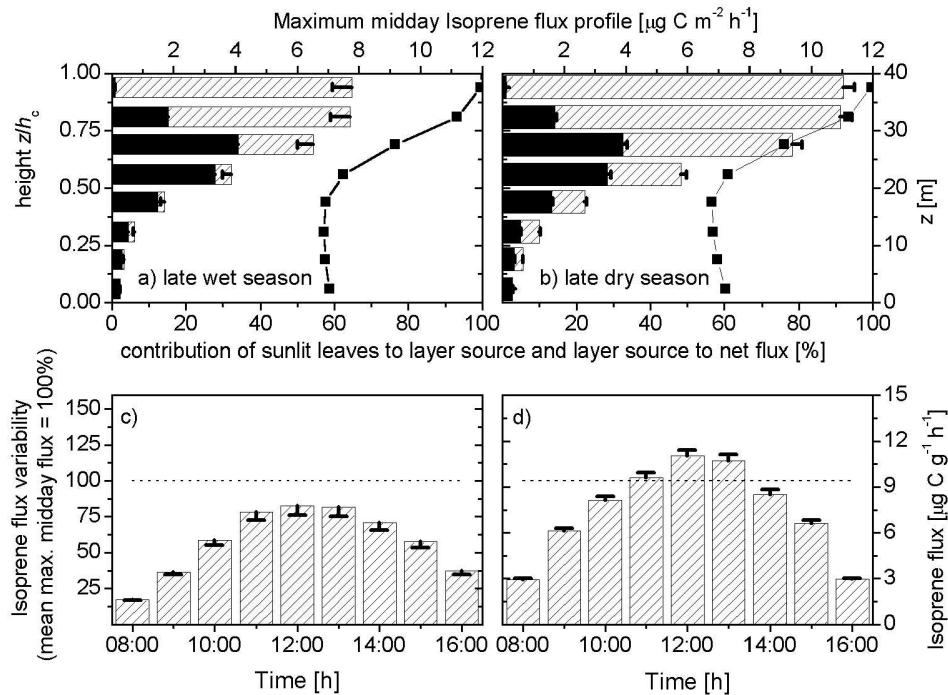


Figure 4.11: Predicted isoprene emissions applying the algorithm of Guenther et al. (1995) with a standard emission factor of $24 \mu\text{g C g}^{-1} \text{ h}^{-1}$ and a specific leaf weight of 125 g m^{-2} . Chemical reactions and deposition are not considered. Midday (12 h) isoprene flux profile (striped bars) for EUST-I (a) and EUST-II (b), relative source distribution (black bars) and contribution of sunlit leaves to layers source (solid line with closed quarters). Diurnal course of isoprene net flux for EUST-I (c) and EUST-II (d) normalized by the mean midday flux ($9.4 \mu\text{g C g}^{-1} \text{ h}^{-1}$, a,b). The model is applied with the reference parameterization and a modified physiology (error bars) with increased stomatal conductances (EUST-I) or decreased photosynthesis (EUST-II, see bold font values in Table 4.2).

1. Light acclimation of emission capacity: Several studies have demonstrated that the emission capacity of single leaves for isoprene and monoterpenes is superimposed by an acclimation to the light and temperature environment (Sharkey et al., 1991; Harley et al., 1994; Hanson and Sharkey, 2001b,a; Staudt et al., 2003). For 20 common tree species in a tropical rain forest in Costa Rica, Geron et al. (2002) compared the emission capacity of sun-exposed foliage to leaves growing in low-light environment. On average, the emission capacities of the shade adapted leaves were reduced to one third of the emission capacity of sun-exposed leaves. Consequently, a vertical scaling of the isoprene standard emission factor ($E_{V_0}^m(z)$) was performed assuming a linear dependence on canopy position, expressed as the accumulated leaf

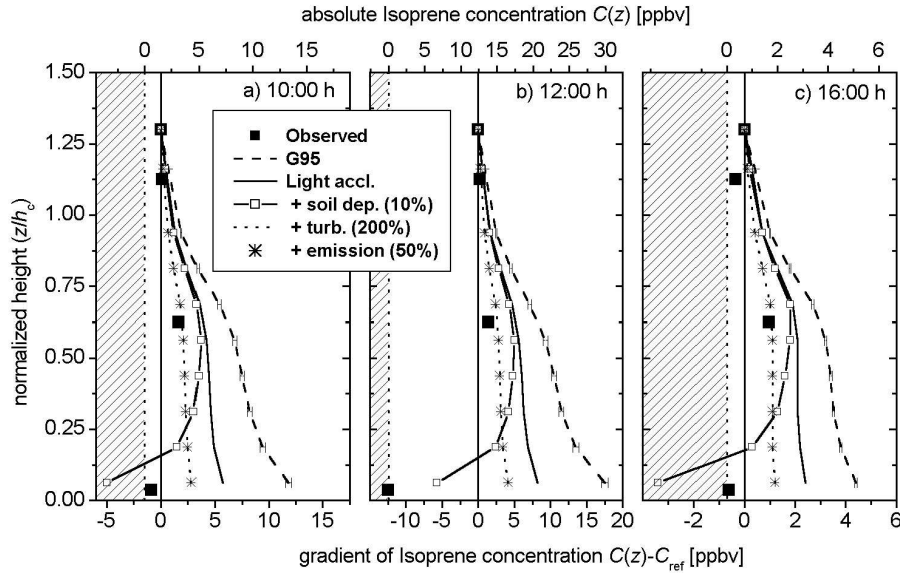


Figure 4.12: Comparison of observed (closed quarters) and predicted profiles of isoprene on 28/29 October at RBJ-A (EUST-II). Predictions are obtained with the reference parameterization by applying the algorithm of Guenther et al. (1995) with no modifications (1 - dashed line, G95), assuming a light acclimation (2 - solid line, Light accl.) of the standard emission factor according to $E_{V_0}^m(GROUND)/E_{V_0}^m(TOP) = 1/3$ with a linear dependence on canopy position (Λ_z), additionally to 2 a soil deposition (3 - line with quarter, soil dep.) of 10% of canopy emission, additionally to 2 a 100% increased friction induced turbulence (4 - dotted, line turb.), and additionally to 2 a 50% reduction of the standard emission factor (5 - stars, emission). Error bars in a) represent the prediction variability for modified photosynthesis parameters (see Table 4.2). For morning and afternoon conditions, the model incorporating soil deposition predicts a negative concentration close to the ground because the deposition is calculated as a fixed fraction of the canopy emission rather than a deposition process that depends on the absolute concentrations (shaded area).

area (Λ_z) above z giving $E_{V_0}^m(\Lambda_z) = 24 - 2.7\Lambda_z \mu\text{g C g}^{-1} \text{h}^{-1}$. For the applied total leaf area index LAI=6, this procedure is equivalent to a 66% reduction of $E_{V_0}^m$ for leaves close to the ground ($E_{V_0}^m(\text{LAI}) = 8 \mu\text{g C g}^{-1} \text{h}^{-1}$) compared to leaves at the canopy top (assuming a fraction of 30% isoprene emitting species, this value agrees well with the $24 \mu\text{g C g}^{-1} \text{h}^{-1}$ estimated for the shade adapted isoprene emitter *Sorocea guillemniana* growing at the Jaru site \rightarrow Kuhn et al., 2004, see also Chapter 5)

2. Deposition to soil: The very low isoprene concentrations observed close to the ground suggest an additional sink process in the lower canopy. In labo-

ratory studies, it has been shown that significant fractions of isoprene were consumed by soil microbes (Cleveland and Yavitt, 1997, 1998). Therefore, an additional simulation with an (arbitrary) assumed soil sink of 10% of the canopy source was performed.

3. Vertical mixing and standard emission factor: To test the sensitivity of the predicted profile to the vertical exchange rate and the uncertainty of the standard emission factor, two further simulations with increased turbulence (200%, see also Section 4.3.3) and a reduced standard emission factor (50%) have been performed.

As discussed briefly below, chemical reactions are regarded to be unimportant within the timescales under investigation. As shown in Fig. 4.12, the predicted profiles for the light acclimation assumption have a significant different shape with a nearly constant isoprene concentration with height in the lower the canopy (1). This is a qualitative improvement compared to the original simulation, where in contrast to the observations, the predicted concentrations increase close to the ground. The disagreement between simulated and observed isoprene concentration close to the ground is not reduced by the enforced vertical mixing or the decreased standard emission factor (3), respectively. However, the agreement between predicted and observed concentrations at the second ($0.68h_c$) and third ($1.13h_c$) canopy levels is better for the reduced standard emission factor. Without the additional sink at the soil surface (2), the profile shape can not be matched by the model. It should be mentioned, that the applied sink strength for isoprene (10% of canopy emission) are very speculative and arbitrary. The midday value applied in Fig. 4.11 is one order of magnitude higher than the uptake, which would result from the estimated deposition value for tropical soils ($2 \times 10^{-5} \text{ min}^{-1} \text{ g}^{-1}$ for 3 cm active soil depth, 850 kg m^{-3} soil bulk density) given by Cleveland and Yavitt (1998). However, the ecosystem values of Cleveland and Yavitt (1998) are based on few laboratory measurements whereby the tropical estimate lies in the middle of a wide range of deposition values covering more than two orders of magnitude. Simulations with a single-column chemistry model (Ganzeveld and Lelieveld, 2002) have predicted similar high isoprene concentrations near the soil surface which can not be explained by chemical processes (*L. Ganzeveld, personal communication, 2004*). For the light acclimation of isoprene emission capacity there is a further indirect evidence. Several ecological studies in Amazonia have found a large variability of specific leaf dry weight (SLW), which may be affected by the light environment, and thus the vertical position within the canopy (Reich et al., 1991; Roberts et al., 1993; McWilliam et al., 1993). Since the standard emission factor is normalized on a mass basis, the predicted emission scales with SLW. Carswell et al. (2000) e.g. found at the ZF2 site near Manaus canopy top and ground SLW values of 114 and 69 g m^{-2} , respectively. Considering this variation in the model calculations causes the emissions to decrease by 40% without changing the standard emission factor (on a mass basis).

4.3.5 Seasonal comparison and evaluation of predicted ozone exchange

In contrast to isoprene, the canopy layer represents an important sink rather than a source for ozone. For the Jaru site it was already explicitly shown, that the ozone flux is dominated by dry deposition to the vegetation and soil surfaces (Gut et al., 2002a; Rummel, 2004). The reaction with nitrogen oxide is negligible for the ozone budget due to relatively low NO concentrations, whereas other photochemical reactions occur mainly above the canopy. As an upper boundary condition, the observed ozone concentration above the canopy is used to calculate the actual deposition fluxes (Section 4.2.1 and 4.2.5). A comparison of the observed and predicted net fluxes and the 12 h vertical profiles of cumulative ozone deposition velocity, sink distribution and the contribution of sunlit leaves to the layer sink is shown in Fig. 4.13.

The net fluxes measured above the canopy have been corrected for canopy storage (Section 4.2.4). The observed and predicted concentration profiles for day- and nighttime conditions are shown in Fig. 4.14. The 14 h profile is selected because the daytime canopy storage is smallest in the early afternoon, which is especially important for the EUST-II data (see Fig. 4.13d). In general, the dry deposition concept applied with the canopy model can explain the observed variability of ozone fluxes quite well ($r^2 > 0.94$). The maximum uptake occurs at noon time, when ambient concentrations and stomatal conductances are highest and the turbulent timescales for ozone transport are lowest. For EUST-II, a considerable flux is also observed and predicted for nighttime conditions. Interestingly, the observed net fluxes during EUST-I are less than 50% lower compared to EUST-II, whereas the levels of ambient concentrations are reduced by a factor of three to four (Table 4.1, Fig. 4.13c-d). Since the dry deposition concept (Section 4.2.5, Eq. 4.1) predicts a linear dependency between concentration and ozone flux, there must be a strong seasonal variability of the ozone deposition velocity (v_{d,O_3}). Whereas the model predictions for EUST-II agree well with observations, the flux for EUST-I is underestimated by 50%. The soil, aerodynamic and boundary-layer resistances are very similar for both periods (for a comparison of soil resistances see Gut et al. 2002a). Consequently, the large seasonal variability of v_{d,O_3} has to be mainly explained by different leaf surface uptake. As pointed out in the last Sections, the stomatal conductance and assimilation during the wetter period EUST-I may have been larger compared to EUST-II. Nevertheless, the systematic underestimation of the observed fluxes is only partly reduced (from 55% to 45%) when the physiological changes are considered. The vertical source/sink distribution (Fig. 4.13a-b) is more uniform compared to the distributions for isoprene and assimilation because the uptake is partly independent from the light environment and physiological control but dependent on the cuticular resistance (see Eq. 4.5). The contribution of the lower canopy (0-20 m) is at least 30% and even 33% for EUST-I and EUST-II, respectively, and the

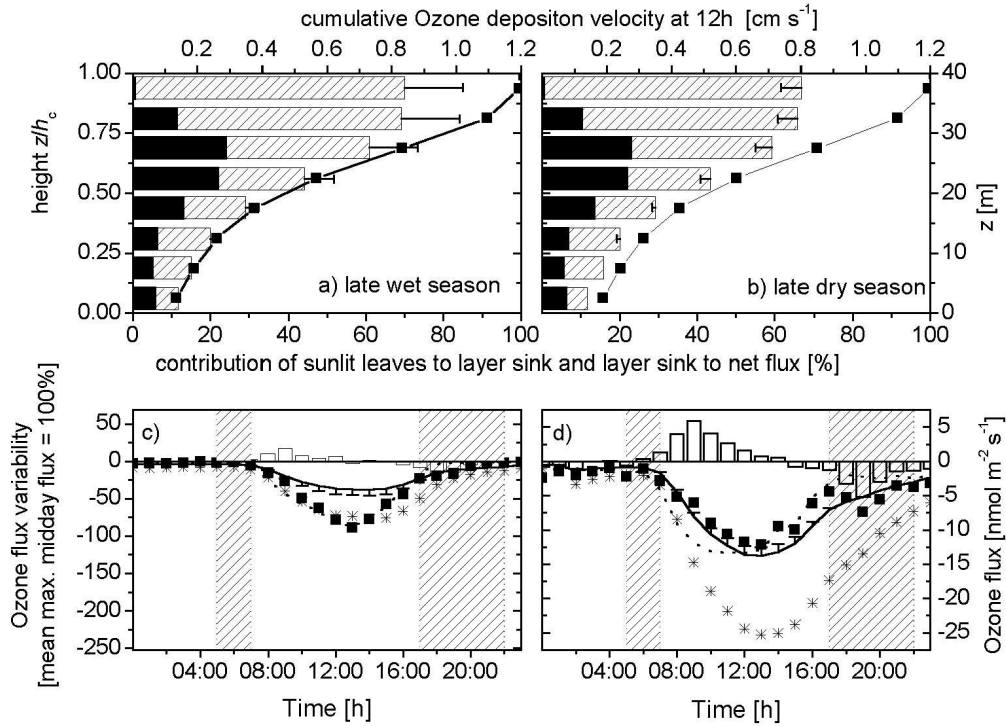


Figure 4.13: Application of the dry deposition concept $F_x = -v_{d,x}C_x$ to ozone uptake. Leaf deposition is calculated as the parallel sum of cuticular and stomatal uptake (Baldocchi et al., 1987) assuming a cuticular resistance of $r_{cut,O_3} = 5000 \text{ s m}^{-1}$ derived for EUST-II (Rummel, 2004), a zero mesophyll resistance and a bulk soil resistance of 700 s m^{-1} (see Section 4.2). a-b) Cumulative ozone deposition velocity (v_{d,O_3} , striped bars), relative vertical sink distribution (black bars) and contribution of sunlit leaves to layer sink (line with closed quarters) for EUST-I (a) and EUST-II (b) meteorology. c-d) Comparison of observed (closed quarters) and predicted (solid lines) net ozone flux for EUST-I (c) and EUST-II (d). The shaded areas represent unsteady periods during sunrise and sunset (Section 4.3.1). Observations (Eddy Covariance measurements, dotted lines) are corrected for canopy storage (open bars). The model is applied with the reference parameterization and modified stomatal (EUST-I) and assimilation (EUST-II) parameters (error bars, see Table 4.2). A second simulation was performed with a lower cuticular resistance $r_{cut,O_3} = 1000 \text{ s m}^{-1}$ (star symbols).

contribution of sunlit leaves to the layer sink is much smaller compared to assimilation and isoprene. The relative contribution of the understory layers to the total uptake increases with cuticular uptake, which is assumed to be independent of the physiological activity. The range of predicted midday deposition velocities for mean meteorological conditions are $0.8\text{-}0.85 \text{ cm s}^{-1}$ for the reference parameter-

ization and $0.7\text{--}1.05\text{ cm s}^{-1}$ for the parameterization with modified conductance and assimilation parameters (Table 4.2). In fact, the observed midday deposition velocity during EUST-I is more than twice as large as the observed v_{d,O_3} for EUST-II. Consequently, the observed flux variability may not be explained by seasonal changes of leaf physiology only. Further model simulations assuming a seasonal change of leaf surface area showed no considerable increase of v_{d,O_3} (results for ozone not shown, see Section 4.3.2).

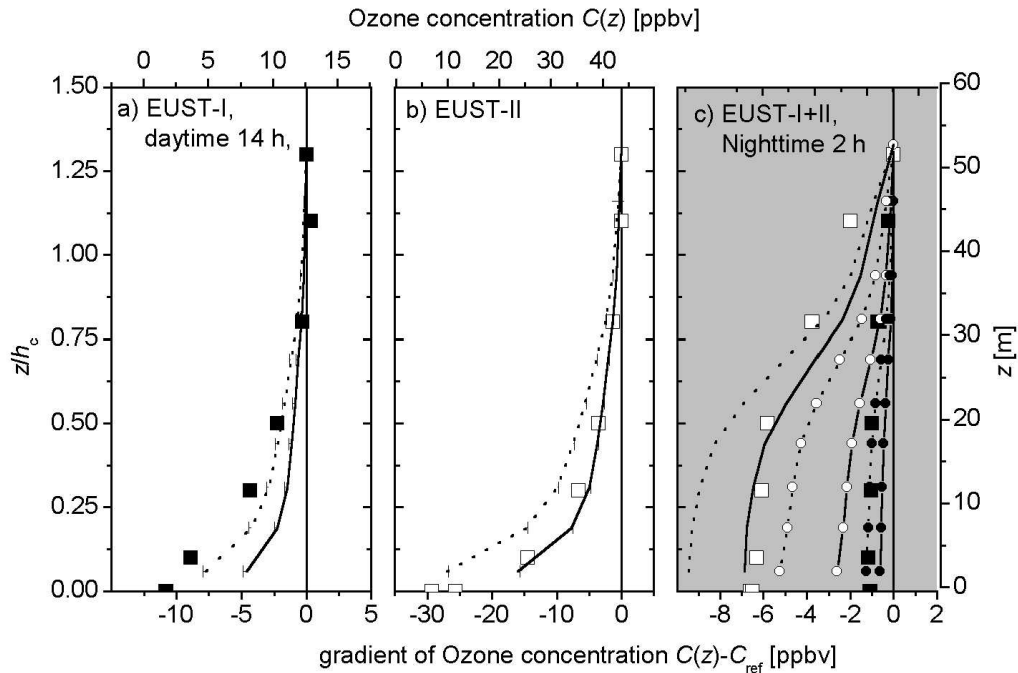


Figure 4.14: Comparison of observed (quarters) and predicted vertical profiles of ozone at 14 h for EUST-I (a) and EUST-II (b) and for nighttime at 2 h (c; EUST-I - closed symbols, EUST-II - open symbols). Predicted profiles are obtained for the reference parameterization (Table 4.2) using a cuticular resistance of $r_{cut,O_3} = 5000\text{ s m}^{-1}$ (solid lines) and $r_{cut,O_3} = 1000\text{ s m}^{-1}$ (dotted lines). Error bars (only positive) represent prediction variability for increased stomatal and decreased photosynthesis parameters (see Fig. 4.13). Nighttime profiles are calculated without (line with symbols) and with storage flux (line without symbols) for EUST-II meteorology assuming a total value of $6\text{ nmol m}^{-2}\text{ s}^{-1}$ representing the integrated mean storage flux from 22–2 h ($1.2\text{ nmol m}^{-2}\text{ s}^{-1}\text{ h}^{-1}$).

Consistent with the net fluxes, also the predicted ozone concentration profiles for EUST-II meteorology show a good agreement with the observations using the cuticular resistance of 5000 s m^{-1} . In contrast, EUST-I observations are

strongly underestimated by the model with a low sensitivity to the physiological parameters (Fig. 4.14a). However, a reduction of 80% in the cuticular resistance (5000 to 1000 s m⁻¹) leads to a doubling of the relative concentrations ($C_i - C_{ref}$) and predicted net fluxes and a much better agreement with the observations. The predicted nighttime profiles for EUST-I, where canopy storage is negligible (Fig. 4.13 c), show a similar agreement for the two applied cuticular resistances. For EUST-II, the situation is similar as for CO₂ nighttime profiles, where the canopy storage has to be considered (Section 4.3.3, Fig. 4.10). The apparent absolute canopy storage fluxes from 23-2 h are < 0.1 and > 1 nmol m⁻² s⁻¹ for EUST-I and EUST-II, respectively. The predicted profiles for 5000 and 1000 s m⁻¹ cuticular resistances (r_{cut,O_3}) and corrected for canopy storage are consistent with the results for the net fluxes. The results obtained with the r_{cut,O_3} inferred for EUST-II agree well with the observations, whereas the results for the lower r_{cut,O_3} overestimate the uptake of the vegetation for EUST-II. Since the cuticular pathway is independent of the physiological leaf activity, the predicted ozone deposition is more sensitive to the choice of r_{cut,O_3} compared to r_s . Whereas the stomatal pathway (first part of the left side of Eq. 4.5) has a strong maximum in the upper canopy and occurs only at the bottom leaf side (hypostomatous leaves), the cuticular uptake is linearly related to the leaf area in each layer and occurs at both leaf sides (indicated by the factor of two in the second part on the left side in Eq. 4.5). Consequently, an increased stomatal conductance affects mainly the ozone uptake in the upper canopy (Fig. 4.13a,b) and may not explain the disagreement between the observed and predicted ozone concentrations in the lower canopy during EUST-I.

However, a strong seasonal variability of r_{cut,O_3} is very unlikely because this implies fundamental changes of leaf structure. In part, the structure and function of leaves changes as a result of lifespan regulation (Reich et al., 1991), which might be synchronized and follow the seasonal cycles of wet and dry periods within evergreen tropical rainforest. A combination of all the potential factors (leaf physiology, canopy and leaf structure) reduce the observed disagreement between the expected and observed seasonal variability of ozone deposition but are still insufficient. As mentioned above, potential chemical sinks within the free air space are also insufficient and would affect both seasonal periods. Because the relative humidity (RH) and rainfall during EUST-I were significantly higher compared to EUST-II (see Fig. 4.1), the ambient air in the lower canopy was nearly saturated with water vapor and large fractions of the leaf surfaces were wetted. The composition and chemistry of the water film on wetted leaf surfaces are not very well understood and deposition models are treading this effect on ozone uptake differently. The earliest models have considered the low solubility of ozone in pure water reducing the ozone uptake of leaves (Chameides, 1987; Baldocchi et al., 1987). However, depending on the origin and composition of the surface water, the opposite effect was also found. Higher than theoretical uptake rates have been observed e.g. on leaf surfaces wetted by dew (Wesely et al.,

1990) or rain water (Fuentes et al., 1992), above a deciduous forest in the winter (Padro et al., 1992), and also over oceans (Wesely and Hicks, 2000). Under the likely assumption, that larger fractions of the leaf surface were wet during the wet season, our results indicate in line with those studies that there might be a significant ozone uptake by wet leaf surfaces.

4.4 Further model application examples

In the following Section, two examples of extended model applications are given. The first one concerns the regional estimate of isoprene emission for Amazonia, which applies the scheme of Guenther et al. (1995) considering some of the results discussed in Section 4.3.4. In the second example, the model is applied to a future scenario of doubled atmospheric CO₂ concentrations.

4.4.1 Global isoprene emissions from tropical rain forest

Global isoprene emission estimates for tropical rain forest are obtained by the temporal integration of the mean diurnal courses for EUST-I and EUST-II and by horizontal integration assuming a forested area of 4.33 million km⁻² (Guenther et al., 1995). The estimated midday isoprene fluxes and total emissions are summarized in Table 4.3. Additionally to the results obtained with the reference parameterization, the table contains the results for the scenario assuming a light acclimation of isoprene emission capacity (Section 4.3.4). To assess the significance of the explicit calculation of leaf temperature, the regional and midday predictions are calculated also for the simplified assumptions $T_s = T_{ref}$ (isothermal surface) and $T_a = T_{ref}$ (isothermal canopy layer).

The reference scheme with a constant standard emission factor predicts a somewhat higher mean regional estimate (96 $\mu\text{g g}^{-1} \text{h}^{-1}$) compared to the 84 $\mu\text{g g}^{-1} \text{h}^{-1}$ of Guenther et al. (1995). When the leaf temperature is not calculated explicitly, the regional estimate is reduced to 70% whereas the explicit calculation of the air temperature within the canopy has an effect of 5%. The maximum midday canopy fluxes show even a higher sensitivity depending on the applied approach. In general, the midday fluxes agree well with recent canopy scale observations of isoprene emission flux in Amazonia. Greenberg et al. (2004) derived for three different sites maximum midday values of 2.2, 5.3, and 9.8 $\mu\text{g g}^{-1} \text{h}^{-1}$ by inverting boundary-layer concentration profiles measured on tethered balloons. The second and last numbers represent the estimated flux for the Manaus and Jaru site, respectively. For Tapajós, Santarém (East Amazon basin), Rinne et al. (2002) obtained a value of 6.0 $\mu\text{g g}^{-1} \text{h}^{-1}$ using the same technique, whereas Stefani et al. (2000) obtained for Manaus a value of 4.6 $\mu\text{g g}^{-1} \text{h}^{-1}$ by Relaxed Eddy Accumulation technique (see Harley et al. 2004 for a comparison of observations and emissions from different Neotropical sites).

Table 4.3: Global estimate of isoprene emissions from tropical rain forest according to Guenther et al. (1995) using the model predicted leaf surface temperatures (T_s) and absorbed radiation. The given ranges (line 2 and 5) represent predictions for an increased stomatal conductance during the wet season (EUST-I) and a decreased photosynthesis during the dry season (EUST-II, see Table 4.2). Mean values represent averaged predictions for EUST-I and EUST-II using the reference parameterization. Line 3-4 represent canopy fluxes at noontime (12 h). Column 2,4,5 represent calculations for the full model scheme with explicit calculation of leaf surface (T_s) and ambient air (T_a) temperature and a constant standard emission factor (2), the bulk approach applying the observed temperature above the canopy (4, $T_s = T_{ref}$), and the iso-thermal approach neglecting vertical temperature gradients inside the canopy volume (5, $T_a = T_{ref}$), respectively. Column 3 is equivalent to column 2 assuming a light acclimation of the standard emission factor (Light accl., see Section 4.3.4).

	Reference	Light accl.	$T_s = T_{ref}$	$T_a = T_{ref}$
<i>Global estimate</i> [Tg C yr ⁻¹]				
range	75.8 – 113.6	52.2 – 77.1	53.6 – 78.8	71.5 – 106.9
mean (ratio %)	95.8 (100)	64.4 (67)	66.2 (69)	90.1 (94)
<i>Canopy flux at noon time</i> [μ g C g ⁻¹ h ⁻¹]				
range (mean)	7.1 – 11.4 (9.4)	4.8 – 7.5 (6.2)	4.9 – 7.8 (6.3)	6.7 – 10.6 (8.7)

4.4.2 Seasonal comparison of predicted climate change due to elevated atmospheric CO₂ levels

The response of Amazon rainforest to elevated atmospheric CO₂ concentrations is simulated by doubling CO₂ mixing ratios observed above the canopy (resulting in 650-900 ppm at z_{ref} , see Fig. 4.1a,b). Theoretically, increased CO₂ levels allow leaves to maintain or even increase the substomatal CO₂ concentration with lower stomatal conductance rates. Consequently, a higher water use efficiency with higher net assimilation rates, surface temperatures and lower latent heat fluxes can be expected.

In practice, the predicted fluxes show a linear correlation ($r^2 > 0.97$) with the original results (Section 4.3.3) leaving all other model parameters constant. Fig. 4.15 shows the relative change of predicted canopy fluxes for increased CO₂. The model predicts a 40% higher daytime bowen ratio and a 20% higher carbon uptake. A fraction of $\approx 20\%$ of the absorbed energy which has been formerly converted into latent heat by transpiration is emitted as sensible heat. The seasonal differences are not very large. Actually for sensible heat, the differences are negligible, if a seasonal change of leaf physiology is assumed. Due to higher surface temperatures, which cause a higher long-wave radiation loss, a slight decrease of the available energy ($< 4\%$) is predicted for the elevated CO₂ scenario. In general

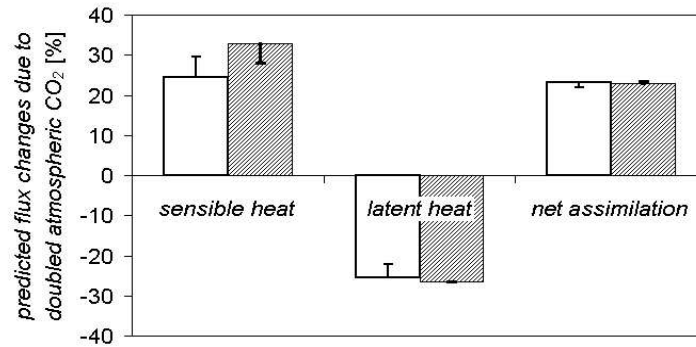


Figure 4.15: Predicted change of canopy net fluxes for EUST-I (open bars) and EUST-II (shaded bars) assuming a doubled level of atmospheric CO₂. Error bars represent predictions using higher stomatal (EUST-I) and lower photosynthesis (EUST-II, see Section 4.2.3) parameters, respectively.

the observed response to elevated atmospheric CO₂ is very similar with regard to kind and magnitude to what has been predicted by similar models (Leuning et al., 1998) and observed for agricultural crops in laboratory experiments (Harley et al., 1992; Grant et al., 1995). However, the long-term response of the rain forest is also affected by other nutrient factors (Oren et al., 2001; Hirose and Bazzaz, 1998), adaptive regulations (Naumburg et al., 2001), and 'mega-development trends' in Amazonia (Laurance, 2000). Furthermore, there is a high chance, that most of the actual Amazon area with primary rainforest will be lost due to deforestation within the next 50 years before we could benefit from a potential counterbalance to elevated atmospheric CO₂.

4.5 Conclusions

The evaluation of scalar exchange with very different pathways, i.e. H₂O and isoprene emission, CO₂ assimilation and ozone deposition has shown, that the presented approach and parameterization can serve for multiple purposes in ecosystem and regional modeling studies. The observed and predicted net fluxes and concentration profiles for day- and nighttime conditions are quite consistent. In alignment with observations, the model predicts a stable thermal stratification of the lower canopy during the day, which is reversed during nighttime. Due to the non-linear temperature response of physiological processes, the explicit calculation of the gradients across the leaf surface and within the canopy air volume is quite significant for the predicted fluxes. In contrast to the modeling approach of Williams et al. (1998) that is applied to a rain forest site near Manaus (Malhi et al., 1998, 2002), the presented approach is not very sensitive

to canopy structure, i.e. total LAI, but to the leaf physiological parameters of stomatal conductance and assimilation. Due to this high sensitivity, the seasonal variability of net primary production and transpiration observed at the Jaru site can be explained by small changes of leaf physiology only. Direct indications for such changes have been already suggested in Chapter 2 where leaf level gas exchange measurements from different seasons are compared. The comparison of observed and predicted in-canopy concentrations of isoprene for dry season and of ozone net flux and in-canopy concentrations for wet season conditions highlights two knowledge gaps, which should be investigated in future studies of in-canopy processes. The vertical scaling of isoprene emission capacity results in much more realistic predictions of isoprene concentrations in the lower canopy and reduced total emissions (30%), which should be considered in regional and global estimates of isoprene emission. Although soil deposition of isoprene contributes less to net exchange, it may significantly affect the concentration profile shape of the lower canopy. The comparison of observed and predicted ozone deposition pointed out the important role of cuticular uptake. Increased deposition rates for wet season conditions gives evidence of important sink processes at wetted leaf surfaces. In general, it would be worthwhile to establish ecological principles for the natural variability of leaves, e.g. their optical properties (albedo), the permeability of the leaf cuticula and the regulation of specific dry weight (SLW). The latter does not only affect the calculated emission of isoprene. If shaded leaves have a lower specific weight, they have simultaneously a larger surface and probably a higher permeability for ozone and other trace gases, which would result in a much higher cuticular uptake.

Chapter 5

Modeling the biogenic emission of volatile organic compounds (VOC) using a neuronal network approach

Abstract

Leaf chamber measurements of isoprene and monoterpene emissions of different tree species during wet and dry season are related to environmental and leaf physiological parameters. The environmental parameters include leaf temperature (T_s), light intensity, relative humidity, water vapor pressure deficit, preceding time averaged ambient temperature and ozone concentration, whereas the physiological parameters include stomatal conductance, assimilation and intercellular CO_2 concentration. With these parameters, 24 different combinations are built and multi-nonlinear regression to VOC emission is applied using a neural network approach. The regression results for single and aggregated data sets are evaluated separately, and compared to the predictions of the quasi standard emission algorithm for isoprene developed by Guenther et al. (1993) (G93), which uses T_s and light as input parameters. When calibration of G93 is applied on single data sets, G93 shows a good agreement with the observations ($r^2 \approx 0.9$). This is also achieved with the network approach using the same input parameters. Nevertheless, the unexplained variance can be reduced significantly by more than 50% with the network technique, when additional information like temperature history or assimilation is added to the network input. When G93 and the network using $\{T_s, \text{light}\}$ as input are calibrated with aggregated data sets from different species, season, developmental stage or light environment, r^2 is reduced to < 0.5 for the most complex aggregation. Remarkably, more than 50% of the unexplained variance can be explained by adding information on temperature history to the network input, with an optimal averaging period of 36 hours. An even better performance is reached with physiological parameter combinations reducing the unexplained variance to $< 10\%$. The results suggest a strong link between VOC emission and leaf physiology, that can be used in modeling attempts.

5.1 Introduction

Non-methane volatile organic compounds (VOC) belong to the major actors in atmospheric chemistry since they are involved in the formation of ozone, secondary aerosols and the depletion of OH radicals in the troposphere. This has an important impact on the cleaning capacity of the lower atmosphere (Roelofs and Lelieveld, 2000; Müller and Brasseur, 1995) and climate forcing (Andreae and Crutzen, 1997). The global budget of VOC's is dominated by biogenic emissions, mainly from plants (Guenther et al., 1995; Kesselmeier and Staudt, 1999). Plants are able to produce a huge number of different VOC's as secondary metabolites and there is a significant lack of understanding their ecological sense and why evolution developed this remarkable diversity (Kesselmeier and Staudt, 1999; Harley et al., 1999; Theis and Lerdau, 2003). Because of their low abundance and high reactivity, the atmospheric concentration of higher terpenes ($> C_{10}$) is very low and usually below detection limit. Indeed, the total atmospheric budget of VOC's is dominated by isoprene and a small number of monoterpenes (Guenther et al., 1995; Kesselmeier and Staudt, 1999).

Against this background it is obvious that current surface-atmosphere exchange simulations use only emission algorithms for monoterpenes and isoprene. Within this context three algorithms are to be discussed. (1) For compounds stored in pools, as observed for monoterpenes with conifer species, a solely temperature dependent relationship is applied (Tingey et al., 1980). (2) For compounds like isoprene or monoterpenes that are produced and released immediately upon biosynthesis, a light and temperature dependent relationship was established by (Guenther et al. 1993, hereafter referred to as G93, see Appendix A). (3) A further complication is covered by observations of combined emissions from storage pools and direct production usually parameterized after Schuh et al. (1997). The reason why G93 has such a widespread use, is that it is simple to parameterize, and that it predicts the short-term temporal emission variability quite successfully. Calibrated with direct observations from a single plant and applied on a short timescale of a few days, the algorithm can reproduce the emission behavior perfectly in case that no additional environmental attributes affect plant physiology. The parameterization of G93 is done with linear regression on the combined temperature and light response of measured emission, which gives a so-called standard emission factor E_{V0} defined as the emission at standard conditions, usually 30°C temperature and 1000 $\mu\text{mol m}^{-2} \text{s}^{-1}$ photosynthetic active radiation (PAR). The measurements are performed on different scales and with differing methods, e.g. on enclosed leaves, branches or whole plants with cuvettes, or on the canopy scale with micrometeorological methods. Since the beginning of the nineties, many field and laboratory studies have been performed and E_{V0} values of many different species could be determined. Global applications use databases with E_{V0} values for different ecosystem types, like the compilation of Guenther et al. (1995) based on 22 field studies, which represent 26 of the ecosys-

tem types defined in the global database of Olson (1992). However, there are large uncertainties associated with this global application of G93. Based on a global chemistry-transport modeling study, the IPCC (2001) found a serious discrepancy between the global isoprene emissions derived by Guenther et al. (1995) giving an estimate of about 500 Tg C/yr, and many observational constraints on carbon monoxide and isoprene itself, which are best matched with a global yearly emission of about 200 Tg C. A main source of this uncertainty is the lack of field data for some ecosystem types, especially the tropics. Of course this can be reduced in future with ongoing field measurements, but it seems unrealistic, that all higher plants can be screened for E_{V_0} values. This may be possible for species-poor ecosystems like many of the mid-latitude forests of the northern hemisphere, but not for the tropical rainforest with its vast bio-diversity. Without appropriate derived E_{V_0} values, the parameter induced uncertainty of G93 has the same magnitude as its observed range, which is of several orders from zero to $E_{V_0} \gg 100 \mu\text{g C g}^{-1} \text{h}^{-1}$ for some species (Kesselmeier and Staudt, 1999). Furthermore it has been shown in many studies, that the short-term emission variability is superimposed by long-term acclimations to seasonal climatic changes (Monson et al., 1994; Schnitzler et al., 1997; Bertin et al., 1997; Geron et al., 2000; Petron et al., 2001) and the microclimatic environment (Lerdau and Throop, 1999; Hanson and Sharkey, 2001a,b; Staudt et al., 2003) and that this variability is closely linked to leaf development (Kuzma and Fall, 1993; Monson et al., 1994). A first attempt to account for this long-term variability is already proposed in the revised version of G93 (Guenther, 1997) where another empirical coefficient is introduced. But up to now, no clear definition of this parameter could be established since it is influenced by too many environmental and species dependent factors.

A common trend of ecological models is the evolution from simple empirical relationships towards more mechanistic based process models, but this has to be accompanied by an increased level of understanding. Remarkable insights have been obtained by molecular biological methods and laboratory studies of enzyme activities, which already led to new or modified emission algorithms (Schnitzler et al., 1997; Fall and Wildermuth, 1998; Zimmer et al., 2000; Sharkey and Yeh, 2001; Fischbach et al., 2002; Schnitzler et al., 2002) that are mechanistically linked to leaf physiology. However, extrapolation to the regional or global scale remains problematic since too little studies have been performed to do a well-founded parameterization of the models. The main idea of this study is to infer the potential benefits of a coupled modeling of VOC emission and the exchange of carbon dioxide and energy. Recently, it has been shown that integrated VOC emission is relatively conservative in relation to the plant carbon fixation over a wide range of species (Kesselmeier et al., 2002a). Thus it is hypothesized, that parameters reflecting the physiological activity of the plant could be more robust predictors of VOC emission than light and leaf temperature. The applicability of individual parameters and parameter combinations is statistically assessed with a neural network technique. A special class of neural networks, called multi-layer

perceptron or backpropagation neural network, is able to generalize patterns and relationships that are given between a set of input and output parameters. Single and aggregated data sets of environmental and physiological gas exchange parameters are related to the measured monoterpene and isoprene emissions from three Amazonian tree species. The detected relationships are purely empirical and give no mechanistic insight into the physiological processes, but they can help to identify mechanistic relationships and to reduce model uncertainties across a wide range of environmental and ecophysiological conditions. Although there is an increasing number of neural network applications in the ecological and atmospheric sciences (e.g. Huntingford and Cox 1997, stomata models; Abuelgasim et al. 1998, canopy reflectance; van Wijk and Bouten 1999, canopy fluxes of CO₂ and H₂O; Dutot et al. 2003, OH chemistry; Papale and Valentini 2003, carbon fluxes; and Gardner and Dorling 1998; Lek and Guegan 1999, review and introduction), to our knowledge this is the first application to plant emission of volatile organic compounds.

5.2 Field measurements and site description

The data used in this study were collected during two intensive campaigns of LBA-EUSTACH¹ in 1999 in a biological reserve 90-km north of Ji-Paraná in the state of Rondônia, Brazil (Jarú site, see Chapter 2). An overview of the whole experiment is given in Andreae et al. (2002). A general description of the local field site, atmospheric concentrations and species composition of VOC is given in Kesselmeier et al. (2002b). A detailed description of the enclosure measurements on isoprenoid emission and physiology is given by Kuhn et al. (2002a, 2004). The bi-directional exchange of oxygenated VOC is described in Kuhn et al. (2002b) and Rottenberger et al. (2004). During the late wet (May) and the late dry season (Sept/Oct) period, branch enclosure measurements were performed to examine leaf trace gas exchange of three different Amazonian tree species: mature leaves from the monoterpene emitter *Apeiba tibourbou* during wet and dry season (spec. 1), young, mature and senescent leaves of the isoprene emitter *Hymenaea courbaril* during the dry season and mature leaves during wet season (spec. 2), and mature leaves from the shade tolerant isoprene emitter *Sorocea guilleminiana* (spec. 3). This gives a total number of seven individual cases (single data sets) with measurements from different tree species at different developmental stages and different environmental conditions as summarized in Table 5.1, also showing the G93 standard emission factor (s.a.) on leaf mass basis. Each time series covers a period of 1-4 days with a time resolution of 1-2 hours for the VOC measurements giving a total number of 13-41 data points for each case. Parameters that have been recorded at a higher time resolution are

¹European Studies on Trace Gases and Atmospheric Chemistry as a Contribution to the Large-Scale Biosphere-Atmosphere Experiment in Amazonia

averaged with respect to the sampling time of the VOC's. Additionally, ambient temperature and ozone concentrations measured above the forest canopy are used (for parameter details see Andreae et al., 2002, , and Section 5.3.2).

Table 5.1: Overview of the chronological ordered seven time series of VOC exchange measured on branches of three Amazonian tree species during wet and dry season 1999 in Rondônia (SLW = specific leaf dry weight in g m^{-2} ; N=number of VOC measurements for each time series; Sx = species 1, 2, 3; $E_{V_0}^m$ = mass based standard emission factor for G93, see also Kuhn et al. (2002a, 2004); IP and MTP = isoprene and monoterpene emitting species, respectively).

Case	Species	Type	Season	SLW	$E_{V_0}^m$	N
C1	S1 <i>Apeiba tibourbou</i>	MTP	wet	88.8	3.6	19
C2	S2 <i>Hymenaea courbaril</i>	IP	wet	118.4	45.4	22
C3	S2 <i>Hymenaea courbaril</i> ^a	IP	dry	80.3	0.7	13
C4	S2 <i>Hymenaea courbaril</i> ^b	IP	dry	25.6	37.6	41
C5	S3 <i>Sorocea guilleminiana</i> ^c	IP	dry	92.0	24.0	26
C6	S1 <i>Apeiba tibourbou</i>	MTP	dry	70.3	2.1	30
C7	S2 <i>Hymeneae courbaril</i>	IP	dry	79.9	111.5	29

^a senescent leaves, ^b young leaves, ^c shade adapted species

5.3 Neuronal approach

A very successful and widely applied class of neural networks is the multi-layer perceptron using the back propagation learning rule (BPN). From a mathematical point of view, it can be seen as a universal approximator of multiple nonlinear problems (Hornick et al., 1989). A full derivation of the algorithm is given e.g. in Rumelhart et al. (1986). A short mathematical description is given in Appendix C. In principle, the network has to approximate the relationships inherent in a population of input and output vector pairs. In the so-called “learning” or “training” phase, a fraction of the population (training set) is repeatedly presented to the network, until the network output matches the desired output. This is reached by applying a general least square method. The remaining data set (test set) is used to evaluate the performance of the trained network. Topologically, a neural network consists of a number of nodes or “neurons” connected among each other. The term “multi-layer perceptron” means that the neurons are arranged in distinct layers and connected feed-forward (without feedback) by weights (Fig. 5.1). The input layer represents the normalized vector of input parameters and is fully connected with a hidden layer, which again is connected with the normalized output vector. The number of input and output neurons is pre-defined by the problem that is analyzed (i.e. number of input and output parameters). The number of neurons in the middle layer has to be chosen appropriately. The

learning phase is characterized by changes of the weight connections, starting with the output and going backward to the input layer (\rightarrow back propagation). The least square method is applied locally to individual weights that are changed towards the desired output.

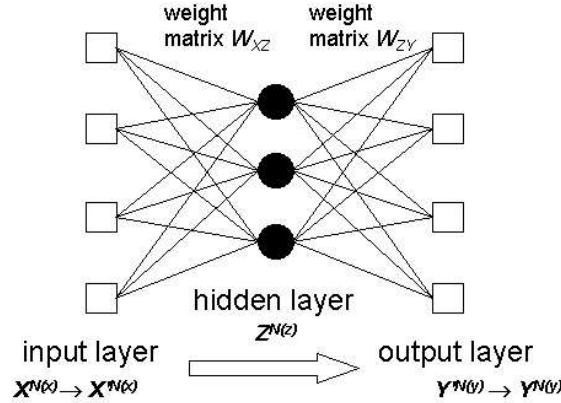


Figure 5.1: Topology of a Back Propagation Neural Network (BPN). Network input and output parameters X' and Y' are normalized ($X \rightarrow X'$ and $Y' \rightarrow Y$).

5.3.1 Simulations performed

Three types of simulation have been performed for the present study (see Fig. 5.2): A perfect noiseless set of vector pairs is used to test the ability of the BPN technique to approximate the non-linear behavior of VOC emission that is implied by G93 (*i*). This data set is created from leaf temperature (T_s) and PAR measurements (Q_{PAR}) of all data sets C1-C7 listed in Table 5.1 and the output of G93 with a standard emission factor of one. The second type of simulation (*ii*) is used to assess the quality of 24 different input parameter combinations (No. k , with $k = 1, \dots, 24$) serving as predictors of the VOC emission measured for each case C1-C7, whereby the G93 input parameter combination (T_s and Q_{PAR}) is referred to as No.1. A higher accuracy of the BPN technique applied with No.1 would indicate a sub-optimal parameterization of G93. A significantly better performance of the other combinations No.2-24 would demonstrate the advantage of a new or modified emission algorithm using other input parameters. The wide-range emission variability is analyzed with simulations performed on aggregated data sets A^U, \dots, F^U of C1-C7, e.g. $A^U = \{C1, C6\}$ (*iii*). In the mathematical set theory, aggregated sets are also called *union* or *join of sets*. The simulations are compared with G93 results obtained after re-calibrating the standard emission factor E_{V0} for each aggregation set. With the last simulation type, it is tested whether the network is able to generalize the observed wide-range variabilities with appropriate input parameters.

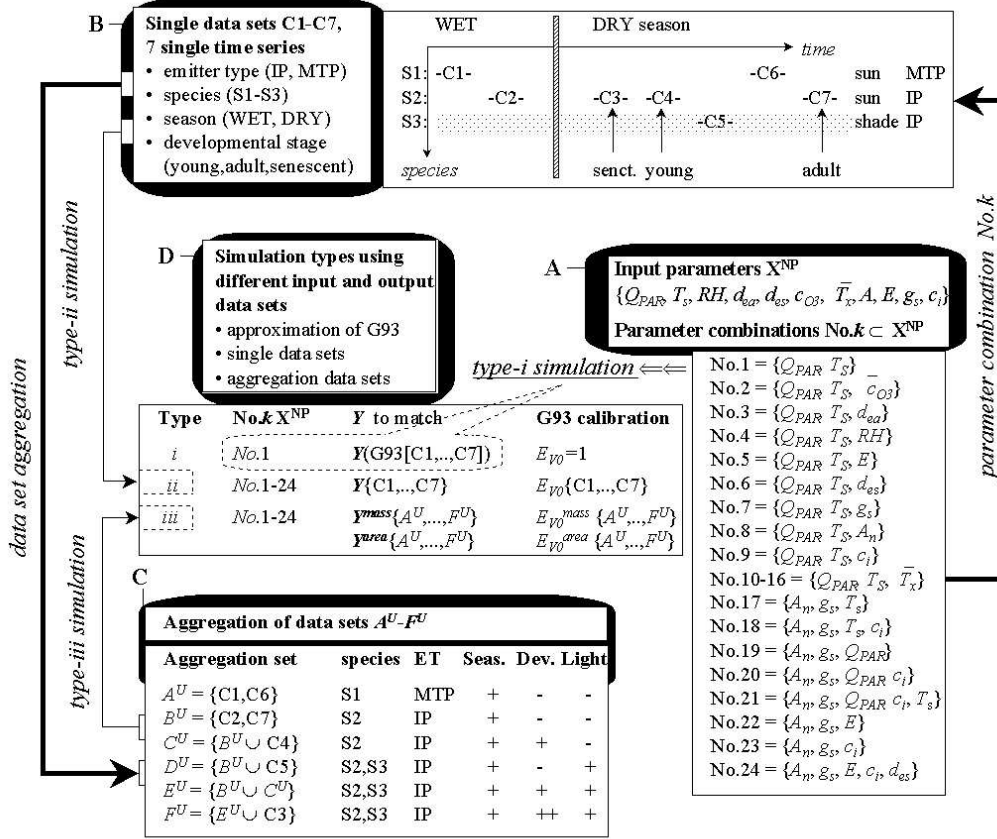


Figure 5.2: Data and model simulation overview. A: Input parameters listed in Table 5.2 and parameter combinations No.k applied to build the input vector for the network (see Section 5.3.3). B: Single measurement sets used for type-ii simulation (see Table 5.1). C: Aggregated data sets used for type-iii simulation including data from different species, season (Seas.), developmental stage (Dev.) and light environment (Light), with emitter types (ET) monoterpene (MTP) and isoprene (IP). (see Section 5.3.4). D: Simulation types with applied parameters combinations No.k, output Y to match, and data sets used to calibrate the standard emission factor E_{V0} for G93 (see Appendix A.9). Simulation i is performed as a proof of concept with parameter combination No.1 from C1-C7 as input for the BPN and G93, and the output of the latter using $E_{V0} = 1$ (noiseless data set, see text).

5.3.2 Selection of input parameters

The selection of different input parameters is practically restricted to the available field measurements. As a further and general guideline, only parameters are

selected, that are commonly available from field measurements and applied in ecophysiological studies of leaf gas exchange. This procedure will allow the BPN application to other field data sets and a further evaluation and/or generalization of the conclusions drawn in the present study. A total number of 11 different parameters of leaf gas exchanges is compiled from the measurements described and listed in Table 5.2. PAR flux and leaf temperature belong to the standard set of measured quantities, since they are used for the application of G93. Beside that, they are important parameters of CO₂ and water vapor exchange. Air humidity is known to be a controlling factor of stomatal conductance and transpiration. Some authors argued and demonstrated that water vapor pressure (Nunez et al., 2002) and/or relative humidity (Llusia and Penuelas, 1999) could also be a driving factor of isoprene and monoterpene emission. To account for this, relative humidity (RH), ambient (D_a) and leaf surface water pressure deficit (D_s) are included to infer potential relationships between air humidity and VOC exchange. RH was measured directly in the air stream leaving the cuvette, D_a and D_s are calculated according to Ball (1987). In several studies it was demonstrated that on timescales from hours to weeks adaptations of the emission behavior to the local climate and growth conditions can occur, in particular to the mean preceding temperature (temperature history) (Monson et al., 1994; Geron et al., 2000; Petron et al., 2001). Therefore, half hourly mean ambient temperature above the canopy (s.a) is averaged over 3, 6, 12, 18, 24, 36, and 48 hours preceding each data point of VOC exchange. Parameters 8-11 listed in Table 5.2 are basic parameters of CO₂ and H₂O exchange and closely linked to leaf physiology. Net assimilation (A_n) and transpiration (E) were measured directly from the mass balance of the cuvette system (see Section 5.2). Stomatal conductance (g_s) and intercellular CO₂ concentration (c_i) is calculated from leaf temperature and the CO₂ and H₂O balance of the cuvette (Ball et al., 1987). Leaf boundary-layer conductance for the cuvette system (necessary for these calculations) was derived by Gut et al. (2002a). A special parameter used for the analysis is ambient ozone concentration (\bar{c}_{O_3} , P06), which is derived from preceding 48 h averages from above measurements above the canopy (s.a.). As reported by Kesselmeier et al. (2002b), averaged daytime ambient ozone concentration varied between < 10 ppb during the wet and > 40 ppb during the dry season. This was speculated to explain seasonal variations of isoprene emission rates (see Kuhn et al., 2004). There are also direct observations, that monoterpene (Heiden et al., 1999) and isoprene (Sparks et al., 2003) emission can be increased under high levels of ozone.

5.3.3 Parameter combinations

A general procedure to built parameter combinations for the network input would be to start using all 17 parameters listed in Table 5.2 as input and to reduce this number then stepwise by removing the parameter that contributes least to the network output. However, for three plausible reasons, the combinations are spec-

Table 5.2: Applied input parameters (Type: ENV = environmental, PHYS = physiological parameter, ENV-T = environmental using temperature history).

	Symbol	Parameter	Unit	Type
P01	Q_{PAR}	PAR flux	$[\mu\text{mol m}^{-2} \text{s}^{-1}]$	ENV
P02	T_s	leaf temperature	[K]	ENV
P03	RH	relative humidity	[]	ENV
P04	D_a	ambient water vapor pressure deficit	[hPa]	ENV
P05	D_s	leaf surface water vapor pressure deficit	[hPa]	ENV
P06	\bar{c}_{O_3}	averaged ambient ozone concentration over the last 48 hours	[ppb]	ENV
P07	\bar{T}_x	averaged ambient temperature, subscript x denoting last 48, 36, 24, 18, 12, 6, or 3 hours	[K]	ENV-T
P08	A_n	net assimilation	$[\mu\text{mol m}^{-2} \text{s}^{-1}]$	PHYS
P09	E	transpiration	$[\text{mmol m}^{-2} \text{s}^{-1}]$	PHYS
P10	g_s	stomatal conductance for H ₂ O	$[\text{mol m}^{-2} \text{s}^{-1}]$	PHYS
P11	c_i	inter cellular CO ₂ concentration	[ppm]	PHYS

ified a priori: (1) The potential number of combinations is very high (e.g. with $N = 17$ input parameters and a maximum number of 6 parameters for each combination there are at least 9000 different parameter combinations possible for one case). (2) Because of its highly non-linear behavior, the network does not necessarily perform best with all parameters as input. (3) A main task of this analysis is to infer possible improvements of the G93 scheme (using combination No.1= $\{Q_{PAR}, T_s\}$) by adding few additional parameters like air humidity or temperature history, and to compare this with “physiological” predictors. The physiological activity is mainly represented by A_n , E , and g_s , whereby the latter links the carbon gain and water loss terms. Therefore, three classes of parameter combinations are specified (Table 5.4): Two classes are extended versions of No.1 plus one additional parameter giving No.2-16 (No.10-16 with temperature history and No.2-9 with all other parameters). The combinations No.17-24 are arbitrary examples of physiological combinations using A_n and g_s as integrative physiological parameters plus 1-3 additional parameters.

5.3.4 Aggregation of data sets

Cases C1-C7 are used to generate new data sets by aggregation to analyze the wide range emission variabilities of the three species under investigation. A total number of 6 aggregated data sets A^U, \dots, F^U with increasing heterogeneity is compiled from Table 5.1 and listed as part of Fig. 5.2. A^U and B^U include two time series from mature leaves of the monoterpene emitter (spec. 1) and the sun adapted isoprene emitter (spec. 2), respectively, during wet and dry season.

C^U to F^U are extended versions of B^U with increasing degree of complexity: C^U and D^U include additionally the data set from young leaves of spec. 2 (C4) and mature leaves of the shade adapted second isoprene emitter (C5, spec. 3), respectively. E^U and F^U are even more complex aggregation sets of the two isoprene emitters. E^U is built by conjunction of C^U and D^U , and F^U includes additionally to E^U the data set from senescent leaves of spec. 2 (C3).

5.3.5 Derivation of network parameters

The neural network parameters have to be specified appropriately for a given problem. There are two sources of stochastic variability of the network predictions: First, the training and test vector pairs are sampled randomly from the investigated data set. And second, the weights are initialized randomly at the beginning of the simulation, as recommended for ecological modeling applications (Lek and Guegan, 1999). Each simulation is repeated several times to get an estimate of the uncertainty that is associated with random selection and to have a higher number of predictive data points. The network output for test and training samples of all repetitions is averaged separately. The regression statistic is applied to the mean predicted values of the test sets, if no other declaration is given. Linear regression and statistical tests are given in Press (1997).

Table 5.3: Setup of the neural network. For a short mathematical description see Appendix C.

size of the training set	$0.75N(x, y)$
repetitions of each simulation	30
hidden layer neurons	8
learning rate η_{net}	const. 0.25
momentum α_{net}	0.1
activation function	$1/(1 + \exp^{-x})$
normalization	linear scaling between Min and Max value
stop criteria	RMSE ^{min} (test set)
maximum iterations	10000

The setup of the neural network is summarized in Table 5.3. For a detailed discussion of the different parameter options, the reader is referred to e.g. Rumelhart et al. (1986) or Bishop (1995). In summary, optimal network parameter values for a given problem cannot be derived straightforward. Although there is no general guideline, range limits of “sufficiently good” values can be derived from practical considerations. The training set should be sufficiently large, so that the essential features of the vector pairs are included (e.g. day and night time values for diurnal time series data). On the other hand, there should be a sufficient number of test data pairs to perform reasonable statistical tests. Following the literature (Lek and Guegan, 1999), a training set size of $0.75N(x, y)$ seems to be reasonable

for a sample size of $N(x, y) = 20$, typically available in the present study (see Table 5.1). This gives only 5 predictive data points in the test data fraction, but since the simulations were repeated 30 times, every data pair is chosen on average 7.5 times for evaluation in the test phase and the probability that it is not chosen at all is $< 1\%$. A disadvantage of the BPN algorithm is its poor scaling performance, i.e the computation time increases on third order with the number of adjustable weights $N(W)$ (Rumelhart et al., 1986). Since the number of input and output neurons is fixed for a given parameter combination, $N(W)$ depends on the number of neurons in the hidden layer, which consequently should be chosen as small as possible but large enough to ensure a high convergence rate. The convergence rate is also determined by the learning rate parameter η given in Eq. C.3. If the value is set too low, the rate of convergence will be slow producing a high computation time, if it is set too high, there is the risk that the network will fail to converge. Various test simulations were performed and it turned out that a combination of 8 hidden neurons in the middle layer and a learning rate of $\eta_{net} = 0.25$ ensures a fast convergence rate for all parameter combinations and data sets. Normalization of input and output values is performed with linear scaling between minimum and maximum values for each parameter in the data set under investigation (training + test set).

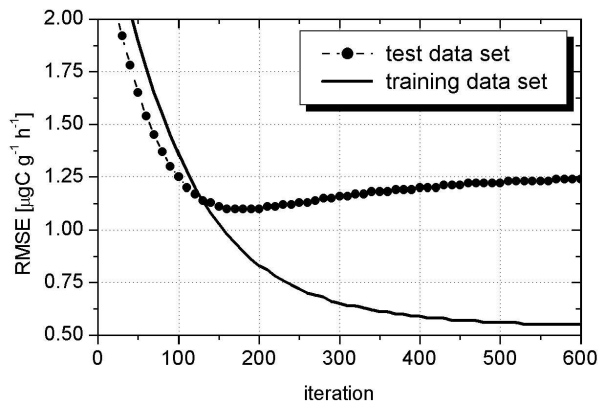


Figure 5.3: Single run example for the evolution of RMSE (root of mean squared error) during the test (solid line) and training (line with closed circles) phase for a type-*ii* simulation (C1 in Table 5.1, see Fig. 5.2).

An important effect that is often observed in the training phase of the BPN algorithm is demonstrated in Fig. 5.3, where the evolution of the root of mean squared error (RMSE) of the training and test data for a single run is shown. Whereas the RMSE value of the training set is decreasing permanently, the value of the test data set (which is not involved in the learning process) decreases to a minimum value before it becomes larger again. This effect is known as “overtraining” or “overfitting” and should be avoided by stopping the learning algorithm at an appropriate iteration step. To account for this, each simulation was evaluated every 100 training iterations and stopped before the RMSE of the test data set increased, but latest after 10,000 iterations. The behavior of overtraining is illustrated by Rumelhart et al. (1995) with the remarks, that “ ...

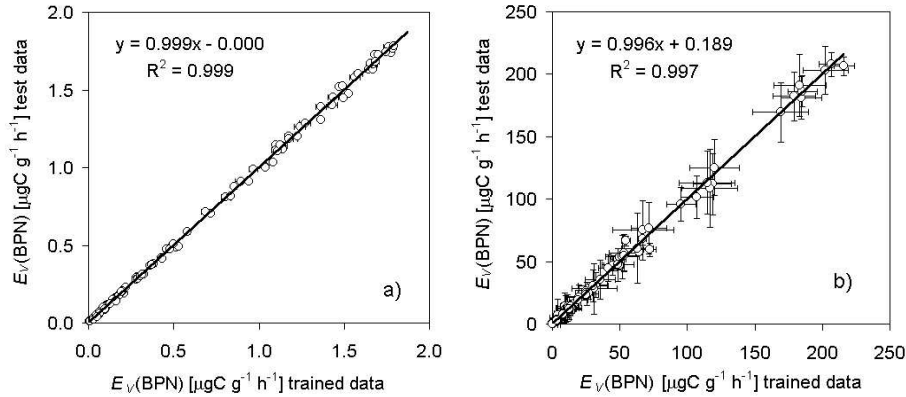


Figure 5.4: Comparison of mean predicted VOC emission for test and trained data ($N = 30$) for a) type- i simulation and b) type- ii simulations.

it is possible to do a great job on 'learning' the data but a poor job of generalizing to new data. [...] We say that the network has truly 'learned' the function when it performs well on unseen cases." Fig. 5.4 shows, that the differences between predictions for seen (trained) and unseen (test) cases are not very large. A type- i and ii simulation (see Fig. 5.2) was repeated 30 times and regression is applied to the averaged predictions for the trained and untrained cases as described above. The simulations with noiseless data (type- i) shows in general less scatter, but for both simulation types no significant discrepancy between predictions for train and test data is found. This is regarded as a strong confirmation, that the network has not only memorized the training data, but generalizes relationships between the input and output data.

5.4 Results and Discussion

5.4.1 Approximating the algorithm of Guenther et al. (1993)

The ability of the BPN approach to approximate the non-linear behavior of VOC emission implied by G93 is tested with repeated simulations using all available T_s and Q_{PAR} measurements as input, and predicted $E_V(\text{G93})$ with $E_{V0} = 1$ as output (see Section 5.3.1). Light and leaf temperature vary within a range of $0 \leq Q_{PAR} \leq 1800 \mu\text{mol m}^{-2} \text{s}^{-1}$ and $290 \leq T_s \leq 314 \text{ K}$, respectively. Fig. 5.5a and b show a comparison of the response functions of G93 and the trained network (i.e. the predicted emission at varying light and temperature at standard conditions of 314 K and $1000 \mu\text{mol m}^{-2}$ PAR, respectively). Fig. 5.5c shows a direct comparison of the predicted emissions for the test data compared to the output of G93. The response functions of the network have a similar shape com-

pared to G93. Light saturation of the network output occurs at somewhat higher light intensities, whereas the temperature dependence is approximated nearly linear in the input range between 290 and 310 K. In general, the combination of both response functions exhibits a reasonable agreement with the desired output ($r^2 > 0.98$). This shows, that the network is able to generalize the G93 model behavior in the observed range of input data and thus demonstrates the applicability of the BPN approach to VOC emission. The response functions should not be over-interpreted, since the network approximates only the combined output. In this case, the desired output E_V results multiplicatively from the nonlinear light (C_L) and temperature (C_T) of G93 terms after $E_V = C_L C_T$. Since network parameters are optimized to match the observed VOC emissions, which are probably rather additive than multiplicative, this parameterization is only sub-optimal to approximate simulated emissions from G93.

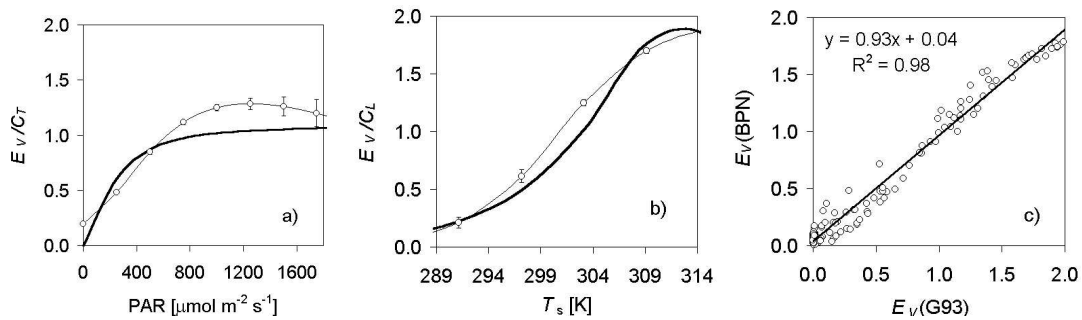


Figure 5.5: Type-*i* simulation testing the ability to predict G93 output by a BPN. The BPN was trained with temperature and light data as input variables and the VOC emission modeled with G93 and a standard emission factor $E_{V0} = 1$ as output variable. a) and b) show the normalized light (C_L) and temperature (C_T) response and c) shows the predicted emission of the network $E(\text{BPN})$ compared to the model emission $E(\text{G93})$. In a) and b) solid lines represent the normalized G93 response curve for standard temperature (303.15K) and light ($1000 \mu\text{mol m}^{-2} \text{s}^{-1}$), respectively. The lines with symbols represent the averaged response functions of the trained network with $N = 30$ repetitions.

5.4.2 Single data sets with different parameter combinations

Each single data set listed in Table 5.1 was run with the 24 parameter combinations listed in Table 5.4, that also shows the results of the linear regression statistics for the mean predicted emissions of the test data fraction for 30 repetitions. The G93 model, applied on each single set, gives a good r^2 value of 0.88. The slope parameter is close to one, and the intercept b is small compared

to the range of absolute values between 0 and 260. These results are close to the values found for the BPN using parameter combination No.1 with T_s and Q_{PAR} as input indicating that G93 is parameterized nearly optimal. However the rank values based on RMSE (24th for G93 and 19th for BPN with No.1) indicate that this performance can be improved by adding additional parameters to the regression procedure. Best results are obtained when information of the temperature history is added to the network. Especially No.10-13, including an averaged temperature of the preceding 48 to 18 hours show significant better correlations with $r^2 \geq 0.95$. A similar performance is also reached by adding assimilation (No.8) or transpiration (No.5) to the input parameters, or instead, by using one of the physiological combinations No.17, 18, 21, or 24. A graphical representation of the results for G93 and the BPN with No.1 and No.13 is given in Fig. 5.6 showing scatter plots of the measured and predicted VOC emission. Both methods show a similar deviation from the measurements, when the BPN is applied with parameter combination No.1. A significant fraction of the deviations is reduced for No.13 including \bar{T}_{18} .

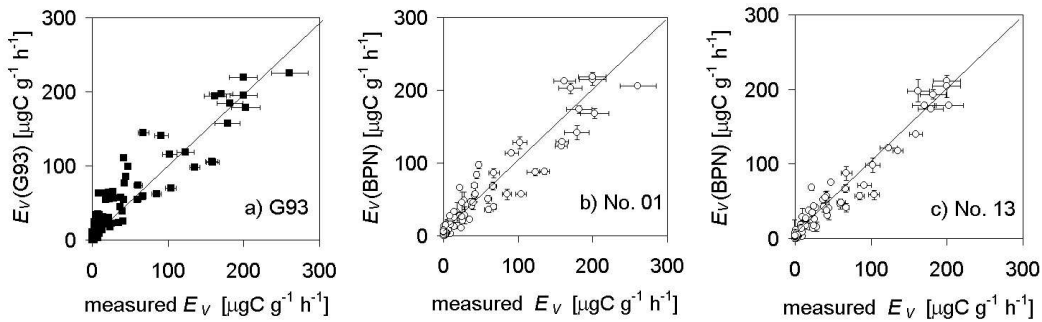


Figure 5.6: Scatter plots of predicted and measured VOC emission E_V from single sets (type-*ii* simulation) modeled with G93 (a) and the BPN approach with the reference parameter combination No.1 (b), and No.13 including \bar{T}_{18} (c), (see Table 5.4). The x -error bars are given by uncertainties associated with the measurements (Kuhn et al., 2002a, 2004), y -error bars are given from the standard deviation of test data predictions after $N = 30$ repetitions.

Large differences are found concerning the performance of individual parameter combinations for different data sets. Since not all results can be shown here, some combinations are selected. Fig. 5.7 shows rRMSE, the root of mean squared error for a given parameter combination and data set, divided by the analogous value for G93. All values for No.1 are close to 100% indicating that both approaches perform in similar quality. For No.8, which includes assimilation, results for C7 (spec. 2, isoprene emitter, mature leaves, dry season) show a better performance with much smaller rRMSE values. Compared to G93 and No.1, the RMSE of No.13 including \bar{T}_{18} for C3 (senescent leaves spec. 2) is in-

Table 5.4: Parameter combinations compiled from Table 5.2 (see Section 5.3.3) and linear regression statistics for G93 and averaged predictions of all single data set simulations (type-ii, $N = 30$, squared Pearson correlation coefficient r^2 , slope and intercept of the regression line a and b , root of mean squared error RMSE, rank of RMSE of all combinations including G93 output, and significance $P(r_{G93})$, that r for a given parameter combination is taken from the same distribution than r_{G93} , \rightarrow Fisher's z transformation of the correlation coefficient in Press (1997)).

No.	Parameters	r^2	a^\dagger	b^\dagger	RMSE †	rank	$P(r_{G93})$
G93	Q_{PAR}, T_s	0.88	0.95	5.7	17.3	24	-
01	Q_{PAR}, T_s	0.92	0.92	3.1	14.0	19	0.072
02	$Q_{PAR}, T_s, \bar{c}_{O3}$	0.93	0.94	2.6	12.6	12	0.018
03	Q_{PAR}, T_s, D_a	0.93	0.93	2.6	13.0	16	0.017
04	Q_{PAR}, T_s, RH	0.92	0.92	3.2	13.2	17	0.026
05	Q_{PAR}, T_s, E	0.94	0.92	2.3	11.9	10	0.001
06	Q_{PAR}, T_s, D_s	0.89	0.89	3.2	15.7	21	0.551
07	Q_{PAR}, T_s, g_s	0.92	0.93	2.8	12.9	14	0.040
08	Q_{PAR}, T_s, A_n	0.95	0.95	1.2	10.0	2	<0.001
09	Q_{PAR}, T_s, c_i	0.93	0.93	1.7	12.5	11	0.006
10	$Q_{PAR}, T_s, \bar{T}_{48}$	0.96	0.93	1.7	10.1	4	<0.001
11	$Q_{PAR}, T_s, \bar{T}_{36}$	0.95	0.97	1.6	10.5	7	<0.001
12	$Q_{PAR}, T_s, \bar{T}_{24}$	0.96	0.94	1.8	10.1	3	<0.001
13	$Q_{PAR}, T_s, \bar{T}_{18}$	0.95	0.97	1.8	9.4	1	<0.001
14	$Q_{PAR}, T_s, \bar{T}_{12}$	0.93	0.92	2.7	12.8	13	0.020
15	Q_{PAR}, T_s, \bar{T}_6	0.92	0.94	3.5	13.4	18	0.025
16	Q_{PAR}, T_s, \bar{T}_3	0.92	0.94	2.5	12.9	15	0.025
17	A_n, g_s, T_s	0.95	0.95	1.7	11.0	9	<0.001
18	A_n, g_s, T_s, c_i	0.95	0.95	1.1	10.2	5	<0.001
19	A_n, g_s, Q_{PAR}	0.90	0.88	1.7	15.4	20	0.469
20	A_n, g_s, Q_{PAR}, c_i	0.88	0.88	1.9	16.8	22	0.914
21	$A_n, g_s, T_s, Q_{PAR}, c_i$	0.94	0.96	0.9	11.0	8	0.001
22	A_n, g_s, E	0.87	0.87	2.7	17.2	23	0.700
23	A_n, g_s, c_i	0.79	0.84	5.2	22.1	25	0.006
24	A_n, g_s, E, c_i, D_s	0.95	0.94	0.9	10.3	6	<0.001

† in units of $\mu\text{g C g}^{-1}\text{h}^{-1}$

creased, whereas it is decreased for C4 (young leaves spec. 2) and C7. This is also a good example to show that an increased number of input parameters does not necessarily result in a better performance of the BPN algorithm (see Section 5.3.3). As shown in Fig. 5.7b, where the averaged rRMSE from the same three selected parameter combinations is plotted against the sample size of the single cases this can be partly attributed to small sample sizes. The large rRMSE value for C3 concurs with only 13 data points in that data set, which is quite a small number, and as sample size increase, the rRMSE decreases.

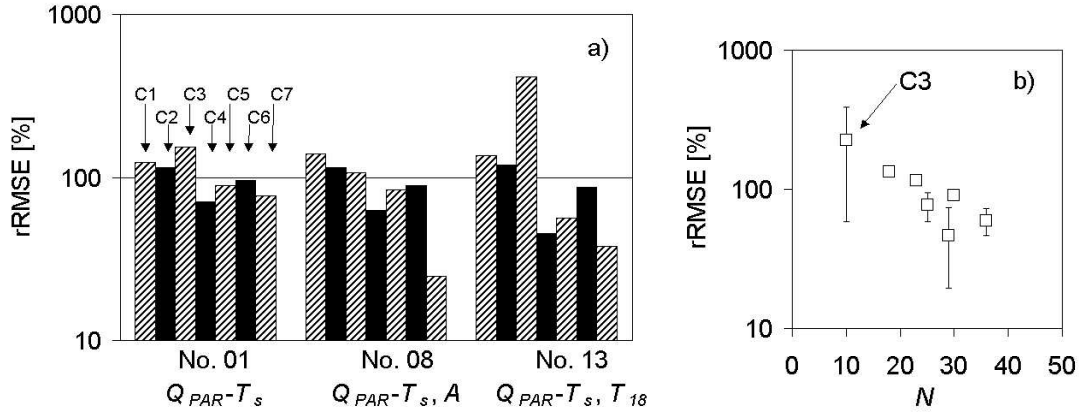


Figure 5.7: Relative performance of selected parameter combinations. a) $rRMSE = RMSE(BPN)/RMSE(G93)$ for three selected parameter combinations. b) mean $rRMSE$ of the three selected parameter combinations versus the sample size of the single time series (single data sets, type-*ii* simulation, see Fig. 5.2).

5.4.3 Aggregated data sets with different parameter combinations

In the following section, G93 and the BPN are applied to VOC emissions related to aggregated data sets (from the different groups $A^U - F^U$). Here, the sample size is in general higher (see Fig. 5.2). Fig. 5.8 shows the relative RMSE ($rRMSE$) for all parameter combinations (No.*k*) derived from mean values for all sets $A^U - F^U$, whereas Fig. 5.9 compares the distribution of $rRMSE$ and r^2 obtained with No.1-24 for each aggregation set $A^U - F^U$. Both, area and mass based emission rates, are used for the aggregation to account for variations of specific leaf weights (Table 5.1). Fig. 5.8 shows that the reference parameter combination No.1 with $rRMSE$ values of about 90% performs only slightly better than G93. In contrast, the regression improves for most parameter combinations on average by 40% and more, for some physiological combinations even more than 50%, with the exception of No.23 and No.15-16. No clear differences between area and mass based aggregation of emission rates are found, although most of the physiological and environmental combinations perform better with area based emission rates, whereas the environmental combinations including temperature history perform better with mass based emission rates. Concerning temperature history (No.10-16), a clear trend can be observed. Using an increasing averaging period from 3-36h, respectively, the $rRMSE$ of the network decreases from 79% to 45% for the mass based emission rates, which gives a 50% reduction of the unexplained variance. This optimal averaging period for ambient temperature is somewhat longer than for single data sets. For comparison, Geron et al. (2000) found optimal length of about 18-24h for the upper crown of a white oak during summer months,

and Petron et al. (2001) a period of a few days to weeks for bur oak investigated in growth chambers.

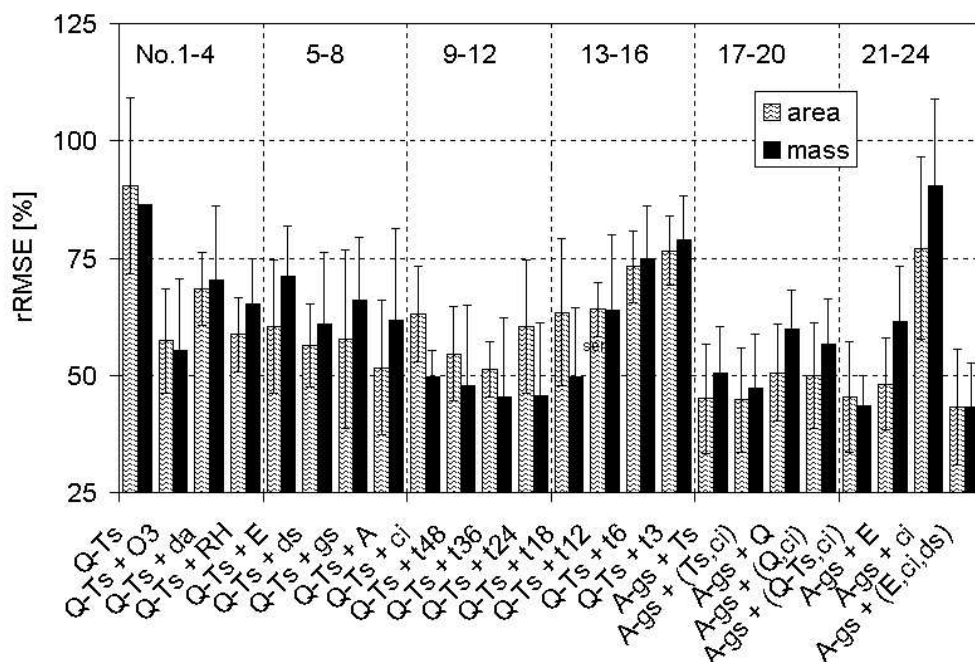


Figure 5.8: Relative performance of all parameter combinations applied to aggregation data sets (type-*iii* simulation, see Fig. 5.2). Mean and standard deviation of rRMSE for aggregations $A^U - F^U$ and parameter combinations No.1-24 (see Fig. 5.2).

As indicated by r^2 values shown in Fig. 5.9, the G93 approach performs best on aggregated sets from mature leaves (A^U , B^U , D^U). The other sets joining data from different development stages (C^U , E^U , F^U) show in general a large difference between the performance of G93 and the BPN with different parameter combinations. The results demonstrate the limitations of a simple light and temperature regression as performed with the BPN technique using No.1 and the G93 algorithm. Only less than 50% of the observed variance of emission rates can be explained with these approaches. A detailed comparison of the results derived for the “simple” aggregation A^U (monoterpene emitter, mature leaves during wet and dry season, mass based aggregation) and the most complex aggregation F^U (two isoprene emitters, one shade adapted species: mature leaves during dry season, and one sun adapted species: mature leaves during wet and dry season, young and senescent leaves during the dry season, area based aggregation) is shown in Table 5.5. For A^U , regression results for G93 and parameter combination No.1 are reasonable good with $r^2 \approx 0.8$, although the rank value

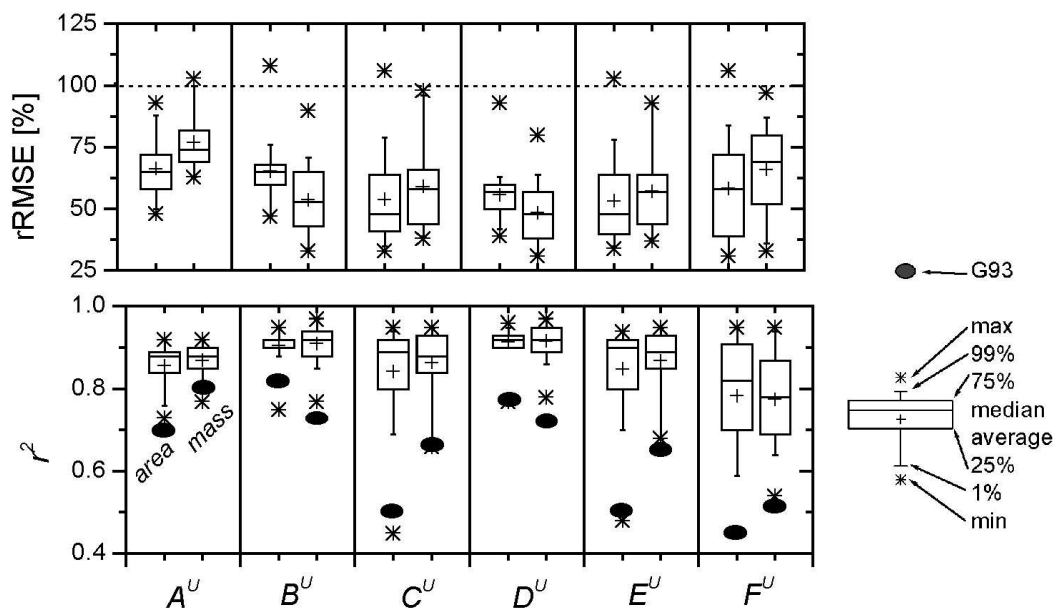


Figure 5.9: Comparison of the performance of G93 and the BPN approach for the aggregation data set. r^2 and rRMSE distribution of all parameter combinations for aggregation sets $A^U - F^U$ listed as part of Fig. 5.2 (type-iii simulations). The left and right box of each field show values derived from area and mass based emission rates, respectively.

indicates that this value is improved by nearly all other parameter combinations. By using the environmental parameter combinations (No.2-9) and the combinations including information on temperature history (No.10-16), rRMSE can be reduced by about 15-30%. The variance that can not be explained by G93 and No.1 ($1 - r^2$) is reduced by 25-50% (except for parameter combinations No.5 and No.7 including transpiration and stomatal conductance, respectively). For the physiological combinations (No.17-24), rRMSE is reduced by 25-30% and the unexplained variance is reduced by 50-75% (except for No.23). For the complex set F^U , even larger differences between G93 and the BPN with No.1 and higher parameter combinations are found. The G93 algorithm and No.1 fail by about one order of magnitude, which reflects the wide range of standard emission factor values derived for the single sets that are included in this aggregation (from 0.7 for C1 to $111.5 \mu\text{g C m}^{-2} \text{ s}^{-1}$ for C7, see Table 5.1). Compared to that, more than half of the parameter combinations show a highly significant improvement of predicted VOC emission with increasing r^2 from about 0.44 and 0.36 for G93 and No.1, respectively, to values > 0.9 which are only obtained with combinations including net assimilation. For the physiological combinations No.17-24 (except No.23), the performance compared to the single set simulation (type-ii) is not

Table 5.5: Linear regression statistics as shown in Table 5.4 for type-*iii* simulation and the two aggregated sets A^U (with mass based emission rates) and F^U (with area based emission rates) according to Fig. 5.2.

No.	A^U : mass based						F^U : area based					
	r^2	a^\dagger	b^\dagger	rRMSE	rank	$P(r_{g93})$	r^2	a^\dagger	b^\dagger	rRMSE	rank	$P(r_{g93})$
G93	0.79	0.79	0.45	100	24	-	0.44	0.44	7.65	100	24	-
01	0.79	0.81	0.28	98	22	0.956	0.36	0.35	6.91	106	25	0.449
02	0.90	0.89	0.17	69	7	0.061	0.70	0.65	3.02	72	18	0.001
03	0.88	0.87	0.19	75	14	0.151	0.63	0.61	3.37	80	21	0.0241
04	0.88	0.86	0.20	74	13	0.127	0.76	0.75	2.30	65	15	<0.001
05	0.79	0.80	0.30	100	23	0.964	0.84	0.84	1.42	53	9	<0.001
06	0.87	0.86	0.23	76	16	0.172	0.83	0.81	1.52	55	10	<0.001
07	0.81	0.84	0.28	94	21	0.789	0.82	0.76	3.18	57	12	<0.001
08	0.90	0.89	0.08	69	8	0.060	0.92	0.91	0.74	37	5	<0.001
09	0.85	0.86	0.16	83	19	0.351	0.82	0.82	1.71	56	11	<0.001
10	0.89	0.87	0.18	71	10	0.079	0.70	0.66	2.79	72	17	<0.001
11	0.90	0.89	0.17	68	5	0.050	0.81	0.78	2.08	58	13	<0.001
12	0.89	0.87	0.19	72	11	0.091	0.72	0.70	3.11	70	16	<0.001
13	0.88	0.87	0.16	73	12	0.116	0.67	0.64	4.01	76	20	0.0054
14	0.86	0.85	0.22	80	17	0.266	0.70	0.66	3.32	73	19	0.0012
15	0.85	0.85	0.22	82	18	0.326	0.59	0.57	4.32	84	23	0.0766
16	0.84	0.85	0.21	86	20	0.444	0.62	0.58	3.90	81	22	0.0275
17	0.90	0.90	0.08	70	9	0.064	0.95	0.91	0.47	31	2	<0.001
18	0.92	0.90	0.06	63	1	0.015	0.94	0.93	0.28	32	3	<0.001
19	0.88	0.87	0.12	75	15	0.147	0.91	0.91	0.48	40	8	<0.001
20	0.90	0.88	0.12	67	4	0.042	0.91	0.91	0.52	39	7	<0.001
21	0.91	0.90	0.09	67	3	0.038	0.94	0.92	0.42	34	4	<0.001
22	0.90	0.88	0.08	69	6	0.047	0.92	0.89	1.30	38	6	<0.001
23	0.77	0.78	0.37	103	25	0.831	0.80	0.80	2.21	59	14	<0.001
24	0.92	0.91	0.07	63	2	0.018	0.95	0.93	0.42	31	1	<0.001

† in units of $\mu\text{g C g}^{-1}\text{h}^{-1}$

even reduced, which indicates a strong link of these parameters with the observed wide-range variability of emission behavior. The results for the included ozone parameter (parameter combination No.2, see Table 5.4 and 5.5) should not be over-interpreted, because the air stream entering the cuvette systems was partly scrubbed out of ozone (Kuhn et al., 2002a). Nevertheless, they show in general a good performance and even a significant improvement for set F^U compared to combination No.1. Possibly this results from the fact, that ozone concentration reflects an integrative environmental parameter that is influenced by many different processes and/or triggers a physiological response of the whole tree.

A comparison of the predicted time series of the two aggregated sets A^U and F^U modeled with G93 and the BPN using the physiological combination No.24 is shown in Fig. 5.10. As already mentioned above, the G93 results are best for A^U , where diurnal courses of VOC emission for the two wet and dry season periods are matched reasonably well, although wet season emission rates

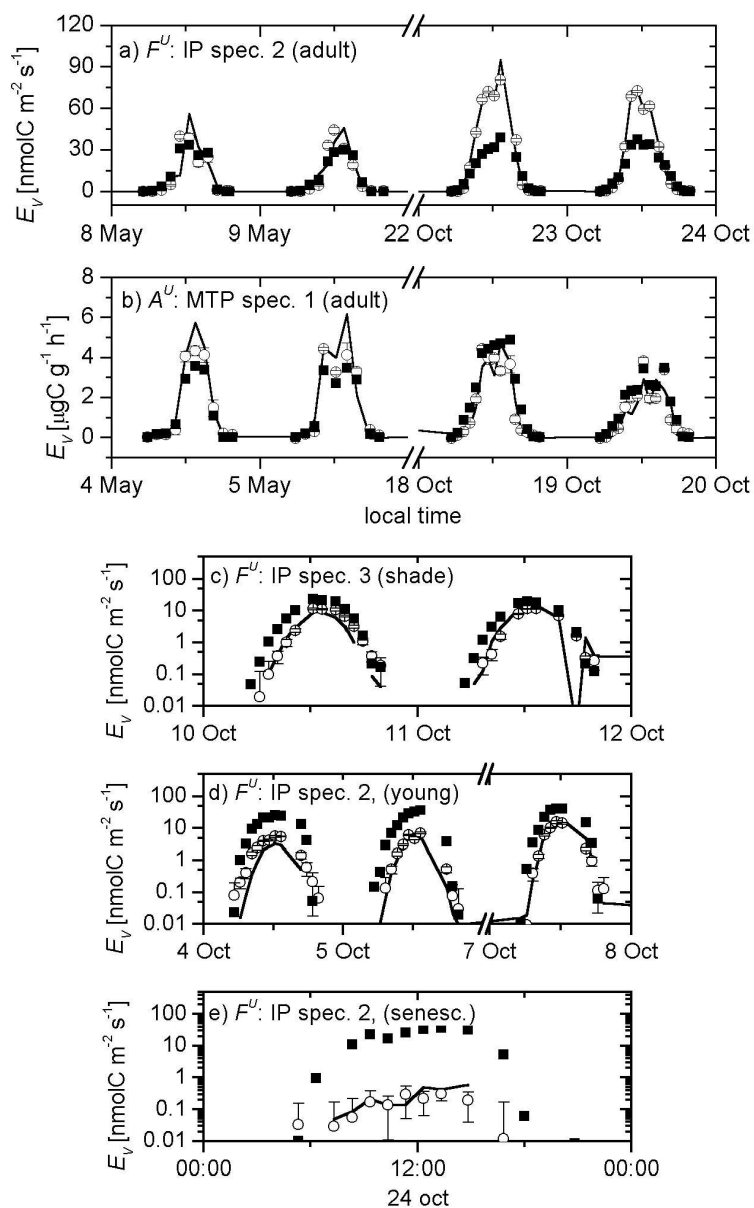


Figure 5.10: Comparison of observed and modeled VOC emission rates (solid lines = measurements, filled quarters=G93 results, open circles = BPN results) for aggregation data sets (type-*iii* simulation, a,c,d,e: area based emission rates for F^U ; b: mass based emission rates for A^U ; see Fig. 5.2). BPN predictions are averaged results from 30 repetitions with parameter combination No.24 (using A_n , g_s , E , c_i and D_s , see Table 5.5).

are slightly underestimated. In the complex isoprene emitter aggregation F^U , G93 matches only spec. 2 for the wet season data. The other subsets are strongly

under- (right side Fig. 5.10a) or overestimated (Fig. 5.10c-e). In contrast, the BPN simulation matches the different emission patterns of the single data sets nearly perfect, when the physiological parameters of combination No.24 are used, e.g. the very low emissions of senescent leaves (species 2, Fig. 5.10e) with values $< 1 \text{ nmol C m}^{-2} \text{ s}^{-1}$ compared to the high emissions of mature leaves of the same species during the dry season (Fig. 5.10a) with values $> 60 \text{ nmol C m}^{-2} \text{ s}^{-1}$. To display the different magnitudes of measurements and model results, Fig. 5.10c-e are on logarithmic scale.

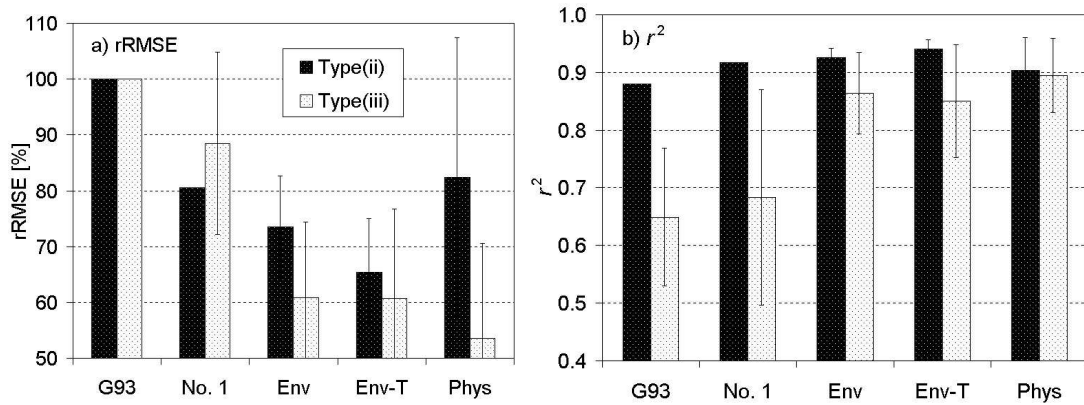


Figure 5.11: Relative performance of different parameter combination types compared to G93 for type-*ii* and type-*iii* simulation. Mean and standard deviation of a) rRMSE and b) r^2 for single (type-*ii*) and aggregation data sets (type-*iii*) from all parameter combination types classified as environmental (ENV, No.2-9, with Q_{PAR}, T_s), environmental plus temperature history (ENV-T, No.10-16, with Q_{PAR}, T_s, \bar{T}_x), and physiological combinations (PHYS, No.17-24, with A_n, g_s).

To get a general picture of different parameter combination types, regression results for rRMSE and r^2 are averaged according to environmental (No.2-9, with Q_{PAR}, T_s), environmental plus temperature history (No.10-16, with Q_{PAR}, T_s, \bar{T}_x), and physiological parameter combinations (No.17-24, with A_n, g_s). Fig. 5.11 shows a comparison for the results obtained with the single (type-*ii*) and the aggregation data (simulation type-*iii*). Compared to G93 and No.1, the single set simulations perform better when other environmental parameters like water pressure deficit or relative humidity (rRMSE \approx 75%), and information of the temperature history (rRMSE \approx 65%) are included. The explained variance increases close to 100%. On the other hand, the significance of these improvements is small since G93 is already close to optimal performance. Moreover, it is not possible to make a generalization of these improvements because they are smaller than the variability between single data sets (see Fig. 5.7). For the simulations with the aggregated sets this is different. Compared to G93 and parameter combination No.1, the unexplained variance can be decreased significantly by about 50% with

environmental and on average 70% with physiological parameter combinations for all sets $A^U - F^U$. Evidently, it is not possible to explain the high degree of variance as observed in the aggregated data sets with light and leaf temperature variability alone. Obviously, there are strong relationships between the developmental stage of individual leaves and the amount of isoprene that is emitted. The results for the physiological parameter combinations confirm also a strong, quantifiable link between VOC and leaf physiological parameters.

5.5 Conclusions

When the G93 model predictors (parameter combination No. 1, leaf temperature and light) are used for the BPN approach, the modeled VOC emission rates are not significantly better compared to G93, indicating an optimal parameterization of the light and temperature response of the algorithm. Nevertheless, the unexplained variance can be reduced to less than 50% by adding other parameters to the regression for single data sets simulations. Especially the inclusion of assimilation or temperature history of the last 18-24h preceding the VOC measurement show highly significant results. Although these improvements are significant, they have to be confirmed with larger data sets, since measurement errors are large compared to data sample size. The hypothesis, that physiological parameters could be more robust predictors of VOC emissions is confirmed by applying the regression analysis to aggregations of the single data sets. In particular, the variability of the most complex aggregation set including emission rates from different season, species, developmental stage, and light environment can only be poorly explained by light and leaf temperature variations. With additional environmental information like the averaged temperature over the last 36 hours, the unexplained variance decreases by more than 60%. An excellent approximation of observed values is achieved with physiological parameter combinations showing the same performance for single and aggregated data sets (best $r^2 = 0.95$) and reducing the unexplained variance by more than 90% compared to G93 and No.1. The network obviously extracts and generalizes relationships between the physiological state and activity of the leaves and their VOC emission variability. Up to now, the mechanistic models mentioned in Section 5.1 require too many parameters, which are not routinely available in field experiments. As a consequence, the G93 algorithm is still the first choice for most applications because of its simplicity. However, the present study demonstrates the great advantage of an indirect approach linking the emission of VOC's to carbon dioxide and water exchange. It is quantitatively shown that the developmental change of leaf area based VOC emission rates scales well with CO_2 primary exchange (see also Kuhn et al. 2004). The presented analysis could also be extended to a larger database containing a wide range of VOC emission and leaf gas exchange data sets. The trained network could then be coupled to a canopy model (Chapter 4),

which includes the calculation of CO₂ and H₂O leaf gas exchange. As a result, VOC emission would scale indirectly with the leaf physiological parameters giving an alternative framework for up-scaling exercises.

Chapter 6

Summary and main findings

Approach The present dissertation focuses on the biogeochemistry of the vegetation layer (canopy) and feedbacks between physiological and environmental processes affecting the climate and chemistry of the lower atmosphere. A detailed one-dimensional multi-layer model of energy and trace gas exchange between the canopy and the atmosphere above (surface layer) is developed, including a Lagrangian description of vertical scalar transport within the canopy air space and a coupled solution of leaf photosynthesis and stomatal conductance determining the surface temperature and the partitioning of available energy into sensible heat and water vapor (latent heat). The coupled surface exchange and transport scheme enables the simulation of vertical source/sink distributions as well as scalar concentration profiles. The photosynthetic capacity of single leaves is linked to the light environment and the vertical distribution of leaf area and leaf nitrogen content. The radiation model simulates the energy absorption of sunlit and shaded leaves and the soil in three different wavebands (visible, near-infrared, and long-wave radiation). The model is constrained with micrometeorological quantities measured above the canopy and the temperature and water content of the soil surface.

Surface parameterization Available data sets from different sites in northeast and southwest Amazonia are used to infer and evaluate model key parameters. The inferred parameterizations include a bi-modal vertical leaf area density distribution, normalized profiles of the mean horizontal and the standard deviation of the vertical wind component, the acclimation of photosynthetic capacity, and the soil surface exchange of heat and CO₂. The evaluation includes parameters related to leaf surface exchange (photosynthesis and stomatal conductance) and the partitioning, reflection and attenuation of radiation.

In-canopy transport The vertical transport scheme is evaluated by comparing observed and predicted mean day- and nighttime vertical profiles of ^{222}Rn activity concentration, which is an inert trace gas emitted by all natural soils (forward problem). Additionally, the transport model is applied in inverse mode to predict the vertical source/sink distributions of CO_2 and H_2O . The resulting values are integrated to the canopy level and compared to net flux measurements.

The forward predicted concentration of ^{222}Rn prove the derived implementation of the transport model. A new approach is derived to quantify the uncertainties of the inverse method in relation to uncertainties of the input concentration profiles. For nighttime conditions, a modified turbulence parameterization is proposed: It could be shown by comparison of observed and simulated dispersion of ^{222}Rn , that nighttime free convection within the lower canopy has to be taken into consideration. Otherwise, ^{222}Rn activity concentrations near the ground are overestimated by approximately two orders of magnitude. Compared to earlier estimates of mean canopy residence time, much lower values less than hour for nighttime conditions have been derived for the investigated site which should be considered in modeling studies.

Canopy model application The derived model parameterization and surface description is evaluated and applied to a rain forest site in Rondônia, southwest Amazonia. Simulated net fluxes and concentration profiles of sensible heat, H_2O , CO_2 , isoprene and ozone for late wet and late dry season conditions are compared to observations during two intensive field campaigns in 1999. Realistic temperature gradients up to 5°C and 1°C between the leaf surface and ambient air and between the canopy air and the surface layer above, respectively, are calculated by the model for typical conditions at noon time. The predicted day- and nighttime stratification of the lower canopy is consistent with observations in dense vegetations showing reversely to the atmospheric boundary layer above positive (stable) temperature gradients with height during the day and negative (unstable) temperature gradients during the night.

In contrast to the parameters related to canopy structure and radiation attenuation, the predicted net fluxes of energy and CO_2 have a high sensitivity to physiological parameters for stomatal conductance and leaf photosynthesis. Assuming leaf physiological changes with higher stomatal conductances and lower leaf photosynthesis for wet and dry season conditions, respectively, results in a very good agreement between observed and predicted canopy fluxes and concentration profiles. The integrated net carbon sink ranges between 2.5 and 1 t C $\text{ha}^{-1} \text{yr}^{-1}$ and the corresponding midday bowen ratio from 0.5 to 0.8 for wet and dry season conditions, respectively.

The predicted dry season net fluxes of ozone showed also a good agreement with the observations. The observed ozone deposition velocities of the wet season exceed those of the dry season by 150-250%, which may not be explained by

realistic physiological changes, nor by changes of canopy structure but in contrast by an additional cuticular uptake mechanism, possibly on wetted surfaces. A comparison of observed and predicted isoprene concentrations within the canopy suggests a reduction of isoprene emission capacity for shade adapted leaves and, additionally, isoprene uptake by the soil which would reduce the regional estimate for Amazonia and global estimate for tropical rain forest by approximately 30%.

Physiological links of VOC emission In a detailed sensitivity study, the VOC emissions from three Amazonian tree species are related to environmental and leaf physiological parameters using a neuronal approach. The performance of individual parameter combinations serving as predictors of leaf VOC emission is compared to predictions of the quasi-standard algorithm for isoprene emission (G93).

When the G93 algorithm and the neuronal network using temperature and light as predictors are calibrated with single data sets (same plant and developmental stage, same season), a high prediction accuracy is obtained ($r^2 \approx 0.9$). However, the network performance is similar or even better for most of the other 23 applied parameter combinations.

When G93 and the neuronal network using temperature and light as predictors are calibrated with aggregated data sets (different developmental stage, season, species and/or light environment), the linear correlation with observations is relatively poor due to the large observed variability of emission capacities.

More than 50% of the unexplained variances ($1-r^2$) can be explained by adding information on temperature history to the network input, with an optimal averaging period of 36 hours, which is consistent with earlier findings. An even better performance is reached with physiological parameter combinations reducing the unexplained variance to less than 10%. The obtained results underline a strong link between VOC emission and leaf physiology, which should be implemented into emission models.

Closing remarks The presented model of vertical exchange of energy and trace gases within the Amazon rain forest represents a comprehensive description of surface vegetative properties. It can serve as an ideal substitution and design tool for costly field experiments focusing on in-canopy processes. The large number of parameters required and the high uncertainty of individual parameter values represent the main disadvantages of such a detailed approach. However, the number of required parameters is less compared to existing top-down soil-vegetation-atmosphere transfer (SVAT) schemes designed for the integration into global circulation models. Furthermore, the Amazon basin is relatively uniform in relation to its spatial dimensions and the extensive field research over the last decade delivered many data sets of gas exchange measurements. This data can

be used to infer and evaluate the model components at their own scale e.g. the surface exchange at the leaf scale using enclosure measurements made at a single leaf or branch and the integrated ecosystem net exchange using Eddy Covariance fluxes measured above the canopy as shown in Chapter 2 and 4, respectively.

Bibliography

- Abuelgasim, A. A., Gopal, S., Strahler, A. H., 1998. Forward and inverse modelling of canopy directional reflectance using a neural network. *Int. J. Remote Sens.* 19 (3), 453–471.
- Andreae, M., Crutzen, P., 1997. Atmospheric aerosols: Biogeochemical sources and role in atmospheric chemistry. *Science* 276, 1052–1058.
- Andreae, M. O., Artaxo, P., Brandao, C., Carswell, F. E., Ciccioli, P., da Costa, A. L., Culf, A. D., Esteves, J. L., Gash, J. H. C., Grace, J., Kabat, P., Lelieveld, J., Malhi, Y., Manzi, A. O., Meixner, F. X., Nobre, A. D., Nobre, C., Ruivo, M., Silva-Dias, M. A., Stefani, P., Valentini, R., von Jouanne, J., Waterloo, M. J., 2002. Biogeochemical cycling of carbon, water, energy, trace gases, and aerosols in Amazonia: The LBA-EUSTACH experiments. *J. Geophys. Res.* 107 (D20), 33.1–33.25.
- Araujo, A., Nobre, A., Kruijt, B., Elbers, J., Dallarosa, R., Stefani, P., von Randow, C., Manzi, A., Culf, A., Gash, J., Valentini, R., Kabat, P., 2002. Comparative measurements of carbon dioxide fluxes from two nearby towers in a central Amazonian rainforest: The Manaus LBA site. *J. Geophys. Res.* 107 (D20), 58.1–58.20.
- Bakwin, P., Wofsy, S., Fan, S.-M., Keller, M., Trumbore, S., Da Costa, J., 1990. Emission of nitric oxide (NO) from tropical forest soils and exchange of NO between the forest canopy and atmospheric boundary layers. *J. Geophys. Res.* 95, 16,755–16,764.
- Baldocchi, D., Harley, P., 1995. Scaling carbon dioxide and water vapour exchange from leaf to canopy in a deciduous forest: Model testing and application. *Plant, Cell Env.* 18, 1157–1173.
- Baldocchi, D., Hicks, B., Camara, P., 1987. A canopy stomatal-resistance model for gaseous deposition to vegetated surfaces. *Atmos. Environ.* 21 (1), 91–101.

- Baldocchi, D., Meyers, T., 1998. On using eco-physiological, micrometeorological and biogeochemical theory to evaluate carbon dioxide, water vapor and trace gas fluxes over vegetation - a perspective. *Agric. For. Meteorol.* 90 (1-2), 1–25.
- Ball, J., 1987. Calculations related to gas exchange. In: Zeiger, E., Farquhar, G., Cowan, I. (Eds.), *Stomatal Function*. Stanford University Press, Stanford, California, pp. 445–476.
- Ball, J., Woodrow, I., Berry, J., 1987. A model predicting stomatal conductance and its contribution to the control of photosynthesis under different environmental conditions. In: Biggins, I. (Ed.), *Progress in Photosynthesis Research*. Martinus Nijhoff, Netherlands, pp. 221–224.
- Bertin, N., Staudt, M., Hansen, U., Seufert, G., Ciccioli, P., Foster, P., Fugit, J. L., Torres, L., 1997. Diurnal and seasonal course of monoterpene emissions from *Quercus ilex* (L.) under natural conditions - applications of light and temperature algorithms. *Atmos. Environ.* 31 (Suppl 1), 135–144.
- Bishop, M., 1995. *Neural Networks for Pattern Recognition*. Clarendon Press, Oxford, UK.
- Bosveld, F., Holtslag, A., Van den Hurk, B., 1999a. Interpretation of crown radiation temperatures of a dense douglas fir forest with similarity theory. *Bound.-Layer Meteorol.* 92, 429–451.
- Bosveld, F., Holtslag, A., Van den Hurk, B., 1999b. Nighttime convection in the interior of a dense douglas forest. *Bound.-Layer Meteorol.* 93, 171–195.
- Brooks, A., Farquhar, G., 1985. Effect of temperature on the CO₂/O₂ specificity of ribulose-1,5-bisphosphate carboxylase/oxygenase and the rate of respiration in the light. Estimates from gas-exchange measurements on spinach. *Planta* 165, 397–406.
- Brutsaert, W., 1975. On a derivable formula for long-wave radiation for clear skies. *Water Resources Res.* 11, 742–744.
- Butterweck, G., Reineking, A., Kesten, J., Porstendörfer, J., 1994. The use of the natural radioactive noble gases radon and thoron as tracers for the study of turbulent exchange in the atmospheric boundary layer - Case study in and above a wheat field. *Atmos. Environ.* 28 (12), 1963–1969.
- Caemmerer, S. v., Farquhar, G. D., 1981. Some relationships between the biochemistry of photosynthesis and the gas exchange of leaves. *Planta* 153, 376–387.

- Carswell, F., Costa, A., Palhete, M., Mahli, Y., Meir, P., Costa, d. P., Ruivo, M. d. L., Leal, L. d. D., Costa, J., Clement, R., Grace, J., 2002. Seasonality in CO₂ and H₂O flux at eastern Amazonian rain forest. *J. Geophys. Res.* 107 (D20), 43.1–43.16.
- Carswell, F., Meir, P., Wandell, E., Bonates, L., Kruijt, B., Barbosa, E., Nobre, A., Grace, J., Jarvis, P., 2000. Photoynthetic capacity in a central Amazonian rain forest. *Tree Physiol.* 20, 179–186.
- Chameides, W., 1987. Acid dew and the role of chemistry in the dry deposition of reactive gases to wetted surfaces. *J. Geophys. Res.* 92, 11895–11908.
- Chameides, W., 1989. The chemistry of ozone deposition to plant leaves: role of ascorbic acid. *Env. Sci. Technol.* 23, 595–600.
- Cleveland, C. C., Yavitt, J. B., 1997. Consumption of atmospheric isoprene in soil. *Geophys. Res. Lett.* 24 (19), 2379–2382.
- Cleveland, C. C., Yavitt, J. B., 1998. Microbial consumption of atmospheric isoprene in a temperate forest soil. *Appl. Env. Microbiol.* 64 (1), 172–177.
- Collatz, G., Ribbas-Carbo, M., Berry, J., 1992. Coupled photosynthesis-stomatal conductance model for leaves of C₄ plants. *Aust. J. Plant Physiol.* 54, 107–136.
- Coppin, P. A., Raupach, M. R., Legg, B. J., 1986. Experiments on scalar dispersion within a model plant canopy, part ii: an elevated plane source. *Bound.-Layer Meteorol.* 35, 21–52.
- Crutzen, P., Lawrence, M., Pöschl, U., 1999. On the background photochemistry of tropospheric ozone. *Tellus* 51 (A-B), 123–146.
- Culf, A., Esteves, J. L., Filho, M. O., Rocha, H. d., 1996. Radiation, temperature and humidity over forest and pasture in Amazonia. In: Gash, J., Nobre, C., Roberts, J., Victoria, R. (Eds.), *Amazonian Deforestation and Climate*. John Wiley and Sons, Chichester, pp. 177–191.
- Culf, A., Fisch, G., Hodnett, M., 1995. The albedo of Amazonian forest ranch land. *J. Clim.* 8 (6), 1543–1554.
- Culf, A. D., Fisch, G., Malhi, Y., Costa, R. C., Nobre, A. D., Marques, A. D., Gash, J. H. C., Grace, J., 1999. Carbon dioxide measurements in the nocturnal boundary layer over Amazonian forest. *Hydrol. Earth Sys. Sci.* 3 (1), 39–53.
- Deardorff, J., 1978. Efficient prediction of ground surface temperature and moisture with inclusion of a layer of vegetation. *J. Geophys. Res.* 83 (C4), 1889–1903.

- Denmead, O. T., Raupach, M. R., 1993. Methods for measuring atmospheric gas transport in agricultural and forest systems. ASA Spec. Pub. 55, 19–43.
- Denmead, O. T., Harper, L. A., Sharpe, R. R., 2000. Identifying sources and sinks of scalars in a corn canopy with inverse Lagrangian dispersion analysis. I: Heat. Agric. For. Meteorol. 104 (1), 67–73.
- Dickinson, R. E., Henderson-Sellers, A., Kennedy, P., August 1993. Biosphere-atmosphere transfer scheme (BATS) version 1e as coupled to the NCAR community climate model. NCAR Technical Note 387, NCAR.
- Dutot, A.-L., Rude, J., Aumont, B., 2003. Neural network method to estimate the aqueous rate constants for the OH reactions with organic compounds. Atmos. Environ. 37, 269–276.
- Ehleringer, J. R., Field, C. B. (Eds.), 1993. Scaling Physiological Processes Leaf to Globe. Academic Press, San Diego - London.
- Eschenbach, C., Kappen, L., 1996. Leaf area index determination in an alder forest - a comparison of three methods. J. Exp. Bot. 47 (302), 1457–1462.
- Evans, J., 1989. Photosynthesis and nitrogen relationships in leaves of C₃ plants. Oecologia 78, 9–19.
- Falge, E., Tenhunen, J., Baldocchi, D., Aubinet, M., Bakwin, P., Berbigier, P., Bernhofer, C., Bonnefond, J. M., Burba, G., Clement, R., Davis, K. J., Elbers, J. A., Falk, M., Goldstein, A. H., Grelle, A., Granier, A., Grunwald, T., Gudmundsson, J., Hollinger, D., Janssens, I. A., Keronen, P., Kowalski, A. S., Katul, G., Law, B. E., Malhi, Y., et al., 2002. Phase and amplitude of ecosystem carbon release and uptake potentials as derived from Fluxnet measurements. Agric. For. Meteorol. 113 (1-4), 75–95.
- Fall, R., Wildermuth, M. C., 1998. Isoprene synthase - from biochemical mechanism to emission algorithm. J. Geophys. Res. 103 (D19), 25599–25609.
- Fan, S.-M., Wofsy, S., Bakwin, P., Jacob, D., Fitzjarrald, D., 1990. Atmosphere-biosphere exchange of CO₂ and O₃ in the central Amazon forest. J. Geophys. Res. 95, 16,851–16,864.
- Farman, J., Gardiner, B., Shanklin, J., 1985. Large losses of total ozone in antarctica reveal seasonal ClO_x/NO_x interaction. Nature 315, 207–210.
- Farquhar, G., Wong, S., 1984. An empirical model of stomatal conductance. Aust. J. Plant Physiol. 11, 191–120.
- Farquhar, G. D., Caemmerer, S. v., Berry, J., 1980. A biochemical model of photosynthetic CO₂ assimilation in leaves of C₃-species. Planta 149, 78–90.

- Field, C., 1983. Allocating leaf nitrogen for the maximization of carbon gain: Leaf age as a control on the allocation program. *Oecologia* 56, 341–347.
- Field, C., Mooney, H., 1986. The photosynthesis-nitrogen relationship in wild plants. In: Givnish, T. (Ed.), *On the Economy of Plant Form and Function*. Cambridge University Press, pp. 25–55.
- Finnigan, J. J., Raupach, M. R., 1987. Transfer processes in plant canopies in relation to stomatal characteristics. In: Zeiger, E., Farquhar, G., Cowan, I. (Eds.), *Stomatal Function*. Stanford University Press, Stanford, California, pp. 385–427.
- Fischbach, R. J., Staudt, M., Zimmer, I., Rambal, S., Schnitzler, J. P., 2002. Seasonal pattern of monoterpene synthase activities in leaves of the evergreen tree *Quercus ilex*. *Physiol. Plant.* 114 (3), 354–360.
- Fuentes, J., Gillespie, T., Hartog, G. d., Neumann, H., 1992. Ozone deposition onto a deciduous forest during dry and wet conditions. *Agric. For. Meteorol.* 62, 1–18.
- Ganzeveld, L., Lelieveld, J., 1995. Dry deposition parameterization in a chemistry general circulation model and its influence on the distribution of reactive trace gases. *J. Geophys. Res.* 100 (D10), 20999–21012.
- Ganzeveld, L., Lelieveld, J., 2002. Atmosphere-biosphere trace gas exchange simulated with a single-column model. *J. Geophys. Res.* 107 (D16), 8.1–8.21.
- Gardner, M., Dorling, S., 1998. Artificial neural networks (the multi-layer perceptron) - a review of applications in the atmospheric sciences. *Atmos. Environ.* 32, 2627–2636.
- Garrat, J., 1992. *The Atmospheric Boundary Layer*. Cambridge atmospheric and space science series. Cambridge University Press, Cambridge.
- Gash, J., Nobre, C., Roberts, J., Victoria, R., 1996. An overview of ABRACOS. In: Gash, J., Nobre, C., Roberts, J., Victoria, R. (Eds.), *Amazonian Deforestation and Climate*. John Wiley and Sons, Chichester, pp. 1–14.
- Geron, C., Guenther, A., Greenberg, J., 2002. Biogenic volatile organic compound emissions from a lowland tropical wet forest in Costa Rica. *Atmos. Environ.* 36, 3793–3802.
- Geron, C., Guenther, A., Sharkey, T., Arnts, R. R., 2000. Temporal variability in basal isoprene emission factor. *Tree Physiol.* 20 (12), 799–805.
- Goudriaan, J., van Laar, H., 1994. *Modelling Crop Growth Processes*. Kluwer, Amsterdam.

- Goulden, M., Munger, J., Fan, S.-M., Daube, B., Wofsy, S., 1996. Measurements of carbon sequestration by long-term eddy covariance: Methods and a critical evaluation of accuracy. *Global Change Biol.* 2, 169–182.
- Grace, J., Lloyd, J., McIntyre, J., Miranda, A., Meir, P., Miranda, H., Moncrieff, J., Massheder, J., Wright, I., Gash, J., 1995. Fluxes of carbon dioxide and water vapour over an undisturbed tropical rain forest in south-west Amazonia. *Glob. Clim. Change* 1, 1–12.
- Grant, R., Kimball, B., Pinter, P., Jr. Wall, G., Garcia, R., La Morte, R., Hunsacker, D., 1995. Carbon dioxide effects on crop energy balance: Testing ecosystems with a free-air CO₂ enrichment (FACE) experiment. *Agron. J.* 87, 446–457.
- Greenberg, J., Guenther, A., Petron, G., Wiedinmyer, C., Vega, O., Gatti, L., Tota, J., Fisch, G., 2004. Biogenic VOC emissions from forested Amazonian landscapes. *Global Change Biol.* 10, 1–12.
- Gu, L. H., Baldocchi, D., 2002. Fluxnet 2000 synthesis - foreword. *Agric. For. Meteorol.* 113 (1-4), 1–2.
- Guenther, A., 1997. Seasonal and spatial variations in the natural volatile organic compound emissions. *Ecol. Appl.* 7 (1), 34–45.
- Guenther, A., Hewitt, C., Erickson, D., Fall, R., Geron, C., Graedel, T., Harley, P., Klinger, L., Lerdau, M., McKay, W., Pierce, T., Scholes, B., Steinbrecher, R., Tallamraju, R., Taylor, J., Zimmerman, P., 1995. A global model of natural volatile organic compound emissions. *J. Geophys. Res.* 100 (D5), 8873–8892.
- Guenther, A., Zimmerman, P., Harley, P., Monson, R., Fall, F., 1993. Isoprene and monoterpene emission rate variability: Model evaluations and sensitivity analysis. *J. Geophys. Res.* 98 (D7), 12,609–12,617.
- Gut, A., Scheibe, M., Rottenberger, S., Rummel, U., Welling, M., Ammann, C., Kirkman, G., Kuhn, U., Meixner, F., Kesselmeier, J., Lehmann, B., Schmidt, J., Müller, E., Piedade, M., 2002a. Exchange of NO₂ and O₃ at soil and leaf surfaces in an Amazonian rain forest. *J. Geophys. Res.* 107 (D20), 27.1–27.15.
- Gut, A., van Dijk, S., Scheibe, M., Rummel, U., Welling, M., Ammann, C., Meixner, F., Kirkman, G., Andreae, M., Lehmann, B., 2002b. NO emission from an Amazonian rain forest soil: Continuous measurements of NO flux and soil concentration. *J. Geophys. Res.* 102 (D20), 24.1–24.10.
- Hanson, D. T., Sharkey, T. D., 2001a. Effect of growth conditions on isoprene emission and other thermotolerance-enhancing compounds. *Plant, Cell Env.* 24 (9), 929–936.

- Hanson, D. T., Sharkey, T. D., 2001b. Rate of acclimation of the capacity for isoprene emission in response to light and temperature. *Plant, Cell Env.* 24 (9), 937–946.
- Harley, P., Litvak, M., Sharkey, T. D., Monson, R., 1994. Isoprene emission from velvet bean leaves. Interactions among nitrogen availability, growth photon flux density, and leaf development. *Plant Physiolog.* 105, 279–285.
- Harley, P., Thomas, R., Reynolds, J., Strain, B., 1992. Modelling photosynthesis of cotton grown in elevated CO₂. *Plant, Cell Env.* 15 (271-282).
- Harley, P., Vasconcellos, P., Vierling, L., Pinheiros, C. C. de S., Greenberg, J., Guenther, A., Klinger, L., Almeida, S. S. de, Neill, D., Baker, T., Philipps, O., Mahli, Y., 2004. Variation in potential for isoprene emissions among neotropical forest sites. *Global Change Biol.* 10, 1–21.
- Harley, P. C., Monson, R. K., Lerdau, M. T., 1999. Ecological and evolutionary aspects of isoprene emission from plants. *Oecologia* 118 (2), 109–123.
- Heiden, A. C., Hoffmann, T., Kahl, J., Kley, D., Klockow, D., Langebartels, C., Mehlhorn, H., Sandermann, H., Schraudner, M., Schuh, G., Wildt, J., 1999. Emission of volatile organic compounds from ozone-exposed plants. *Ecol. Appl.* 9 (4), 1160–1167.
- Hirose, T., Bazzaz, F. A., 1998. Trade-off between light- and nitrogen-use efficiency in canopy photosynthesis. *Ann. Bot.* 82 (2), 195–202.
- Hirose, T., Werger, M., 1987. Nitrogen use efficiency in instantaneous and daily photosynthesis of leaves in the canopy of a *Solidago altissima* stand. *Physiol. Plant.* 70, 215–222.
- Hirose, T., Werger, M., Pons, T., Rheeßen, J. v., 1988. Canopy structure and leaf nitrogen distribution in a stand of *Lysimachia vulgaris* L. as influenced by stand density. *Oecologia* 77 (145-150).
- Hofmann, D., Pyle, J., 1999. Predicting future ozone changes and detection of recovery. In: *Global Ozone Research and Monitoring Project (Ed.), Scientific Assessment of Ozone Depletion: 1998. Vol. Report No. 44.* World Meteorological Organization, Geneva, Switzerland, pp. 12.1–12.57.
- Hornick, K., Stinchcombe, M., White, H., 1989. Multilayer feedforward networks are universal approximators. *Neural Networks* 2, 359–366.
- Hsieh, C., Siqueira, M., Katul, G., Chu, C.-R., 2003. Predicting scalar source-sink and flux distributions within a forest canopy using a 2-D Lagrangian stochastic dispersion model. *Bound.-Layer Meteorol.* 109, 113–138.

- Huntingford, C., Cox, P. M., 1997. Use of statistical and neural network techniques to detect how stomatal conductance responds to changes in the local environment. *Ecol. Model.* 97 (3), 217–246.
- IPCC, 2001. *Climate Change 2001: The Scientific Basis*. Contribution of Working Group 1 to the Third Assessment Report of the Intergovernmental Panel on Climate Change. Cambridge University Press, Cambridge, UK.
- Jacob, D., Bakwin, P., 1991. Cycling of NO_x in tropical forest canopies. In: Rogers, J., Whitman, W. (Eds.), *Microbial Production and Consumption of Greenhouse Gases: Methane, Nitrogen Oxides and Halomethanes*. American Society of Microbiology, pp. 237–253.
- Jacob, D., Wofsy, S., 1990. Budgets of reactive nitrogen, hydrocarbons, and ozone over the Amazon forest during the wet season. *J. Geophys. Res.* 95 (D10), 16,737–16,754.
- Jacobs, A., Van Boxel, J., El-Kilani, R., 1994. Nighttime free convection characteristics within a plant canopy. *Bound.-Layer Meteorol.* 71, 375–391.
- Jarvis, P., 1993. Scaling physiological processes. In: Ehleringer, J. R., Field, C. B. (Eds.), *Scaling Physiological Processes Leaf to Globe*. Academic Press, San Diego - London, pp. 115–126.
- Jarvis, P. G., 1976. The interpretation of variations in leaf water potential and stomatal conductance found in canopies in the field. *Phil. Trans. Roy. Soc. London* 273 (B), 593–610.
- Jones, H., 1992. *Plants and Microclimate: A Quantitative Approach to Plant Physiology*. Cambridge University Press, Cambridge.
- Kaimal, J., Finnigan, J. J., 1994a. *Atmospheric Boundary Layer Flows*. Oxford University Press, New York.
- Kaimal, J., Finnigan, J. J., 1994b. Flow over plant canopies. In: *Atmospheric Boundary Layer Flows*. Oxford University Press, New York, pp. 66–108.
- Kaiser, J., Schmidt, K., 1998. Closing the carbon circle. *Science* 281 (5376), 504.
- Katul, G., Oren, R., Ellsworth, D., Hsieh, C., Phillipps, N., Lewin, K., 1997. A Lagrangian dispersion model for predicting CO_2 sources and sinks, and fluxes in a uniform loblolly pine (*Pinus taeda* L.) stand. *J. Geophys. Res.* 102 (D8), 9309–9321.
- Katul, G. G., Albertson, J. D., 1999. Modeling CO_2 sources, sinks, and fluxes within a forest canopy. *J. Geophys. Res.* 104 (D6), 6081–6091.

- Kesselmeier, J., Bode, K., 1997. Biological knowledge needed for the measurements and interpretation of exchange processes between plants and the atmosphere. In: Helas, G., Slanina, S., Steinbrecher, R. (Eds.), *Biogenic Volatile Organic Compounds in the Atmosphere - Summary of the Present Knowledge*. SPB Academic Publishers, Amsterdam, pp. 9–25.
- Kesselmeier, J., Ciccioli, P., Kuhn, U., Stefani, P., Biesenthal, T., Rottenberger, S., Wolf, A., Vitullo, M., Valentini, R., Nobre, A., Kabat, P., Andreae, M., 2002a. Volatile organic compound emissions in relation to plant carbon fixation and the terrestrial carbon budget. *Global Biogeochem. Cycles* 16 (4), 73.1–73.9.
- Kesselmeier, J., Kuhn, U., Rottenberger, S., Biesenthal, T., Wolf, A., Schebeske, G., Andreae, M., Ciccioli, P., Brancaleoni, E., Frattoni, M., Oliva, S., Botelho, M., Silva, C., Tavares, T., 2002b. Concentrations and species composition of atmospheric volatile organic compounds (VOC) as observed during wet and dry season in Rondônia (Amazonia). *J. Geophys. Res.* 10.1029 (2000JD000267).
- Kesselmeier, J., Staudt, M., 1999. Biogenic volatile organic compounds (VOC): An overview on emission, physiology and ecology (review). *J. Atmos. Chem.* 33 (1), 23–88.
- Klinge, H., 1973. Struktur und Artenreichtum des zentralamazonischen Regenwaldes. *Amazoniana* 4, 283–292.
- Klinge, H., Rodrigues, W., Brunig, E., Fittkau, E., 1975. Biomass and structure in a central Amazonian rain forest. In: Golley, F., Medina, E. (Eds.), *Tropical Ecological Systems. Trends in Terrestrial and Aquatic Research*. Springer, Berlin, pp. 115–122.
- Kruijt, B., Lloyd, J., Grace, J., MacIntyre, J., Farquhar, G., Miranda, A., McCracken, P., 1996. Sources and sinks of CO₂ in Rondônia tropical rainforest. In: Gash, J., Nobre, C., Robers, J., Victoria, R. (Eds.), *Amazonian Deforestation and Climate*. John Wiley, Chichester, pp. 331–351.
- Kruijt, B., Malhi, Y., Lloyd, J., Nobre, A., Miranda, A., Pereira, M., Culf, A., Grace, J., 2000. Turbulence statistics above and within two Amazon rain forest canopies. *Bound.-Layer Meteorol.* 94, 297–331.
- Kuhn, U., Rottenberger, S., Biesenthal, T., Ammann, C., Wolf, A., Schebeske, G., Ciccioli, P., Branaleoni, E., Frattoni, M., Tavares, T., Kesselmeier, J., 2002a. Isoprene and monoterpene emissions of Amazonian tree species during the wet season: Direct and indirect investigations on controlling environmental functions. *J. Geophys. Res.* 107 (D20), 38.1–38.13.
- Kuhn, U., Rottenberger, S., Biesenthal, T., Ammann, C., Wolf, A., Schebeske, G., Oliva, S., Tavares, T., Kesselmeier, J., 2002b. Exchange of short-chained

- monocarboxylic acids by vegetation at a remote tropical forest site in Amazonia. *J. Geophys. Res.* 107 (D20), 36.1–36.18.
- Kuhn, U., Rottenberger, S., Biesenthal, T., Wolf, A., Schebeske, G., Ciccioli, P., Branaleoni, E., Frattoni, M., Tavares, T., Kesselmeier, J., 2004. Seasonal differences in isoprene and light-dependent monoterpene emission by Amazonian tree species. *Global Change Biol.* 10, 663–682.
- Kuzma, J., Fall, R., 1993. Leaf isoprene emission rate is dependent on leaf development and the level of isoprene synthase. *Tree Physiol.* 101, 435–440.
- Laurance, W. F., 2000. Mega-development trends in the Amazon: Implications for global change. *Env. Monit. Assessment* 61 (1), 113–122.
- Legg, B. J., Raupach, M. R., Coppin, P. A., 1986. Experiments on scalar dispersion within a model plant canopy, part iii: an elevated line source. *Bound.-Layer Meteorol.* 35, 277–302.
- Lehmann, B., Ihly, B., Salzmann, S., Conen, F., Simon, E., 2004. An automatic chamber for continuous ^{220}Rn and ^{222}Rn flux measurements from soil. *Radiation Meas.* 38, 43–50.
- Lehmann, B., Lehmann, M., 2000. Radon-222 monitoring of soil diffusivity. *Geophys. Res. Lett.* 27 (23), 3917–3920.
- Lehmann, B., Lehmann, M., Gut, A., Neftel, A., 1999. Radon-220 calibration of near-surface turbulent gas transport. *Geophys. Res. Lett.* 26 (5), 607–610.
- Lek, S., Guegan, J. F., 1999. Artificial neural networks as a tool in ecological modelling, an introduction. *Ecol. Model.* 120 (2-3), 65–73.
- Lelieveld, J., Dentener, F., 2000. What controls tropospheric ozone? *J. Geophys. Res.* 105, 3531–3551.
- Lerdau, M. T., Throop, H. L., 1999. Isoprene emission and photosynthesis in a tropical forest canopy: Implications for model development. *Ecol. Appl.* 9 (4), 1109–1117.
- Leuning, R., 1990. Modelling stomatal behaviour and photosynthesis of *Eucalyptus grandis*. *Aust. J. Plant Physiol.* 17, 159–175.
- Leuning, R., 1995. A critical appraisal of a combined stomatal-photosynthesis model for C_3 plants. *Plant, Cell Env.* 18, 339–357.
- Leuning, R., 2000. Estimation of scalar source/sink distributions in plant canopies using Lagrangian dispersion analysis: Corrections for atmospheric stability and comparison with a multilayer canopy model. *Bound.-Layer Meteorol.* 96 (1-2), 293–314.

- Leuning, R., Denmead, O. T., Miyata, A., Kim, J., 2000. Source/sink distribution of heat, water vapor, carbon dioxide and methane in a rice canopy estimated using Lagrangian dispersion analysis. *Agric. For. Meteorol.* 104, 233–249.
- Leuning, R., Dunin, F. X., Wang, Y.-P., 1998. A two-leaf model for canopy conductance, photosynthesis and partitioning of available energy. ii: Comparison with measurements. *Agric. For. Meteorol.* 91, 113–125.
- Leuning, R., Kelliher, F. M., de Pury, D. G. G., Schulze, E. D., 1995. Leaf nitrogen, photosynthesis, conductance and transpiration - scaling from leaves to canopies. *Plant, Cell Env.* 18 (10), 1183–1200.
- Lloyd, 1991. Modelling stomatal responses to environment in *Macadamia integrifolia*. *Aust. J. Plant Physiol.* 18, 649–660.
- Lloyd, J., Grace, J., Miranda, A. C., Meir, P., Wong, S. C., Miranda, B. S., Wright, I. R., Gash, J. H. C., McIntyre, J., 1995a. A simple calibrated model of Amazon rainforest productivity based on leaf biochemical properties. *Plant, Cell Env.* 18 (10), 1129–1145.
- Lloyd, J., Wong, S. C., Styles Julie, M., Batten, D., Priddle, R., Turnbull, C., McConchie, C. A., 1995b. Measuring and modelling whole-tree gas exchange. *Aust. J. Plant Physiol.* 22 (6), 987–1000.
- Llusia, J., Penuelas, J., 1999. *Pinus halepensis* and *Quercus ilex* terpene emission as affected by temperature and humidity. *Biol. Plant.* 42 (2), 317–320.
- Lohammer, T., Larsson, S., Linder, S., Falk, S., 1980. FAST - simulation models of gaseous exchange in scots pine. *Ecol. Bull.* 32 (505-523).
- Mahrt, L., 1999. Stratified atmospheric boundary layers. *Bound.-Layer Meteorol.* 90 (3), 375–396.
- Malhi, Y., Nobre, A. D., Grace, J., Kruijt, B., Pereira, M. G. P., Culf, A., Scott, S., 1998. Carbon dioxide transfer over a central Amazonian rain forest. *J. Geophys. Res.* 103 (D24), 31593–31612.
- Malhi, Y., Pegoraro, E., Nobre, A. D., Pereira, M. G. P., Grace, J., Culf, A., Clement, R., 2002. Energy and water dynamics of a central Amazonian rain forest. *J. Geophys. Res.* 107 (D20), 45.1–45.17.
- Martens, D., Shay, T., Mendlovitz, H., Menton, M., Mauro, J., Lima, R., De Moraes, O., Crill, P., 2002. Radon-222 determination of CO₂ and trace gas exchange rates between forest canopies and the troposphere in Brazilian Amazonia. *Goldschmidt Conference Abstracts, Davos.*

- Massman, W., 1999 A review of the molecular diffusivities of H₂O, CO₂, CO, O₃, SO₂, NH₃, N₂O, NO and NO₂ in air, O₂ and N₂ near STP. *Atmos. Environ.*, 32, 1111-1127.
- McNaughton, H., 1994. Effective stomatal boundary-layer resistances of heterogeneous surfaces. *Plant, Cell Env.* 17, 1061–1068.
- McWilliam, A.-L., Cabral, O. M. R., Gomes, B., Esteves, J. L., Roberts, J., 1996. Forest and pasture leaf-gas exchange in south-west Amazonia. In: Gash, J., Nobre, C., Robers, J., Victoria, R. (Eds.), *Amazonian Deforestation and Climate*. John Wiley, Chichester, pp. 265–285.
- McWilliam, A.-L., Roberts, J., Cabral, O., Leitao, M., Costa, A. d., Maitelli, G., Zamparoni, C., 1993. Leaf area index and above-ground biomass of terra firme rain forest and adjacent clearings in Amazonia. *Funct. Ecol.* 7, 310–317.
- Meir, P., Grace, J., Miranda, A., Lloyd, J., 1996. Soil respiration in a rainforest in Amazonia and in cerrado in central Brazil. In: Gash, J., Nobre, C., Robers, J., Victoria, R. (Eds.), *Amazonian Deforestation and Climate*. John Wiley, Chichester, pp. 319–329.
- Meir, P., Kruijt, B., Broadmeadow, M., Barbosa, E., Kull, O., Carswell, F., Nobre, A., Jarvis, P. G., 2002. Acclimation of photosynthetic capacity to irradiance in tree canopies in relation to leaf nitrogen concentration and leaf mass per unit area. *Plant, Cell Env.* 25 (3), 343–357.
- Meixner, F. X., Eugster, W., 1999. Effects of landscape pattern and topography on emission and transport. In: Tenhunen, J., Kabat, P. (Eds.), *Integrating Hydrology, Ecosystem Dynamics, and Biogeochemistry in Complex Landscapes*, Dahlem Workshop Report. Wiley, Dahlem, pp. 147–175.
- Meyers, T., Paw, K., 1986. Testing of a higher-order closure model for modeling airflow within and above plant canopies. *Bound.-Layer Meteorol.* 37, 297–311.
- Molina, L., Molina, M., 1987. Production of Cl₂O₂ from the self-reaction of the ClO radical. *Journal of Physics and Chemistry* 91, 433–436.
- Monson, R., Harley, P., Litvak, M., Wildermuth, M., 1994. Environmental and developmental controls over the seasonal pattern of isoprene emission from aspen leaves. *Oecologia* 99, 260–270.
- Monteith, J., 1965. Evaporation and environment. *Symp. Soc. Exp. Biol.* 19, 206–234.
- Monteith, J., 1973. *Principles of Environmental Physics*. Edward Arnold, London.

- Moore, C., Fisch, G. F., 1986. Estimating heat storage in Amazonian tropical forest. *Agric. For. Meteorol.* 38, 147–169.
- Müller, J.-F., Brasseur, G., 1995. Images: a three-dimensional chemical transport model of the global troposphere. *J. Geophys. Res.* 100 (D), 16,445–90.
- Naumburg, E., Ellsworth, D. S., Katul, G. G., 2001. Modeling dynamic understory photosynthesis of contrasting species in ambient and elevated carbon dioxide. *Oecologia* 126 (4), 487–499.
- Nazaroff, W., 1992. Radon transport from soil to air. *Rev. Geophys.* 30 (2), 137–160.
- Nemitz, E., Sutton, M. A., Gut, A., San Jose, R., Husted, S., Schjoerring, J. K., 2000. Sources and sinks of ammonia within an oilseed rape canopy. *Agric. For. Meteorol.* 105 (4 SI), 385–404.
- Neubert, A., Kley, D., Wildt, J., 1993. Uptake of NO, NO₂ and O₃ by sunflower (*Helianthus annuus* L.) and tobacco plants (*Nicotiana tabacum* L.): dependence on stomatal conductivity. *Atmos. Environ.* 27 (A), 2137–2145.
- Niinemets, U., Oja, V., Kull, O., 1999. Shape of leaf photosynthetic electron transport versus temperature response curve is not constant along canopy light gradients in temperate deciduous trees. *Plant, Cell Env.* 22 (12), 1497–1513.
- Noilhan, J., Planton, S., 1989. A simple parameterization of land surface processes for meteorological models. *Mon. Wea. Rev.* 117, 536–549.
- Nunez, L., Plaza, J., Perez-Pastor, R., Pujadas, M., Gimeno, B. S., Bermejo, V., Garcia-Alonso, S., 2002. High water vapour pressure deficit influence on *Quercus ilex* and *Pinus pinea* field monoterpene emission in the central Iberian peninsula (Spain). *Atmos. Environ.* 36 (28), 4441–4452.
- Olson, J., 1992. World ecosystems (we1.4): Digital raster data on a 10 minute geographic 1080 x 2160 grid. In: *Global Ecosystem Database, Version 1.0: DISC A*, NOAA National Geophysical Data Center (Ed.), Boulder, CO.
- Oren, R., Ellsworth, D. S., Johnsen, K. H., Phillips, N., Ewers, B. E., Maier, C., Schafer, K. V. R., McCarthy, H., Hendrey, G., McNulty, S. G., Katul, G. G., 2001. Soil fertility limits carbon sequestration by forest ecosystems in a CO₂-enriched atmosphere. *Nature* 411 (6836), 469–472.
- Padro, J., Neumann, H., den Hartog, G., 1992. Modelled and observed dry deposition velocity of O₃ above a deciduous forest in the winter. *Atmos. Environ.* 26A, 775–784.

- Papale, D., Valentini, R., 2003. A new assessment of European forests carbon exchanges by eddy fluxes and artificial neural network spatialization. *Global Change Biol.* 9, 525–535.
- Petron, G., Harley, P., Greenberg, J., Guenther, A., 2001. Seasonal temperature influence isoprene emission. *Geophys. Res. Lett.* 28, 1707–1710.
- Press, W. H., 1997. *Numerical Recipes in C: the Art of Scientific Computing.*, 2nd Edition. Vol. 1. University presss, Cambridge.
- Raupach, M. R., 1988. Canopy transport process. In: Steffen, W. L., Denmead, O. T. (Eds.), *Flow and Transport in the Natural Environment: Advances and Applications.* Springer V., Berlin Heidelberg, pp. 95–127.
- Raupach, M. R., 1989a. Applying Lagrangian fluid mechanics to infer scalar source distributions from concentration. *Agric. For. Meteorol.* 47, 85–108.
- Raupach, M. R., 1989b. A practical Lagrangian method for relating scalar concentrations to source distributions in vegetation canopies. *Q. J. Met. Soc.* 115, 609–632.
- Raupach, M. R., 1989c. Stand overstorey processes. *Phil. Trans. Roy. Soc. London B* 324, 175–190.
- Raupach, M. R., Denmead, O. T., Dunin, F. X., 1992. Challenges in linking atmospheric CO₂ concentrations to fluxes at local and regional scales. *Aust. J. Bot.* 40, 697–716.
- Raupach, M. R., Finnigan, J. J., Brunet, Y., 1996. Coherent eddies and turbulence in vegetation canopies - the mixing-layer analogy. *Bound.-Layer Meteorol.* 78 (3-4), 351–382.
- Reich, P., Uhl, C., Walters, M., Ellsworth, D., 1991. Leaf lifespan as a determinant of leaf structure and function among 23 Amazonian tree species. *Oecologia* 86, 16–24.
- Reich, P., Walters, M., 1994. Photosynthesis-nitrogen relations in Amazonian tree species. *Oecologia* 97, 73–81.
- Reynolds, A., 1998. On the formulations of Lagrangian stochastic models of scalar dispersion within plant canopies. *Bound.-Layer Meteorol.* 87, 333–344.
- Ribeiro, J. d. S., Hopkins, M., Vicentini, A., Sothers, C., Costa, M. d. S., Brito, J. d., Souza, M. d., Martins, L., Lohmann, L., Assuncao, P., Pereira, E. d. C., Silva, C. d., Mesquita, M., Procopio, L., 1999. *Flora da Reserva Ducke: Guia de identificacao das plantas vasculares de uma floresta de terra-firme na Amazonia Central.* INPA, Manaus.

- Rinne, H., Guenther, A., Greenberg, J., 2002. Isoprene and monoterpenes fluxes measured above Amazonian rainforest and their dependence on light and temperature. *Atmos. Environ.* .
- Roberts, J., Cabral, O., Aguiar, d. L., 1990. Stomatal and boundary-layer conductances in an Amazonian terra firm rain forest. *J. Appl. Ecol.* 27, 336–353.
- Roberts, J., Cabral Osvaldo, M. R., Fisch, G., Molion, L. C. B., Moore, C. J., Shuttleworth, W. J., 1993. Transpiration from an Amazonian rainforest calculated from stomatal conductance measurements. *Agric. For. Meteorol.* 65 (3-4), 175–196.
- Roelofs, G.-J., Lelieveld, J., 2000. Tropospheric ozone simulation with a chemistry-general circulation model: influence of higher hydrocarbon chemistry. *J. Geophys. Res.* D105, 22,697–12.
- Rosenstiel, T. N., Potosnak, M. J., Griffin, K. L., Fall, R., Monson, R. K., 2003. Increased CO₂ uncouples growth from isoprene emission in an agriforest ecosystem. *Nature* 421 (6920), 256–259.
- Rottenberger, S., Kuhn, U., Wolf, A., Schebeske, G., Oliva, S., Tavares, T., Kesselmeier, J., 2004. Exchange of short-chain aldehydes between Amazonian vegetation and the atmosphere at a remote forest site in Brazil. *Ecological Applications* (in press) .
- Rumelhart, D., Durbin, R., Golden, R., Chauvin, Y., 1995. Backpropagation: The basic theory. In: Chauvin, Y., Rumelhart, D. (Eds.), *Backpropagation: Theory, Architectures, and Applications*. Developments in connectionist theory. Lawrence Erlbaum Associates, Hillsdale, New Jersey, pp. 1–34.
- Rumelhart, D., Hinton, G., Williams, R., 1986. Learning internal representation by error propagation. In: McClelland, J., Rumelhart, D. (Eds.), *Parallel Distributed Processing: Explorations in the Microstructure of Cognition*. Vol. 1. MIT Press, Cambridge, MA, pp. 318–362.
- Rummel, U., 2004. Turbulent exchange of ozone and nitrogen oxides from a tropical rain forest in Amazonia. Phd thesis, Universität Bayreuth, Abt. Mikrometeorologie, Germany.
- Rummel, U., Ammann, C., Gut, A., Meixner, F., Andreae, M., 2002. Eddy covariance measurements of nitric oxide flux within an Amazonian rain forest. *J. Geophys. Res.* 107 (D20), 17.1–17.9.
- Schnitzler, J. P., Bauknecht, N., Bruggemann, N., Einig, W., Forkel, R., Hampp, R., Heiden, A. C., Heizmann, U., Hoffmann, T., Holzke, C., Jaeger, L., Klauer, M., Komenda, M., Koppmann, R., Kreuzwieser, J., Mayer, H., Rennenberg,

- H., Smiatek, G., Steinbrecher, R., Wildt, J., Zimmer, W., 2002. Emission of biogenic volatile organic compounds: An overview of field, laboratory and modelling studies performed during the 'tropospheric research program' (TFS) 1997-2000. *J. Atmos. Chem.* 42 (1), 159–177.
- Schnitzler, J. P., Lehning, A., Steinbrecher, R., 1997. Seasonal pattern of isoprene synthase activity in *Quercus robur* leaves and its significance for modeling isoprene emission rates. *Bot. Acta* 110 (3), 240–243.
- Schuh, G., Heiden, A. C., Hoffmann, T., Kahl, J., Rockel, P., Rudolph, J., Wildt, J., 1997. Emissions of volatile organic compounds from sunflower and beech: Dependence on temperature and light intensity. *J. Atmos. Chem.* 27 (3), 291–318.
- Schulze, E.-D., Kelliher, F., Körner, C., Lloyd, J., Leuning, R., 1994. Relationship between maximum stomatal conductance, ecosystem surface conductance, carbon assimilation and plant nitrogen nutrition: A global ecology scaling exercise. *Annu. Rev. Ecol. Syst.* 25, 629–660.
- Sellers, P., Berry, J., Collatz, G., Field, C., Hall, F., 1992. Canopy reflectance, photosynthesis and transpiration. iii: A reanalysis using improved leaf models and a new canopy integration scheme. *Remote Sens. Environ.* 42, 187–216.
- Sellers, P., Bounoua, L., Collatz, G., Randall, D., Dazlich, D., Los, S., Berry, J., Fung, I., Tucker, C., Field, C., Jemsem, T., 1996. Comparison of radiative and physiological effects of doubled atmospheric CO₂ on climate. *Science* 271, 1402–1406.
- Sellers, P., Mintz, Y., Sud, Y., Dalcher, A., 1986. A simple biosphere model (sib) for use within general circulation models. *J. Atmos. Sci.* 43, 505–531.
- Sharkey, T. D., Loreto, F., Delwiche, C., 1991. High carbon dioxide and sun/shade effects on isoprene emission from oak and aspen tree leaves. *Plant, Cell Env.* 14, 333–338.
- Sharkey, T. D., Yeh, S. S., 2001. Isoprene emission from plants. *Ann. Rev. Plant Physiol. Plant Molec. Biol.* 52, 407–436.
- Simon, E., 1999. Quellensenkenverteilung von Energie und Spurengasen in einem seneszenten Getreidefeld: Modellierung und Vergleich mit Meßdaten. Diploma thesis, Joh.-Gutenberg Universität, Fachbereich Biologie, Mainz, Germany.
- Simon, E., Ammann, C., Busch, J., Meixner, F., Kesselmeier, J., 2002. Applying Lagrangian dispersion analysis to the exchange of water and sensible heat within a cereale crop canopy: A sensitivity study and comparison with leaf level measurements. In: 15th Symposium on Boundary Layers and Turbulence. American Meteorological Society, Wageningen, Netherlands, pp. 535–538.

- Siqueira, M., Katul, G., 2002. Estimating heat sources and fluxes in thermally stratified canopy flows using higher-order closure models. *Bound.-Layer Meteorol.* 103 (1), 125–142.
- Siqueira, M., Lai, C.-T., G., K., 2000. Estimating scalar sources, sinks, and fluxes in a forest canopy using Lagrangian, Eulerian, and hybrid inverse models. *J. Geophys. Res.* 105 (D24), 29475–29488.
- Sparks, J., Greenberg, J., Harley, P., Guenther, A., 2003. Field observations of increased isoprene emissions under ozone fumigation: Implications for tropospheric chemistry? *EOS Transact. AGU* 84 (46), Abstract A21F-05.
- Splitter, C., 1986. Separating the diffusive and direct component of global radiation and its implications for modelling canopy photosynthesis, part ii: Calculation of canopy photosynthesis. *Agric. For. Meteorol.* 38, 231–242.
- Staudt, M., Joffre, R., Rambal, S., 2003. How growth conditions affect the capacity of *Quercus ilex* leaves to emit monoterpenes. *New Phytol.* 158 (2), 61.
- Stefani, P. R., Valentini, R., Ciccioli, P., 2000. Preliminary assessment of VOC fluxes from a primary rainforest performed at the LBA site at Manaus. In: Artaxo, P., Keller, M. (Eds.), *Proceedings of the First LBA Scientific Conference*. MCT, Belem, Brazil.
- Stull, R. B., 1988. *An Introduction to Boundary Layer Meteorology*. Atmospheric Science Library. Kluwer Academic Publishers, Dordrecht.
- Theis, N., Lerdau, M., 2003. The evolution of function in plant secondary metabolites. *Int. J. Plant Sci.* 164 (3 Suppl.), 93–102.
- Tingey, D. T., Manning, M., Grothaus, L. C., Burns, W. F., 1980. Influence of light and temperature on monoterpene emission rates from slash pine (*Pinus elliotii*). *Plant Physiology.* 65, 797–801.
- Trumbore, S., Keller, M., Wolfsy, S., Costa, J. D., 1990. Measurements of soil and canopy exchange rates in the Amazon rain forest using ^{222}Rn . *J. Geophys. Res.* 95 (No. D10), 16865–16873.
- Tuzet, A., Perrier, A., Leuning, R., 2003. A coupled model of stomatal conductance, photosynthesis and transpiration. *Plant, Cell Env.* 26, 1097–1116.
- Ussler, W. I., Chanton, J., Kelley, C., Martens, C., 1994. Radon 222 tracing of soil and forest canopy trace gas exchange in an open canopy boreal forest. *J. Geophys. Res.* 99 (D1), 1953–1963.

- van Wijk, M. T., Bouten, W., 1999. Water and carbon fluxes above European coniferous forests modelled with artificial neural networks. *Ecol. Model.* 120 (2-3), 181–197.
- Walters, M., Field, C., 1987. Photosynthetic light acclimation in two rainforest piper species with different ecological amplitudes. *Oecologia* 72, 449–456.
- Wang, Y.-P., Leuning, R., 1998. A two-leaf model for canopy conductance, photosynthesis and partitioning of available energy. i: Model description and comparison with a multi-layered model. *Agric. For. Meteorol.* 91, 89–111.
- Warland, J. S., Thurtell, G. W., 2000. A Lagrangian solution to the relationship between a distributed source and concentration profile. *Bound.-Layer Meteorol.* 96 (3), 453–471.
- Wesely, M., 1989. Parameterization of surface resistance to gaseous dry deposition in regional-scale numerical models. *Atmos. Environ.* 23, 1293–1304.
- Wesely, M., Hicks, B., 2000. A review of the current status of knowledge on dry deposition. *Atmos. Environ.* 34, 2261–2282.
- Wesely, M., Sisterson, D., Jastrow, J., 1990. Observations of the chemical properties of dew on vegetation that affect the dry deposition of SO₂. *J. Geophys. Res.* 95 (7501-7514).
- Wilkening, M., Clements, D., Stanley, D., 1972. Radon-222 flux measurements in widely separated regions. In: Adams, J. (Ed.), *Proceedings of the Natural Radiation Environment II*. National Technical Information Service, Springfield, Va., pp. 717–730.
- Williams, M., Malhi, Y., Nobre, A. D., Rastetter, E. B., Grace, J., Pereira, M. G. P., 1998. Seasonal variation in net carbon exchange and evapotranspiration in a Brazilian rain forest: a modelling analysis. *Plant, Cell Env.* 21 (10), 953–968.
- Wilson, K., Goldstein, A., Falge, E., Aubinet, M., Baldocchi, D., Berbigier, P., Bernhofer, C., Ceulemans, R., Dolman, H., Field, C., Grelle, A., Ibrom, A., Law, B. E., Kowalski, A., Meyers, T., Moncrieff, J., Monson, R., Oechel, W., Tenhunen, J., Valentini, R., Verma, S., 2002. Energy balance closure at Fluxnet sites. *Agric. For. Meteorol.* 113 (1-4), 223–243.
- Wullschlegel, S., 1993. Biochemical limitations to carbon assimilation in C₃ plants - A retrospective analysis of the A/c_i curves from 109 species. *J. Exp. Bot.* 44, 907–920.
- Yienger, J., Levy, H. I., 1995. Empirical model of global soil-biogenic NO_x emissions. *J. Geophys. Res.* 100 (D.6), 11447–11464.

Zimmer, W., Bruggemann, N., Emeis, S., Giersch, C., Lehning, A., Steinbrecher, R., Schnitzler, J. P., 2000. Process-based modelling of isoprene emission by oak leaves. *Plant, Cell Env.* 23 (6), 585–595.

Appendix A

Calculations related to the canopy exchange scheme

A.1 The biochemical model of leaf photosynthesis

According to Farquhar et al. (1980) and Caemmerer and Farquhar (1981), the Rubisco limited rate of gross photosynthesis ('dark reaction'), is given by

$$A_v = v_{cmax} \frac{c_i - \Gamma_*}{c_i + K_c(1 + o_i/K_o)} \quad (\text{A.1})$$

where v_{cmax} is the maximum catalytic activity of Rubisco, when RuP₂ is not limiting, Γ_* is the CO₂ compensation point in the absence of day respiration, o_i is the intercellular oxygen concentration, and K_c and K_o are the Michaelis coefficients for CO₂ and O₂, respectively. The gross photosynthesis limited by electron transport rate (A_J) is given by

$$A_J = \frac{J}{4} \frac{c_i - \Gamma_*}{c_i + 2\Gamma_*} \quad (\text{A.2})$$

where J is the electron transport rate for a given absorbed radiation (Q_{abs}). Farquhar and Wong (1984) used a non-rectangular hyperbola to describe the dependence of J on its maximum rate (J_{max}), the initial quantum yield of whole-chain electron transport (α) and Q_{abs} according to

$$\theta J^2 - (\alpha Q_{abs} + J_{max})J + \alpha Q_{abs} J_{max} = 0 \quad (\text{A.3})$$

where θ determines the shape of the non-rectangular hyperbola. The absorbed radiation is related to the incident photosynthetic active radiation (Q_{PAR}) by $Q_{abs} = (1 - \text{reflectance} - \text{transmission})Q_{PAR}$ (Farquhar and Wong, 1984). For given values of Q_{abs} and J_{max} , J is derived as the smallest root of the quadratic

Table A.1: Photosynthesis and stomatal conductance model parameters. Marked values are taken from *Leuning et al. (1995) and †Harley et al. (1992). Values in brackets are derived from leaf level gas exchange measurements (see Section 2.3.6 for further explanations).

Parameter	Value (optimized)	Unit
a_A	10	[-]
g_{s0}	0.01	[mol m ⁻² s ⁻¹]
D_{s0}	15	[hPa]
$v_{cmax0hc}$	50	[μmol m ⁻² s ⁻¹]
k_N	0.2	[-]
T_{s0}	298.15	[K]
J_{max0}	$2.1v_{cmax0}$	[μmol m ⁻² s ⁻¹]
R_{d0}	$0.01v_{cmax0}$	[μmol m ⁻² s ⁻¹]
o_i	210	[mmol mol ⁻¹]
α	0.2* (0.15)	[mol e mol ⁻¹ quanta]
θ	0.9*	[-]
K_{c0}	302*	[μmol ⁻¹]
K_{o0}	256*	[mmol ⁻¹]
H_{Kc}	59.4†	[kJ mol ⁻¹]
H_{Ko}	36†	[kJ mol ⁻¹]
H_{Rd}	53†	[kJ mol ⁻¹]
H_{vV}	116.3†	[kJ mol ⁻¹]
H_{dV}	202.9†	[kJ mol ⁻¹]
H_{vJ}	79.5† (108)	[kJ mol ⁻¹]
H_{dJ}	201†	[kJ mol ⁻¹]
S_v	0.65†	[kJ mol ⁻¹]
S_j	0.65 (0.66)	[kJ mol ⁻¹]
γ_0	34.6*	[μmol mol ⁻¹]
γ_1	0.0451*	[-]
γ_2	0.000347*	[-]

Eq. A.3. Most physiological parameters are strongly dependent on temperature. Γ_* is given by the empirical polynomial

$$\Gamma_* = \gamma_0[1 + \gamma_1(T_s - T_{s0}) + \gamma_2(T_s - T_{s0})^2] \quad (\text{A.4})$$

with the coefficients $\gamma_0, \gamma_1, \gamma_2$, for a reference temperature T_{s0} (Brooks and Farquhar, 1985). The Michaelis coefficients K_c and K_o and R_d are calculated by a normalized Arrhenius curve according to Leuning et al. (1995) with

$$\{K_c, K_o, R_d\} := x = x_0 \exp[(H_p/RT_{s0})(1 - T_{s0}/T_s)] \quad (\text{A.5})$$

where R is the universal gas constant, H_p the activation energy, and $x_0 = x(T_{s0})$. For v_{cmax} and J_{max} , the optimum function

$$\{v_{cmax}, J_{max}\} := x = x_0 \frac{\exp[(H_v/RT_{s0})(1 - T_{s0}/T_s)]}{1 + \exp[(S_v T_s - H_d)/(RT_s)]} \quad (\text{A.6})$$

is applied where H_v , H_d , and S_v are the activation and deactivation energy and an entropy term, respectively (Harley et al., 1992). Predicted optimum leaf temperature for v_{cmax} and J_{max} are calculated from zero values of the first derivatives of Eq. A.6 (Niinemets et al., 1999).

A.2 Radiative transfer parameters

Given the scattering and canopy reflection coefficients for diffusive radiation (σ_l and ρ_{cd} with subscripts V and N denoting visible and near-infrared radiation, respectively, Table 2.5), the extinction coefficients for diffusive and direct beam radiation (k_d and k_b , Eq. 1.6) are calculated from values for black leaves (k^B) according to

$$k = k^B(1 - \sigma_l) \quad (\text{A.7})$$

where k^B is approximated by $k_d^B = 0.8$ and $k_b^B = 0.5 \sin(\beta_c)$ for a spherical leaf angle distribution. The calculation of the solar elevation angle β_c is described in Appendix A.4. The canopy reflection coefficient for beam radiation ρ_{cb} is related to the canopy reflection coefficient for horizontal leaves ρ_h according to

$$\rho_{cb} = 1 - \exp\left(\frac{-2\rho_h k_b}{1 + k_b}\right) \quad (\text{A.8})$$

$$\rho_h = \frac{1 - \sqrt{1 - \sigma_l}}{1 + \sqrt{1 - \sigma_l}} \quad (\text{A.9})$$

A.3 Long-wave radiation

Long-wave emissivity ϵ is given by different values for soil, canopy, and the atmosphere with

$$\epsilon_\Lambda = \begin{cases} \epsilon_{soil}, & \Lambda = \Lambda_0 \\ \epsilon_c, & 0 < \Lambda_z < \Lambda_0 \\ \epsilon_{a0}, & \Lambda = 0 \end{cases} \quad (\text{A.10})$$

whereas $\epsilon_c = 0.96$ and $\epsilon_{soil} = 0.94$ (Wang and Leuning, 1998). Incoming long-wave radiation ($Q_{LW\downarrow}$) is calculated analogously to diffusive radiation according to

$$Q_{LW\downarrow}(\Lambda_z) = \epsilon_{a0} \sigma_B T_{ref}^4 k_d^B \exp(-k_d^B \Lambda_z) \quad (\text{A.11})$$

The outgoing long wave radiation given as $Q_{LW\uparrow}(\Lambda_z) = \epsilon_\Lambda \sigma_B T_s(\Lambda_z)^4$ can not be solved directly, since T_s is part of the leaf energy balance. Instead, the isothermal outgoing long wave radiation ($Q_{LW\uparrow}^*$), equivalent to the long wave radiation that would be lost, if the surface were at ambient temperature (Jones, 1992) is calculated by replacing T_{ref} and ϵ_{a0} in Eq. A.11 by $T_a(\Lambda_z)$ and ϵ_c , respectively. The isothermal net radiation (Q_n^*) is then given by

$$Q_n^* = Q_{SW\downarrow} - Q_{SW\uparrow} + Q_{LW\downarrow} - Q_{LW\uparrow}^*. \quad (\text{A.12})$$

Combining Eq. A.12 and 1.11 leads to

$$Q_n^* = Q_n + \sigma_B \epsilon_\Lambda (T_s^4 - T_a^4). \quad (\text{A.13})$$

The substitution $T_s = T_a + \Delta T$ followed by multiplication gives

$$Q_n^* = Q_n + \sigma_B \epsilon_\Lambda [4T_a^3(\Delta T) + 6T_a^2(\Delta T)^2 + 4T_a(\Delta T)^3 + (\Delta T)^4] \quad (\text{A.14})$$

where T_a^4 cancels out. All terms including ΔT with second or higher power can be neglected because $\Delta T \ll T_a$. It remains

$$Q_n \simeq Q_n^* - \sigma_B \epsilon_\Lambda 4T_a^3 \Delta T \quad (\text{A.15})$$

where $g_{rad} = \epsilon \sigma_B 4T_a^3 / c_p^m$ is defined as the radiative conductance.

A.4 Solar parameters

According to Goudriaan and van Laar (1994), the fraction of incoming diffusive radiation (f_{d0}) is dependent on atmospheric transmissivity (τ_a) according to

$$f_{d0} = \begin{cases} 1 & , \tau_a < 0.3 \\ 1 - 2(\tau_a - 0.3) & , 0.3 \leq \tau_a \leq 0.7 \\ 0.2 & , \tau_a > 0.7 \end{cases} \quad (\text{A.16})$$

Since the measured incoming global radiation ($gRad$) is given as input (Table 1.1), τ_a can be estimated from the ratio of actual to potential global radiation ($\tau_a = gRad/gRad_0$). $gRad_0$ is calculated according to

$$gRad_0 = S_c \sin(\beta_c) \quad (\text{A.17})$$

where S_c is the flux density of solar radiation normal to the sun's beam outside the Earth's atmosphere given as

$$S_c = 13671 + 0.033 \cos\left(\frac{2\pi(t_d - 10)}{365}\right). \quad (\text{A.18})$$

t_d and β_c are the time of the year (in days) and the sun elevation angle (degree), respectively. The latter is calculated as

$$\sin \beta_c = a_{s1} + a_{s2} \cos[2\pi(t_h - 12)/24] \quad (\text{A.19})$$

where t_h is local solar time in hours and

$$a_{s1} = \sin \lambda_l \sin \delta_s \quad (\text{A.20})$$

$$a_{s2} = \cos \lambda_l \cos \delta_s \quad (\text{A.21})$$

$$\sin \delta_s = -\sin \left(\frac{23.5\pi}{180} \right) \cos \left(\frac{2\pi(t_d + 19)}{365} \right) \quad (\text{A.22})$$

λ_l and δ_s are the degree of latitude and declination of the sun with respect to the equator, respectively. From a_{s1} and a_{s2} , the day length in hours t_{dl} can be calculated as

$$t_{dl} = 12 \left(1 + \frac{2}{\pi} \arcsin \left(\frac{a_{s1}}{a_{s2}} \right) \right) \quad (\text{A.23})$$

A.5 The numerical solution of the leaf energy balance

Surface values of CO₂ concentration (c_s) and water vapor pressure deficit (D_s) can be calculated for a given ΔT and c_i by rewriting Eqns 1.15 and 1.13 to

$$c_s = c_i + (c_a - c_i) \frac{g_{tc}}{N_{LS} g_{sc}} \quad (\text{A.24})$$

$$D_s = (D_a + s\Delta T) \frac{g_{tw}}{g_{sw}} \quad (\text{A.25})$$

where s and N_{LS} are the slope of the curve relating saturation water vapor pressure to temperature and the number of active leaf sides (hypostomatous leaves = 1, amphistomatous leaves = 2), respectively. ΔT is calculated for given values of g_{tw} and g_{th} according to

$$\Delta T = \frac{\gamma^*}{s + \gamma^*} \frac{Q_n^*}{g_{tH} + g_{rad}} - \frac{D_a}{s + \gamma^*} \quad (\text{A.26})$$

$$\gamma^* = \gamma \frac{g_{tH} + g_{rad}}{g_{tw}} \quad (\text{A.27})$$

where γ^* is the modified psychrometric constant, and g_{rad} the radiative conductance (see Appendix A.3). g_{tH} equals the double-sided leaf boundary layer

conductance for heat g_{bH} whereas the inverse total conductance for water equals the sum of the stomatal and boundary layer resistance ($1/g_{tw} = 1/g_{sw} + 1/g_{bw}$). c_i can be solved analytically (Leuning, 1990) by writing

$$c_i = \frac{-b_1 + \sqrt{b_1^2 - 4b_0b_2}}{2b_2} \quad (\text{A.28})$$

$$A_n = d_2 \frac{c_i - \Gamma^*}{c_i + d_3} - R_d \quad (\text{A.29})$$

with substitutions

$$b_0 = -(1 - d_1c_s)(d_2\Gamma^* + d_3R_d) - g_{sc0}d_3c_s \quad (\text{A.30})$$

$$b_1 = (1 - d_1c_s)(d_2 - R_d) + g_{sc0}(d_3 - c_s) - d_1(d_2\Gamma^* + d_3R_d) \quad (\text{A.31})$$

$$b_2 = g_{s0} + d_1(d_2 - R_d) \quad (\text{A.32})$$

$$d_1 = \frac{a_A f(\psi_{soil})}{(c_s - \Gamma)(1 + D_s/D_{s0})}. \quad (\text{A.33})$$

For RuBP- limited photosynthesis d_2 and d_3 are given by

$$d_2 = 0.25J \quad (\text{A.34})$$

$$d_3 = 2\Gamma^* \quad (\text{A.35})$$

and for Rubisco-limited photosynthesis

$$d_2 = v_{cmax} \quad (\text{A.36})$$

$$d_3 = K_c(1 + o_i/K_o). \quad (\text{A.37})$$

Eqns A.34-A.37 have to be solved for both, RuBP- and Rubisco-limited photosynthesis and the solution giving the higher c_i and lower A_n values has to be chosen. Γ can be calculated analytical by setting A_n to zero.

A.6 Parameterization of soil surface exchange

According to Garrat (1992), the actual soil evaporation (E_{soil}) is dependent on soil relative humidity (RH_{soil}) and potential evaporation (E_{soil}^P) according to

$$E_{soil} = E_{soil}^P - g_{soilw} \left(1 - \frac{s}{s + \gamma_{air}}\right) (1 - RH_{soil}) e_{sat}(T_{soil}) \quad (\text{A.38})$$

$$E_{soil}^P = \frac{s}{s + \gamma_{air}} (Q_n(\Lambda_0) - G) / \lambda^m + g_{soilw} \left(1 - \frac{s}{s + \gamma_{air}}\right) D_{soil} \quad (\text{A.39})$$

whereby e_{sat} and $Q_n(\Lambda_0)$ are the saturated water vapor pressure and net radiation at the soil surface, respectively, and $D_{soil} = RH_{soil}e_{sat}$. The bulk soil surface conductance for water (g_{soilw}) is derived from the input parameter g_{soilH} (Ball, 1987). RH_{soil} is related to the soil matrix potential (ψ_{soil}) according to

$$RH_{soil} = \exp\left(\frac{-g\psi_{soil}}{RT_{soil}}\right) \quad (\text{A.40})$$

whereas g and R are the gravity and gas constant, respectively. ψ_{soil} is calculated from the volumetric soil water content (η_w) according to

$$\psi_{soil} = \psi_{soil}^* (\eta_w/\eta_w^*)^{-a_\psi} \quad (\text{A.41})$$

with η_w^* , ψ_{soil}^* , and a_ψ being the total soil pore space, the saturated value of ψ_{soil} and an empirical coefficient, respectively.

For soil respiration (F_{csoil}), the simple Arrhenius curve

$$F_{csoil} = F_{csoil0} \exp [H_{asoil}/RT_{soil0} (1 - T_{soil0}/T_{soil})] \quad (\text{A.42})$$

is applied, whereas F_{csoil0} is the soil respiration at a reference soil temperature T_{soil0} and H_{asoil} the activation energy for F_{csoil} (Tuzet et al., 2003).

A.7 Special functions

As already mentioned by Press (1997), there is nothing particularly special about the following “special” functions and one might also simply call them “useful functions”. Numerical calculations for all of them are included in most modern software packages for data analysis. A complete derivation and discussion for each equation are given in Press (1997). The incomplete gamma function $P_x(a)$ is related to the gamma function $\Gamma(a)$ and given by

$$P_x(a) \equiv \frac{x^{a-1}e^{-x}}{\Gamma(a)} \quad (\text{A.43})$$

$$\Gamma(a) = \int_0^\infty t^{a-1}e^{-t}dt \quad (\text{A.44})$$

with $a > 0; x \geq 0$.

The incomplete beta function $I_x(a_1, a_2)$ is a statistical distribution function and related to the beta function $B(a_1, a_2)$ by

$$I_x(a_1, a_2) \equiv \frac{1}{B(a_1, a_2)} \int_0^x t^{a_1-1}(1-t)^{a_2-1}dt \quad (\text{A.45})$$

$$B(a_1, a_2) = \int_0^1 t^{a_1-1}(1-t)^{a_2-1}dt \quad (\text{A.46})$$

It is characterized by two positive parameters a_1 and a_2 and a defined input and output range between zero and one with $I_0(a_1, a_2) = 0$ and $I_1(a_1, a_2) = 1$.

A.8 The normalized height function for the standard deviation of vertical wind speed (σ_w)

The friction based function for σ_w scaling (Section 3.3.1) is a beta distribution (Press, 1997, see Appendix A.7 and Chapter 2) given by

$$a_{\sigma f}(z) = \max [a_{f0}, I_{x(z)}(a_{f1}, a_{f2})] \quad (\text{A.47})$$

where $x(z) = z/z_{\sigma f}$ for the scaling height $z_{\sigma f}$ above which $a_{\sigma f} = 1$. a_{f1} and a_{f2} are dimensionless coefficients determining the shape of the distribution and a_{f0} is a minimum value close to the ground. The free convective scaling is performed with a gamma density function (Press, 1997, see Appendix A.7) given by

$$a_{\sigma c} = \frac{P_{x(z)}(a_{c1})}{a_{c2}} \quad (\text{A.48})$$

with the transformation $x(z) = z_{\sigma c}z/(a_{c2}h_c)$. a_{c1} , a_{c2} and $z_{\sigma c}$ are parameters determining the profile shape, maximum size and location.

A.9 The isoprene emission algorithm of Guenther et al. (1993)

According to Guenther (1997) biogenic VOC emission is estimated as

$$E_V = E_{V0}C_Q C_T \delta_{EV0} \quad (\text{A.49})$$

where E_{V0} is the experimentally determined standard emission factor. C_Q and C_T are a light and temperature dependent term, respectively. The dimensionless factor δ_{EV0} represents a modification of the original model version (Guenther et al., 1993) and accounts for long-term (> 1 hour) emission variations although it is usually set to one. The light dependent term C_Q is given by

$$C_Q = \alpha_Q c_{Q1} Q_{PAR} (1 + \alpha_Q^2 Q_{PAR}^2)^{-1/2} \quad (\text{A.50})$$

with empirical determined coefficients $\alpha_Q = 0.0027$ and $c_{Q1} = 1.066$ and incident PAR flux Q_{PAR} . The temperature dependent term C_T is given by

$$C_T = \exp \left[\frac{c_{T1}(T_s - T_0)}{RT_0 T_s} \right] \left[c_{T3} + \exp \frac{c_{T2}(T_s - T_{opt})}{RT_0 T_s} \right]^{-1} \quad (\text{A.51})$$

with the empirical determined coefficients $c_{T1} = 95,000 \text{ J mol}^{-1}$, $c_{T2} = 23,000 \text{ J mol}^{-1}$ and $c_{T3} = 0.961$, the optimum temperature $T_{opt} = 314 \text{ K}$, the standard temperature $T_0 = 303.15 \text{ K}$, and the gas constant $R = 8.314 \text{ J K}^{-1} \text{ mol}^{-1}$. Both dimensionless terms are normalized and have a value of 1 at standard conditions, which is $Q_{PAR} = 1000 \text{ } \mu\text{mol m}^{-2} \text{ s}^{-1}$ for C_Q and $T_S = T_0$ for C_T . All empirical coefficients used in Eq. A.50 and A.51 were derived by nonlinear best fit procedures using emission rates measured during experiments with eucalyptus, sweet gum, aspen, and velvet bean (Guenther et al., 1993). Ongoing applications of the model showed that these parameter values show only slight variations over a wide range of species and environmental conditions.

Appendix B

Calculations related to ^{220}Rn and ^{222}Rn flux measurements

The radon soil fluxes are determined with a static chamber system, which is described in detail by Lehmann et al. (2004). As the traveling time in the closed circuit of the static chamber system is very large compared to the life time of ^{220}Rn , the activity reaches an equilibrium (C_{220}^{eq}) that balances the flux from the soil (J_{220}) and the decay inside the chamber system. Since the measured equilibrium activity ($C_{220}^{eq,obs}$) is smaller than C_{220}^{eq} due to radioactive decay on the way to the detector, a correction factor has to be applied which is ≈ 4.2 for our chamber system. The flux is then calculated according to

$$J_{220} = 4.2C_{220}^{eq,obs} \frac{q_{V0} + \lambda_{220}V_0}{S_{V0}} \quad (\text{B.1})$$

where q_{V0} , V_0 and S_{V0} are the flow rate through the chamber system, its volume, and its bottom surface, respectively.

^{222}Rn has a much longer life-time (≈ 5.5 days) compared to the traveling time in the chamber system. Thus the activity inside the chamber increases during the period of a single measurement. Approximately, this increase term is linear and can be related to the flux by

$$J_{222} = \frac{V_0}{S_{V0}} \beta_{222} \quad (\text{B.2})$$

where β_{222} represents the linear slope $\Delta C_{222}/\Delta t$.

For illustration, Fig. B.1 shows the evolution of C_{222} and C_{220} during a single flux measurement on 15th July 2001. As a consequence of the high time resolution, the measured activity is in general very scattered. In addition to the measured data, the adjacent average is also shown. $C_{222}(t)$ (Fig. B.1a) increases more or less linear with time until the end of the measurement. The coefficient β_{222} (Eq. B.2) is derived by linear fitting. In contrast to $C_{222}(t)$, $C_{220}(t)$ saturates after a short period of approx. 5 min (Fig. B.1b). $C_{220}^{eq,obs}$ (Eq. B.1) is calculated

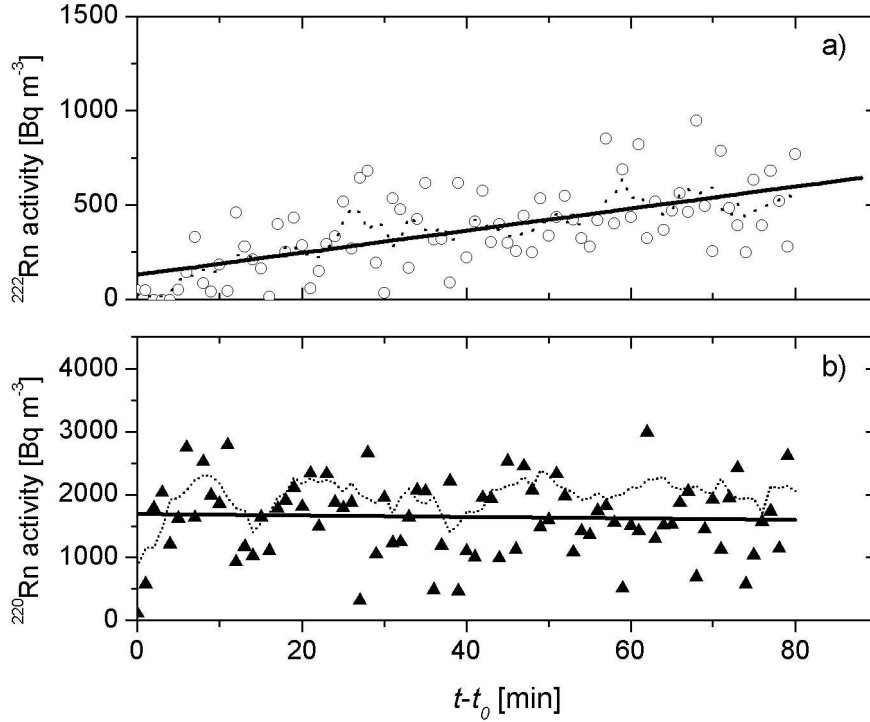


Figure B.1: Radon flux measurement example

from the mean value of observations. To account for possible complications due to decreasing flow rate as discussed in Lehmann et al. (2004), a linear detrending was performed between the mean activities derived for the first and second half of the period.

The correlation between the observed fluxes of ^{220}Rn and ^{222}Rn is analyzed with a simple soil diffusion model. The approach of Nazaroff (1992) describes the diffusion of ^{220}Rn and ^{222}Rn within the soil mainly as a function of soil porosity, fraction of water, and air filled pore space. Below a specific soil depth, the activity concentration of both scalars reaches a maximum activity C^∞ which balances the production from rock material and the flux to upper soil layers and the atmosphere. The combined solution of the soil model solved for J_{222} predicts the linear dependence

$$J_{222} = \sqrt{\frac{\lambda_{220} C_{222}^\infty}{\lambda_{222} C_{220}^\infty}} J_{220} \quad (\text{B.3})$$

Appendix C

The neuronal network with back propagation learning rule (BPN)

The neuronal network applied in Chapter 5 is implemented as a multilayer feed-forward perceptron with back propagation learning rule (BPN). The topology of the canonical BPN is shown in Fig. 5.1. It has an in- and output layer, \mathbf{X} and \mathbf{Y} , and a hidden layer \mathbf{Z} with $N(x)$, $N(y)$, $N(z)$ number of neurons, respectively. Input and middle layer and middle and output layer are connected by weight matrices \mathbf{W}_{XZ} and \mathbf{W}_{ZY} connecting each input and output neuron with \mathbf{Z} . Given a population of $\mathbf{X} = x_1, \dots, x_N$ input and $\mathbf{Y} = y_1, \dots, y_N$ output patterns, it has to minimize the sum of squared differences between desired output patterns y_μ and network output $\psi(\mathbf{W}x_\mu)$ over all patterns:

$$f_{\text{BPN}} = \frac{1}{2} \sum_{\mu}^N \|y_\mu - \psi(\mathbf{W}, x_\mu)\|^2 \quad (\text{C.1})$$

Each neuron node of layer i has an input signal, which is part of the normalized input vector x_μ if i is in the first layer or $\sum w_{ji}o_j$ as the weighted output of the precursors which are connected with that node. The neuron output o_j is given by a differentiable, monotone activation function (squashing function) with lower bounds 0 and upper bounds 1. In the present study, the most popular activation function is used, which is the sigmoidal function

$$f(x) = \frac{1}{1 + \exp^{-x}} \quad (\text{C.2})$$

Since the activation function is differentiable, the partial gradient of Eq. C.1 can be used to calculate the weight changes according to

$$\Delta \mathbf{w} = -\eta_{\text{net}} \nabla_{\mathbf{w}} f_{\text{BPN}} \quad (\text{C.3})$$

with the constant learning rate $\eta_{\text{net}} > 0$. Eq.C.1 and C.3 can be combined to a local rule for a single weight change $\Delta w_{ij} = \eta_{\text{net}} \delta_i o_j$ according to

$$\delta_i = \begin{cases} \sum_{\mu} (y_i^{\mu} - \psi_i(\mathbf{W}, \mathbf{x}^{\mu})) \cdot f'(x_i) & , \text{ if } i \text{ is input neuron} \\ \sum_{k \in S(i)} \delta_k w_{ki} \cdot f'(\sum w_{ji} o_j) & , \text{ else} \end{cases} \quad (\text{C.4})$$

The updating process is started in the output layer and then continued backward to the input layer (\rightarrow back propagation). If the weight change term becomes very small (which is sometimes observed near the optimum solution), it is recommended to include a momentum term $\alpha_{net} \Delta w(t_{net} - 1)$ so that Eq. C.3 becomes

$$\Delta \mathbf{w} = -\eta_{net} \nabla_{\mathbf{w}} f_{\text{BPN}} + \alpha_{net} \Delta w(t_{net} - 1) \quad (\text{C.5})$$

By including a constant fraction of the previous change $\delta w(t_{net} - 1)$, it is ensured that the solutions converges in the direction of the optimum.

Appendix D

List of symbols and abbreviations

D.1 Abbreviations

ABRACOS	Anglo-Brazilian Amazonian Climate Observation Study
BPN	back propagation neuronal network
EC	Eddy Covariance technique
ENV(-T)	environmental parameter (temperature history)
EUSTACH	European Studies on Trace gases and Atmospheric Chemistry
EUST-I+II	EUSTACH'99 I (Apr-May) and II (Sep-Nov) in Rondônia
G93	the algorithm of Guenther et al. (1993)
GCM	general circulation model
IP	isoprene emitting species
LAI	leaf area index
LBA	Large scale Biosphere-Atmosphere Experiment in Amazonia
LNF	Localized Near-Field theory after Raupach (1989b)
MTP	monoterpene emitting species
NEE	net ecosystem exchange
NIR	near-infrared radiation
No.1-24	parameter combinations P01-11 for the BPN application
P01-11	regression parameters for the BPN application
PHYS	physiological parameter
RBJ-A	Reserva Rebio Jaru site, tower A
RBJ-B	Reserva Rebio Jaru site, tower B
RMSE	root of mean squared error
rRMSE	relative RMSE (as ratio to RMSE(G93))
SLA	specific leaf area in $\text{cm}^2 \text{g}^{-1}$
SLW	specific leaf (dry) weight in g m^{-2}
SVAT	soil-vegetation-atmosphere transfer scheme
VIS	visible radiation
VOC	volatile organic compound
ZF2-C14	Cuieiras site, tower at km 14 of the road ZF2
ZF2-K34	Cuieiras site, tower at km 34 of the road ZF2

D.2 Greek symbols

α	[mol mol ⁻¹]	quantum yield of whole-chain electron transport
β_{222}	[Bq m ⁻³ s ⁻¹]	slope increase of ²²² Rn activity concentration during a chamber flux measurement
β_c	[degrees]	solar elevation
δ_s	[rad]	declination of the sun
ϵ_x	[-]	long-wave emissivity with subscripts $\Lambda_z, soil, s, a$ and $a0$ denoting the canopy position, soil, surface, ambient air and atmosphere, respectively
η_w, η_w^*	[-]	water filled pore space, total soil pore space
Γ	[μ mol mol ⁻¹]	CO ₂ compensation point
γ^*	[hPa K ⁻¹]	modified psychrometric constant
Γ^*	[μ mol mol ⁻¹]	CO ₂ compensation point in the absence of day respiration
$\gamma_{0,1,2}$	[-]	empirical constants (Eq. A.4)
γ_{air}	[hPa K ⁻¹]	psychrometric constant
λ_{220}	[s ⁻¹]	decay constant for ²²⁰ Rn (0.012 s ⁻¹)
λ_{222}	[s ⁻¹]	decay constant for ²²² Rn (2.1×10^{-6} s ⁻¹)
λ^m	[J mol ⁻¹]	latent heat of vaporization for water
λ^C	[J μ mol]	chemical energy stored by CO ₂ fixation
Λ_0	[m ² m ⁻²]	accumulated leaf area above ground (total leaf area index, LAI)
λ_1	[degrees]	latitude
Λ_z	[m ² m ⁻²]	accumulated leaf area above z
$\nu_{ref}(z_i)$	[m s ⁻¹]	effective velocity for transfer from layer height z_i to z_{ref}
ψ_{soil}	[m]	soil matrix potential (superscript * denoting maximum ψ_{soil})
ρ_{cx}	[-]	canopy reflection coefficient with subscripts $x = d, b$ and N, V denoting diffuse or beam, and visible or near-infrared radiation, respectively
ρ_h	[-]	canopy reflection coefficient for horizontal leaves
σ_B	[W m ⁻² K ⁻⁴]	Stefan-Boltzmann constant (5.67051×10^{-8})
σ_{lx}	[-]	scattering coefficient with subscripts $x = d, b$ and N, V denoting diffuse or beam, and visible or near-infrared radiation, respectively
$\tau_{ref}(z_i)$	[s]	timescale for transfer from layer height z_i to z_{ref}
τ_a	[-]	atmospheric transmissivity
θ	[-]	shape coefficient of the hyperbolic light response function for photosynthesis

D.3 Latin symbols

A_J	[μ mol m ⁻² s ⁻¹]	gross rate of photosynthesis limited by RuP ₂ regeneration
A^{U-FU}		aggregated data sets for the BPN application
A_n	[μ mol m ⁻² s ⁻¹]	net assimilation rate
A_v	[μ mol m ⁻² s ⁻¹]	gross rate of photosynthesis limited by Rubisco activity
a_{σ_c}	[m s ⁻¹]	height function for convective scaling of $\sigma_w(z)$
a_{σ_f}	[-]	normalized height function for friction scaling of $\sigma_w(z)$
a_A	[-]	empirical parameter relating stomatal conductance to assimilation
$a_{c1,2}$	[-]	coefficients for a_{σ_c} (Appendix A.8)

$a_{f0,1,2}$	[-]	coefficients for $a_{\sigma f}$ (Appendix A.8)
$a_{i1,2}$	[-]	coefficients for the Λ_z function with $i = T, B$ for top and bottom canopy layer, respectively
$a_{s1,2}$	[-]	coefficients in Eq. A.19
a_{u0}	[m s ⁻¹]	intercept of the linear regression $u(z) = a_{u0} + a_{u1}u_{ref}$
a_{u1}	[-]	slope of the linear regression $u(z) = a_{u0} + a_{u1}u_{ref}$
b_x	[-]	substitutions of the coupled leaf model equations with subscripts 0-2 (see Appendix A.5)
C1-C7		single data sets (cases) for the BPN application
C_x		scalar concentration with subscripts s, a, ref denoting the leaf surface, ambient air, and reference height level, respectively
c_N	[g m ⁻²]	leaf nitrogen concentration
\bar{c}_{o3}	[ppb]	mean ozone concentration of the preceding 48 hours
c_p^m	[J mol ⁻¹ K ⁻¹]	specific heat of air
c_x	[μ mol mol ⁻¹]	CO ₂ concentration with subscripts $soil, i, s, a, ref$ denoting the soil, intercellular, leaf surface, ambient air, and reference height level, respectively
D_H	[m ² s ⁻¹]	molecular diffusivity of heat
D_{s0}	[hPa]	empirical coefficient reflecting sensitivity of the stomata to D_s
D_x	[hPa]	water vapor pressure deficit with subscripts $soil, i, s, a, ref$ denoting the soil, intercellular, leaf surface, ambient air, and reference height level, respectively
d_h	[m]	zero length displacement height
$d(i, j)$	[s m ⁻¹]	dispersion coefficient from layer i to layer j with superscripts far and $near$ denoting the far and near field, respectively
d_x		substitutions to solve the coupled leaf model (Appendix A.5)
E	[mmol m ⁻² s ⁻¹]	leaf transpiration
E_v^a	[nmol m ⁻² s ⁻¹]	VOC emission on leaf area basis (subscript 0 denotes the standard emission factor)
E_v^m	[μ g C g ⁻¹ h ⁻¹]	VOC emission on leaf mass basis (subscript 0 denotes the standard emission factor)
e_x	[mmol mol ⁻¹]	water vapor concentration with subscripts $soil, i, s, a, ref$ denoting the soil, intercellular, leaf surface, ambient air, and reference height level, respectively
F		trace gas flux expressed on ground area
F_{csoil}	[μ mol m ⁻² s ⁻¹]	soil respiration (subscript 0 denotes F_{csoil} at T_{soil0})
F_{leaf}		trace gas flux expressed on leaf area
f_ψ	[-]	empirical function expressing stomatal sensitivity to water availability in the root zone
$f_{SL,SH}$	[-]	sunlit (SL) or shaded (SH) leaf fraction
$f_{d,b}$	[-]	diffusive (d) or direct beam (b) fraction of radiation
G	[W m ⁻²]	soil heat flux
Gr	[-]	Grashof number
g_b	[mol m ⁻² s ⁻¹]	leaf boundary layer conductance with subscripts H, w, c denoting the scalars heat, water, and CO ₂ , and u, f denoting the convective and forced part of g_b , respectively
g_{rad}	[mol m ⁻² s ⁻¹]	radiative conductance
g_s	[mol m ⁻² s ⁻¹]	stomatal conductance with subscripts w and c denoting the scalars water and CO ₂
g_t	[mol m ⁻² s ⁻¹]	total conductance with subscripts H, w, c denoting the scalars heat, water, and CO ₂

$gRad$	$[W\ m^{-2}]$	incoming global radiation (subscript 0 denotes the potential global radiation)
H	$[W\ m^{-2}]$	sensible heat flux
H_x	$[J\ mol^{-1}]$	energy with subscripts d and v and Ko, Kc, Rd, V, J , and $soil$ denoting the activation and deactivation of $K_c, K_o, R_d, v_{cmax}, J_{max}$, and F_{csoil} , respectively
h_c	$[m]$	mean canopy height
I_x		the beta function (Appendix A.7)
J	$[\mu mol\ m^{-2}\ s^{-1}]$	electron transport rate
$J_{220,222}$	$[Bq\ m^{-2}\ s^{-1}]$	soil flux of ^{220}Rn and ^{222}Rn
J_{max}	$[\mu mol\ m^{-2}\ s^{-1}]$	potential rate of whole-chain electron transport (subscript 0 denotes J_{max} at T_{s0})
K_c	$[\mu mol\ m^{-2}\ s^{-1}]$	Michaelis coefficient for CO_2
K_o	$[mmol\ m^{-2}\ s^{-1}]$	Michaelis coefficient for O_2
k_N	$[-]$	extinction coefficient for c_N
$k_{d,b}^{(B)}$	$[-]$	extinction coefficient for diffusive (d) or beam (b) radiation with superscript B denoting black leaves
k_u	$[-]$	extinction coefficient for u
L_s	$[m]$	canopy length scale
L_w	$[m]$	the Eulerian length scale
LE	$[W\ m^{-2}]$	latent heat flux
N_{LS}	$[-]$	exchanging leaf sides (hypostomatous=1, amphistomatous=2)
o_i	$[mmol\ mol^{-1}]$	intercellular oxygen concentration
P_0	$[hPa]$	air pressure at the reference height
Q_{10}	$[m^3\ s^{-1}]$	change rate of a biological process for a temperature increase of $10^\circ C$
Q_{LW}	$[W\ m^{-2}]$	long wave radiation (\downarrow and \uparrow indicate incoming and outgoing direction, respectively)
$Q_{N0,V0}$	$[W\ m^{-2}]$	visible ($V0$) or near-infrared ($N0$) radiation
Q_{PAR}	$[\mu mol\ m^{-2}\ s^{-1}]$	photosynthetic active radiation
$Q_{SH,SL}$	$[W\ m^{-2}]$	radiation absorbed by sunlit (SL) or shaded (SH) leaves
Q_{SW}	$[W\ m^{-2}]$	short-wave radiation
$Q_{d,b,sb}$	$[W\ m^{-2}]$	diffusive (d), direct beam (b) or scattered (sb) beam radiation
Q_n	$[W\ m^{-2}]$	net radiation
Q_n^*	$[W\ m^{-2}]$	isothermal net radiation assuming $T_s = T_a$
q_{V0}	$[m^3\ s^{-1}]$	flow rate in the static chamber system
R	$[J\ mol^{-1}\ K^{-1}]$	universal gas constant (8.3145)
R_d	$[\mu mol\ m^{-2}\ s^{-1}]$	day respiration
RH_x	$[-]$	relative humidity with subscripts $soil, i, s, a, ref$ denoting the soil, intercellular, leaf surface, ambient air, and reference height level, respectively
r_x	$[s\ m^{-1}]$	resistance with subscript $a, b, c, leaf, m, root, s$, and $soil$ denoting the aerodynamic, leaf-boundary layer, cuticular, leaf, mesophyll, root, stomatal, soil bulk resistance, respectively
S_{V0}	$[m^2]$	static chamber surface
$S_{v,d}$	$[J\ mol^{-1}]$	entropy for activation (v) and deactivation (d)
S_c	$[W\ m^{-2}]$	solar constant
S_i		source/sink of layer i
s	$[hPa\ K^{-1}]$	slope of the curve relating saturation water vapor pressure to temperature
T_E	$[s]$	the Eulerian timescale

T_L	[s]	the Lagrangian timescale
T_x	[K]	temperature with subscripts <i>soil, i, s, a, ref</i> denoting the soil, intercellular, leaf surface, ambient air, and reference height level, respectively
T_{x0}	[K]	reference temperature
\bar{T}_x	[K]	temperature history with subscript x denoting the 3, 6, 12, 18, 24, 36 and 48 preceding hours
t_d	[days]	time of the year
t_{dl}	[hours]	day length
t_h	[hours]	local solar time
u	[m s ⁻¹]	horizontal wind speed (subscript <i>ref</i> denotes the reference height)
u_*	[m s ⁻¹]	friction velocity
V_0	[m ⁻³]	volume of the static chamber system
v_{cmax}	[$\mu\text{mol e m}^{-2}$ s ⁻¹]	maximum catalytic activity of Rubisco, (subscripts 0 and <i>hc</i> denote v_{max} at T_{s0} and at the canopy top, respectively)
v_d	[cm s ⁻¹]	deposition velocity
w_i	[-]	weight coefficients for the parameterization of Λ_z with $i = T$ and $i = B$ for top and bottom canopy maximum leaf area density
w_l	[m]	mean leaf width
z	[m]	height above ground
z_0	[m]	roughness length
$z_{\sigma c}$	[m]	scaling height for $a_{\sigma c}$
$z_{\sigma f}$	[m]	scaling height above which $a_{\sigma f} = 1$
z_{ref}	[m]	reference height above h_c
z_i	[m]	mean layer height
z_i^*	[m]	scaling height for parameterization of canopy structure

List of Figures

1.1	Comparison of different canopy exchange schemes	4
1.2	Components of the multi-layer canopy model	7
2.1	Illustration of site specific parameter profiles	15
2.2	Tower location and wetlands of the Amazon basin	18
2.3	Parameterization of canopy structure and accumulated leaf area .	22
2.4	Parameterization of the vertical profile of horizontal wind speed .	23
2.5	Comparison of observed and predicted atmospheric emissivity and incoming long-wave radiation	24
2.6	Absorbed radiation and albedo in relation to the number of canopy layers, leaf area index, and leaf optical parameters	25
2.7	Observed and predicted incoming PAR and in-canopy light gradients	28
2.8	Comparison of observed and predicted soil heat flux	30
2.9	Vertical distribution of maximum carboxylation rate and leaf ni- trogen concentration	31
2.10	Scaling of leaf physiology for the evaluation of leaf model parameters	32
2.11	Light response and comparison of observed and predicted net as- similation for different seasonal conditions and tree species	33
2.12	Observed and predicted stomatal conductance for single tree species	35
3.1	Sample heights and discretization scheme of source layers and con- centration heights for ^{222}Rn , CO_2 , and H_2O at the Cuieiras site .	43
3.2	Canopy structure observed at the Jaru and Cuieiras sites	45
3.3	Observed profiles of the standard deviation of vertical wind speed	49
3.4	Parameterization of the standard deviation of vertical wind speed	50
3.5	Parameterization of the Lagrangian timescale (T_L)	51
3.6	Meteorological conditions at the Cuieiras site	52
3.7	Observed ^{220}Rn and ^{222}Rn soil fluxes	53
3.8	Comparison of observed and predicted ^{222}Rn concentrations	55

3.9	Significance of nighttime free convection on vertical profiles of ^{222}Rn	55
3.10	Observed and predicted timescales and transfer velocities	57
3.11	Inversely predicted source/sink distribution of ^{222}Rn and sensitivity to the input concentration profile	58
3.12	Comparison of observed and predicted net fluxes of CO_2 and H_2O	59
3.13	Mean observed and inversely predicted source/sink distribution of CO_2 and H_2O	61
3.14	Inversely predicted integrated net carbon exchange	62
4.1	Typical meteorological conditions during the late wet (EUST-I) and late dry (EUST-II) season in Rondônia	69
4.2	Diurnal course of the predicted temperature gradients and the number of required model iterations	74
4.3	Simulated vertical profiles of surface and canopy air temperature .	75
4.4	Model sensitivity to leaf optical parameters and canopy structure	77
4.5	Model sensitivity to stomatal and leaf photosynthesis parameters	78
4.6	Comparison of observed and predicted energy fluxes for EUST-I and EUST-II	80
4.7	Comparison of observed and predicted CO_2 fluxes for EUST-I and EUST-II	81
4.8	Seasonal comparison of predicted midday source/sink distributions and flux profiles for energy and net assimilation	82
4.9	Comparison of observed and predicted day- (14 h) and nighttime (2 h) H_2O and CO_2 concentration profiles	83
4.10	Comparison of observed and predicted nighttime CO_2 profiles and model sensitivity to parameter uncertainty	85
4.11	Predicted isoprene emission fluxes and midday source/sink distribution	87
4.12	Comparison of observed (closed quarters) and predicted isoprene concentration profiles for EUST-II	88
4.13	Simulated midday sink distribution and comparison of observed and predicted ozone net fluxes for EUST-I and EUST-II	91
4.14	Comparison of observed and predicted vertical ozone concentration profiles for day- and nighttime conditions	92
4.15	Predicted change of canopy net fluxes for doubled atmospheric CO_2 concentrations	96
5.1	Topology of a Back Propagation Neural Network (BPN).	104
5.2	Data and model simulation overview.	105
5.3	Overtraining during the training phase of a BPN simulation.	109
5.4	Comparison of mean predicted VOC emission for test and trained data.	110
5.5	A simulation testing the ability to predict G93 output by a BPN.	111

5.6	Comparison of observed and predicted VOC emission for single data sets.	112
5.7	Relative performance of selected parameter combinations applied to single data sets.	114
5.8	Relative performance of all parameter combinations applied to aggregation data sets.	115
5.9	Comparison of the performance of G93 and the BPN approach for aggregation data sets.	116
5.10	Comparison of observed and predicted VOC emission rates.	118
5.11	Relative performance of different parameter combination types compared to G93 for single and aggregation data sets.	119
B.1	Radon flux measurement example	158

List of Tables

1.1	Micrometeorological input parameters	6
2.1	Site and tower locations	18
2.2	Field data used for derivation and evaluation of model parameters	19
2.3	Parameter values for the height function of cumulative leaf area .	27
2.4	Applied length scales	27
2.5	Leaf optical parameters	27
3.1	Different parameterizations of the standard deviation of vertical wind speed given in the literature	47
3.2	Parameters for the normalized profiles of the standard deviation of vertical wind speed	51
3.3	Comparison of mean observed radon soil flux (J_{222}) with other measurements in the Amazon basin.	54
4.1	Seasonal comparison of climatic variables observed at the Jaru site in Rondônia.	70
4.2	Values of key parameters applied in the sensitivity study	71
4.3	Up-scaling of isoprene emission	95
5.1	Applied single data sets of VOC exchange measurements.	103
5.2	Applied input parameters.	107
5.3	Setup of the neural network.	108
5.4	Applied parameter combinations and regression results for G93 and the BPN approach for single data sets.	113
5.5	Regression results for two selected aggregation data sets.	117
A.1	Photosynthesis and stomatal conductance model parameters . . .	148

Zusammenfassung

Die vorliegende Dissertation untersucht die biogeochemischen Vorgänge in der Vegetationsschicht (Bestand) und die Rückkopplungen zwischen physiologischen und physikalischen Umweltprozessen, die das Klima und die Chemie der unteren Atmosphäre beeinflussen. Ein besondere Schwerpunkt ist die Verwendung theoretischer Ansätze zur Quantifizierung des vertikalen Austauschs von Energie und Spurengasen (Vertikalfluss) unter besonderer Berücksichtigung der Wechselwirkungen der beteiligten Prozesse. Es wird ein differenziertes Mehrschicht-Modell der Vegetation hergeleitet, implementiert, für den amazonischen Regenwald parametrisiert und auf einen Standort in Rondônia (Südwest Amazonien) angewendet, welches die gekoppelten Gleichungen zur Energiebilanz der Oberfläche und CO₂-Assimilation auf der Blattskala mit einer Lagrange-Beschreibung des Vertikaltransports auf der Bestandesskala kombiniert. Die hergeleiteten Parametrisierungen beinhalten die vertikale Dichteverteilung der Blattfläche, ein normiertes Profil der horizontalen Windgeschwindigkeit, die Lichtakklimatisierung der Photosynthesekapazität und den Austausch von CO₂ und Wärme an der Bodenoberfläche. Desweiteren werden die Berechnungen zur Photosynthese, stomatären Leitfähigkeit und der Strahlungsabschwächung im Bestand mithilfe von Feldmessungen evaluiert. Das Teilmodell zum Vertikaltransport wird im Detail unter Verwendung von ²²²Radon-Messungen evaluiert. Die "Vorwärtslösung" und der "inverse Ansatz" des Lagrangeschen Dispersionsmodells werden durch den Vergleich von beobachteten und vorhergesagten Konzentrationsprofilen bzw. Bodenflüssen bewertet. Ein neuer Ansatz wird hergeleitet, um die Unsicherheiten des inversen Ansatzes aus denjenigen des Eingabekonzentrationsprofils zu quantifizieren. Für nächtliche Bedingungen wird eine modifizierte Parametrisierung der Turbulenz vorgeschlagen, welche die freie Konvektion während der Nacht im unteren Bestand berücksichtigt und im Vergleich zu früheren Abschätzungen zu deutlich kürzeren Aufenthaltszeiten im Bestand führt. Die vorhergesagte Stratifizierung des Bestandes am Tage und in der Nacht steht im Einklang mit Beobachtungen in dichter Vegetation. Die Tagesgänge der vorhergesagten Flüsse und

skalaren Profile von Temperatur, H_2O , CO_2 , Isopren und O_3 während der späten Regen- und Trockenzeit am Rondônia-Standort stimmen gut mit Beobachtungen überein. Die Ergebnisse weisen auf saisonale physiologische Änderungen hin, die sich durch höhere stomatäre Leitfähigkeiten bzw. niedrigere Photosyntheseraten während der Regen- und Trockenzeit manifestieren. Die beobachteten Depositionsgeschwindigkeiten für Ozon während der Regenzeit überschreiten diejenigen der Trockenzeit um 150-250%. Dies kann nicht durch realistische physiologische Änderungen erklärt werden, jedoch durch einen zusätzlichen cuticulären Aufnahmemechanismus, möglicherweise an feuchten Oberflächen. Der Vergleich von beobachteten und vorhergesagten Isoprenkonzentrationen im Bestand weist auf eine reduzierte Isoprenemissionskapazität schattenadaptierter Blätter und zusätzlich auf eine Isoprenaufnahme des Bodens hin, wodurch sich die globale Schätzung für den tropischen Regenwald um 30% reduzieren würde. In einer detaillierten Sensitivitätsstudie wird die VOC Emission von amazonischen Baumarten unter Verwendung eines neuronalen Ansatzes in Beziehung zu physiologischen und abiotischen Faktoren gesetzt. Die Güte einzelner Parameterkombinationen bezüglich der Vorhersage der VOC Emission wird mit den Vorhersagen eines Modells verglichen, das quasi als Standardemissionsalgorithmus für Isopren dient und Licht sowie Temperatur als Eingabeparameter verwendet. Der Standardalgorithmus und das neuronale Netz unter Verwendung von Licht und Temperatur als Eingabeparameter schneiden sehr gut bei einzelnen Datensätzen ab, scheitern jedoch bei der Vorhersage beobachteter VOC Emissionen, wenn Datensätze von verschiedenen Perioden (Regen/Trockenzeit), Blattentwicklungsstadien, oder gar unterschiedlichen Spezies zusammengeführt werden. Wenn dem Netzwerk Informationen über die Temperatur-Historie hinzugefügt werden, reduziert sich die nicht erklärte Varianz teilweise. Eine noch bessere Leistung wird jedoch mit physiologischen Parameterkombinationen erzielt. Dies verdeutlicht die starke Kopplung zwischen VOC Emission und Blattphysiologie.

Selbständigkeitserklärung

Hiermit erkläre ich, die vorliegende Arbeit selbständig ohne unerlaubte Hilfsmittel verfaßt und nur die angegebene Literatur verwendet zu haben.

Eric Simon,
23. Mai 2004